Propagation multimodale par éléments finis appliquée au contrôle de structures intelligentes

Tianli Huang

To cite this version:

Tianli Huang. Propagation multimodale par éléments finis appliquée au contrôle de structures intelligentes. Other. Ecole Centrale de Lyon, 2012. English. NNT : 2012ECDL0041 . tel-00946214

HAL Id: tel-00946214
https://theses.hal.science/tel-00946214

Submitted on 13 Feb 2014

Numéro d'ordre: 2012-41 Année: 2012

Thèse de Doctorat

présentée pour obtenir le titre de

DOCTEUR

de l'ÉCOLE CENTRALE DE LYON

dans le cadre de l'**École Doctorale MEGA**

(Mécanique, Énergétique, Génie civil, Acoustique)

Spécialité : ACOUSTIQUE

par

Tianli HUANG

Ingénieur de l'École Centrale de Lyon

Multi-modal propagation through finite elements applied for the control of smart structures

Présentée et soutenue publiquement le 20/11/2012 à l'École Centrale de Lyon, devant le jury d'examen:

A. Benjeddou, Professeur, Supméca	Rapporteur
H. Lissek, Directeur de recherche, EPFL	Rapporteur
B. Troclet, Senior Expert, Astrium & Professeur ENS Cachan	Examinateur
M. Ouisse, Professeur, ENSMM	Examinateur
M.A. Galland, Professeur, ECL	Examinateur
M.N. Ichchou, Professeur, ECL	Directeur de thèse
M. Collet, Directeur de recherche, FEMTO-ST	Co-directeur
O. Bareille, Maître de conférences, ECL	Co-encadrant

Laboratoire de Tribologie et Dynamique des Systèmes, UMR-CNRS 5513
36 Avenue Guy de Collongue, 69134 Ecully Cedex, FRANCE

ÉCOLE CENTRALE LYON **Direction de la recherche**

Liste des personnes Habilitées à Diriger des Recherches en poste à l'Ecole Centrale de Lyon

Nom-Prénom	Corps grade	Laboratoire ou à défaut département ECL	Etablissement
BEROUAL Abderrahmane	professeur	AMPERE	ECL
BURET François	professeur	AMPERE	ECL
JAFFREZIC-RENAULT Nicole	directeur de recherche	AMPERE	CNRS/ECL
KRÄHENBÜHL Laurent	directeur de recherche	AMPERE	CNRS/ECL
NICOLAS Alain	professeur	AMPERE	ECL
NICOLAS Laurent	directeur de recherche	AMPERE	CNRS/ECL
SCORLETTI Gérard	professeur	AMPERE	ECL
SIMONET Pascal	directeur de recherche	AMPERE	CNRS/ECL
VOLLAIRE Christian	professeur	AMPERE	ECL

Nbre Ampère 9

HELLOUIN Yves	maître de conférences	DER EEA	ECL

Nbre DER EEA 1

GUIRALDENQ Pierre	professeur émérite	DER STMS	ECL
VINCENT Léo	professeur	DER STMS	ECL

Nbre DER STMS 2

LOHEAC Jean-Pierre	maître de conférences	ICJ	ECL
MAITRE Jean-François	professeur émérite	ICJ	ECL
MARION Martine	professeur	ICJ	ECL
MIRONESCU Elisabeth	professeur	ICJ	ECL
MOUSSAOUI Mohand	professeur	ICJ	ECL
MUSY François	maître de conférences	ICJ	ECL
ZINE Abdel-Malek	maître de conférences	ICJ	ECL

Nbre ICJ 7

CALLARD Anne-Ségolène	professeur	INL	ECL
CLOAREC Jean-Pierre	maître de conférences	INL	ECL
GAFFIOT Frédéric	professeur	INL	ECL
GAGNAIRE Alain	maître de conférences	INL	ECL
GARRIGUES Michel	directeur de recherche	INL	CNRS/ECL
GENDRY Michel	directeur de recherche	INL	CNRS/ECL
GRENET Geneviève	directeur de recherche	INL	CNRS/ECL
HOLLINGER Guy	directeur de recherche	INL	CNRS/ECL
KRAWCZYK Stanislas	directeur de recherche	INL	CNRS/ECL
LETARTRE Xavier	chargé de recherche	INL	CNRS/ECL
O'CONNOR Ian	professeur	INL	ECL
PHANER-GOUTORBE Magali	professeur	INL	ECL
ROBACH Yves	professeur	INL	ECL
SAINT-GIRONS Guillaume	chargé de recherche	INL	CNRS/ECL
SEASSAL Christian	directeur de recherche	INL	CNRS/ECL

SOUTEYRAND Eliane	*directeur de recherche*	INL	CNRS/ECL
TARDY Jacques	*directeur de recherche*	INL	CNRS/ECL
VIKTOROVITCH Pierre	*directeur de recherche*	INL	CNRS/ECL

Nbre INL 18

CHEN Liming	*professeur*	LIRIS	ECL
DAVID Bertrand	*professeur*	ICTT	ECL

Nbre LIRIS 2

BAILLY Christophe	*professeur*	LMFA	ECL
BERTOGLIO Jean-Pierre	*directeur de recherche*	LMFA	CNRS/ECL
BLANC-BENON Philippe	*directeur de recherche*	LMFA	CNRS/ECL
BOGEY Christophe	*chargé de recherche*	LMFA	CNRS/ECL
CAMBON Claude	*directeur de recherche*	LMFA	CNRS/ECL
CARRIERE Philippe	*directeur de recherche*	LMFA	CNRS/ECL
CHAMPOUSSIN J-Claude	*professeur émérite*	LMFA	ECL
COMTE-BELLOT genevièvre	*professeur émérite*	LMFA	ECL
FERRAND Pascal	*directeur de recherche*	LMFA	CNRS/ECL
GALLAND Marie-Annick	*professeur*	LMFA	ECL
GODEFERD Fabien	*directeur de recherche*	LMFA	CNRS/ECL
GOROKHOVSKI Mikhail	*professeur*	LMFA	ECL
HENRY Daniel	*directeur de recherche*	LMFA	CNRS/ECL
JEANDEL Denis	*professeur*	LMFA	ECL
JUVE Daniel	*professeur*	LMFA	ECL
LE RIBAULT Catherine	*chargée de recherche*	LMFA	CNRS/ECL
LEBOEUF Francis	*professeur*	LMFA	ECL
PERKINS Richard	*professeur*	LMFA	ECL
ROGER Michel	*professeur*	LMFA	ECL
SCOTT Julian	*professeur*	LMFA	ECL
SHAO Liang	*directeur de recherche*	LMFA	CNRS/ECL
SIMOENS Serge	*chargé de recherche*	LMFA	CNRS/ECL
TREBINJAC Isabelle	*maître de conférences*	LMFA	ECL

Nbre LMFA 23

BENAYOUN Stéphane	*professeur*	LTDS	ECL
CAMBOU Bernard	*professeur*	LTDS	ECL
COQUILLET Bernard	*maître de conférences*	LTDS	ECL
DANESCU Alexandre	*maître de conférences*	LTDS	ECL
FOUVRY Siegfrid	*chargé de recherche*	LTDS	CNRS/ECL
GEORGES Jean-Marie	*professeur émérite*	LTDS	ECL
GUERRET Chrystelle	*chargé de recherche*	LTDS	CNRS/ECL
HERTZ Dominique	*past*	LTDS	ECL
ICHCHOU Mohamed	*professeur*	LTDS	ECL
JEZEQUEL Louis	*professeur*	LTDS	ECL
JUVE Denyse	*ingénieur de recherche*	LTDS	ECL
KAPSA Philippe	*directeur de recherche*	LTDS	CNRS/ECL
LE BOT Alain	*directeur de recherche*	LTDS	CNRS/ECL
LOUBET Jean-Luc	*directeur de recherche*	LTDS	CNRS/ECL
MARTIN Jean-Michel	*professeur*	LTDS	ECL
MATHIA Thomas	*directeur de recherche*	LTDS	CNRS/ECL
MAZUYER Denis	*professeur*	LTDS	ECL
PERRET-LIAUDET Joël	*maître de conférences*	LTDS	ECL
SALVIA Michelle	*maître de conférences*	LTDS	ECL
SIDOROFF François	*professeur*	LTDS	ECL
SINOU Jean-Jacques	*professeur*	LTDS	ECL
STREMSDOERFER Guy	*professeur*	LTDS	ECL

THOUVEREZ Fabrice	*professeur*	LTDS	ECL
TREHEUX Daniel	*professeur*	LTDS	ECL
VINCENS Eric	*maître de conférences*	LTDS	ECL
		Nbre LTDS 25	
	Total HdR ECL	91	

Remerciements

Tout d'abord, je voudrais remercier mon directeur de thèse, Professeur Mohammed Ichchou, de son guide, son soutien, et sa patience pour moi, et également sa confiance sur moi pendant ces années de thèse. Il est la personne qui m'a influencé le plus durant mes 5 ans d'études en France depuis l'année 2007, quand j'ai été sélectionné par le programme d'échange entre l'Université de Beihang et l'Ecole Centrale de Lyon. Non seulement un directeur de thèse, mais aussi un tuteur mental, avec non seulement le transfert de savoir-faires mais aussi le guide pour moi de devenir un homme que je souhaite devenir, n'ayant peur de rien.

Je voudrais exprimer mes gratitudes à Dr. Olivier Bareille pour son aide et son guide pendant le travail de ma thèse, et mes études d'ingénieur aussi. C'était lui qui m'a donné le premier cours de français scientifique et m'a introduit dans le monde d'études d'ingénieur en France. Non seulement un chercheur et professeur très doué, mais aussi un génie en langues, surtout en chinois.

J'aimerais bien donner un grand merci à Dr. Manuel Collet pour son aide et soutien pendant mon travail dans le projet CALIOP. Je suis influencé profondément par son attitude strict vers soi-même et sa façon rigoureuse de faire la recherche.

Je veux remercier sincèrement Dr. Wenjin Zhou de son aide pratique et son guide depuis le début de mon stage de Master jusqu'à son départ de notre laboratoire. Il a établi un très bon exemple pour tous les étudiants dans l'équipe et il nous encourage toujours à devenir de plus en plus bon en recherche.

Je voudrais bien aussi exprimer mes gratitudes à Madame Cheng Sun pour sa gentillesse et son soutien dès le début de mes études en France, et pour sa confiance sur moi durant les cours de chinois aux élèves-ingénieurs à l'école. Je me suis beaucoup amusé en donnant les cours de chinois et cette expérience me permet d'améliorer mon niveau de français d'une façon continue, et d'apprendre comment bien interagir avec des élèves en tant qu'un enseignant compétent.

Mes remerciements sincères sont aussi étendus à tous mes collègues dans l'équipe D2S et à l'institut FEMTO-ST, et à tous mes amis pour leurs soutiens techniques et personnels, et surtout leur amitié. Je n'oublierai jamais des moments heureux passés avec vous pendant les conférences, les buffets internationaux, les barbecues, et bien sûr au terrain de basketball...et un grand merci pour vous de partager mes douleurs et difficultés.

Finalement, je veux exprimer mes grands remerciements à mes chers parents, et tous les autres membres de famille, pour leurs encouragements et soutiens pendant mes études en France. Dans la poursuite de mon rêve, si je n'avais pas eu leurs amours, je n'aurais pas pu continuer à avancer. J'espère qu'ils sont toujours fiers de moi et qu'ils ont bien vu comment j'ai grandi et développé. Je reviendrai vers eux en tant qu'un vrai homme, et je ne serai plus le garçon il y a 5 ans.

Je vous aime.

Acknowledgements

First of all, I would like to thank my supervisor, Professor Mohammed Ichchou, for his guidance, support and patience for me, as well as his confidence in me through all these years. He is the person who influences me most during my 5 years' study in France, since the year 2007 when I was selected by the exchange program between Beihang University and Ecole Centrale de Lyon. Not only a thesis supervisor but also a mental tutor, with not only the transfer of knowledge and idea, but also the guidance on my way to be a man that I want to be, fearing nothing.

I wish to express my gratitude to Dr. Olivier Bareille, for his kind help and guidance during my thesis work as well as my engineer study. It was him who gave me the first scientific French course and introduced me into the world of French engineer study. Not only a talented researcher and teacher, but also a genius on languages, especially on Chinese.

I would like to give my thanks to Dr. Manuel Collet for his great help and support during my work in the CALIOP project. I'm deeply influenced by his strict attitude and rigorous way of research.

My sincere thanks to Dr. Wenjin Zhou for his practical help and support since the beginning of my Master internship until his departure from our laboratory. He sets up a good example for all the students, and encourages us to become better and better.

I would like to give my acknowledgements to Madam Cheng Sun for her kind help and support since the beginning of my study in France, and for her confidence in me during the Chinese courses for engineer students. I really enjoyed a lot by giving Chinese courses, and this experience enables me to improve my French in a continuous way, and to learn to interact well with my students as a competent teacher.

My sincere acknowledgements are also extended to all my colleagues in the D2S group and in FEMTO-ST institute, and all my friends at Ecole Centrale de Lyon for their continuing technical and personal support, especially their friendship. I'll never forget the joyful moments passed with them during the conferences, international buffets, barbecue parties, and of course on the basketball court...and great thanks for sharing my pain and difficulties.

Finally, I would like to express my huge thanks to my beloved parents, and all other family members for their encouragement and support for my study in France. On my way to realize my dream, without their love, I wouldn't be able to keep going on. Hope that they are always proud of me and see my growth and progress. I will be returning to them as a man, no longer like the boy 5 years ago.

I love you all.

致谢

首先我要感谢我的导师Mohammed Ichchou教授对我悉心的指导和支持，还有这几年以来对我的信任。自从2007年我被北航和里昂中央理工大学的交换项目选中以来，他是我在法国这5年的学业里对我影响最深的人。既是博士生导师，又是精神导师，不但传授我知识，而且还指导我去成为我想要成为的人，无所畏惧。

我同样要感谢Olivier Bareille博士，感谢他在我博士工作阶段，以及在工程师学习阶段对我的帮助和支持。他给我讲授了第一堂科技法语课，把我带进了法国工程师学习的大门。他既是一位出色的研究员和老师，也是一位语言天才，尤其是汉语天赋异禀。

我也想对Manuel Collet博士表达我的谢意，他的帮助和支持让我在CALIOP项目里获益匪浅。他严于律己的态度和严谨的科研风格让我印象深刻。

对周文晋师兄的感谢我也很难用言语表达了。真的没什么办法回报他这几年以来对我的帮助，只有把他发表过的论文多加以引用，以表敬意了。这些论文都是我博士阶段工作重要的参考文献。文晋师兄为我们实验室所有中国学生设定了一个优秀的标准，鼓励我们不断进步。

我同样要对白澄女士表达我衷心的感谢，自从我来法国开始学习的那一天起，就一直受到她的关照。非常感谢她对我的信任，我觉得我也合格地完成了她交给我的汉语教学任务。这段教学经历不但让我能进一步提高我的法语水平，也让我学习怎么样更好地跟学生交流，好好体验了一下当老师的感觉。

我的谢意同样要传达给D2S小组和贝桑松微机电学院的同事们，还有我在里昂中央理工大学的朋友们。感谢他们在技术方面对我的支持和对我个人的关心，这份友谊我会铭记于心。毫不客气地说，D2S小组是里昂中央理工大学里人文关怀最好的小组，里昂中央理工是所有中央理工学校里最让人觉得温暖的学校。我永远不会忘记跟他们在各种聚会，派对，还有篮球场上度过的愉快的时光，也很感激他们在我困苦的时候能分担我的忧伤。

最后，我要对我亲爱的爸爸妈妈说一句感谢，也要感谢我的其他亲人们对我在法国留学期间的关心、支持和鼓励。在我追求梦想的道路上，没有他们的爱，我可能坚持不下去。希望他们看得到我的成长和发展，也希望他们一直为我而骄傲。我会在不远的将来，作为一个真正的男人回到他们的身边，不会再像5年以前那个的男孩一样了。

我爱你们。

Multi-modal propagation through finite elements applied for the control of smart structures

Abstract: The analysis of wave propagation in complex structures and its application for the semi-active control of smart structures and health monitoring of these structures are dealt with in this thesis. The design of composite structures with shunted piezoelectric patches is one of the main objectives of all the investigations. This kind of smart composite structures is equipped with periodically distributed shunted piezoelectric patches. Former studies have shown the great interest of such a configuration for the active damping of structural modes at low frequencies. This thesis is focused on the extension of all these interesting characteristics of the smart structures to a larger frequency band: low and medium frequencies. The mastering of the propagation parameters and energy diffusion characteristics is targeted.

In this context, the proposed work is based on techniques specifically developed in the research team "Dynamics of Systems and Structures"(D2S): the Wave Finite Element(WFE) method and Diffusion Matrix Model(DMM). The WFE approach is constructed via the finite element model of a unit cell, representative of the waveguide structure. It enables the calculation of essential wave propagation parameters like wavenumbers. The DMM, associated with the WFE approach, enables the calculation of energy diffusion characteristics like reflection and transmission coefficients of specific wave modes. These approaches are extended to consider shunted piezoelectric elements and then to evaluate the performance of shunted piezoelectric patches on the control of wave propagation in the aforementioned smart composite structures. Intensive optimizations can be carried out, with these tools, so as to obtain optimal geometric and electric parameters in the design of these smart structures.

The present work is integrated in the CALIOP project in cooperation with the Laboratory of Applied Mechanics R.Chaléat at FEMTO-ST Institute and the G.W. Woodruff School of Mechanical Engineering of Georgia Institute of Technology.

Keywords: Wave propagation, wave finite element, piezoelectricity, semi-active control, energy diffusion

Propagation multimodale par éléments finis appliquée au contrôle de structures intelligentes

Résumé: Le sujet de thèse concerne l'analyse de la propagation des ondes dans les structures complexes et leurs exploitations pour le contrôle semi-actif et le contrôle de santé de structures intelligentes. Les structures composites munies de patches piézoélectriques sont la cible principale des investigations. Les patches piézoélectriques sont disposés avec une périodicité. Des travaux précédents ont montré l'intérêt de ce type de configuration pour l'amortissement actif de modes de structures en basses fréquences. L'objectif principal de cette thèse est l'extension de ces constatations dans une bande de fréquences plus large : basses et moyennes fréquences. La maîtrise des paramètres de propagation et de diffusion des ondes est la finalité recherchée. Dans ce cadre, les travaux proposés se baseront sur une technique particulière développée au sein de l'équipe Dynamique des Systèmes et des Structures : la technique WFE (Wave Finite Element), Ondes par éléments finis. Cette approche, construite à l'aide d'un modèle éléments finis d'une cellule représentative de l'essentiel des paramètres de propagation et de diffusion des ondes dans les structures. Elle a été validée sur des cas simples de structures, principalement isotrope monodimensionnel. La modélisation dans ce cas des sandwichs plaques composites munies de couches piézoélectriques sera opérée. Des simulations numériques poussées seront effectuées afin de cerner le cadre d'application de la WFE pour ce type de structures. Des optimisations pourront être réalisées avec ces outils numériques afin d'obtenir des paramètres géométriques et électriques optimaux dans la conception des structures intelligentes.

Les travaux de cette thèse sont intégrés dans le projet CALIOP en collaborant avec le laboratoire de Mécanique Appliquée R.Chaléat de l'Institut FEMTO-ST et G.W. Woodruff School of Mechanical Engineering de Georgia Institute of Technology.

Mots clés: Propagation d'ondes, wave finite element, piézoélectricité, contrôle semi-actif, diffusion d'énergie

Contents

List of Abbreviations

- CFT: Continuous Fourier Transform
- DFT: Discrete Fourier Transform
- DMM: Diffusion Matrix Model
- DOF: Degree Of Freedom
- FE: Finite Element
- FEM: Finite Element Method
- FRF: Frequency Response Function
- FT: Fourier Transform
- FWFE: Forced Wave Finite Element
- HF: High Frequency
- IDFT: Inverse Discrete Fourier Transform
- IWC: Inhomogeneous Wave Correlation
- LF: Low Frequency
- MF: Medium Frequency
- MWFE: Modified Wave Finite Element
- NDT: Non-Destructive Testing
- SLDV: Scanning Laser Doppler Vibrometer
- WFE: Wave Finite Element

Chapter 1

Introduction

Contents

1.1 Smart structures and control architectures

1.1.1 Background

Smart structures have always been a research topic during recent years. They can offer the opportunity to create engineered material systems that are empowered with sensing, actuation, and artificial intelligence features. The typical smart structure sensors used in discrete or distributed locations to measure the performance of the system comprise fiber optics, piezoelectric ceramics and piezoelectric polymers. The actuators used in the smart materials technologies include applications of piezoelectric ceramics, piezoelectric polymers, electrostrictive, magnetostrictive materials and piezofibres [1].

Researchers define smart structures in different ways: in the work of Sahin *et al.* [1], smart structure is defined as the structure that can sense external disturbance and respond to that with active control in real time to maintain the mission requirements; according to Bandyopadhyay *et al.* [2], a smart structure is a distributed parameter system that employs sensors and actuators at different finite element locations on it. It then makes use of one or more microprocessors to analyze the responses obtained from the sensors and uses different control logics to command the actuators. It can hence apply localized strains to the plant to respond in a desired fashion and brings the system to equilibrium. It has been mentioned in the work of Giurgiutiu [3] that there are two different ways to define smart structures. "The first definition is based upon a technology paradigm: the integration of actuators, sensors, and controls with a material or structural component. Multifunctional elements form a complete regulator circuit resulting in a novel structure displaying reduced complexity, low weight, high functional density, as well as economic efficiency. This definition describes the components of an adaptive material system, but does not state a goal or objective of the system. The other definition is based upon a science paradigm, and attempts to capture the essence of biologically inspired materials by addressing the goal as creating material systems with intelligence and life features integrated in the microstructure of the material system to reduce mass and energy and produce adaptive functionality. It is important to note that the science paradigm does not define the type of materials to be utilized. It does not even state definitively that there are sensors, actuators, and controls, but instead describes a philosophy of design".

The concept of smart structures is as difficult to describe precisely as it can be to list all the ways they have been designed and realized. The most important thing still remains to put the theories into practice. The control law with the set of embedded or bonded sensors and actuators in the structure can be very complex in order to achieve objectives like vibration control. Questions like stability and experimental implementation arise and should be taken into account carefully.

Recently, a revolution has taken place in the field of integrated microelectromechanical systems(MEMS) which offers new opportunities for smart structure design and optimization. The next generation of smart composite structures [4, 5] is created via the mechanical integration of active smart materials, electronics, chip sets and power supply systems. The material's intrinsic passive mechanical behavior can be controlled through electromechanical transducers in order to attain new desired functionalities [6]. The design of this kind of smart structures is addressed in the present work. It considers the problem of integration of electromechanical smart transducers into composite or standard materials for controlling their vibroacoustical behavior and also optimizes their dynamical response. The main issue of the proposed design is the optimization and the integration of a dense set of self-shunted piezoelectric elements for controlling mechanical wave's diffusion into beams and plates representing general engineering structural elements. The chosen technological system, based on self-shunted piezoelectric materials is well dedicated for mechatronics integration because of its intrinsic simplicity and its low energy consumption. This proposed architecture could also be miniaturized and integrated by mean of MEMS technology and could lead us to create a new class of metamaterials.

1.1.2 Shunt architectures for the control of smart structures

Among the control configurations found in published works, a well-known technique is the piezoelectric damping using external resistor-inductor shunt circuit [6, 7, 8, 9, 10, 11, 12]. This semi-active configuration has the advantage of guaranteeing stability, and can be obtained by bonding piezoelectric elements onto a structure and connecting the electrodes to the external shunt circuit. Due to straining of the host structure, and through the direct piezoelectric effect, a part of the mechanical energy is converted into electrical energy. The latter is subsequently dissipated by Joule heating via the connected resistor. The $R-L$ shunt circuit on piezoelectric patches can be regarded as light oscillators instead of heavy mass-spring structures. By varying the inductance L in the shunt circuit, the tuning frequency can be adjusted to the targeted frequency band. It should be noted that with the $R-L$ resonant shunt circuit, the controlled frequency band is limited(around the tuning frequency of the circuit).

In order to improve the efficiency of passive connected networks on the piezoelectric patch, different shunt circuits have been proposed in the literature. In the work of Tsai and Wang [13], active-passive hybrid piezoelectric network is proposed. This type of shunt circuit can not only provide passive damping, but also enhance the active action authority if tuned correctly. Multi-mode resonant shunt has been studied by Behrens *et al.* [14] and Wu [15]. This kind of resonant shunt is able to damp several structural modes with one single piezoelectric patch. Wu [15] proposed blocking circuits while Behrens *et al.* [14] provided current flowing circuits. It should be mentioned that all resonant shunt circuits have a major drawback: their damping performance is very sensitive to the parameters of the system. And in case of mistuning, the resonant shunts won't provide any damping. Online tuned resonant shunts [16] were developed to overcome these difficulties, but the suggested tuning algorithms did not lead to satisfying results as they are slow and difficult to implement.

Niederberger *et al.* [17] developed and implemented a novel online-tuned multi-mode resonant shunts for piezoelectric damping. This resonant shunt adapts itself for the optimal vibration suppression of one or several modes with better rapidity and precision. The implementation is feasible with a simple analogical circuit.

In $R-L$ shunt circuits, energy is dissipated principally through the connected resistance R. This amount of dissipated energy is not too high because of the reactive power components of the piezoelectric capacitor. In order to overcome these limitations, the vibration control of structures through piezoelectric shunts with negative capacitance has been developed during recent years. The negative capacitance eliminates the piezoelectric capacitance and allows the resistance to maximally dissipate energy. It is considered a promising technique according to previous work. Theoretical, numerical analysis and experimental validation are carried out to evaluate and assess the efficiency of this control technique [6, 18, 19, 20, 21, 22, 23]. Tuning theories developed by Behrens *et al.* [24], Park and Palumbo [25] and Cunefare [19] all showed that a negative capacitance was needed to allow for maximum performance of the shunt. However, during the experimental implementation, stability problems can arise if the absolute value of the negative capacitance is smaller than the piezoelectric capacitance at constant stress. Despite this difficulty, its capability of tailoring the dynamic behavior of the structure in a large frequency range [26] makes this technique extremely interesting for numerous industrial applications.

The shunt techniques mentioned above are mainly linear shunts. There are also non-linear shunts with switches [27, 28, 29] that can change the dynamics of the shunt to improve vibration damping. They do not require external power sources. There are also many other shunt architectures, but the most concerned shunt techniques in the present work are the $R-L$ resonant shunt and negative capacitance shunt.

Structures with periodically distributed shunted piezoelectric patches using these two shunt techniques will be considered to obtain intelligent vibroacoustical interfaces in order to realize optimal reflection or optimal damping of unwanted incident energy from excitation sources, which is the main objective of the CALIOP project presented thereafter. This project aims at studying all induced problems such as mathematical homogenization, low to high frequency structural modeling, optimization and of course experimental tests, characterizations and technological issues.

1.2 CALIOP Project

CALIOP is an ambitious project which involves in-depth theoretical and numerical development as well as advanced technological aspects, which is why the 4-year ANR French project involves three academic partners: the Laboratory of Applied Mechanics R.Chaléat at FEMTO-ST Institute (Besançon, France), G.W. Woodruff School of Mechanical Engineering of Georgia Institute of Technology(Atlanta, USA) and the Laboratory of Tribology and System Dynamics (Lyon, France). It gave the frame of work for this Ph.D. thesis. The general objectives of the project are to draw together academic research teams with diverse skills and expertise with a common interest in low and mid-frequency vibration and acoustic analysis involving smart materials and structural design. Bringing the research groups together removes existing fragmentation and achieve a critical mass of research efforts unparalleled anywhere in France. It encourages cross-fertilization of the ideas behind the various approaches and the emergence of new hybrid integrated material structures. The specific scientific objectives of the CALIOP project concern research in the following tasks:

- To determine efficient theoretical active/passive optimization tools for controlling mechanical power flow in complex structures with respect to phenomenological criteria (transmission, absorption, damping) and the corresponding operator for technological implementation. The optimization will also adopt a design-oriented perspective in order to facilitate the choice and the integration of these solutions.

- To understand and to analyze clearly multiphysical interactions between piezoelectric elements, supporting structures and shunt electrical circuits when dense distributed integration into composite structures is considered for physical implementation of optimal control operator.

- To develop integrated electromechanical prototype for characterizing vibroacoustical properties of such new generation of hybrid smart materials.

- To explore new concepts in passive, adaptive or active mechanical integrated composite interfaces with different kinds of electronic circuits and others electro mechanical transducers with a view toward MEMS integration in a near future.

- To develop and to improve numerical models in view of the structural complexity of the components and their assemblies. Significant effort will be focused on the mid-frequency modeling of systems, including the development of accurate reduced-order models and the development of homogenization techniques in the presence of highly fluctuating kinematic fields.

- Finally to produce design robust numerical tools for implementing such hybrid materials for industrial applications.

It is a multidisciplinary project that corresponds to the generic "smart materials and structure" framework, covering various disciplines such as structural mechanics, mechatronic interaction, materials science and systems.

The goal of this research project is to cover the main methodological and technological aspects of this specific application, with particular attention to some new and strategic issues, including new materials, reduced models, mid-frequency and multi-scale approaches and vibroacoustical design optimization tools. The final deliveries will be:

- New theoretical results concerning generalized impedance differential and pseudo differential operators and temporal realization.
- Two integrated shunted piezoelectric composite prototypes (one beam and one plate) demonstrating our capability in designing and realizing such new generation of smart structures.
- Dedicated numerical robust optimization tools implemented into AE-SOP software for future industrial design and manufacturing process [5, 30].
- New technological methodologies for piezo-composite and electronic integration.

To achieve these goals, the generic idea proposed in Figure 1.1(a) introduces the notion of "mechanical hybrid interfaces" often of a "dissipative" nature. As depicted on Figure 1.1(a), this interface can be made of a simply layered material or multi-layered hybrid composite system including smart and passive materials, integrated electronic control devices, potentially fluids, etc. The interface here is considered as located between two solid media (joints). Figure 1.1(b) shows the considered interface made of shunted piezoelectric composite materials. This kind of interface acts on the whole structure as a "generalized" impedance linking power flow between each separated systems. The optimization of its "composite material" behavior induces application of specific interface impedance able to confer specific properties for energy diffusion.
This enables control of numerous desirable engineering properties such as "insertion loss, absorption, reflection, damping" usually considered as the design criteria for optimizing structural vibroacoustical behavior. This aspect demands to solve different theoretical problems regarding optimization and realization of complex differential and pseudo differential operators. The technological implementation of such concepts requires the integration, in the interface itself, of a hybrid distributed system including smart transducers (here piezoelectric elements) and electronic components (here semi-passive shunt devices). The global induced structural behavior should exhibit the desired vibroacoustical properties and should be able to guarantee efficiency, while limiting structural alterations and modifications.

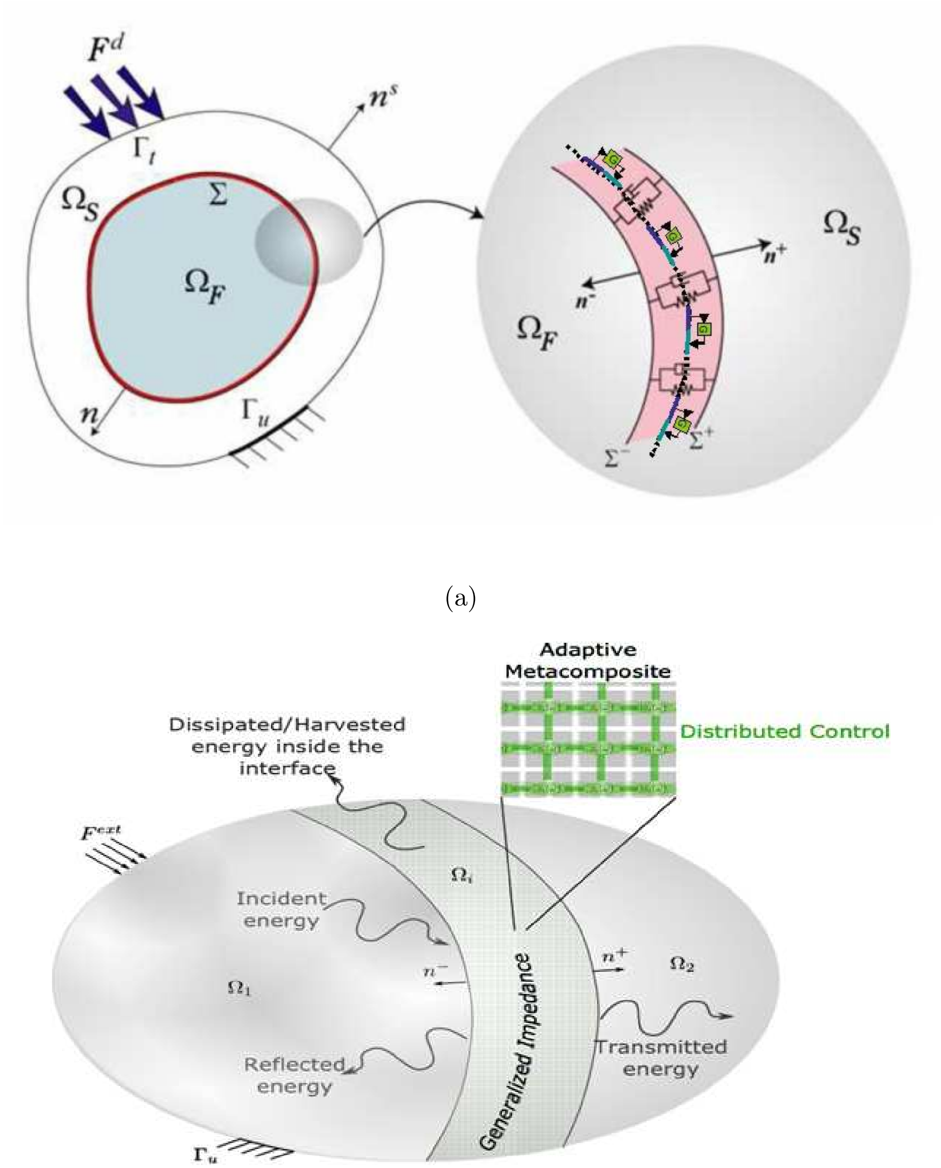

(a)

(b)

Figure 1.1: (a)Illustration of a dissipative interface, analyzed by means of the Kelvin-Voigt model and smart skin for structure-structure interaction problem. (b)Illustration of a dissipative interface, using shunted piezoelectric materials.

The feasibility of developing and realizing such materials and these "integrated distributed smart structures" will be studied through the physical implementations on simple examples. The paradigm application concerns the implementation of the proposed smart piezo-composite interface into a beam (Figure 1.2(a)) and a plate (Figure 1.2(b)) for controlling its mechanical power flow diffusion. The considered piezoelectric control will be based on semi-active shunt circuit in a decentralized (Figure 1.3(a)) or non-decentralized

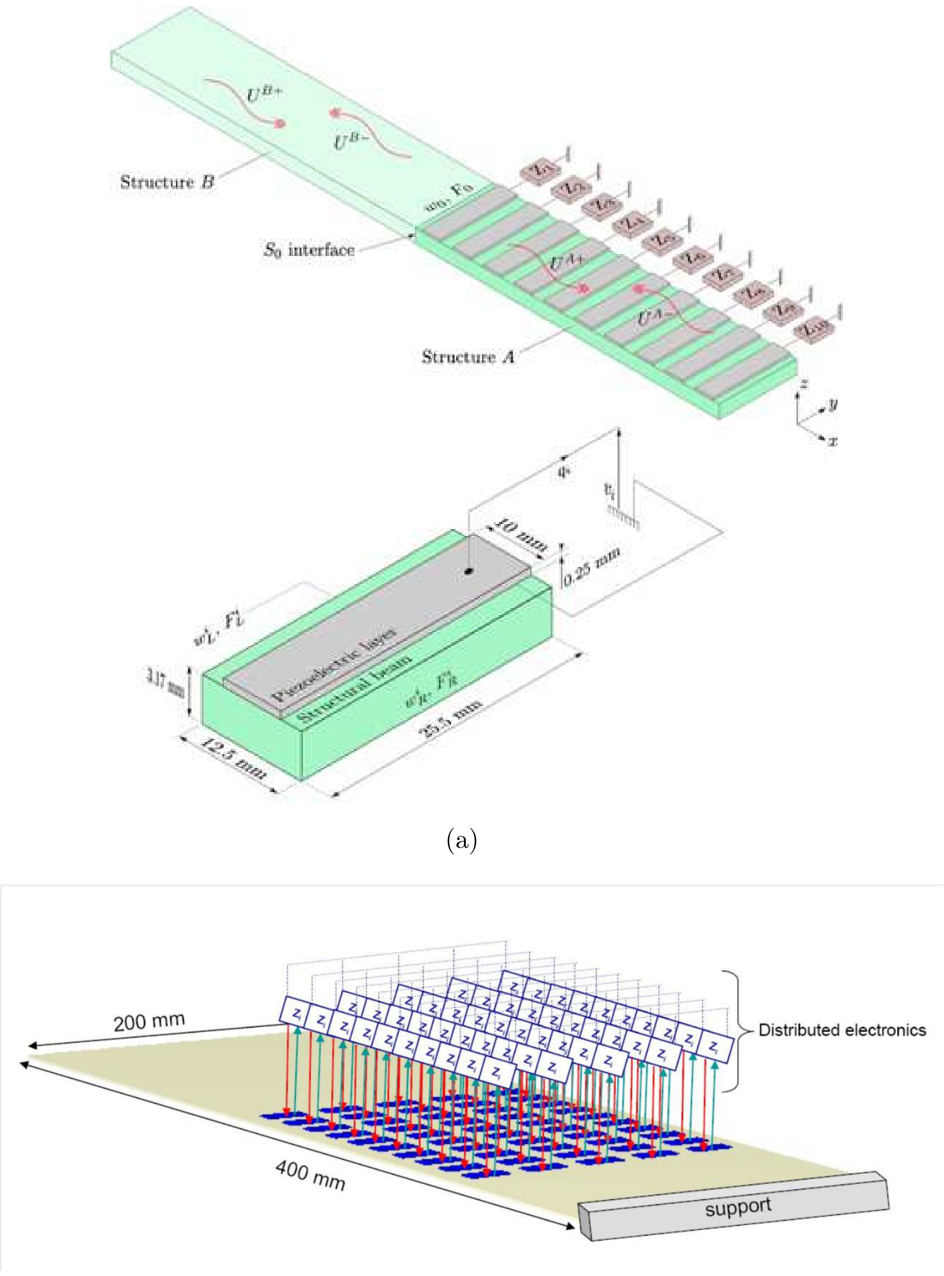

(a)

(b)

Figure 1.2: Periodically distributed shunted piezo-composite (a)beam (b)plate.

(Figure 1.3(b)) architecture, depending on the order of the corresponding optimal "impedance" operator. The investigated controlling operator consists of innovative shunt circuits (Figure 1.4) connected to each individual piezoelectric cell (decentralized approach) or between two nearby cells (non-decentralized approach). By using the proposed new point of view based on implementation of distributed shunt circuit, we could also produce "stable" localized subdomain for sensitive system isolation, wave absorption for panel stabilization or mechanical energy concentration for energy harvesting device implementation [6, 31, 32]. Low and mid frequency dynamical characterization of such smart piezoelectric composite structure will also be made. The aim is to experimentally highlight the specific vibroacoustical effect of such device for controlling the energy diffusion between the passive and active part of the system. Depending on the applied distributed impedance, absorption

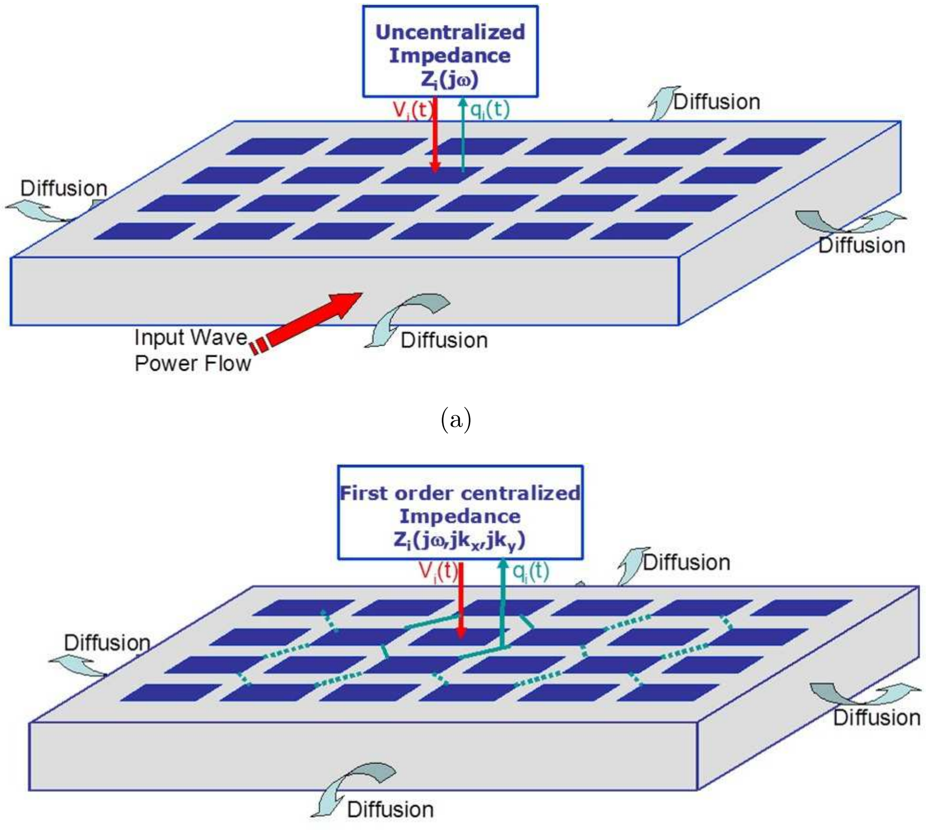

(a)

(b)

Figure 1.3: Description of Integrated and periodically distributed shunted piezoelectric patches for power flow diffusion optimization (a)Decentralized architecture (b)First order centralized architecture.

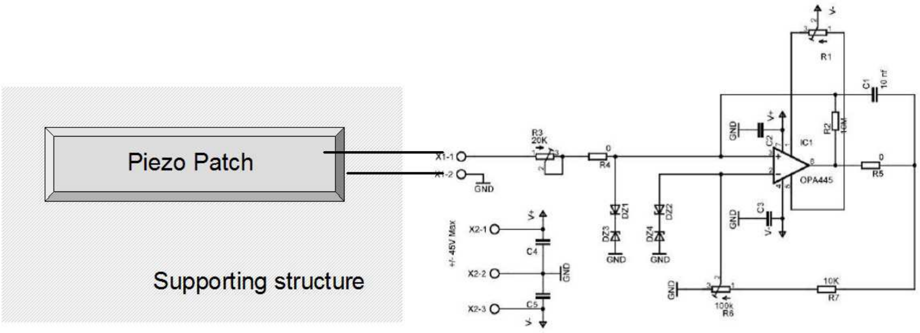

Figure 1.4: Electro mechanical architecture : piezoelectric patch + negative capacitance circuit.

and/or reflection of flexural waves will be analyzed.

1.3 Motivation of the work

From the numerical and simulation perspective, many theoretical problems are to be considered. These fundamental questions are related to the complexity of the integrated solution shown in Figure 1.1(a) and to the wide frequency band of analysis (the audible frequency range, strictly speaking). In this context, the dynamical features of a low frequency (LF), medium frequency (MF) as well as high frequency (HF) (high and uniform modal density) nature arise. Numerical investigations of the generic problem (Figure 1.1(a)) are complex in the LF range and it is still a major challenge in the MF domain.
In the LF domain, for the resolution of structural-acoustic vibration problems, two types of methods can be distinguished, whether they are based on analytical or numerical discrete approaches. Analytical methods are typically restricted to simple geometries and boundary conditions. Methods based on discretization of the structural-acoustic governing equations, such as the finite element method, are not restricted to specific boundary conditions but require a higher computational effort. The originality of LF theoretical and numerical investigations lies in:

1. new modal formulations of the fully coupled electromechanical interface;

2. the development of a computationally inexpensive and accurate adaptive elements;

3. "smart" substructuring techniques, among other ideas.

A semi-analytical approach can also be used to reduce computational costs.
In the MF range, fundamental issues should be addressed: the non-validity of traditional assumptions related to the analytical models regarding small wavelengths (for instance, the Kirchhoff hypothesis for 1D and 2D elastic systems; the mass law used for complex subsystem modeling [33]); non-convergence of traditional numerical models and conventional homogenization techniques [33], with regards to kinematic fields showing strong gradients and/or highly oscillating [34]; prohibitive computational time associated with the simulation of large numerical models; uncertainties (poor understanding of system complexity) and parametric variability (related to the manufacturing process), whose influence on the dynamic response of systems becomes significant in the MF domain [33, 35, 36, 37, 38].
One further fundamental difficulty to be tackled is the numerical description of strongly coupled problems. Indeed, there is still a need for fast and efficient numerical design tools capable of describing the coupling between multi-physic systems (elastic structures, viscoelastic materials, fluids, electric fields, electromagnetic fields, discrete electronics...) highlighting multi-scale behavior. Multi-scale behavior is due to heterogeneities in terms of different field wavelengths and is also due to the systems and structures. It is obvious that the size of the interface will be small in comparison with the solid domains covered. Each of these considered domains has its own dynamic and conventional numerical methods and are thus inappropriate. This property is known in the open literature as the MF dynamical situation. It concerns for instance, a deterministic LF structure coupled to complex MF elastic subsystems, or, an elastic flexible HF structure connected to an LF electronic one (cf. Figure 1.4). One fundamental question will be to determine how refined the interface modeling, should be to properly integrate it in numerical design. Dedicated approaches will be carried out for the applications. They should allow the computation of the obtained structural behavior to evaluate effective performance of our solutions and potential evolution for MF treatments. Goals of this task lie also in the development of numerical tools for the LF and MF - reduced modeling investigations - Model comparisons and validity domains.
In order to accomplish this task, techniques for the prediction of dynamical behavior of smart structures need to be developed. In the literature, a lot of analytical models have been already proposed. A uniform strain model for a beam with piezoelectric actuators bonded on the surface or embedded in it was developed by Crawley and de Luis [39]. This model also incorporates shear lag effects of the adhesive layer the piezoelectric actuator and the beam. Lee [40] treated the induced strain as equivalent thermal effects, and presented a model based on classical laminate theory. Zhang and Sun [41] constructed

a new adaptive sandwich structure using the shear mode of piezoelectric materials. Governing equations for the proposed beam and its surface-mounted counterpart are derived based on the variational principle. Later, Hu and Yao [42] derived the elasticity solution of PZT generated wave propagation in terms of the wave reflection and transmission matrices based on the Timoshenko beam theory. Hagood and von Flotow [7] provided a comprehensive description of the dynamic of shunted piezoelectric patch. Based on the work of Hagood and von Flotow [7], Park [43] studied the vibration attenuation of beams via shunted piezoelectric elements, and proposed a mathematical model to describe the flexural vibration behavior of a cantilevered beam system with resonant shunt circuits.

The development of the finite element method(FEM) enabled the numerical modeling of various structures with piezoelectric elements [44]. It is an effective tool for the prediction of structural dynamic behavior as it possesses the advantages of widespread use in the engineering domain due to its capability of treating complex geometries. Structures with shunted piezoelectric elements were properly treated with FEM [10, 11]. However, the excessive computational time associated with large models constitutes one of the major limitations of this approach. As an alternative, the numerical description based on waves traveling into waveguides and slender structures can be applied. This description provides a low cost and efficient way to capture the dynamic behavior of those structures as it only requires the treatment of a typical unit subsystem [45]. The dimensions of this unit cell are related to the cross-section dynamics only. The Wave Finite Element(WFE) method [46, 47, 48, 49, 50, 51, 52], which is based on the classic finite element description of a typical unit cell extracted from a given global system, is an appropriate tool for the prediction of wave propagation in waveguides such as beams [53, 54] and plates [55, 56] in a wide frequency band.

During the CALIOP project, Spadoni *et al.* [9] and Casadei *et al.* [12] have studied the control of wave propagation in plates with periodic arrays of shunted piezoelectric patches. Efforts have been dedicated firstly to developing the finite element formulation of shunted piezoelectric elements, then to characterizing the dispersion relation of waves propagating over the surface of plate structures and the band gaps in the frequency domain. An experimental investigation was carried out in the work of Casadei *et al.* [12] to test the performance of shunted piezoelectric patches via the forced response of the structure. The paper published by the project leaders M. Collet *et al.* [6] provided a full finite element description of a beam with periodic shunted piezoelectric patches via the WFE method, with a particular emphasis was placed on the optimization of shunt impedance. The energy diffusion is supposed to occur at the interface between the part of the beam without shunted piezoelectric patches and the part of the beam with a set of periodic shunted piezoelectric patches. The energy diffusion related to a unit cell in the set of periodic patches is not analyzed.

Suitable numerical tools which can characterize energy diffusion properties for structures with shunted piezoelectric elements still need to be properly developed. These tools will be applied for intensive computations aiming at the design of the piezoelectric patch and the electronic shunt circuit on the patch.

In the present work, general formulations for smart structures with shunted piezoelectric patches are proposed. These formulations can be applied for all kinds of slender smart structures. On the whole, this work focuses on two main objectives:

- Offering efficient numerical tools for the prediction of wave propagation and diffusion characteristics and dynamic behavior such as reflection and transmission coefficients of the wave modes, frequency and time responses of beam structures with shunted piezoelectric patches for design purpose. Optimization of the unit cell in the periodic set of piezoelectric patches can be carried out with these tools to obtain optimal geometric and electric parameters.

- Providing effective verification and validation approaches to evaluate wave propagation characteristics and dynamic behavior in order to test the efficiency of all the numerical techniques.

1.4 Organization of the dissertation

This Ph.D. dissertation is organized as follows:

- In Chapter 1, the background and the motivation of this work are briefly presented, as well as the CALIOP project in which LTDS participates as the task leader of "Numerical modeling of complex multi-physical interface".

- Chapter 2 is devoted to introduce the formulations of the numerical methods applied in this work. The Wave Finite Element (WFE) method(Subsection 2.1.1) and its associated Diffusion Matrix Model(DMM)(Subsection 2.1.2) are firstly described. Thereafter, the numerical tool to evaluate the forced response of the structure, namely the Forced Wave Finite Element(FWFE) approach, is described in Subsection 2.1.3. The approach to acquire time response of the structure is introduced in Section 2.1.4. Then the Modified Wave Finite Element(MWFE) formulation is given in detail(Subsection 2.2), which is dedicated for the analysis of wave propagation and diffusion characteristics in multi-layered slender waveguides. And finally in Section 2.3, finite element modeling of piezoelectric domain is described, and the approaches to take the shunt circuit into consideration are given. It should be noted that all kinds of shunt circuits can be considered with these formulations.

- In Chapter 3, all the numerical techniques provided are applied in various simulations. Wave propagation and diffusion characteristics of specific wave modes propagating in solid beams(Subsection 3.1) and hollow beams(Subsection 3.2), through the WFE approach and the associated DMM, so as to investigate the control of propagating waves in such smart structures.

- Later in Chapter 4, multi-layered beams with $R-L$ shunted piezoelectric patches are calculated using the MWFE formulation in order to study the control of wave modes propagating in such heterogeneous systems. Parametric studies are also carried out to investigate the influence of reduced local mode bases of the layers on wave propagation and energy diffusion characteristics in these multi-layered composite smart structures.

- In Chapter 5, the issue of wave propagation control in smart structures with shunted piezoelectric patches using negative capacitance is addressed. In Subsection 5.2, wave energy diffusion characteristics and forced response of beam structures with $R-C_{neg}$ shunted piezoelectric patches are firstly investigated. Subsequently in Subsection 5.3, optimizations of the shunt impedance and the thickness of the piezoelectric patch are performed via pertinent optimization criterions like power flow transmission and absorption of specific wave modes propagating in the system.

- Chapter 6 focuses on the application of the guided waves for the damage detection in stiffened panels at medium frequencies. The novel technique provided in this chapter, named Inhomogeneous Wave Correlation (IWC) technique, is able to provide a global vision of the vibration signature of the structure through a wave propagation approach (instead of modal analysis) by extracting propagation information like wavenumber from measurements or simulations. With integrated signal processing and filtering methods, waves containing no information about defects can be eliminated as the influence of local singularities on the vibration signature of the structure can be highlighted.

CHAPTER 2

Outline of the numerical tools for the design of smart structures with shunted piezoelectric patches

---

Contents

2.1 Wave propagation and energy diffusion through finite elements in slender structures

The idea of the Wave Finite Element(WFE) method is firstly proposed by Mead [57] as a general theory in order to determine harmonic wave propagation characteristics, where both one-dimensional and two-dimensional periodic systems are considered. Later, a lot of studies have focused on the extension of this idea to the homogeneous structures rather than the generally periodic systems comprised of an arbitrary substructure [58, 59]. This method considers the homogeneous waveguide structure as a periodic system assembled by identical unit cells representative of the whole structure. Thus the method for periodic systems can be seamlessly transplanted to the WFE method for eigenmode extraction. The unit cell can be discretized with the aid of some commercial FE procedures, rather than the development of a relatively new FE code for specific elements. This allows the existing element libraries and powerful grid generation procedures to be used for many engineering structures. The WFE method is easy to apply due to its perfect connection with the standard FE method [60]. This method was applied for the structural vibration analysis [53, 61, 54, 31, 32], the wave propagation in elastic waveguides [46, 62, 63]. Mencik and Ichchou [46] proposed a hybrid approach to study the diffusion of multiple wave modes based on this method, and later Ichchou *et al.* [48] investigated the numerical sensitivity of this method. The energy propagation features in rib-stiffened panels over a wide frequency range were studied via this method in the work of Ichchou *et al.* [32], where the comparisons of numerical and experimental results are provided. Huang *et al.* [64] applied the WFE method and its associated Diffusion Matrix Model(DMM) [49] to study the defect detection in damaged ribbed stiffened panels. Chen and Wilcox [63] applied this method to investigate the effect of load on guided wave propagating properties in rails. The method was also implemented for wave propagation and dynamic problems in the homogeneous structures with internal fluid [38, 65, 47], where the studies were based on the WFE method for the one-dimensional wave propagation problem and concentrated on the lower frequency problems. It is also known that the transfer matrix method can be applied to calculate the wave propagation in periodic or nearly periodic structures [66, 67]. However, this method is less advantageous than the WFE and DMM approaches, as the latter give full finite element description of the waveguide's cross-section dynamics, for the coupling element as well. Model reduction techniques can also be applied in the WFE and DMM approaches [68, 49].

2.1.1 Wave propagation through finite elements in slender structures

This section is concerned with a description of the dynamical behavior of a slender structure, as illustrated in Figure 2.1, which is composed, along a specific direction (say X-axis), of N identical substructures. Note that this general description can be applied to homogeneous systems whose cross-sections are constant. The dynamic of the global system is formulated from the description of the waves propagating along the X-axis. Let us consider a finite element model of a given substructure k ($k \in \{1, \ldots, N\}$) belonging to the waveguide (cf. Figure 2.1). The left and right boundaries of the discretized substructure are assumed to contain n degrees of freedom (DOFs). Displacements $\mathbf{q}$ and forces $\mathbf{F}$ which are applied on these boundaries are denoted by $(\mathbf{q}_{\mathrm{L}}, \mathbf{q}_{\mathrm{R}})$ and $(\mathbf{F}_{\mathrm{L}}, \mathbf{F}_{\mathrm{R}})$, respectively. It is assumed that the kinematic quantities are represented through state vectors $\mathbf{u}_{\mathrm{L}}^{(k)} = ((\mathbf{q}_{\mathrm{L}}^{(k)})^{\mathrm{T}}(-\mathbf{F}_{\mathrm{L}}^{(k)})^{\mathrm{T}})^{\mathrm{T}}$ and $\mathbf{u}_{\mathrm{R}}^{(k)} = ((\mathbf{q}_{\mathrm{R}}^{(k)})^{\mathrm{T}}(\mathbf{F}_{\mathrm{R}}^{(k)})^{\mathrm{T}})^{\mathrm{T}}$, and that the internal DOFs of substructure k are not submitted to external forces.

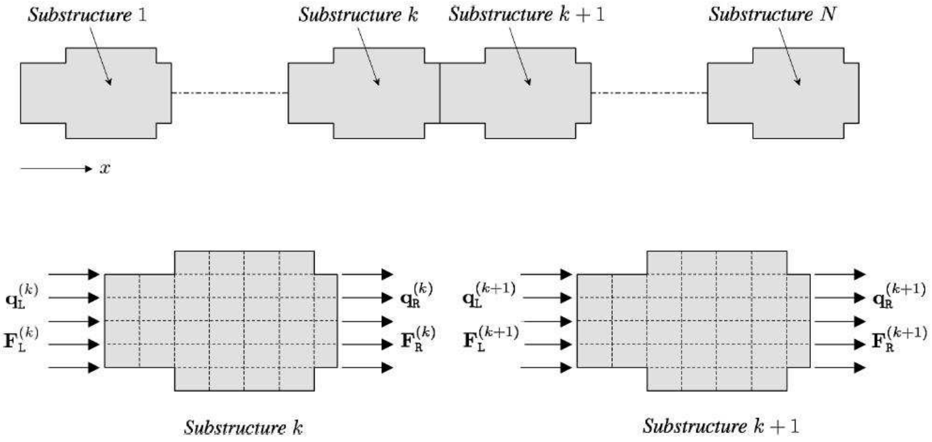

Figure 2.1: An illustration of a periodic waveguide [46].

The dynamical equilibrium of any substructure k can be formulated in this manner (full development of the dynamics can be found in Appendix B):

$$\mathbf{D}^* \begin{pmatrix} \mathbf{q}_{\mathrm{L}}^{(k)} \\ \mathbf{q}_{\mathrm{R}}^{(k)} \end{pmatrix} = \begin{pmatrix} \mathbf{F}_{\mathrm{L}}^{(k)} \\ \mathbf{F}_{\mathrm{R}}^{(k)} \end{pmatrix}, \tag{2.1}$$

where $\mathbf{D}^*$ stands for the dynamical stiffness matrix of substructure k, condensed on the DOFs of the left and right boundaries, and $\mathbf{q}_{\mathrm{I}}$ represents the displacements of the internal DOFs of the substructure.

$$\mathbf{D}^* = \begin{bmatrix} \mathbf{D}_{\mathrm{LL}}^* & \mathbf{D}_{\mathrm{LR}}^* \\ \mathbf{D}_{\mathrm{RL}}^* & \mathbf{D}_{\mathrm{RR}}^* \end{bmatrix}. \tag{2.2}$$

From equations (2.1) and (2.2), state vector $\mathbf{u}_{\mathrm{L}}^{(k)}$ can be expressed from state vector $\mathbf{u}_{\mathrm{R}}^{(k)}$ — in the present case, $\mathbf{u}_{\mathrm{L}}^{(k)} = ((\mathbf{q}_{\mathrm{L}}^{(k)})^{\mathrm{T}}(-\mathbf{F}_{\mathrm{L}}^{(k)})^{\mathrm{T}})^{\mathrm{T}}$ and $\mathbf{u}_{\mathrm{R}}^{(k)} = ((\mathbf{q}_{\mathrm{R}}^{(k)})^{\mathrm{T}}(\mathbf{F}_{\mathrm{R}}^{(k)})^{\mathrm{T}})^{\mathrm{T}}$. Hence,

$$\mathbf{u}_{\mathtt{R}}^{(k)} = \mathbf{S}\mathbf{u}_{\mathtt{L}}^{(k)}, \tag{2.3}$$

where

$$\mathbf{S} = \left[\begin{array}{c|c} -(\mathbf{D}^{*}_{\mathtt{LR}})^{-1}\mathbf{D}^{*}_{\mathtt{LL}} & -(\mathbf{D}^{*}_{\mathtt{LR}})^{-1} \\ \hline \mathbf{D}^{*}_{\mathtt{RL}} - \mathbf{D}^{*}_{\mathtt{RR}}(\mathbf{D}^{*}_{\mathtt{LR}})^{-1}\mathbf{D}^{*}_{\mathtt{LL}} & -\mathbf{D}^{*}_{\mathtt{RR}}(\mathbf{D}^{*}_{\mathtt{LR}})^{-1} \end{array}\right]. \tag{2.4}$$

The matrix **J** is defined in the following manner:

$$\mathbf{J}_n = \begin{bmatrix} \mathbf{0} & \mathbf{I}_n \\ -\mathbf{I}_n & \mathbf{0} \end{bmatrix} \quad , \quad \mathbf{J}_n^{\mathtt{T}} = \mathbf{J}_n^{-1} = -\mathbf{J}_n. \tag{2.5}$$

The following boundary value problem issued from equation (2.3) can be established as follows:

$$\mathbf{S}\mathbf{\Phi}_i = \mu_i\mathbf{\Phi}_i \quad , \quad |\mathbf{S} - \mu_i\mathbf{I}_{\mathbf{2}n}| = \mathbf{0}. \tag{2.6}$$

To avoid numerical ill-conditioning, this problem can be solved using the approach proposed by Zhong and Williams in reference [45]. Solutions $\{(\mu_i, \mathbf{\Phi}_i)\}_{i=1,\ldots,2n}$ of equation (2.6) refer to the wave modes of the heterogeneous waveguide. For the sake of clarity, it is assumed that eigenvectors $\{\mathbf{\Phi}_i\}_i$ are linearly independent (i.e. eigenvalues $\{\mu_i\}_i$ are distinct).
Alternatively, if the kinematic quantities are represented through state vectors $\mathbf{u}_{\mathtt{L}}^{(k)} = ((\mathbf{q}_{\mathtt{L}}^{(k)})^{\mathtt{T}}(\mathbf{F}_{\mathtt{L}}^{(k)})^{\mathtt{T}})^{\mathtt{T}}$ and $\mathbf{u}_{\mathtt{R}}^{(k)} = ((\mathbf{q}_{\mathtt{R}}^{(k)})^{\mathtt{T}}(-\mathbf{F}_{\mathtt{R}}^{(k)})^{\mathtt{T}})^{\mathtt{T}}$, then

$$\mathbf{u}_{\mathtt{R}}^{(k)} = \mathbf{S}'\mathbf{u}_{\mathtt{L}}^{(k)}, \tag{2.7}$$

where

$$\mathbf{S}' = \left[\begin{array}{c|c} -(\mathbf{D}^{*}_{\mathtt{LR}})^{-1}\mathbf{D}^{*}_{\mathtt{LL}} & (\mathbf{D}^{*}_{\mathtt{LR}})^{-1} \\ \hline -\mathbf{D}^{*}_{\mathtt{RL}} + \mathbf{D}^{*}_{\mathtt{RR}}(\mathbf{D}^{*}_{\mathtt{LR}})^{-1}\mathbf{D}^{*}_{\mathtt{LL}} & -\mathbf{D}^{*}_{\mathtt{RR}}(\mathbf{D}^{*}_{\mathtt{LR}})^{-1} \end{array}\right]. \tag{2.8}$$

It can be easily proved that the eigenvalues of matrix $\mathbf{S}'$ are the same of those of matrix **S** (see Appendix B). More over, the eigenvalues can be defined such that:

$$\mu_{n+i} = \frac{1}{\mu_i} \quad \forall n \in \{1, \ldots, n\}. \tag{2.9}$$

Thus, if eigenvalues $\{\mu_i\}_{i=1,\ldots,n}$ are associated with eigenvectors $\{\mathbf{\Phi}_i\}_{i=1,\ldots,n}$ traveling in the $x-$positive direction, eigenvalues $\{\mu_i\}_{i=n+1,\ldots,2n}$ are associated with eigenvectors $\{\mathbf{\Phi}_i\}_{i=n+1,\ldots,2n}$ traveling in the $x-$negative direction. And as mentioned in reference [6], the sign of the real part of the wavenumber k_i,$Re(k_i)$, represents the direction of the phase velocity of the corresponding waves: if $Re(k_i) > 0$, the phase propagates in the positive x direction; if $Re(k_i) < 0$, the phase propagates in the negative direction, and if it is zero,

k_i corresponds to the wavenumber of a pure evanescent wave that only occurs when an undamped system is considered [56]. Hence, matrix $\mathbf{\Phi}$ of the eigenvectors can be described in this way:

$$\mathbf{\Phi} = \begin{bmatrix} \mathbf{\Phi}_{\mathbf{q}}^{\mathtt{inc}} & \mathbf{\Phi}_{\mathbf{q}}^{\mathtt{ref}} \\ \mathbf{\Phi}_{\mathbf{F}}^{\mathtt{inc}} & \mathbf{\Phi}_{\mathbf{F}}^{\mathtt{ref}} \end{bmatrix}, \tag{2.10}$$

where subscripts $\mathbf{q}$ and $\mathbf{F}$ refer to the components which are related to the displacements and the forces, respectively; $((\mathbf{\Phi}_{\mathbf{q}}^{\mathtt{inc}})^{\mathtt{T}}(\mathbf{\Phi}_{\mathbf{F}}^{\mathtt{inc}})^{\mathtt{T}})^{\mathtt{T}}$ and $((\mathbf{\Phi}_{\mathbf{q}}^{\mathtt{ref}})^{\mathtt{T}}(\mathbf{\Phi}_{\mathbf{F}}^{\mathtt{ref}})^{\mathtt{T}})^{\mathtt{T}}$ stand for the modes which are incident to and reflected by a specific boundary (left or right) of the heterogeneous waveguide, respectively; $\mathbf{\Phi}_{\mathbf{q}}^{\mathtt{inc}}$, $\mathbf{\Phi}_{\mathbf{F}}^{\mathtt{inc}}$, $\mathbf{\Phi}_{\mathbf{q}}^{\mathtt{ref}}$ and $\mathbf{\Phi}_{\mathbf{F}}^{\mathtt{ref}}$ are $n \times n$ matrices. As mentioned in reference [38], the eigenvalue problem defined by equation (2.6) must be solved at chosen frequencies. This means that the wave modes established by equation (2.10) have to be classified at each frequency. The orthogonality properties of eigenvectors $\{\mathbf{\Phi}_i\}_i$ (see for instance [45]), providing

$$(\mathbf{\Phi}_j)^{\mathtt{T}}\mathbf{J}_n\mathbf{\Phi}_i = 0 \quad \text{for } \mu_j \neq 1/\mu_i, \tag{2.11}$$

allow one to propose a simple criterion to classify the wave modes, as suggested in [38]. Indeed, if $\mathbf{\Phi}_i(\omega)$ stands for the ith mode at frequency ω, then the ith mode $\mathbf{\Phi}_i(\omega + \Delta_\omega)$ at frequency $\omega + \Delta_\omega$ (Δ_ω represents the frequency step) must be chosen such that the quantity

$$A_i(\omega) = (\mathbf{\Phi}_l(\omega))^{\mathtt{T}}\mathbf{J}_n\mathbf{\Phi}_i(\omega + \Delta_\omega) \quad , \quad \mu_l(\omega) = 1/\mu_i(\omega) \tag{2.12}$$

is maximized. In fact, the validity of this criterion is based on the assumption that frequency step Δ_ω remains small enough such that eigenvector $\mathbf{\Phi}_i$ varies weakly between ω and $\omega + \Delta_\omega$.

Finally, assuming modal decomposition, state vectors $\mathbf{u}_{\mathtt{L}}^{(k)}$ and $\mathbf{u}_{\mathtt{R}}^{(k)}$ of any substructures k can be expressed from eigenvectors $\{\mathbf{\Phi}_i\}_{i=1,\dots,2n}$ [45]:

$$\mathbf{u}_{\mathtt{L}}^{(k)} = \mathbf{\Phi}\mathbf{Q}^{(k)} \quad , \quad \mathbf{u}_{\mathtt{R}}^{(k)} = \mathbf{\Phi}\mathbf{Q}^{(k+1)} \quad \forall k \in \{1, \dots, N\}. \tag{2.13}$$

Here, vector $\mathbf{Q}$ stands for the amplitudes of the wave modes, which can be expressed by (cf. equation (2.10)):

$$\mathbf{Q} = \begin{pmatrix} \mathbf{Q}^{\mathtt{inc}} \\ \mathbf{Q}^{\mathtt{ref}} \end{pmatrix}. \tag{2.14}$$

Summarizing, it appears that the dynamical behavior of a periodic waveguide can be simply expressed from a basis of modes representing waves traveling in the positive and negative directions of the system. An analysis of the dynamical response consists of evaluating a set of amplitudes $\{(\mathbf{Q}^{\mathtt{inc}(k)}, \mathbf{Q}^{\mathtt{ref}(k)})\}_k$

associated with the incident and reflected modes. Nevertheless, this evaluation requires us to formulate the boundary conditions of the system.

2.1.2 Coupling conditions between two periodic waveguides

The present section is concerned with the characterization, in terms of wave modes, of coupling conditions between two different periodic waveguides. The two systems are assumed to be connected, in a general manner, through an elastic coupling element (see Figure 2.2). This study aims to enable a prediction of the dynamics of complex systems which are composed of different periodic waveguides.

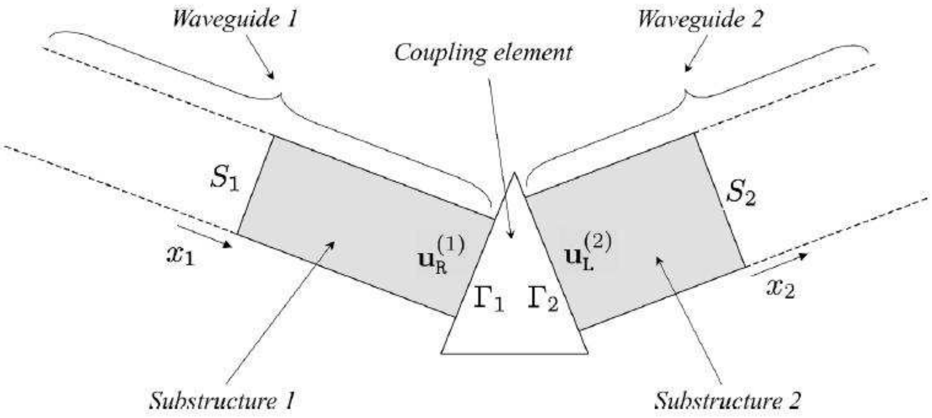

Figure 2.2: An illustration of the coupling between two different periodic waveguides [46].

Let us consider two periodic waveguides which are coupled through a coupling element and let us consider two corresponding substructures (1 and 2) which are located at the ends of the waveguides (see Figure 2.2). These substructures are coupled with the coupling element at surfaces Γ_1 and Γ_2 and are coupled with the other substructures, into waveguides, at surfaces S_1 and S_2. It is assumed that the coupling element is only subject to the coupling actions (that is, there is no force inside the element).
As mentioned in Mencik and Ichchou [46], the dynamical equilibrium of a discretized substructure i ($i = 1, 2$) and the coupling element can be formulated in this way:

$$\mathbf{D}^{(i)}\begin{pmatrix}\mathbf{q}_{\mathtt{L}}^{(i)}\\ \mathbf{q}_{\mathtt{I}}^{(i)}\\ \mathbf{q}_{\mathtt{R}}^{(i)}\end{pmatrix}=\begin{pmatrix}\mathbf{F}_{\mathtt{L}}^{(i)}\\ \mathbf{0}\\ \mathbf{F}_{\mathtt{R}}^{(i)}\end{pmatrix}\quad (i=1,2)\quad\text{and}\quad \mathbb{K}\begin{pmatrix}\mathbf{q}_{1}^{\mathtt{c}}\\ \mathbf{q}_{\mathtt{I}}^{\mathtt{c}}\\ \mathbf{q}_{2}^{\mathtt{c}}\end{pmatrix}=\begin{pmatrix}\mathbf{F}_{1}^{\mathtt{c}}\\ \mathbf{0}\\ \mathbf{F}_{2}^{\mathtt{c}}\end{pmatrix}, \tag{2.15}$$

where matrix $\mathbb{K}$ stands for the complex dynamical stiffness of the coupling element, $(\mathbf{q}_{1}^{\mathtt{c}},\mathbf{F}_{1}^{\mathtt{c}})$ and $(\mathbf{q}_{2}^{\mathtt{c}},\mathbf{F}_{2}^{\mathtt{c}})$ represent the displacements and the forces applied at the DOFs of the coupling element on surfaces Γ_1 and Γ_2, respectively. Assuming that the meshes at the interfaces Γ_1 and Γ_2 between waveguides and the coupling element are compatible (the same mesh is applied on the interfaces), the constraints introduced at these coupling surfaces can be formulated in this way:

$$\begin{pmatrix}\mathbf{F}_{\mathtt{R}}^{(1)}\\ \mathbf{F}_{\mathtt{L}}^{(2)}\end{pmatrix}=-\begin{pmatrix}\mathbf{F}_{1}^{\mathtt{c}}\\ \mathbf{F}_{2}^{\mathtt{c}}\end{pmatrix}\quad,\quad\begin{pmatrix}\mathbf{q}_{1}^{\mathtt{c}}\\ \mathbf{q}_{2}^{\mathtt{c}}\end{pmatrix}=\begin{pmatrix}\mathbf{q}_{\mathtt{R}}^{(1)}\\ \mathbf{q}_{\mathtt{L}}^{(2)}\end{pmatrix}, \tag{2.16}$$

The dynamical equilibrium of the coupling element can be expressed in a condensed form,

$$\mathbb{D}^{c*}\begin{pmatrix}\mathbf{q}_{1}^{\mathtt{c}}\\ \mathbf{q}_{2}^{\mathtt{c}}\end{pmatrix}=\begin{pmatrix}\mathbf{F}_{1}^{\mathtt{c}}\\ \mathbf{F}_{2}^{\mathtt{c}}\end{pmatrix}, \tag{2.17}$$

where $\mathbb{D}^{c*}$ stands for the dynamical stiffness matrix of the coupling element, condensed on the DOFs located on surfaces Γ_1 and Γ_2. The relation between forces $(\mathbf{F}_{\mathtt{R}}^{(1)},\mathbf{F}_{\mathtt{L}}^{(2)})$ applied at the right and left boundaries of substructures 1 and 2 and displacements $(\mathbf{q}_{\mathtt{R}}^{(1)},\mathbf{q}_{\mathtt{L}}^{(2)})$ is easily found by considering equations (2.17) and (2.16):

$$\mathbb{D}^{c*}\begin{pmatrix}\mathbf{q}_{\mathtt{R}}^{(1)}\\ \mathbf{q}_{\mathtt{L}}^{(2)}\end{pmatrix}=\begin{pmatrix}\mathbf{F}_{\mathtt{R}}^{(1)}\\ \mathbf{F}_{\mathtt{L}}^{(2)}\end{pmatrix}. \tag{2.18}$$

In short, a relation is proposed between the forces applied by the common coupling element to waveguides 1 and 2, on surfaces Γ_1 and Γ_2, and for the corresponding displacements as well. In the context of the Subsection 2.1, it can be shown that the dynamical behavior of a given coupled periodic waveguide i $(i=1,2)$ can be simply expressed in terms of wave modes $((\mathbf{\Phi}_{\mathbf{q}}^{\mathtt{inc}(i)})^{\mathtt{T}}(\mathbf{\Phi}_{\mathbf{F}}^{\mathtt{inc}(i)})^{\mathtt{T}})^{\mathtt{T}}$ incident to the coupling element and wave modes $((\mathbf{\Phi}_{\mathbf{q}}^{\mathtt{ref}(i)})^{\mathtt{T}}(\mathbf{\Phi}_{\mathbf{F}}^{\mathtt{ref}(i)})^{\mathtt{T}})^{\mathtt{T}}$ reflected by the coupling element. In this sense, it can be shown that amplitudes $(\mathbf{Q}^{\mathtt{ref}(1)},\mathbf{Q}^{\mathtt{ref}(2)})$ of the modes reflected by the coupling element can be related to amplitudes $(\mathbf{Q}^{\mathtt{inc}(1)},\mathbf{Q}^{\mathtt{inc}(2)})$ of the modes incident to the coupling element through a diffusion matrix.

Indeed, from equations (2.10) and (2.13), state vectors $\mathbf{u}_{\mathtt{R}}^{(1)}$ and $\mathbf{u}_{\mathtt{L}}^{(2)}$ of substructures 1 and 2 can be expressed in this manner:

$$\begin{pmatrix} \mathbf{q}_{\mathrm{R}}^{(1)} \\ \mathbf{F}_{\mathrm{R}}^{(1)} \end{pmatrix} = \begin{bmatrix} \boldsymbol{\Phi}_{\mathbf{q}}^{\mathtt{inc}(1)} & \boldsymbol{\Phi}_{\mathbf{q}}^{\mathtt{ref}(1)} \\ \boldsymbol{\Phi}_{\mathbf{F}}^{\mathtt{inc}(1)} & \boldsymbol{\Phi}_{\mathbf{F}}^{\mathtt{ref}(1)} \end{bmatrix} \begin{pmatrix} \mathbf{Q}^{\mathtt{inc}(1)} \\ \mathbf{Q}^{\mathtt{ref}(1)} \end{pmatrix}, \tag{2.19}$$

$$\begin{pmatrix} \mathbf{q}_{\mathrm{L}}^{(2)} \\ \mathbf{F}_{\mathrm{L}}^{(2)} \end{pmatrix} = \begin{bmatrix} \boldsymbol{\Phi}_{\mathbf{q}}^{\mathtt{inc}(2)} & \boldsymbol{\Phi}_{\mathbf{q}}^{\mathtt{ref}(2)} \\ \boldsymbol{\Phi}_{\mathbf{F}}^{\mathtt{inc}(2)} & \boldsymbol{\Phi}_{\mathbf{F}}^{\mathtt{ref}(2)} \end{bmatrix} \begin{pmatrix} \mathbf{Q}^{\mathtt{inc}(2)} \\ \mathbf{Q}^{\mathtt{ref}(2)} \end{pmatrix}. \tag{2.20}$$

Equations ((2.19)) and ((2.20)) lead to:

$$\begin{pmatrix} \mathbf{q}_{\mathrm{R}}^{(1)} \\ \mathbf{q}_{\mathrm{L}}^{(2)} \end{pmatrix} = \left[\begin{array}{cc|cc} \boldsymbol{\Phi}_{\mathbf{q}}^{\mathtt{inc}(1)} & \mathbf{0} & \boldsymbol{\Phi}_{\mathbf{q}}^{\mathtt{ref}(1)} & \mathbf{0} \\ \mathbf{0} & \boldsymbol{\Phi}_{\mathbf{q}}^{\mathtt{inc}(2)} & \mathbf{0} & \boldsymbol{\Phi}_{\mathbf{q}}^{\mathtt{ref}(2)} \end{array} \right] \begin{pmatrix} \mathbf{Q}^{\mathtt{inc}(1)} \\ \mathbf{Q}^{\mathtt{inc}(2)} \\ \mathbf{Q}^{\mathtt{ref}(1)} \\ \mathbf{Q}^{\mathtt{ref}(2)} \end{pmatrix}, \tag{2.21}$$

and

$$\begin{pmatrix} \mathbf{F}_{\mathrm{R}}^{(1)} \\ \mathbf{F}_{\mathrm{L}}^{(2)} \end{pmatrix} = \left[\begin{array}{cc|cc} \boldsymbol{\Phi}_{\mathbf{F}}^{\mathtt{inc}(1)} & \mathbf{0} & \boldsymbol{\Phi}_{\mathbf{F}}^{\mathtt{ref}(1)} & \mathbf{0} \\ \mathbf{0} & \boldsymbol{\Phi}_{\mathbf{F}}^{\mathtt{inc}(2)} & \mathbf{0} & \boldsymbol{\Phi}_{\mathbf{F}}^{\mathtt{ref}(2)} \end{array} \right] \begin{pmatrix} \mathbf{Q}^{\mathtt{inc}(1)} \\ \mathbf{Q}^{\mathtt{inc}(2)} \\ \mathbf{Q}^{\mathtt{ref}(1)} \\ \mathbf{Q}^{\mathtt{ref}(2)} \end{pmatrix}, \tag{2.22}$$

From equations (2.21) and (2.22), equation (2.18) can be written in this manner:

$$\mathbb{D}^{c*} \left[\begin{array}{c|c} \boldsymbol{\Psi}_{\mathbf{q}}^{\mathtt{inc}} & \boldsymbol{\Psi}_{\mathbf{q}}^{\mathtt{ref}} \end{array} \right] \begin{pmatrix} \mathbf{Q}^{\mathtt{inc}(1)} \\ \mathbf{Q}^{\mathtt{inc}(2)} \\ \mathbf{Q}^{\mathtt{ref}(1)} \\ \mathbf{Q}^{\mathtt{ref}(2)} \end{pmatrix} = \left[\begin{array}{c|c} \boldsymbol{\Psi}_{\mathbf{F}}^{\mathtt{inc}} & \boldsymbol{\Psi}_{\mathbf{F}}^{\mathtt{ref}} \end{array} \right] \begin{pmatrix} \mathbf{Q}^{\mathtt{inc}(1)} \\ \mathbf{Q}^{\mathtt{inc}(2)} \\ \mathbf{Q}^{\mathtt{ref}(1)} \\ \mathbf{Q}^{\mathtt{ref}(2)} \end{pmatrix}, \tag{2.23}$$

where matrices $\boldsymbol{\Psi}_{\mathbf{q}}^{\mathtt{inc}}$, $\boldsymbol{\Psi}_{\mathbf{q}}^{\mathtt{ref}}$, $\boldsymbol{\Psi}_{\mathbf{F}}^{\mathtt{inc}}$ and $\boldsymbol{\Psi}_{\mathbf{F}}^{\mathtt{ref}}$ have been introduced for the sake of clarity and are expressed by

$$\begin{aligned} \boldsymbol{\Psi}_{\mathbf{q}}^{\mathtt{inc}} &= \begin{bmatrix} \boldsymbol{\Phi}_{\mathbf{q}}^{\mathtt{inc}(1)} & \mathbf{0} \\ \mathbf{0} & \boldsymbol{\Phi}_{\mathbf{q}}^{\mathtt{inc}(2)} \end{bmatrix} \quad , \quad \boldsymbol{\Psi}_{\mathbf{q}}^{\mathtt{ref}} = \begin{bmatrix} \boldsymbol{\Phi}_{\mathbf{q}}^{\mathtt{ref}(1)} & \mathbf{0} \\ \mathbf{0} & \boldsymbol{\Phi}_{\mathbf{q}}^{\mathtt{ref}(2)} \end{bmatrix} \\ \boldsymbol{\Psi}_{\mathbf{F}}^{\mathtt{inc}} &= \begin{bmatrix} \boldsymbol{\Phi}_{\mathbf{F}}^{\mathtt{inc}(1)} & \mathbf{0} \\ \mathbf{0} & \boldsymbol{\Phi}_{\mathbf{F}}^{\mathtt{inc}(2)} \end{bmatrix} \quad , \quad \boldsymbol{\Psi}_{\mathbf{F}}^{\mathtt{ref}} = \begin{bmatrix} \boldsymbol{\Phi}_{\mathbf{F}}^{\mathtt{ref}(1)} & \mathbf{0} \\ \mathbf{0} & \boldsymbol{\Phi}_{\mathbf{F}}^{\mathtt{ref}(2)} \end{bmatrix}. \end{aligned} \tag{2.24}$$

Finally, equation (2.23) can be expressed in this way,

$$\left[\ \mathbb{D}^{c*}\,\mathbf{\Psi}_{\mathbf{q}}^{\mathtt{inc}} + \mathbf{\Psi}_{\mathbf{F}}^{\mathtt{inc}} \ \middle|\ \mathbb{D}^{c*}\,\mathbf{\Psi}_{\mathbf{q}}^{\mathtt{ref}} + \mathbf{\Psi}_{\mathbf{F}}^{\mathtt{ref}}\ \right] \begin{pmatrix} \mathbf{Q}^{\mathtt{inc}(1)} \\ \mathbf{Q}^{\mathtt{inc}(2)} \\ \mathbf{Q}^{\mathtt{ref}(1)} \\ \mathbf{Q}^{\mathtt{ref}(2)} \end{pmatrix} = \mathbf{0} \tag{2.25}$$

Assuming that matrix $\left[\mathbb{D}^{c*}\,\mathbf{\Psi}_{\mathbf{F}}^{\mathtt{ref}} + \mathbf{\Psi}_{\mathbf{q}}^{\mathtt{ref}}\right]$ is invertible, amplitudes $(\mathbf{Q}^{\mathtt{ref}(1)}, \mathbf{Q}^{\mathtt{ref}(2)})$ of the modes reflected by the coupling element can be expressed from amplitudes $(\mathbf{Q}^{\mathtt{inc}(1)}, \mathbf{Q}^{\mathtt{inc}(2)})$ of the modes incident to the coupling element through a diffusion matrix, namely $\mathbb{C}$, which expresses the reflection and transmission coefficients of the wave modes:

$$\begin{pmatrix} \mathbf{Q}^{\mathtt{ref}(1)} \\ \mathbf{Q}^{\mathtt{ref}(2)} \end{pmatrix} = \mathbb{C} \begin{pmatrix} \mathbf{Q}^{\mathtt{inc}(1)} \\ \mathbf{Q}^{\mathtt{inc}(2)} \end{pmatrix}, \tag{2.26}$$

where

$$\mathbb{C} = -\left[\mathbb{D}^{c*}\,\mathbf{\Psi}_{\mathbf{q}}^{\mathtt{ref}} + \mathbf{\Psi}_{\mathbf{F}}^{\mathtt{ref}}\right]^{-1}\left[\mathbb{D}^{c*}\,\mathbf{\Psi}_{\mathbf{q}}^{\mathtt{inc}} + \mathbf{\Psi}_{\mathbf{F}}^{\mathtt{inc}}\right] \tag{2.27}$$

One must keep in mind that diffusion matrix $\mathbb{C}$ directly depend on the normalization of eigenvectors $\{\mathbf{\Phi}_j^{(1)}\}_j$ and $\{\mathbf{\Phi}_k^{(2)}\}_k$. It seems advantageous to normalize the eigenvectors of the two waveguides in a similar manner.
If the DOFs at the interfaces Γ_1 and Γ_2 are not compatible, Lagrange multipliers will be applied to consider this problem and detailed formulations can be found in Appendix C.

2.1.3 Forced Wave Finite Element formulation

The WFE formulation provides wave propagation predictions under free boundary conditions. In order to obtain the forced response of the structure, the Forced Wave Finite Element(FWFE) formulation [47, 69, 70] can be employed. Based on equation (2.13) and equation (2.26), amplitudes $\mathbf{Q}^{(k)}$ which reflect for instance the kinematic variable $\mathbf{u}_L^{(k)}$ for substructure k, are described from amplitudes $\mathbf{Q}^{(1)}$ and $\mathbf{Q}^{(N+1)}$ representing kinematic variables $\mathbf{u}_L^{(1)}$ and $\mathbf{u}_R^{(N)}$ at the waveguide boundaries. According to the coupling relations between two consecutive substructures k and $k-1$ ($k \in \{2, \ldots, N\}$),$\mathbf{q}_L^{(k)} = \mathbf{q}_R^{(k-1)}$ and $-\mathbf{F}_L^{(k)} = \mathbf{F}_R^{(k-1)}$, the following relation can be found:

$$\mathbf{u}_L^{(k)} = \mathbf{u}_R^{(k-1)} \quad \forall k \in \{2, \ldots, N\} \tag{2.28}$$

which leads to

$$\mathbf{u}_L^{(k)} = \mathbf{S}\mathbf{u}_L^{(k-1)} \quad \forall k \in \{2, \ldots, N\} \tag{2.29}$$

Equation (2.29) allows to write:

$$\mathbf{u}_L^{(k)} = \mathbf{S}^{k-1}\mathbf{u}_L^{(1)} \quad \forall k \in \{1,\dots,N\} \tag{2.30}$$

with $\mathbf{S}^0 = \mathbf{I}_{2n}$, and:

$$\mathbf{u}_R^{(N)} = \mathbf{S}^N\mathbf{u}_L^{(1)} \tag{2.31}$$

Equation (2.30) and equation (2.31) are projected on the basis $\{\mathbf{\Phi}_i\}_i$ considering equation (2.13). Since matrix $\mathbf{\Phi}$ is invertible (it has been assumed that $det[\mathbf{\Phi}] \neq 0$), one obtains [71]:

$$\mathbf{Q}^{(k)} = \mathbf{\Phi}^{-1}\mathbf{S}^{k-1}\mathbf{\Phi}\mathbf{Q}^{(1)} \quad \forall k \in \{1,\dots,N+1\} \tag{2.32}$$

that is (cf. Equation (B.18))

$$\mathbf{Q}^{(k)} = \begin{bmatrix} \mathbf{\Lambda} & \mathbf{0} \\ \mathbf{0} & \mathbf{\Lambda}^{-1} \end{bmatrix}^{k-1} \mathbf{Q}^{(1)} \quad \forall k \in \{1,\dots,N+1\} \tag{2.33}$$

where $\mathbf{\Lambda}$ stands for the $(n \times n)$ diagonal eigenvalue matrix for wave modes propagating in x positive direction, expressed by equation (2.34) [71].

$$\mathbf{\Lambda} = \begin{bmatrix} \mu_1 & 0 & \dots & 0 \\ 0 & \mu_2 & \dots & 0 \\ \vdots & \vdots & \ddots & \vdots \\ 0 & 0 & \dots & \mu_n \end{bmatrix} \tag{2.34}$$

Expressing the boundary conditions of the waveguides in terms of amplitudes $\mathbf{Q}^{(1)}$ and $\mathbf{Q}^{(\mathtt{N+1})}$ allows us to express, from equation (2.33), the dynamics of a given substructure k. In a general manner, the boundary conditions at a specific boundary of the waveguide can be formulated in this way:

$$\mathbf{Q}^{\mathtt{ref}} \mid_{\mathtt{lim}} = \mathbb{C}\mathbf{Q}^{\mathtt{inc}} \mid_{\mathtt{lim}} + \boldsymbol{\mathcal{F}} \tag{2.35}$$

where $\mathbb{C}$ stands for the diffusion matrix of the coupling element, and $\boldsymbol{\mathcal{F}}$ denotes the effects of the excitations sources [47, 72]. It is demonstrated in the work of Mencik *et al.* [72] that the general relation in equation (2.35) can be applied to describe classical Neumann and Dirichlet boundary conditions. These conditions can be expressed as follows:

$$[\mathbf{0} \mid \mathbf{I}]\,\mathbf{u} = \mathbf{F}_0 \qquad (Neumann) \tag{2.36a}$$

$$[\mathbf{I} \mid \mathbf{0}]\,\mathbf{u} = \mathbf{q}_0 \qquad (Dirichlet) \tag{2.36b}$$

They can be rewritten in the following manner via the projection of the state vector $\mathbf{u}$ onto the wave mode basis (see equation (2.13)):

$$\mathbf{\Phi}_{\mathbf{F}}^{\mathtt{inc}}\mathbf{Q}^{\mathtt{inc}} + \mathbf{\Phi}_{\mathbf{F}}^{\mathtt{ref}}\mathbf{Q}^{\mathtt{ref}} = \mathbf{F}_0 \qquad (Neumann) \tag{2.37a}$$

$$\mathbf{\Phi}_{\mathbf{q}}^{\mathtt{inc}}\mathbf{Q}^{\mathtt{inc}} + \mathbf{\Phi}_{\mathbf{q}}^{\mathtt{ref}}\mathbf{Q}^{\mathtt{ref}} = \mathbf{q}_0 \qquad (Dirichlet) \tag{2.37b}$$

2.1.4 Wave Finite Element method in time domain

Based on frequency response of the structure issued from the FWFE method, the time response of the structure can be obtained in a rather simple way. For example, if a structure is subjected to an excitation force $\mathbf{f}_{\texttt{exc}}$ in time domain $[t_k]_{k=1\ldots M}$, through a Discrete Fourier Transform(DFT), the spectrum of this excitation force $\hat{\mathbf{f}}_{\texttt{exc}}$ can be expressed in the frequency domain $[\omega_k]_{k=1\ldots M}$.

$$\hat{\mathbf{f}}_{\texttt{exc}}(\omega_k) = \sum_{m=1}^{M} \mathbf{f}_{\texttt{exc}}(t_m) e^{-jt_m\omega_k} \tag{2.38}$$

This spectrum is then used in the FWFE approach to calculate the nodal displacement response $\hat{\mathbf{u}}(\omega_{\mathbf{m}})$ frequency by frequency. Subsequently, by applying an Inverse Discrete Fourier Transform(IDFT) to the frequency response, the time response can be acquired.

$$\mathbf{u}(t_k) = \frac{1}{M} \sum_{m=1}^{M} \hat{\mathbf{u}}(\omega_m) e^{-jt_k\omega_m} \tag{2.39}$$

It should be noted that M, the number of samples should be large enough to ensure the quality of the frequency and time response.

2.1.5 Dynamics of the system expressed in reduced modal basis

The wave formulations established above constitutes the framework of the WFE formulation and appears well suited for predicting the spatial distribution of the kinematic variables along the global system. The technique is based on the expansion of either the state vector $\mathbf{u}_{\mathrm{L}}^{(k)}$ or the state vector $\mathbf{u}_{\mathrm{R}}^{(k)}$ of any subsystem k on a *reduced* wave mode basis, say $\{\tilde{\mathbf{\Phi}}\}_{j=1,\ldots,2m}$, extracted from the global wave mode basis $\{\mathbf{\Phi}\}_{j=1,\ldots,2n}$ $(m \leq n)$. In this case, the following relationship can be written:

$$\begin{aligned}
\mathbf{u}_{\mathrm{L}}^{(k)} &= \begin{pmatrix} \mathbf{q}_{\mathrm{L}}^{(k)} \\ \mathbf{F}_{\mathrm{L}}^{(k)} \end{pmatrix} = \begin{bmatrix} \tilde{\mathbf{\Phi}}_{\mathbf{q}}^{\texttt{inc}} & \tilde{\mathbf{\Phi}}_{\mathbf{q}}^{\texttt{ref}} \\ \tilde{\mathbf{\Phi}}_{\mathbf{F}}^{\texttt{inc}} & \tilde{\mathbf{\Phi}}_{\mathbf{F}}^{\texttt{ref}} \end{bmatrix} \begin{pmatrix} \tilde{\mathbf{Q}}^{\texttt{inc}(k)} \\ \tilde{\mathbf{Q}}^{\texttt{ref}(k)} \end{pmatrix} \\
\mathbf{u}_{\mathrm{R}}^{(k)} &= \begin{pmatrix} \mathbf{q}_{\mathrm{R}}^{(k)} \\ \mathbf{F}_{\mathrm{R}}^{(k)} \end{pmatrix} = \begin{bmatrix} \tilde{\mathbf{\Phi}}_{\mathbf{q}}^{\texttt{inc}} & \tilde{\mathbf{\Phi}}_{\mathbf{q}}^{\texttt{ref}} \\ \tilde{\mathbf{\Phi}}_{\mathbf{F}}^{\texttt{inc}} & \tilde{\mathbf{\Phi}}_{\mathbf{F}}^{\texttt{ref}} \end{bmatrix} \begin{pmatrix} \tilde{\mathbf{Q}}^{\texttt{inc}(k+1)} \\ \tilde{\mathbf{Q}}^{\texttt{ref}(k+1)} \end{pmatrix} \quad k = 1, \ldots, N
\end{aligned} \tag{2.40}$$

The diffusion matrix $\tilde{\mathbb{C}}$, unlike the diffusion matrix $\mathbb{C}$ obtained in equation (2.27), can thus be rewritten in the following manner:

$$\tilde{\mathbb{C}} = -\left[\mathbb{D}^{c*}\,\tilde{\mathbf{\Psi}}_{\mathbf{q}}^{\texttt{ref}} + \tilde{\mathbf{\Psi}}_{\mathbf{F}}^{\texttt{ref}}\right]^{+} \left[\mathbb{D}^{c*}\,\tilde{\mathbf{\Psi}}_{\mathbf{q}}^{\texttt{inc}} + \tilde{\mathbf{\Psi}}_{\mathbf{F}}^{\texttt{inc}}\right] \tag{2.41}$$

The superscript $+$ of a matrix denotes the pseudoinverse of this matrix, and:

$$\tilde{\boldsymbol{\Psi}}_{\mathbf{q}}^{\texttt{inc}} = \begin{bmatrix} \tilde{\boldsymbol{\Phi}}_{\mathbf{q}}^{\texttt{inc}(1)} & \mathbf{0} \\ \mathbf{0} & \tilde{\boldsymbol{\Phi}}_{\mathbf{q}}^{\texttt{inc}(2)} \end{bmatrix} \quad , \quad \tilde{\boldsymbol{\Psi}}_{\mathbf{q}}^{\texttt{ref}} = \begin{bmatrix} \tilde{\boldsymbol{\Phi}}_{\mathbf{q}}^{\texttt{ref}(1)} & \mathbf{0} \\ \mathbf{0} & \tilde{\boldsymbol{\Phi}}_{\mathbf{q}}^{\texttt{ref}(2)} \end{bmatrix} \tag{2.42}$$
$$\tilde{\boldsymbol{\Psi}}_{\mathbf{F}}^{\texttt{inc}} = \begin{bmatrix} \tilde{\boldsymbol{\Phi}}_{\mathbf{F}}^{\texttt{inc}(1)} & \mathbf{0} \\ \mathbf{0} & \tilde{\boldsymbol{\Phi}}_{\mathbf{F}}^{\texttt{inc}(2)} \end{bmatrix} \quad , \quad \tilde{\boldsymbol{\Psi}}_{\mathbf{F}}^{\texttt{ref}} = \begin{bmatrix} \tilde{\boldsymbol{\Phi}}_{\mathbf{F}}^{\texttt{ref}(1)} & \mathbf{0} \\ \mathbf{0} & \tilde{\boldsymbol{\Phi}}_{\mathbf{F}}^{\texttt{ref}(2)} \end{bmatrix} .$$

The matrix $\tilde{\mathbf{Q}} = ((\tilde{\mathbf{Q}}^{\texttt{inc}})^T (\tilde{\mathbf{Q}}^{\texttt{ref}})^T)^T$ stand for the modal amplitudes which can be obtained via the following boundary value problem:

$$\tilde{\mathbf{Q}}^{(k)} = \begin{bmatrix} \tilde{\boldsymbol{\Lambda}} & \mathbf{0} \\ \mathbf{0} & \tilde{\boldsymbol{\Lambda}}^{-1} \end{bmatrix}^{k-1} \tilde{\mathbf{Q}}^{(1)} \quad \text{and} \tag{2.43}$$
$$\tilde{\mathbf{Q}}^{\texttt{ref}} \,|_{\texttt{lim}} = \tilde{\mathbb{C}} \tilde{\mathbf{Q}}^{\texttt{inc}} \,|_{\texttt{lim}} + \tilde{\boldsymbol{\mathcal{F}}} \quad \forall k \in \{1, \ldots, N+1\}$$

Here, $\tilde{\boldsymbol{\Lambda}}$ is the diagonal eigenvalue matrix associated with the eigenvectors $\{\tilde{\boldsymbol{\Phi}}\}_{j=1,\ldots,2m}$; $\tilde{\mathbb{C}}$ and $\tilde{\boldsymbol{\mathcal{F}}}$ denote the diffusion matrix and the effects of the excitation sources. The latter are expressed as $\tilde{\boldsymbol{\mathcal{F}}}(\mathbf{F}_0) = (\tilde{\boldsymbol{\Phi}}_{\mathtt{F}}^{\texttt{ref}})^{+}\mathbf{F}_0$ for an imposed force field $\mathbf{F}_0$ and $\tilde{\boldsymbol{\mathcal{F}}}(\mathbf{q}_0) = (\tilde{\boldsymbol{\Phi}}_{\mathtt{q}}^{\texttt{ref}})^{+}\mathbf{q}_0$ for an imposed displacement field $\mathbf{q}_0$ [72].
In general, in order to ensure the validity of the expansion in equation (2.40), the reduced modal basis must contain the modes which are the most solicited by the excitation [68], that is, for which the excitation sources $\{\boldsymbol{\mathcal{F}}_j\}_j$ are large. This criterion allows in particular the representation of local behavior around singularities(sharp gradients), since propagating as well as evanescent and complex wave modes are involved in the boundary value problem (2.43). From a practical point of view, if the excitations $\mathbf{F}_0$ and/or $\mathbf{q}_0$ are uniformly distributed over the cross-section boundaries, the most solicited modes should be related to wavenumbers with imaginary parts close to zero (propagating modes or cut-on propagating modes) or nearly close to zero (nearly cutting-on propagating wave modes) [54].

2.2 Modified wave finite element formulation

Multi-layered systems are widely used in many engineering domains, offering structural designers plenty of attractive features like high specific stiffness, good buckling resistance, formability into complex shapes, easy reparability, etc. Understanding, predicting and tailoring their vibratory behavior has always been an important issue in vibroacoustics. With the development of the finite element method (FEM), the analysis of the dynamic behavior of such structures is becoming more and more convenient, as this method possessed the advantages of widespread use in engineering domain and the capability of treating complex geometry. However, problems arise when large size models are treated, as the computational cost of the resolution becomes unacceptable, especially for time response calculations. As an alternative, the dynamic analysis of multi-layered systems based on the numerical descriptions of waves traveling in these structures can be applied, as it provides a low cost and efficient way to capture the dynamic behavior with relatively small models. This technique appears especially well suited for the short wavelength domain as the dynamics of systems can be accurately described by highly convergent reduced bases containing essential wave motions.
The study of low-frequency (LF) and mid-frequency (MF) wave propagation in slender multi-layered elastic systems is focused on in this section. Such systems exhibit large scale behavior associated with uniform cross-sections where are confined high regular "rigid body" and elastic modes, and fine scale behavior associated with low regular propagating components [68]. The frequency ranges can be defined as follows: the LF range refers to the frequency domain for which a typical cross-section contains a small number of elastic modes, e.g. the related "cross-section" modal density is small, while the MF range corresponds to an intermediate frequency domain between the LF range and the high-frequency (HF) range for which the cross-section modal density exhibits large variations [73]. The WFE method mentioned in Section 2.1, which is based on the classic finite element description of a typical cell extracted from a given global system, is developed as an appropriate method for predicting the propagation in waveguides in a wide frequency range. Nevertheless, the WFE method suffers from a number of numerical problems especially when multi-layered structures are concerned. In order to address this issue, Mencik and Ichchou [68] developed a substructuring technique named modified wave finite element (MWFE) for analyzing wave propagation in multi-layered systems, allowing the standard wave motions of multi-layered systems to be correctly captured. This technique will be applied in this work to study the wave propagation in slender multi-layered elastic beams.

2.2.1 Associated substructuring scheme

We consider a typical multi-layered unit cell, say sub system k, belonging to a composite structure(see Figure 2.3).
In the present work, the unit cell representative of the composite waveguide is assumed to represent a set of M connected straight homogeneous layers, whose left and right boundaries are denoted, respectively, as $\{S^i_{\mathtt{L}}\}$ and $\{S^i_{\mathtt{R}}\}$: for each layer $i (i = 1, \ldots, M)$, the surfaces $\{S_{\mathtt{L}}\}$ and are assumed to contain the same number of DOFs, say n^i. Let us denote as Γ^i the coupling interface between each layer i and its surroundings, that is, the set of coupled layers $\{j\}_{j\neq i}$. $\mathbf{q}^i$ and $\mathbf{F}^i$ are the displacements and the forces applied to the uncoupled layer on $\{S^i_{\mathtt{L}}\} \cup \{S^i_{\mathtt{R}}\}$.

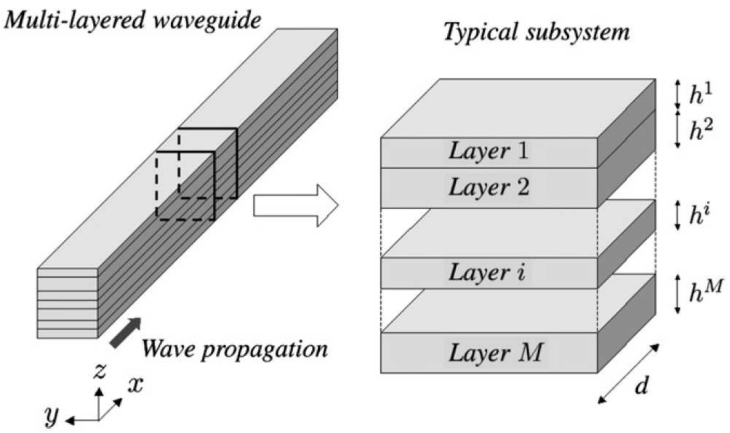

Figure 2.3: An illustration of a multi-layered elastic system with a rectangular cross-section [68].

Following what was previously presented for the WFE approach, the dynamic equilibrium equation of the unit cell is reformulated into a state vector representation: the displacements $\mathbf{q}^i$ and forces $\boldsymbol{\mathcal{F}}^i$ can be expressed in this way [45]:

$$\mathbf{q}^i = \begin{pmatrix} \mathbf{q}^i_{\mathtt{L}} \\ \mathbf{q}^i_{\mathtt{I}} \\ \mathbf{q}^i_{\mathtt{R}} \end{pmatrix} \quad \boldsymbol{\mathcal{F}}^i = \begin{pmatrix} \boldsymbol{\mathcal{F}}^i_{\mathtt{L}} \\ \boldsymbol{\mathcal{F}}^i_{\mathtt{I}} \\ \boldsymbol{\mathcal{F}}^i_{\mathtt{R}} \end{pmatrix} \quad i = 1, \ldots, M \tag{2.44}$$

where, for each layer i, the subscripts `L`, `R` and `I` refer, respectively, to the nodes which are located on $S^i_{\mathtt{L}}$ and $S^i_{\mathtt{R}}$, and to the internal nodes, which don't belong to $S^i_{\mathtt{L}}$ and $S^i_{\mathtt{R}}$. Introducing the orthogonal operator $\mathbf{L}$ such that

$$\begin{pmatrix} \mathbf{q}^1 \\ \vdots \\ \mathbf{q}^M \end{pmatrix} = \mathbf{L} \begin{pmatrix} \mathbf{q}^1_{\mathtt{L}} \\ \vdots \\ \mathbf{q}^M_{\mathtt{L}} \\ \hline \mathbf{q}^1_{\mathtt{I}} \\ \vdots \\ \mathbf{q}^M_{\mathtt{I}} \\ \hline \mathbf{q}^1_{\mathtt{R}} \\ \vdots \\ \mathbf{q}^M_{\mathtt{R}} \end{pmatrix} \tag{2.45}$$

With the operator $\mathbf{L}$, the order of the DOFs in the unit cell will be rearranged. The following dynamic equilibrium equation of the unit cell extracted from the multi-layered composite waveguide can be written as follows:

$$\boldsymbol{\mathcal{D}} \begin{pmatrix} \mathbf{q}^1_{\mathtt{L}} \\ \vdots \\ \mathbf{q}^M_{\mathtt{L}} \\ \hline \mathbf{q}^1_{\mathtt{I}} \\ \vdots \\ \mathbf{q}^M_{\mathtt{I}} \\ \hline \mathbf{q}^1_{\mathtt{R}} \\ \vdots \\ \mathbf{q}^M_{\mathtt{R}} \end{pmatrix} = \begin{pmatrix} \boldsymbol{\mathcal{F}}^1_{\mathtt{L}} \\ \vdots \\ \boldsymbol{\mathcal{F}}^M_{\mathtt{L}} \\ \hline \boldsymbol{\mathcal{F}}^1_{\mathtt{I}} \\ \vdots \\ \boldsymbol{\mathcal{F}}^M_{\mathtt{I}} \\ \hline \boldsymbol{\mathcal{F}}^1_{\mathtt{R}} \\ \vdots \\ \boldsymbol{\mathcal{F}}^M_{\mathtt{R}} \end{pmatrix} = \mathcal{G} \begin{pmatrix} \mathbf{F}^1_{\mathtt{L}} \\ \vdots \\ \mathbf{F}^M_{\mathtt{L}} \\ \hline \mathbf{F}^1_{\mathtt{I}} \\ \vdots \\ \mathbf{F}^M_{\mathtt{I}} \\ \hline \mathbf{F}^1_{\mathtt{R}} \\ \vdots \\ \mathbf{F}^M_{\mathtt{R}} \end{pmatrix}, \tag{2.46}$$

$\boldsymbol{\mathcal{D}}$ represents the dynamic stiffness matrix, and $\mathcal{G}$ imposes the continuity conditions of the forces between the uncoupled layers

$$\begin{aligned} \boldsymbol{\mathcal{D}} &= \mathbf{L}^{\mathtt{T}} \left[\mathbf{D}^{\mathtt{local}} + \mathbf{D}^{\mathtt{coupling}}\right] \mathbf{L} \\ \mathcal{G} &= \mathbf{L}^{\mathtt{T}} \left[\mathbf{I} + \mathbf{E}^{\mathtt{coupling}}\right] \mathbf{L} \end{aligned} \tag{2.47}$$

Detailed deduction of the previous relations can be found in Appendix D. Assuming that the internal DOFs of the subsystem are not submitted to external forces, that is $\boldsymbol{\mathcal{F}}^i_{\mathtt{I}} = \mathbf{0} \quad \forall i$, leads to the following condensed state vector representations for the associated substructuring scheme:

$$\begin{pmatrix} \mathbf{q}_{\mathrm{R}}^{1} \\ \vdots \\ \mathbf{q}_{\mathrm{R}}^{M} \\ \hline \boldsymbol{\mathcal{F}}_{\mathrm{R}}^{1} \\ \vdots \\ \boldsymbol{\mathcal{F}}_{\mathrm{R}}^{M} \end{pmatrix} = \mathcal{S} \begin{pmatrix} \mathbf{q}_{\mathrm{L}}^{1} \\ \vdots \\ \mathbf{q}_{\mathrm{L}}^{M} \\ \hline -\boldsymbol{\mathcal{F}}_{\mathrm{L}}^{1} \\ \vdots \\ -\boldsymbol{\mathcal{F}}_{\mathrm{L}}^{M} \end{pmatrix}. \tag{2.48}$$

Here, $\mathcal{S}$ is a $(2\sum_i n^i \times 2\sum_i n^i)$ matrix, expressed by

$$\mathcal{S} = \begin{bmatrix} -(\boldsymbol{\mathcal{D}}_{\mathrm{LR}}^{*})^{-1}\boldsymbol{\mathcal{D}}_{\mathrm{LL}}^{*} & -(\boldsymbol{\mathcal{D}}_{\mathrm{LR}}^{*})^{-1} \\ \boldsymbol{\mathcal{D}}_{\mathrm{RL}}^{*} - \boldsymbol{\mathcal{D}}_{\mathrm{RR}}^{*}(\boldsymbol{\mathcal{D}}_{\mathrm{LR}}^{*})^{-1}\boldsymbol{\mathcal{D}}_{\mathrm{LL}}^{*} & -\boldsymbol{\mathcal{D}}_{\mathrm{RR}}^{*}(\boldsymbol{\mathcal{D}}_{\mathrm{LR}}^{*})^{-1} \end{bmatrix} \tag{2.49}$$

More over, observing that, for each layer i, the contribution of the surroundings Θ^i to the forces applied on a specific boundary, either S_{L}^{i} or S_{R}^{i}, is null except on the boundary $S_{\mathrm{L}}^{\Theta^i}$ or $S_{\mathrm{R}}^{\Theta^i}$, respectively, leads to the following relationships:

$$\begin{pmatrix} \boldsymbol{\mathcal{F}}_{\mathrm{R}}^{1} \\ \vdots \\ \boldsymbol{\mathcal{F}}_{\mathrm{R}}^{M} \end{pmatrix} = \boldsymbol{\mathcal{G}}^{*} \begin{pmatrix} \mathbf{F}_{\mathrm{R}}^{1} \\ \vdots \\ \mathbf{F}_{\mathrm{R}}^{M} \end{pmatrix} \quad \begin{pmatrix} -\boldsymbol{\mathcal{F}}_{\mathrm{L}}^{1} \\ \vdots \\ -\boldsymbol{\mathcal{F}}_{\mathrm{L}}^{M} \end{pmatrix} = \boldsymbol{\mathcal{G}}^{*} \begin{pmatrix} -\mathbf{F}_{\mathrm{L}}^{1} \\ \vdots \\ -\mathbf{F}_{\mathrm{L}}^{M} \end{pmatrix} \tag{2.50}$$

where $\boldsymbol{\mathcal{G}}^{*} = \boldsymbol{\mathcal{G}}_{\mathrm{LL}} = \boldsymbol{\mathcal{G}}_{\mathrm{RR}}$. The substructuring scheme provided by equations (2.48) and (2.50) is interesting compared to the classic model as it allows the local kinematic variables (displacements and forces) of each layer cross-section to be considered independently from the surroundings. Specifically, the method appears interesting for constructing the global wave modes of the multi-layered system from a set of local wave mode bases attached to the layers with free interfaces $\{\Gamma^i\}_i$ and whose dimensions can be individually tuned to "fit" with each cross-section dynamics. This constitutes the framework of the MWFE formulation presented below.

2.2.2 Construction of the global wave mode basis

Considering the coupling conditions between two consecutive subsystems $k-1$ and k, established for each layer i

$$\mathbf{q}_{\mathrm{L}}^{i(k)} = \mathbf{q}_{\mathrm{R}}^{i(k-1)} \quad \boldsymbol{\mathcal{F}}_{\mathrm{L}}^{i(k)} = \boldsymbol{\mathcal{F}}_{\mathrm{R}}^{i(k-1)}$$

$$k = 2, \ldots, N \quad i = 1, \ldots, M \tag{2.51}$$

and considering, according to Bloch's theorem [74], wave solutions $\{\mathbf{\Phi}_j\}_j$ in equation (2.48) leads to the following eigenvalue problem

$$\mathcal{S}\begin{pmatrix}(\mathbf{\Phi}_{\mathtt{q}})_{j|1}\\ \vdots\\ (\mathbf{\Phi}_{\mathtt{q}})_{j|M}\\ \hline (\mathbf{\Phi}_{\boldsymbol{\mathcal{F}}})_{j|1}\\ \vdots\\ (\mathbf{\Phi}_{\boldsymbol{\mathcal{F}}})_{j|M}\end{pmatrix} = \mu_j\begin{pmatrix}(\mathbf{\Phi}_{\mathtt{q}})_{j|1}\\ \vdots\\ (\mathbf{\Phi}_{\mathtt{q}})_{j|M}\\ \hline (\mathbf{\Phi}_{\boldsymbol{\mathcal{F}}})_{j|1}\\ \vdots\\ (\mathbf{\Phi}_{\boldsymbol{\mathcal{F}}})_{j|M}\end{pmatrix}, \quad |\mathcal{S}-\mu_j\mathbf{I}| = 0 \tag{2.52}$$

where $(\mathbf{\Phi}_{\mathtt{q}})_{j|i}$ and $(\mathbf{\Phi}_{\boldsymbol{\mathcal{F}}})_{j|i}$ are $(n^i\times 1)$ vectors which represent the restriction of the $(n\times 1)$ global mode components $(\mathbf{\Phi}_{\mathtt{q}})_j$ and $(\mathbf{\Phi}_{\mathtt{F}})_j$ to S_L^i or S_R^i. Furthermore, expressing equation (2.50) in terms of the wave mode components allows us to define the set $\{(\mathbf{\Phi}_{\mathtt{F}})_{j|i}\}_i$ as

$$\begin{pmatrix}(\mathbf{\Phi}_{\boldsymbol{\mathcal{F}}})_{j|1}\\ \vdots\\ (\mathbf{\Phi}_{\boldsymbol{\mathcal{F}}})_{j|M}\end{pmatrix} = \boldsymbol{\mathcal{G}}^*\begin{pmatrix}(\mathbf{\Phi}_{\mathtt{F}})_{j|1}\\ \vdots\\ (\mathbf{\Phi}_{\mathtt{F}})_{j|M}\end{pmatrix} \tag{2.53}$$

which is related to the set of forces $\{\mathbf{F}^i\}_i$ applied to the layers with free interfaces $\{\Gamma^i\}_i$. Hereafter, the global wave modes $\{\mathbf{\Phi}_j\}_j$ of the multi-layered system are constructed from a set of reduced local bases $\{\{\tilde{\mathbf{\Phi}}_j^i\}_{j=1,\ldots,2m^i}\}_i = \{\{\mathbf{\Phi}_j^1\}_j, \{\mathbf{\Phi}_k^2\}_k, \ldots, \{\mathbf{\Phi}_l^M\}_l\}$ attached to the homogeneous uncoupled layers and having specific dimensions $\{2m^i\}_i$. Two different modelings for the global wave mode construction are described below: the first MWFE modeling enforces the convergence of the wave mode expansion used in the global wave mode construction, while the second MWFE modeling is based on a relatively well-conditioned eigenvalue problem.

The first MWFE modeling consists of constructing the global wave modes $\{\mathbf{\Phi}_j\}_j$ from a set of reduced local bases $\{\tilde{\mathbf{\Phi}}_i\}_i$, having specific dimensions $\{2m^i\}$, as follows:

$$\begin{aligned}(\mathbf{\Phi}_{\mathtt{q}})_{j|i} &= \sum_{l=1,\ldots,2m^i} a_{jl}^i(\tilde{\mathbf{\Phi}}_{\mathtt{q}}^i)_l,\\ (\mathbf{\Phi}_{\mathtt{F}})_{j|i} &= \sum_{l=1,\ldots,2m^i} a_{jl}^i(\tilde{\mathbf{\Phi}}_{\mathtt{F}}^i)_l, \quad i=1,\ldots,M,\end{aligned} \tag{2.54}$$

where the set $\{a_{jl}^i\}$ describes generalized coordinates. The expansion (2.54) is natural as both the global and local wave component sets $\{(\mathbf{\Phi}_{\mathtt{F}})_{j|i}\}_i$ and $\{\{(\mathbf{\Phi}_{\mathtt{F}}^i)_l\}_l\}_i$ reflect the forces applied to the uncoupled layers. The continuity of the global wave force component set $\{(\boldsymbol{\Phi}_{\mathcal{F}})_{j|i}\}_i$ at the coupling interfaces $\{\Gamma^i\}_i$ is provided by Equation (2.53), which enforces the convergence of the first MWFE modeling.

According to equation (2.54), the construction of the global wave modes $\{\boldsymbol{\Phi}_j\}_j$ can be established as follows: accounting for equations (2.53) and (2.54) results in the following matrix form:

$$\begin{pmatrix} (\boldsymbol{\Phi}_{\mathtt{q}})_{j|1} \\ \vdots \\ (\boldsymbol{\Phi}_{\mathtt{q}})_{j|M} \\ \hline (\boldsymbol{\Phi}_{\mathcal{F}})_{j|1} \\ \vdots \\ (\boldsymbol{\Phi}_{\mathcal{F}})_{j|M} \end{pmatrix} = \boldsymbol{\mathcal{B}}\mathbf{a}_j \tag{2.55}$$

where the matrix $\boldsymbol{\mathcal{B}}$ is written

$$\boldsymbol{\mathcal{B}} = \begin{bmatrix} \mathbf{I} & \mathbf{0} \\ \mathbf{0} & \boldsymbol{\mathcal{G}}^* \end{bmatrix} \begin{bmatrix} \tilde{\boldsymbol{\Phi}}_{\mathtt{q}}^{\mathtt{local}} \\ \tilde{\boldsymbol{\Phi}}_{\mathtt{F}}^{\mathtt{local}} \end{bmatrix}. \tag{2.56}$$

With the second MWFE formulation, the following expansion is considered, which is quite different from equation (2.54):

$$\begin{aligned} (\boldsymbol{\Phi}_{\mathtt{q}})_{j|i} &= \sum_{l=1,\dots,2m^i} a_{jl}^i (\tilde{\boldsymbol{\Phi}}_{\mathtt{q}}^i)_l, \\ (\boldsymbol{\Phi}_{\mathcal{F}})_{j|i} &= \sum_{l=1,\dots,2m^i} a_{jl}^i (\tilde{\boldsymbol{\Phi}}_{\mathtt{F}}^i)_l, \quad i = 1,\dots,M. \end{aligned} \tag{2.57}$$

The expansion (2.57) doesn't appear natural since the global and local wave force component sets $\{(\boldsymbol{\Phi}_{\mathcal{F}})_{j|i}\}_i$ and $\{\{(\boldsymbol{\Phi}_{\mathtt{F}}^i)_l\}_l\}_i$ are attached to the coupled and uncoupled layers respectively. As a result, the continuity of the global wave force component set $\{(\boldsymbol{\Phi}_{\mathcal{F}})_{j|i}\}_i$ at the coupling interfaces $\{\Gamma^i\}_i$ can't be established in the present case, as opposed to the first MWFE expansion, which might result in poor convergence of the formulation. To solve this problem, the representation is assumed to include a significant number of high order MF local modes.

In the present context, equation (2.57) is then expressed from the following matrix:

$$\boldsymbol{\mathcal{B}} = \begin{bmatrix} \tilde{\boldsymbol{\Phi}}_{\mathtt{q}}^{\mathtt{local}} \\ \tilde{\boldsymbol{\Phi}}_{\mathtt{F}}^{\mathtt{local}} \end{bmatrix}. \tag{2.58}$$

In the two MWFE formulations, the matrix $\boldsymbol{\mathcal{B}}$ is expressed from the following $(\sum_i n^i \times 2\sum_i m^i)$ matrices $\tilde{\mathbf{\Phi}}_{\mathtt{q}}^{\mathtt{local}}$ and $\tilde{\mathbf{\Phi}}_{\mathtt{F}}^{\mathtt{local}}$

$$\tilde{\mathbf{\Phi}}_{\mathtt{q}}^{\mathtt{local}} = \begin{bmatrix} \tilde{\mathbf{\Phi}}_{\mathtt{q}}^{1} & \mathbf{0} & \dots & \mathbf{0} \\ \mathbf{0} & \tilde{\mathbf{\Phi}}_{\mathtt{q}}^{2} & \dots & \mathbf{0} \\ \vdots & \vdots & \ddots & \vdots \\ \mathbf{0} & \mathbf{0} & \dots & \tilde{\mathbf{\Phi}}_{\mathtt{q}}^{M} \end{bmatrix}$$

$$\tilde{\mathbf{\Phi}}_{\mathtt{F}}^{\mathtt{local}} = \begin{bmatrix} \tilde{\mathbf{\Phi}}_{\mathtt{F}}^{1} & \mathbf{0} & \dots & \mathbf{0} \\ \mathbf{0} & \tilde{\mathbf{\Phi}}_{\mathtt{F}}^{2} & \dots & \mathbf{0} \\ \vdots & \vdots & \ddots & \vdots \\ \mathbf{0} & \mathbf{0} & \dots & \tilde{\mathbf{\Phi}}_{\mathtt{F}}^{M} \end{bmatrix}. \tag{2.59}$$

In equation (2.55), $\{\mathbf{a}_j\}_j$ stands for the set of $(2\sum_i m^i \times 1)$ generalized coordinate vectors

$$\mathbf{a}_j = \begin{bmatrix} \mathbf{a}_j^1 \\ \mathbf{a}_j^2 \\ \vdots \\ \mathbf{a}_j^M \end{bmatrix}, \quad \mathbf{a}_j^i = \begin{bmatrix} a_{j1}^i \\ a_{j2}^i \\ \vdots \\ a_{jm^i}^i \end{bmatrix} \quad i = 1, \dots, M. \tag{2.60}$$

which has to be determined in the MWFE context by means of the substructuring scheme described below: Inserting equation (2.55) into equation (2.52) results in the following $(2\sum_i n^i \times 2\sum_i m^i)$ overdetermined system:

$$\boldsymbol{\mathcal{S}}\boldsymbol{\mathcal{B}}\mathbf{a}_j = \mu_j \boldsymbol{\mathcal{B}}\mathbf{a}_j \tag{2.61}$$

The overdetermined system (2.61) can be simplified and reduced to a square $(2\sum_i m^i \times 2\sum_i m^i)$ system when it is projected on the space spanned by the adjoint reduced basis $-\mathbf{J}\boldsymbol{\mathcal{B}}$. Multiplying equation (2.61) by $[-\mathbf{J}\boldsymbol{\mathcal{B}}]^{\mathrm{T}}$ and considering that $-\mathbf{J}^{\mathrm{T}} = \mathbf{J}$, results in

$$\boldsymbol{\mathcal{B}}^{\mathrm{T}}\mathbf{J}\boldsymbol{\mathcal{S}}\boldsymbol{\mathcal{B}}\mathbf{a}_j = \mu_j \boldsymbol{\mathcal{B}}^{\mathrm{T}}\mathbf{J}\boldsymbol{\mathcal{B}}\mathbf{a}_j \tag{2.62}$$

Thus, the set of modal participations $\{\mathbf{a}_j\}_j$ can be evaluated by solving a square $(2\sum_i m^i \times 2\sum_i m^i)$ classic eigenvalue problem

$$\mathbf{S}^{\mathtt{MWFE}}\mathbf{a}_j = \mu_j \mathbf{a}_j, \quad |\mathbf{S}^{\mathtt{MWFE}} - \mu_j \mathbf{I}| = 0 \tag{2.63}$$

where

$$\mathbf{S}^{\mathtt{MWFE}} = \left[\boldsymbol{\mathcal{B}}^{\mathrm{T}}\mathbf{J}\boldsymbol{\mathcal{B}}\right]^{-1} \boldsymbol{\mathcal{B}}^{\mathrm{T}}\mathbf{J}\boldsymbol{\mathcal{S}}\boldsymbol{\mathcal{B}} \tag{2.64}$$

The eigenvalue problem (2.63) in central to the MWFE formulation. Given a set of reduced local bases $\{\{\tilde{\mathbf{\Phi}}_j^i\}_j\}_i$ having appropriate dimensions, the formulation consists of finding the eigenvalues $\{\mu_j\}_j$, which describe the global wave mode velocities, and the eigenvectors $\{\mathbf{a}_j\}_j$, providing, by means of equation (2.52), the restrictions of the global wave mode shapes, say $\{\{\mathbf{\Phi}_{j|i}\}_i\}_j$, to the set of surfaces $\{S^i_{\mathtt{L}}\}$ or $\{S^i_{\mathtt{R}}\}$.

The frequency revolution of the global wave mode parameters, obtained using the MWFE formulation, can not be performed in a standard manner using the criterion provided by equation (2.12), as the operator $\mathbf{S}^{\mathtt{MWFE}}$ is not symplectic [68]. Instead, an alternative criterion based on the Hermitian scalar product of the wave displacement components is suggested: for global wave mode j defined at the angular frequency ω, we find global wave mode j at the angular frequency $\omega + \Delta_\omega$ such that:

$$\mathbf{A}_j^{MWFE}(\omega) = (\boldsymbol{\mathcal{B}}\mathbf{a}_j(\omega + \Delta_\omega))^{\mathtt{H}}_{\mathtt{q}}(\boldsymbol{\mathcal{B}}\mathbf{a}_j(\omega))_{\mathtt{q}} \tag{2.65}$$

is maximized. Here, $(\boldsymbol{\mathcal{B}}\mathbf{a}_j(\omega))_{\mathtt{q}} = ((\mathbf{\Phi}_q)^T_{j|1} \dots (\mathbf{\Phi}_q)^T_{j|M})^T$. The choice of a small frequency step Δ_ω and the normalization of each modal displacement component $(\boldsymbol{\mathcal{B}}\mathbf{a}_j)_{\mathtt{q}}$ relative to the adimensioned Hermitian norm $\sqrt{(\boldsymbol{\mathcal{B}}\mathbf{a}_j)^H_{\mathtt{q}}(\boldsymbol{\mathcal{B}}\mathbf{a}_j)_{\mathtt{q}}}$ enforce the validity of the criterion; however, unlike the classic criterion provided by equation (2.12), the criterion provided by equation (2.65) does not make any distinction between incident and reflected waves, which means that this former classification [38, 46] has to be completed in a first step, before the use of the criterion (2.65).

In brief, the advantages of the MWFE formulation compared to the WFE formulation are [68]:

- The size of the eigenvalue problem (2.63) corresponds to a sum of dimensions which exactly capture the dynamics of the layer cross-section: the dependency between eigenvectors is removed and the essential behavior is captured.

- The size of the eigenvalue problem (2.63) is generally smaller than the classic eigenvalue problem (2.6), allowing a reduction of the numerical cost.

- All the components of the operator $\mathbf{S}^{\mathtt{MWFE}}$ are homogeneous and are not partitioned into displacement and force components: the problem of the ill-conditioned classic operator $\mathbf{S}$ is removed, *a priori*.

2.3 Finite element modeling of piezoelectric structures

2.3.1 Variational principle

The three-dimensional piezoelectric constitutive law can be written as:

$$T_{ij} = c^{E}_{ijkl} S_{kl} - e_{kij} E_k \tag{2.66a}$$

$$D_i = e_{ikl} S_{kl} + \varepsilon^{S}_{ik} E_k \tag{2.66b}$$

where E denotes the electric field, T the mechanical stress, S the mechanical strain, and D the electric displacement; c^E represents the material stiffness, e describes the piezoelectric stress coupling, and ε^S is the permittivity under constant strain. Equation (2.66a) represents the indirect piezoelectric effect, whereas equation (2.66b) characterizes the direct piezoelectric effect.

Considering that this flexible piezoelectric continuum is occupying the volume V_s with regular boundary surface S_s, the governing equations of mechanical, dynamic and electrostatic equilibriums are given as follows:

$$T_{ij,j} + f_i = \rho \ddot{u}_i \tag{2.67}$$

$$D_{i,i} - q = 0 \tag{2.68}$$

where f_i, q and ρ are mechanical body force components, electric body charge and mass density, respectively. T_{ij} and D_i are related to the components of linear Lagrange symmetric tensor S_{ij} and electric field vector E_i through the converse and direct linear piezoelectric constitutive equations (2.66a) and (2.66b). The strain tensor and electric field vector components are linked to mechanical displacement components u_i and electric field potential φ via the following relations:

$$S_{ij} = \frac{1}{2}(u_{i,j} + u_{j,i}) \tag{2.69}$$

$$E_i = -\varphi_{,i} \tag{2.70}$$

The piezoelectric domain V_s could be subjected to either essential or natural mechanical and electric boundary conditions on its boundary surface S_s:

$$u_i = U_i \text{ on } S_u \tag{2.71a}$$

$$T_{ij} n_j = F_i \text{ on } S_f \tag{2.71b}$$

$$\varphi = V \tag{2.72a}$$

or

$$D_i n_i = -Q \text{ on } S_q \tag{2.72b}$$

where U_i, F_i, V and n_i are specified mechanical displacement and surface force components, electric potential and surface charge, and outward unit normal vector components.

For arbitrary space-variable and admissible virtual displacement δu_i and potentials $\delta\varphi$, equations (2.67) and (2.68) are equivalent to:

$$\int_{V_s}(T_{ij,j}+f_i-\rho\ddot{u}_i)\delta u_i dV_s+\int_{V_s}(D_{i,i}-q)\delta\varphi dV_s=0 \tag{2.73}$$

Integrating by parts and using the divergence theorem, this equation leads to:

$$\begin{aligned}&-\int_{V_s}T_{ij,j}\delta u_{i,j}dV_s+\int_{S_s}T_{ij}n_j\delta u_i dS_s+\int_{V_s}f_i\delta u_i dV_s\\&-\int_{V_s}\rho\ddot{u}_i\delta u_i dV_s-\int_{V_s}D_i\delta\varphi_{,i}dV_s+\int_{S_s}D_i n_i\delta\varphi dS_s\\&-\int_{V_s}q\delta\varphi dV_s=0\end{aligned} \tag{2.74}$$

Using the symmetry property of the stress tensor, the natural boundary conditions (2.71b) and (2.72b) and the electric field-potential relation (2.70), the following relation can be obtained:

$$\begin{aligned}&-\int_{V_s}T_{ij}\delta S_{ij}dV_s+\int_{S_s}F_i\delta u_i dS_s+\int_{V_s}f_i\delta u_i dV_s\\&-\int_{V_s}\rho\ddot{u}_i\delta u_i dV_s-\int_{V_s}D_i\delta E_i dV_s-\int_{S_s}Q\delta\varphi dS_s\\&-\int_{V_s}q\delta\varphi dV_s=0\end{aligned} \tag{2.75}$$

The dynamic equations of a piezoelectric continuum can also be derived from the Hamilton principle, in which the Lagrangian and the virtual work are properly adapted to include the electrical contributions as well as the mechanical ones [44]. The dymanic equations of a piezoelectric continuum can be derived using Hamilton's principle:

$$\delta\int_{t_1}^{t_2}(\mathcal{L}+\mathcal{W})dt=0 \tag{2.76}$$

where t_1 and t_2 define the time interval (all variations must vanish at $t=t_1$ and $t=t_2$), $\mathcal{L}$ is the Lagrangian and $\mathcal{W}$ is the virtual work of external mechanical and electrical forces.

According to the Hamilton's principle (2.76), the Lagrangian $\mathcal{L}$ can be written as the difference between the kinetic energy J and extended potential energy

U(including the electric contribution), defined by the following expressions:

$$J = \frac{1}{2}\int_{V_s} \rho \dot{u}_i^2 dV_s \tag{2.77}$$

$$U = \frac{1}{2}\int_{V_s} T_{ij}S_{ij}dV_s - \frac{1}{2}\int_{V_s} D_i E_i dV_s \tag{2.78}$$

$$\mathcal{L} = J - U \tag{2.79}$$

The virtual work done by the external mechanical forces and the applied electric charges for an arbitrary variation of the displacement field δu and of the electric potential $\delta\varphi$ both compatible with the essential boundary conditions (2.71a) and (2.72a) can be written as:

$$\delta\mathcal{W} = \int_{V_s} f_i \delta u_i dV_s + \int_{S_f} F_i \delta u_i dS_f - \int_{S_q} \delta\varphi Q dS_q - \int_{V_s} q\delta\varphi dV_s \tag{2.80}$$

Noting that by integrating the variation of kinetic energy J by part over the time interval, one gets:

$$\int_{t_1}^{t_2} \rho \dot{u}_i \delta\dot{u}_i dt = [\rho\dot{u}_i\delta u_i]_{t_1}^{t_2} - \int_{t_1}^{t_2} \rho\ddot{u}_i\delta\dot{u}_i dt \tag{2.81}$$

of which the first term vanishes as δu_i being equal to 0 in $t = t_1$ and $t = t_2$. The Hamilton's principle (2.76) can finally be written in the following manner, for admissible δu_i and $\delta\varphi$:

$$\delta J - \delta U + \delta\mathcal{W} = 0 \tag{2.82}$$

Taking into account the consititutive equations (2.66a) and (2.66b) and substituing the Lagrangian and virtual work into equation (2.82) yields:

$$\begin{aligned}&\int_{V_s} \left[\rho\ddot{u}_i\delta u_i - \delta S_{ij}c^E_{ijkl}S_{kl} + \delta S_{ij}e_{kij}E_k + \delta E_k e_{ikl}S_{kl} + \delta E_k \varepsilon^S_{ik}E_k + \delta u_i f_i - \delta\varphi q\right] dV_s \\ &- \int_{S_f} F_i\delta u_i dS_f + \int_{S_q} \delta\varphi Q dS_q = 0\end{aligned} \tag{2.83}$$

In matrix form, equation (2.83) can be written as:

$$\begin{aligned}&\int_{V_s} \left[\rho\{\delta u\}^T\{\ddot{u}\} - \{\delta S\}^T\mathbf{c}^E\{S\} + \{\delta S\}^T\mathbf{e}^T\{E\} + \{\delta E\}^T\mathbf{e}\{S\} + \{\delta E\}^T\boldsymbol{\varepsilon}^S\{E\} + \{\delta u\}^T\{f\} - \delta\varphi q\right] dV_s \\ &- \int_{S_f} \{\delta u\}^T\{F\}dS_f + \int_{S_q} \delta\varphi Q dS_q = 0\end{aligned} \tag{2.84}$$

2.3.2 Finite element formulation

The displacement field $\{u\}$ and the electric potential φ over an element are related to the corresponding node values $\{u_i\}$ and $\{\varphi_i\}$ by the mean of the shape functions $\mathbf{N}_u$ and $\mathbf{N}_v$:

$$\{u\} = \mathbf{N}_u\{u_i\} \tag{2.85}$$

$$\boldsymbol{\varphi} = \mathbf{N}_v\{\varphi_i\} \tag{2.86}$$

Therefore, the strain field $\{S\}$ and the electric field $\{E\}$ are related to the nodal displacements and potential by the shape functions derivatives $\mathbf{B}_u$ and $\mathbf{B}_v$ defined by:

$$\{S\} = \boldsymbol{\mathcal{D}}^p\mathbf{N}_u\{u_i\} = \mathbf{B}_u\{u_i\} \tag{2.87}$$

$$\{E\} = -\nabla\mathbf{N}_v\{\varphi_i\} = -\mathbf{B}_v\{\varphi_i\} \tag{2.88}$$

$\boldsymbol{\mathcal{D}}^p$ is the linear differential operator matrix which relates the strains to the structural displacements $\{u\}$ in this manner: $\{S\} = \boldsymbol{\mathcal{D}}^p\{u\}$:

$$\boldsymbol{\mathcal{D}}^p = \begin{pmatrix} \frac{\partial}{\partial x} & 0 & 0 \\ 0 & \frac{\partial}{\partial y} & 0 \\ 0 & 0 & \frac{\partial}{\partial z} \\ \frac{\partial}{\partial y} & \frac{\partial}{\partial x} & 0 \\ 0 & \frac{\partial}{\partial z} & \frac{\partial}{\partial y} \\ \frac{\partial}{\partial z} & 0 & \frac{\partial}{\partial x} \end{pmatrix} \tag{2.89}$$

Substituting expressions (2.85) to (2.89) into the variational principle (2.84) yields:

$$\begin{aligned} \{\delta u_i\}^T \int_{V_s} \rho\mathbf{N}_u^T\mathbf{N}_u dV_s\{\ddot{u}_i\} + \{\delta u_i\}^T \int_{V_s} \mathbf{B}_u^T\mathbf{c}^E\mathbf{B}_u dV_s\{u_i\} \\ \{\delta u_i\}^T \int_{V_s} \mathbf{B}_u^T\mathbf{e}^T\mathbf{B}_v dV_s\{\varphi_i\} + \{\delta \varphi_i\}^T \int_{V_s} \mathbf{B}_v^T\mathbf{e}\mathbf{B}_u dV_s\{u_i\} \\ -\{\delta \varphi_i\}^T \int_{V_s} \mathbf{B}_v^T\boldsymbol{\varepsilon}^S\mathbf{B}_v dV_s\{\varphi_i\} - \{\delta u_i\}^T \int_{V_s} \mathbf{N}_u^T\{f\}dV_s \\ -\{\delta u_i\}^T \int_{S_f} \mathbf{N}_u^T\{F\}dS_f + \{\delta \varphi_i\}^T \int_{S_q} \mathbf{N}_v^T Q dS_q + \{\delta \varphi_i\}^T \int_{V_s} \mathbf{N}_v^T q dV_s = 0 \end{aligned} \tag{2.90}$$

which must be verified for any arbitrary variation of the displacements $\{\delta u_i\}$ and electrical potentials $\{\delta\varphi_i\}$ compatible with the essential boundary conditions.

The discretized electro-elastic system of equations can be written in the form shown in equations (2.91a) and (2.91b).

$$\mathbf{M}_{uu}\{\ddot{u}_i\} + \mathbf{K}_{uu}\{u_i\} + \mathbf{K}_{uv}\{\varphi_i\} = \{f_i\} \tag{2.91a}$$

$$\mathbf{K}_{uv}^T\{u_i\} + \mathbf{K}_{vv}\{\varphi_i\} = \{q_i\} \tag{2.91b}$$

with:

$$\mathbf{M}_{uu} = \int\limits_{V_s} \mathbf{N}_u^{\mathbf{T}} \rho \mathbf{N}_u dV_s \tag{2.92a}$$

$$\mathbf{K}_{uu} = \int\limits_{V_s} \mathbf{B}_u^{\mathbf{T}} \mathbf{c}^E \mathbf{B}_u dV_s \tag{2.92b}$$

$$\mathbf{K}_{uv} = \int\limits_{V_s} \mathbf{B}_u^{\mathbf{T}} \mathbf{e}^{\mathbf{T}} \mathbf{B}_v dV_s \tag{2.92c}$$

$$\mathbf{K}_{vv} = -\int\limits_{V_s} \mathbf{B}_v^{\mathbf{T}} \varepsilon^s \mathbf{B}_v dV_s \tag{2.92d}$$

respectively the element mass, stiffness, piezoelectric coupling and capacitance matrix, and:

$$\{f_i\} = \int\limits_{S_f} \mathbf{N}_u^{\mathbf{T}} \{F\} dS_f + \int\limits_{V_s} \mathbf{N}_u^{\mathbf{T}} \{f\} dV_s \tag{2.93a}$$

$$\{q_i\} = -\int_{S_q} \mathbf{N}_v^T Q dS_q - \int_{V_s} \mathbf{N}_v^T q dV_s \tag{2.93b}$$

the external mechanical force and electric charge.

Each element k of the mesh is connected to its adjoint elements at the global nodes and the displacement is continuous from one element to the next. The element degrees of freedom (DOFs)($\{u_i\}^{(k)}, \{\varphi_i\}^{(k)}$) are related to the global DOFs ($\{\mathcal{U}\}, \{\mathcal{V}\}$) by means of the localization matrices $\mathbf{L}_u^{(k)}$ and $\mathbf{L}_v^{(k)}$ [75]:

$$\{u_i\}^{(k)} = \mathbf{L}_u^{(k)} \{\mathcal{U}\} \tag{2.94}$$

$$\{\varphi_i\}^{(k)} = \mathbf{L}_v^{(k)} \{\mathcal{V}\} \tag{2.95}$$

The element ij of $\mathbf{L}_u^{(k)}$ is equal to 1 if the i^{th} mechanical DOFs of the element k corresponds to the j^{th} global DOFs and is 0 otherwise. The element ij of $\mathbf{L}_v^{(k)}$ is equal to 1 if the i^{th} electric DOFs of the element k is connected to the j^{th} global electric DOFs and is zero otherwise.

The Hamilton's principle (2.76) must be verified for the whole structure, which results in (by summation of the contribution of each finite element):

$$\begin{aligned} &\{\delta\mathcal{U}\}^T \left\{ \left[\sum_k \mathbf{L}_u^{(k)T} \mathbf{M}_{uu}^{(k)} \mathbf{L}_u^{(k)} \right] \{\ddot{\mathcal{U}}\} + \left[\sum_k \mathbf{L}_u^{(k)T} \mathbf{K}_{uu}^{(k)} \mathbf{L}_u^{(k)} \right] \{\mathcal{U}\} + \left[\sum_k \mathbf{L}_u^{(k)T} \mathbf{K}_{uv}^{(k)} \mathbf{L}_v^{(k)} \right] \{\mathcal{V}\} - \sum_k \mathbf{L}_u^{(k)T} \{f_k\} \right\} \\ &+ \{\delta\mathcal{V}\}^T \left\{ \left[\sum_k \mathbf{L}_v^{(k)T} \mathbf{K}_{uv}^{(k)T} \mathbf{L}_u^{(k)} \right] \{\mathcal{U}\} + \left[\sum_k \mathbf{L}_v^{(k)T} \mathbf{K}_{vv}^{(k)} \mathbf{L}_v^{(k)} \right] \{\mathcal{V}\} - \sum_k \mathbf{L}_v^{(k)T} \{q_k\} \right\} \end{aligned} \tag{2.96}$$

In matrix form, equation (2.96) can be written as:

$$\boldsymbol{\mathcal{M}}_{UU}\{\ddot{\mathcal{U}}\} + \mathbf{K}_{UU}\{\mathcal{U}\} + \mathbf{K}_{UV}\{\mathcal{V}\} = \{\boldsymbol{\mathcal{F}}\} \tag{2.97}$$

$$\mathbf{K}_{UV}^{T}\{\mathcal{U}\} + \mathbf{K}_{VV}\{\mathcal{V}\} = \{\mathcal{Q}\} \tag{2.98}$$

where the assembled matrices are:

$$\boldsymbol{\mathcal{M}}_{UU} = \sum_i \mathbf{L}_{ui}^{T}\mathbf{M}_{uu}^{(i)}\mathbf{L}_{ui} \tag{2.99a}$$

$$\mathbf{K}_{UU} = \sum_i \mathbf{L}_{ui}^{T}\mathbf{K}_{uu}^{(i)}\mathbf{L}_{ui} \tag{2.99b}$$

$$\mathbf{K}_{UV} = \sum_i \mathbf{L}_{ui}^{T}\mathbf{K}_{uv}^{(i)}\mathbf{L}_{vi} \tag{2.99c}$$

$$\mathbf{K}_{VV} = \sum_i \mathbf{L}_{vi}^{T}\mathbf{K}_{vv}^{(i)}\mathbf{L}_{vi} \tag{2.99d}$$

$$\{\boldsymbol{\mathcal{F}}\} = \sum_i \mathbf{L}_{ui}^{T}\{f_i\} \tag{2.99e}$$

$$\{\mathcal{Q}\} = \sum_i \mathbf{L}_{vi}^{T}\{q_i\} \tag{2.99f}$$

2.3.3 Shunt circuit on piezoelectric element

The finite element model of the beam with $R-L$ shunted piezoelectric patches is represented in Figure 2.4. This model contains two beam waveguides

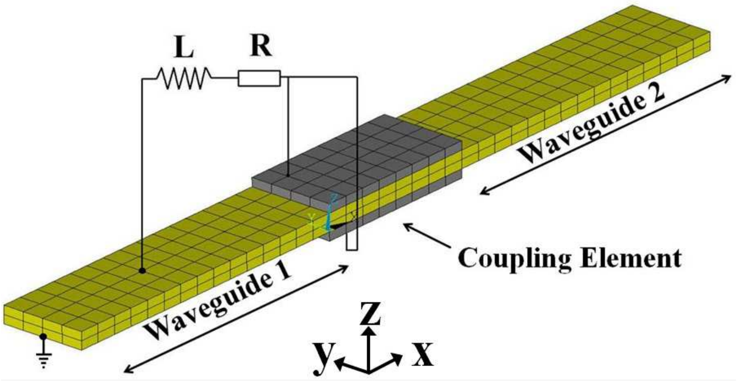

Figure 2.4: Finite element model of a coupled beam system with a pair of $R-L$ shunted piezoelectric patches.

with 3D linear brick finite elements and a coupling element with 3D linear brick piezoelectric finite elements. The piezoelectric element has 8 nodes and 4 degrees of freedom(DOFs) per node. Each node has 3 structural DOFs and 1 electrical DOF (electrical potential). All electrical potential DOFs that are placed on electrode surfaces of the patches are reduced such that only one potential master DOF remains on each piezoelectric patch. All electrical potential DOFs on the patch surfaces bonded to the beam are grounded. The whole structure has free mechanical boundary conditions.

After finite element assembly, the discretized coupled piezoelectric and structural field equations are finally given in terms of nodal displacements $\{\mathcal{U}\}$ and nodal electric potential $\{\mathcal{V}\}$. Following the electrode definitions mentioned in the work of [11], the electrical potential DOFs in the piezoelectric patches are partitioned into three different groups:

- For nodes on the outer surfaces of the piezoelectric patches, their associated electrical DOFs are called $\{\mathcal{V}\}_p$, and they have the same electrical potential;
- For nodes on the inner surfaces of the piezoelectric patches bonded to the beam, their associated electrical DOFs are called $\{\mathcal{V}\}_g$, and they are grounded ($\{\mathcal{V}\}_g = 0$);
- For nodes inside the piezoelectric patches, their associated electrical DOFs are called $\{\mathcal{V}\}_i$.

The equations of motion are subsequently written in the form shown in equation (2.100).

$$\begin{bmatrix} \boldsymbol{\mathcal{M}}_{UU} & 0 & 0 & 0 \\ 0 & 0 & 0 & 0 \\ 0 & 0 & 0 & 0 \\ 0 & 0 & 0 & 0 \end{bmatrix} \begin{bmatrix} \{\ddot{\mathcal{U}}\} \\ \{\ddot{\mathcal{V}}\}_i \\ \{\ddot{\mathcal{V}}\}_p \\ \{\ddot{\mathcal{V}}\}_g \end{bmatrix} + \begin{bmatrix} \mathbf{K}_{UU} & \mathbf{K}_{Ui} & \mathbf{K}_{Up} & \mathbf{K}_{Ug} \\ \mathbf{K}_{Ui}^{\mathbf{T}} & \mathbf{K}_{ii} & \mathbf{K}_{ip} & \mathbf{K}_{ig} \\ \mathbf{K}_{Up}^{\mathbf{T}} & \mathbf{K}_{ip}^{\mathbf{T}} & K_{pp} & \mathbf{K}_{pg} \\ \mathbf{K}_{Ug}^{\mathbf{T}} & \mathbf{K}_{ig}^{\mathbf{T}} & K_{pg}^{\mathbf{T}} & \mathbf{K}_{gg} \end{bmatrix} \begin{bmatrix} \{\mathcal{U}\} \\ \{\mathcal{V}\}_i \\ \{\mathcal{V}\}_p \\ \{\mathcal{V}\}_g \end{bmatrix} = \begin{bmatrix} \{\boldsymbol{\mathcal{F}}\} \\ \{\mathcal{Q}\}_i \\ \{\mathcal{Q}\}_p \\ \{\mathcal{Q}\}_g \end{bmatrix} \tag{2.100}$$

As $\{\mathcal{V}\}_g = 0$, the fourth equation and fourth column in the mass and stiffness matrices can be eliminated. Internal potential DOFs can be determined by exact static condensation from Equation (2.100) since internal electric charges $\{\mathcal{Q}\}_i = 0$:

$$\{\mathcal{V}\}_i = -\mathbf{K}_{ii}^{-1}\mathbf{K}_{Ui}^{\mathbf{T}}\{\mathcal{U}\} - \mathbf{K}_{ii}^{-1}\mathbf{K}_{ip}\{\mathcal{V}\}_p \tag{2.101}$$

Since all the nodes on the potential electrode surfaces have identical potentials, an explicit transformation matrix $\mathbf{T}_m$ can be used to define the master potential DOF $\{\mathcal{V}\}_m$, as shown in equation (2.102).

$$\{\mathcal{V}\}_p = \mathbf{T_m}\{\mathcal{V}\}_m \tag{2.102}$$

The use of equation (2.102) yields the fully coupled dynamics:

$$\begin{bmatrix} \boldsymbol{\mathcal{M}}_{UU} & 0 \\ 0 & 0 \end{bmatrix} \begin{bmatrix} \{\ddot{\mathcal{U}}\} \\ \{\ddot{\mathcal{V}}\}_m \end{bmatrix} + \begin{bmatrix} \mathbf{H}_{UU} & \mathbf{H}_{Up} \\ \mathbf{H}_{Up}^{\mathbf{T}} & \mathbf{H}_{pp} \end{bmatrix} \begin{bmatrix} \{\mathcal{U}\} \\ \{\mathcal{V}\}_m \end{bmatrix} = \begin{bmatrix} \{\boldsymbol{\mathcal{F}}\} \\ \{\mathcal{Q}\}_m \end{bmatrix} \tag{2.103}$$

with

$$\mathbf{H}_{UU} = \mathbf{K}_{UU} - \mathbf{K}_{Ui}\mathbf{K}_{ii}^{-1}\mathbf{K}_{Ui}^{\mathbf{T}} \tag{2.104a}$$
$$\mathbf{H}_{Up} = (\mathbf{K}_{Up} - \mathbf{K}_{Ui}\mathbf{K}_{ii}^{-1}\mathbf{K}_{ip})\mathbf{T}_m \tag{2.104b}$$
$$\mathbf{H}_{pp} = \mathbf{T}_m^{\mathbf{T}}(\mathbf{K}_{pp} - \mathbf{K}_{ip}^{\mathbf{T}}\mathbf{K}_{ii}^{-1}\mathbf{K}_{ip})\mathbf{T}_m \tag{2.104c}$$
$$\{\mathcal{Q}\}_m = \mathbf{T}_m^{\mathbf{T}}\{\mathcal{Q}\}_p \tag{2.104d}$$

After the definition of the master DOF, the R-L shunt circuit can be considered. The electrical impedance of the circuit under harmonic excitation can be written as:

$$Z_{sh} = R + j\omega L \tag{2.105}$$

If only one Master electric DOF is considered, $\mathcal{Q}_m$ and $\mathcal{V}_m$ become scalar, the current I_{sh} in the shunt circuit can be expressed as Equation (2.90)

$$I_{sh} = j\omega\mathcal{Q}_m = \frac{\mathcal{V}_m}{Z_{sh}} \tag{2.106}$$

By substituting Equation (2.106) into Equation (2.103), the electrical DOFs can be condensed and the equation that governs the structural dynamics under harmonic excitation is shown in Equation (2.107).

$$[\mathbf{H}_{UU} - \omega^2\boldsymbol{\mathcal{M}}_{UU} + \mathbf{H}_{Up}(\frac{1}{j\omega Z_{sh}} - \mathbf{H}_{pp})^{-1}\mathbf{H}_{Up}^{\mathbf{T}}]\{\mathcal{U}\} = \mathbb{D}^c\{\mathcal{U}\} = \{\boldsymbol{\mathcal{F}}\} \tag{2.107}$$

Here matrix $\mathbb{D}^c$ represents the dynamical stiffness matrix of the coupling element. Equation (2.107) gives a full finite element description of the coupling element with two shunted piezoelectric patches, which can be applied in the DMM mentioned in Subsection 2.1.2.

If multiple master electrical DOFs are defined, the above formulation is slightly different. Assuming that there are k piezoelectric patches with their independent shunt circuit, the electric potential on the electrodes $\{\mathcal{V}\}_m$ and the associated electric charge $\{\mathcal{Q}\}_m$ can be written in the following manner:

$$\{\mathcal{V}\}_m = \begin{bmatrix} \mathcal{V}_{m1} \\ \mathcal{V}_{m2} \\ \vdots \\ \mathcal{V}_{mk} \end{bmatrix} \quad \{\mathcal{Q}\}_m = \begin{bmatrix} \mathcal{Q}_{m1} \\ \mathcal{Q}_{m2} \\ \vdots \\ \mathcal{Q}_{mk} \end{bmatrix} \tag{2.108}$$

In the same way, equation (2.102) can be applied to define Master DOF for each piezoelectric patches. The impedance in the shunt circuit of the patch p can be expressed in this way:

$$Z_{shp} = R_p + j\omega L_p \tag{2.109}$$

And the current I_{shp} in the p^{th} shunt circuit can be written as:

$$I_{shp} = j\omega \mathcal{Q}_{mp} = \frac{\mathcal{V}_{mp}}{Z_{shp}} \tag{2.110}$$

By substituting equation (2.110) into equation (2.103), with equation (2.108), the following relation can be obtained:

$$[\mathbf{H}_{UU} - \omega^2 \boldsymbol{\mathcal{M}}_{UU} + \mathbf{H}_{Up}(\mathcal{Y}_{sh} - \mathbf{H}_{pp})^{-1}\mathbf{H}_{Up}^{\mathbf{T}}]\{\mathcal{U}\} = \mathbb{D}^c\{\mathcal{U}\} = \{\boldsymbol{\mathcal{F}}\} \tag{2.111}$$

where

$$\{\mathcal{Y}\}_{sh} = \begin{bmatrix} \frac{1}{j\omega Z_{sh1}} \\ \frac{1}{j\omega Z_{sh2}} \\ \vdots \\ \frac{1}{j\omega Z_{shk}} \end{bmatrix} \tag{2.112}$$

With these relations, the shunt circuit on the piezoelectric patches can be considered properly.

2.4 Conclusions

In this chapter, general formulations of the numerical tools for the characterization of wave propagation and energy diffusion properties in smart structures with shunted piezoelectric patches are proposed. The WFE method and the associated DMM (Section 2.1) are generalized, through the finite element modeling of shunted piezoelectric patches (Section 2.2). The combination of these two numerical tools enables the evaluation of the control efficiency of the smart structures, in both frequency and time domains. Numerical applications of these numerical tools are carried out in the following chapters to study the control of propagation and diffusion parameters.

The procedure for the numerical applications of the numerical tools can be summarized as follows:

1. Calculation of dispersion curves using WFE. Distinction of wave modes with their deformed modal shapes. Selection of wave modes propagating in the smart structure.

2. Analysis of energy diffusion in smart structures with shunted piezoelectric patches via the DMM: reflection and transmission coefficients of specific wave modes propagating in the structure will be obtained.

3. Calculation of the forced response of the structure under different types of excitations in the frequency domain (white noise, wave packet).

4. Calculation of the time responses of the structure by applying IDFT on the frequency response. Identification of reflection coefficients through an extraction procedure based on time response.

Chapter 3

Wave propagation and diffusion in smart homogeneous beam structures with $R-L$ shunted piezoelectric patches

---

Contents

3.1 Numerical simulations of solid beams with shunted piezoelectric patches

In this section, the DMM with shunted piezoelectric elements is firstly employed to calculate the reflection and transmission coefficients of the Z-axis flexural wave and the X-axis tension/compression wave in solid beams. The influence of the shunted piezoelectric patches on the propagation of these wave modes is carefully investigated, and an analytical model is developed to verify the numerical results. Subsequently, the FWFE approach is applied for the evaluation of the dynamical behavior of the structure in frequency domain. Unlike the DMM approach which gives predictions for the beam structure with free boundary conditions, frequency response functions can be obtained for the beam structure with forced boundary conditions. Waveguides are of finite length in this case. Thereafter, based on the frequency responses, the calculation of time responses of the structure under wave packet excitation is carried out. An extraction procedure is proposed to calculate reflection coefficients of the X-axis tension/compression mode so as to verify the results issued from the DMM approach.

It should be mentioned that the problem of a piezoelectric patch shunted through a $R-L$ circuit that acts as a vibration absorber or noise controller has been used extensively in the past and its behavior has been examined thoroughly via analytical or numerical models. However, no numerical tools that can predict wave propagation and diffusion in a unit cell belonging to a set of periodically distributed shunted piezoelectric patches are proposed in the literature. The effects of a piezoelectric patch shunted through a $R-L$ circuit as a vibration absorber on the energy diffusion of a specific wave mode propagating in a slender system are never studied in detail. The focus of the present work lies in the wave propagation and energy diffusion problems in such systems, and new efficient numerical tools aiming at achieving these goals are provided and tested in this section.

3.1.1 DMM approach applied for Z-axis flexural wave

The structures to be studied here are beams with two symmetric bonded $R-L$ shunted piezoelectric patches. The finite element model of the couple system is shown in Figure 3.1. In the first case of study (Case A), the widths of the beam and the patches are the same. The finite element model of the coupling element is shown in Figure 3.2, with the definition of geometric parameters. The parameter L_{beam} represents the length of the beam involved in the coupling element. Numerical values of those geometric parameters are listed in Table 3.1. The material of the beam is aluminium and considered as isotropic, with Young's modulus $E_{beam} = 70\ GPa$ and Poisson's ratio $\nu_{beam} = 0.34$, and density $\rho_{beam} = 2700\ kg/m^3$. The piezoelectric patches are fabricated by Saint Gobain Quartz (type SG P189) and the corresponding material characteristics are listed in Appendix A. This type of piezoelectric patch works mainly in the 3-1 mode, and the two piezoelectric patches should work in phase (both stretched

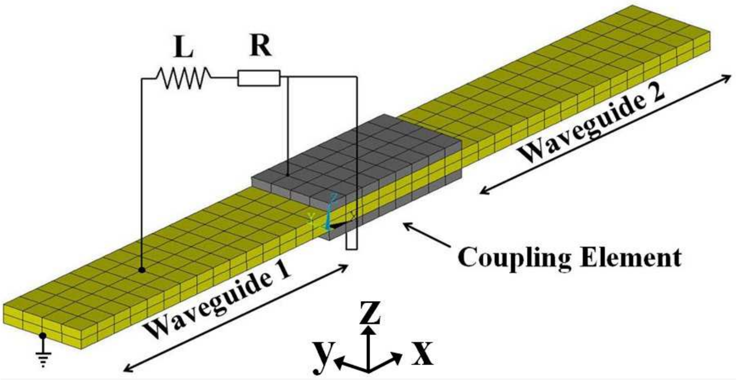

Figure 3.1: Finite element model of a coupled beam system with a pair of $R-L$ shunted piezoelectric patches.

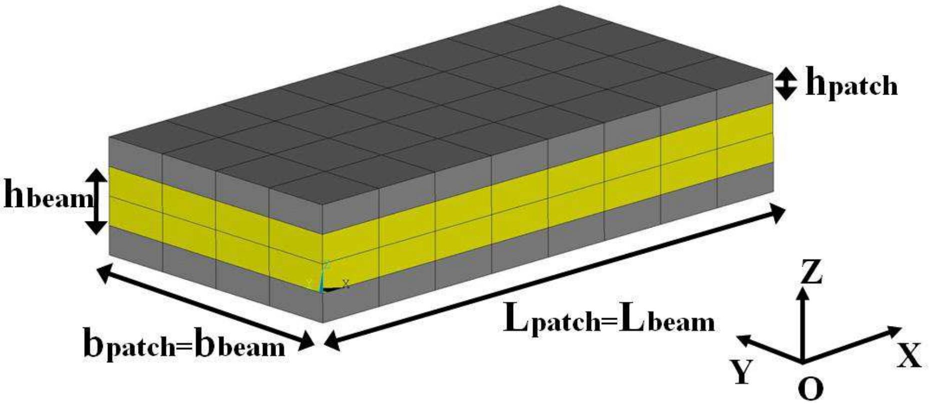

Figure 3.2: Finite element model of the coupling element and definition of geometric parameters in case A.

or compressed) for the control of the tension/compression wave, whereas for the flexural mode, they should work in opposite phase (one stretched, the other compressed). At first, the beam is treated as a waveguide and the corresponding dispersion curves of the wave modes propagating in the beam are extracted via the WFE approach, as shown in Figure 3.3. Based on this calculation, the mesh resolution is chosen to be $0.005 \times 0.005 \times 0.002$ m^3, as the minimum wavelength of the Z-axis flexural wave mode is about 0.1m in the concerned frequency band. The DMM calculation of this wave mode gives the reflection and transmission coefficients as displayed in Figure 3.4, with $R = 100$ Ω and $L = 2$ H. The tuning frequency f_{tune} of the piezoelectric patches is about 1340 Hz. In fact, around this frequency, the impedance of the structure is greatly modified by the shunted piezoelectric patches so that the

Table 3.1: Numeric values of the geometric parameters in the coupling element shown in Figure 3.2(case A), Figure 3.7(a)(case B) and Figure 3.7(b)(case C). The units of all the parameters are in meter (m).

Case	L_{beam}	L_{patch}	b_{beam}	b_{patch}	h_{beam}	h_{patch}
A	0.04	0.04	0.02	0.02	0.004	0.002
B	0.03	0.03	0.03	0.01	0.003	0.001
C	0.03	0.01	0.03	0.03	0.003	0.001

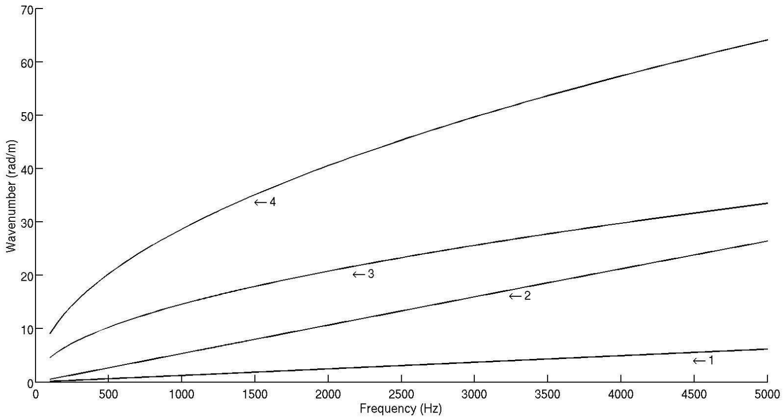

Figure 3.3: Dispersion curves of the wave modes propagating in the beam in case A: (1)Tension/compression wave in X-axis (2)Torsional wave in X-axis (3)Flexural wave in Y-axis (4)Flexural wave in Z-axis. These wave modes are identified through their mode shapes (eigenvectors) issued from the WFE approach.

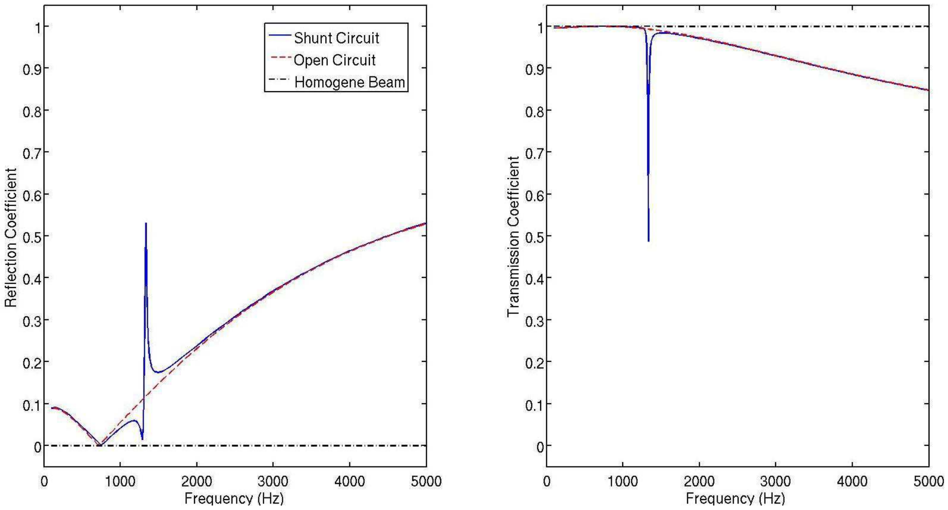

Figure 3.4: Reflection and transmission coefficients of the Z-axis flexural wave mode propagating in the beam in case A. (Solid line)With R-L shunt circuit (Dashed line)Open circuit (Dash-dotted line)Beam without piezopatches.

wave propagation characteristics change significantly. The tuning frequency can be calculated according to equation (3.1):

$$f_{tune} = \frac{1}{2\pi\sqrt{2LC_{p3}^S}} \tag{3.1}$$

where $C_{p3}^S = (1-k_{31}^2)C_{p3}^T$ is the capacitance of the piezoelectric patch measured at constant strain, and the 2 in front of L is due to the fact that the two piezoelectric patches are connected in parallel. If each piezoelectric patch has an independent shunt circuit, the 2 in front of L will disappear. The subscript 1 represents the X-axis direction while the subscript 3 denotes the Z-axis direction. k_{31} is the electromechanical coupling coefficient. C_{p3}^T is the capacitance of the piezoelectric patch measured at constant stress. It can be calculated in the following manner:

$$C_{p3}^T = \frac{\varepsilon^T A_3}{L_3} \tag{3.2}$$

where A_3 is the area of the surface of the piezoelectric patch perpendicular to Z-axis, $L_3 = h_{patch}$ is the length of the piezoelectric patch in Z-axis direction. Thereafter, these numerical results are compared to results derived from an analytical beam model. This beam can be divided into 3 propagation mediums, as shown in Figure 3.5. It is a combination of 3 analytical models:

- For wave propagation in the beam, the classical Euler-Bernoulli beam model [76] is employed;

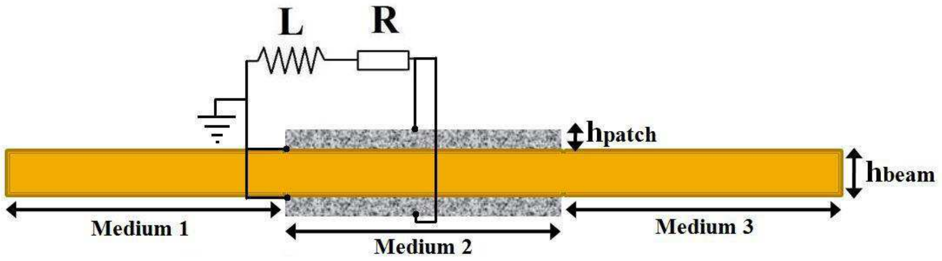

Figure 3.5: Homogenized Euler-Bernoulli beam model with two symmetric R-L shunted piezoelectric patches.

- For the part of the beam covered with 2 piezoelectric patches (Medium 2), a homogenization procedure [77] is applied;
- For the piezoelectric patches with shunted circuit, the model in the work of Hagood and von Flotow [7] is used.

This homogenized Euler-Bernoulli beam model with shunted piezoelectric patches offers analytical solutions to the reflection and transmission coefficients of the flexural wave. Assuming that the Young's modulus and density of the shunted piezoelectric patches are E_{patch} and ρ_{patch}. According to Hagood and von Flotow [7], the shunt circuit modifies the material properties of the piezoelectric patch in the following way:

$$s^{sh}_{patch\ jj} = s^{E}_{patch\ jj} - \bar{Z}^{el}_{i}\frac{d^{2}_{ij}}{\varepsilon^{\mathbf{T}}_{i}} \tag{3.3a}$$

$$E^{sh}_{patch\ jj} = \frac{\mathbf{c}^{E}_{patch\ jj}}{1-k^{2}_{ij}\bar{Z}^{el}_{i}} \tag{3.3b}$$

where $s^{sh}_{patch\ jj}$ represents the shunted piezoelectric compliance in the jth direction and $s^{E}_{patch\ jj}$ the mechanical compliance in the jth direction, while $E^{sh}_{patch\ jj}$ denotes the shunted piezoelectric stiffness in the jth direction, and $\mathbf{c}^{E}_{patch\ jj}$ the mechanical stiffness in the jth direction. k_{ij} is the electromechanical coupling coefficient defined as shown in equation (3.4a), and d_{ij} is the piezoelectric strain coupling coefficient. $\bar{Z}^{el}_{i}$ denotes the relative electrical impedance defined as shown in equation (3.4b). ε^{T}_{i} is the permittivity under constant strain in the ith direction.

$$k_{ij} = \frac{d_{ij}}{\sqrt{s^{E}_{jj}\varepsilon^{\mathbf{T}}_{i}}} \tag{3.4a}$$

$$\bar{Z}^{el}_{i} = \frac{j\omega C^{T}_{pi} Z_{shi}}{j\omega C^{T}_{pi} Z_{shi} + 1} \tag{3.4b}$$

In the case of this work, there is no shunt circuit in the 1st(X-axis) and 2nd(Y-axis) directions, so $Z_{sh1} = Z_{sh2} = \infty$ and then $\bar{Z}_1^{el} = \bar{Z}_2^{el} = 1$. C_{pi}^T is the capacitance between the surfaces of the piezoelectric patch perpendicular to ith direction (at constant stress). For the considered beam to be homogenized, only the loading in the 1st direction (X-axis) is taken into account, thus the Young's modulus of the piezoelectric patch can be calculated as $E_{patch} = E_{patch\ 11}^{sh}$. The effective Young's Modulus E_{eff} of Medium 2 can subsequently be expressed in the form shown in equation (3.5).

$$E_{eff} = E_{beam}\frac{12}{h_{eff}^3}(\frac{h_1^3}{6} + 2d_1^2 h_1) + E_{patch}\frac{12}{h_{eff}^3}(\frac{h_2^3}{6} + 2d_2^2 h_2) \tag{3.5}$$

where

$$\begin{aligned} h_{eff} &= h_{beam} + 2h_{patch}, h_1 = \frac{1}{2}h_{beam}, h_2 = h_{patch} \\ d_1 &= \frac{1}{4}h_{beam}, d_2 = \frac{1}{2}(h_{beam} + h_{patch}) \end{aligned} \tag{3.6}$$

The effective density ρ_{eff}, area A_{eff} and moment of inertia I_{eff} are shown in equations (3.7a), (3.7b), and (3.7c) respectively.

$$\rho_{eff} = \frac{h_{beam}\rho_{beam}}{h_{beam} + 2h_{patch}} + \frac{2h_{patch}\rho_{patch}}{h_{beam} + 2h_{patch}} \tag{3.7a}$$

$$A_{eff} = b_{beam}(h_{beam} + 2h_{patch}) \tag{3.7b}$$

$$I_{eff} = \frac{b_{beam}(h_{beam} + 2h_{patch})^3}{12} \tag{3.7c}$$

Reflection and transmission coefficients of the flexural wave propagating in the beam in case A are calculated analytically and the results are compared to those acquired through the DMM approach, as shown in Figure 3.6. The results issued from the DMM approach and those from the homogenized Euler-Bernoulli model correspond well below 2 kHz. However, at higher frequencies, as the homogenization method becomes inaccurate [78, 79], those two approaches give different predictions of reflection and transmission coefficients of the flexural wave. Furthermore, the Euler-Bernoulli analytical model becomes also incorrect at middle and high frequencies, as its plane wave description of the bending mode is not a priori satisfied in this frequency range [46]. Nevertheless, these two different approaches give the same tuning frequency f_{tune}. On the whole, the prediction performance of the DMM approach is well manifested in this case.

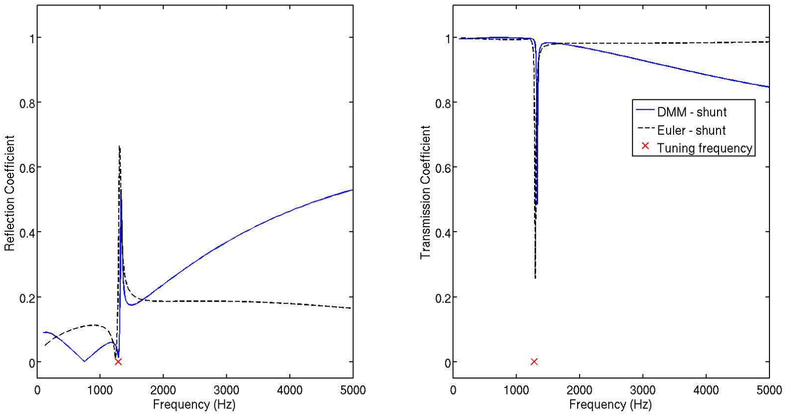

Figure 3.6: Comparison of reflection and transmission coefficients of the flexural mode in Z-axis between the results of the homogenized Euler-Bernoulli beam model and those of the DMM approach in case A. (Solid line)DMM results (Dashed line)Homogenized model results.

3.1.2 Application of DMM and FWFE for the choice of configuration

3.1.2.1 Prediction of reflection and transmission coefficients with DMM

Two other numerical simulations are performed for an aluminium beam with two symmetric bonded shunted piezoelectric patches. All the material properties are the same as those used in case A, but the dimensions piezoelectric patch in these two cases (case B and case C) are $0.03 \times 0.01 \times 0.001$ m^3, and the dimensions of the beam section are 0.03×0.003 m^2. These values are defined according to available materials in the laboratory so that the numerical results can be later validated experimentally. Two different configurations are tested: in case B, the two piezoelectric patches are bonded in the longitudinal direction of the beam, as shown in Figure 3.7(a), whereas in case C, these patches are bonded transversally on the same beam, as displayed in Figure 3.7(b). Numerical values of the geometric parameters are listed in Table 3.1, and there definitions can be found in Figure 3.7(a) and Figure 3.7(b). At first, the dispersion curves of the wave modes propagating in the beam in case B and case C are calculated using the WFE approach. The results are shown in Figure 3.8. The wavelength of the flexural mode in Z-axis is shown in Figure 3.9. According to the wavelength, the mesh resolution in these two cases is chosen as $0.005 \times 0.005 \times 0.0015$ m^3 for the beam, and $0.005 \times 0.005 \times 0.001$ m^3 for the patches. In the frequency band from 0 to 5

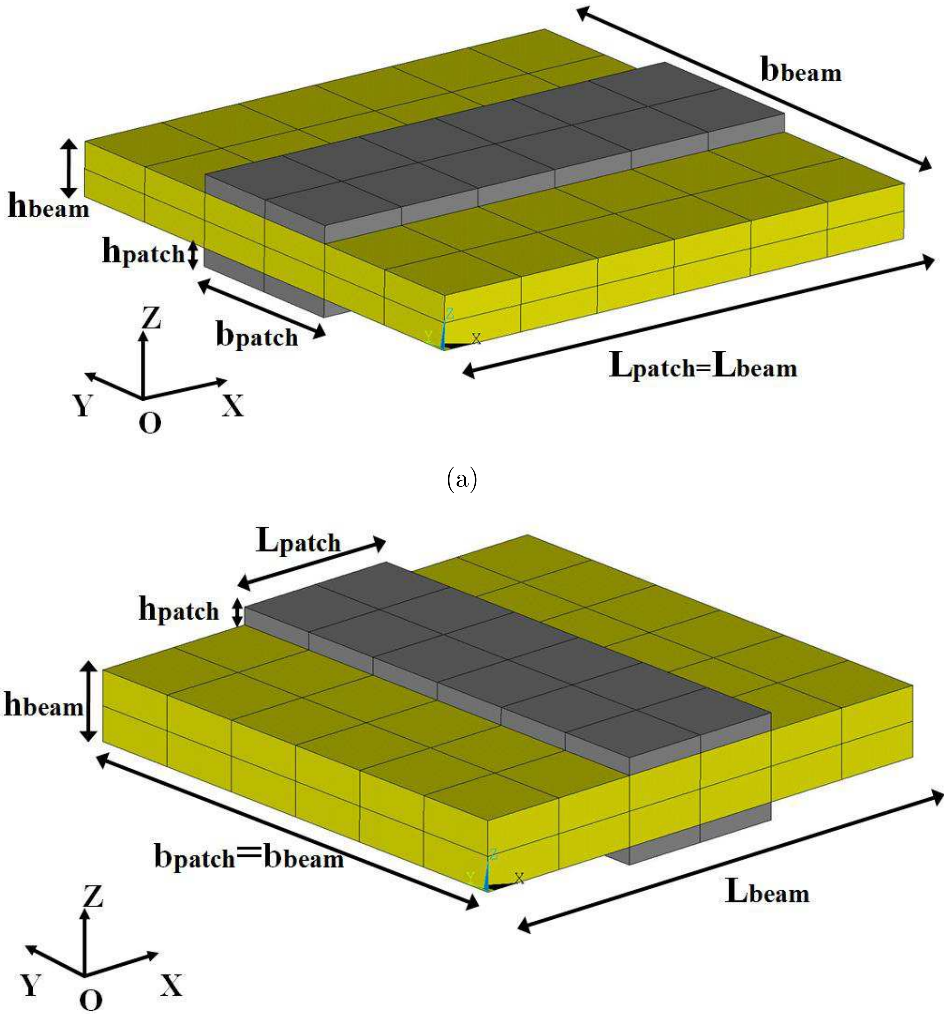

(a)

(b)

Figure 3.7: Finite element model of the coupling element and definition of geometric parameters (a)in case B: the two piezoelectric patches are placed longitudinally (b)in case C: the two piezoelectric patches are placed transversally.

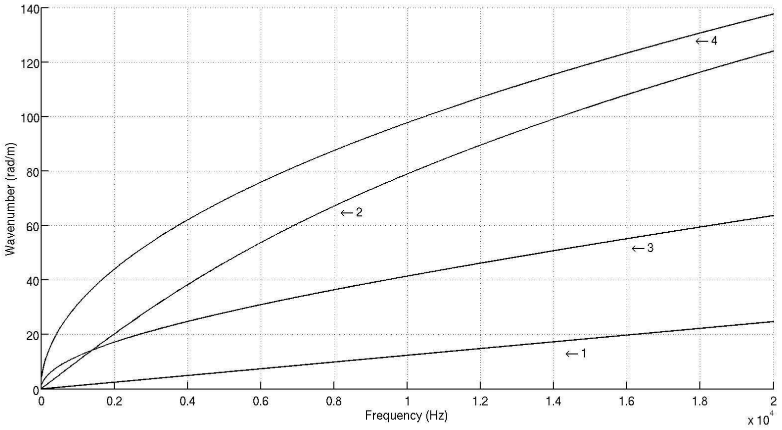

Figure 3.8: Dispersion curves of the wave modes propagating in the beam in case B and case C: (1)Tension/compression mode in X-axis (2)Torsional wave in X-axis (3)Flexural wave in Y-axis (4)Flexural wave in Z-axis. These wave modes are identified through their mode shapes (eigenvectors) issued from the WFE approach.

kHz, for the Z-axis flexural wave mode, this mesh resolution is fine enough.

The DMM approach is applied subsequently to calculate the reflection and transmission coefficients of the Z-axis flexural wave in the two cases, with $R = 100\ \Omega$ and $L = 2\ H$ in the shunt circuit. The results are shown in Figure 3.10. It can be observed from the DMM results that the propagation of the flexural wave is tuned around 1.5 kHz, as the reflection and transmission coefficients vary significantly. The tuning frequency calculated according to Equation (3.1) is about 1550 Hz, which is quite consistent with the results Figure 3.10(a) and Figure 3.10(b). It can also be concluded that the longitudinally bonded shunted piezoelectric patches (case B) results in a higher reflection of the flexural wave mode in the beam than those bonded transversally (case C).

3.1.2.2 Forced response prediction with FWFE

In order to predict the forced response of the beam with shunted piezoelectric patches, the FWFE method mentioned in Chapter 2 Subsection 2.1.3 can be applied. The same beam with a pair of shunted piezoelectric patches in case B is taken as an example, as displayed in Figure 3.11(a). To calculate the forced response, boundary conditions and the lengths of the waveguides should be specified. As shown in Figure 3.11(a), one extremity of the beam is excited by a punctual force $\mathbf{F}_{\texttt{exc}}$, and the other extremity is free. The amplitude

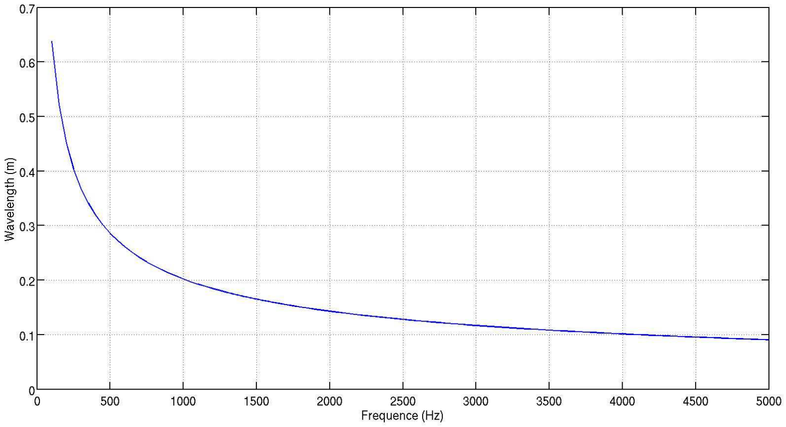

Figure 3.9: Wavelength of the flexural wave in Z-axis in case B and case C.

of the excitation force remains constant in the frequency domain. The first waveguide consists of N_1 identical unit cells while the second one consists of N_2 identical unit cells. The part of the beam covered with the pair of shunted piezoelectric patches is considered to be the coupling element. For the sake of simplicity, it is assumed that $N_1 = N_2 = N$. The two waveguides are identical as they belong to the same beam, thus $\mathbf{\Lambda}_1^{\mathtt{inc}} = \mathbf{\Lambda}_2^{\mathtt{ref}} = \mathbf{\Lambda}$, and $\mathbf{\Lambda}_1^{\mathtt{ref}} = \mathbf{\Lambda}_2^{\mathtt{inc}} = \mathbf{\Lambda}^{-1}$(see equation (2.34)). The boundary conditions of the system can be written in the following manner:

$$\mathbf{\Phi}_{\mathbf{F1}}^{\mathtt{inc}}\mathbf{Q}_1^{\mathtt{inc(1)}} + \mathbf{\Phi}_{\mathbf{F1}}^{\mathtt{ref}}\mathbf{Q}_1^{\mathtt{ref(1)}} = \mathbf{F}_{\mathtt{exc}} \tag{3.8a}$$

$$\mathbf{\Phi}_{\mathbf{F2}}^{\mathtt{inc}}\mathbf{Q}_2^{\mathtt{inc(N+1)}} + \mathbf{\Phi}_{\mathbf{F2}}^{\mathtt{ref}}\mathbf{Q}_2^{\mathtt{ref(N+1)}} = \mathbf{0} \tag{3.8b}$$

The boundary condition at the left extremity of Waveguide 1 is a Dirichlet boundary condition(equation (3.8a)), whereas the boundary condition at the right extremity of Waveguide 2 is a Neumann one(equation (3.8b)).
The continuity conditions of displacement and force between the waveguides and the coupling element form the coupling condition and can be expressed as:

$$\begin{bmatrix} \mathbf{q}_{\mathtt{LC}} \\ \mathbf{F}_{\mathtt{LC}} \end{bmatrix} = \begin{bmatrix} \mathbf{q}_{\mathtt{R1}}^{\mathtt{(N+1)}} \\ -\mathbf{F}_{\mathtt{R1}}^{\mathtt{(N+1)}} \end{bmatrix} \tag{3.9a}$$

$$\begin{bmatrix} \mathbf{q}_{\mathtt{RC}} \\ \mathbf{F}_{\mathtt{RC}} \end{bmatrix} = \begin{bmatrix} \mathbf{q}_{\mathtt{L2}}^{\mathtt{(1)}} \\ -\mathbf{F}_{\mathtt{L2}}^{\mathtt{(1)}} \end{bmatrix} \tag{3.9b}$$

where $\mathbf{q}_{\mathtt{LC}}$ and $\mathbf{F}_{\mathtt{LC}}$ stand for the nodal displacement and the nodal force at the left boundary of the coupling element, and $\mathbf{q}_{\mathtt{RC}}$ and $\mathbf{F}_{\mathtt{RC}}$ at the right boundary

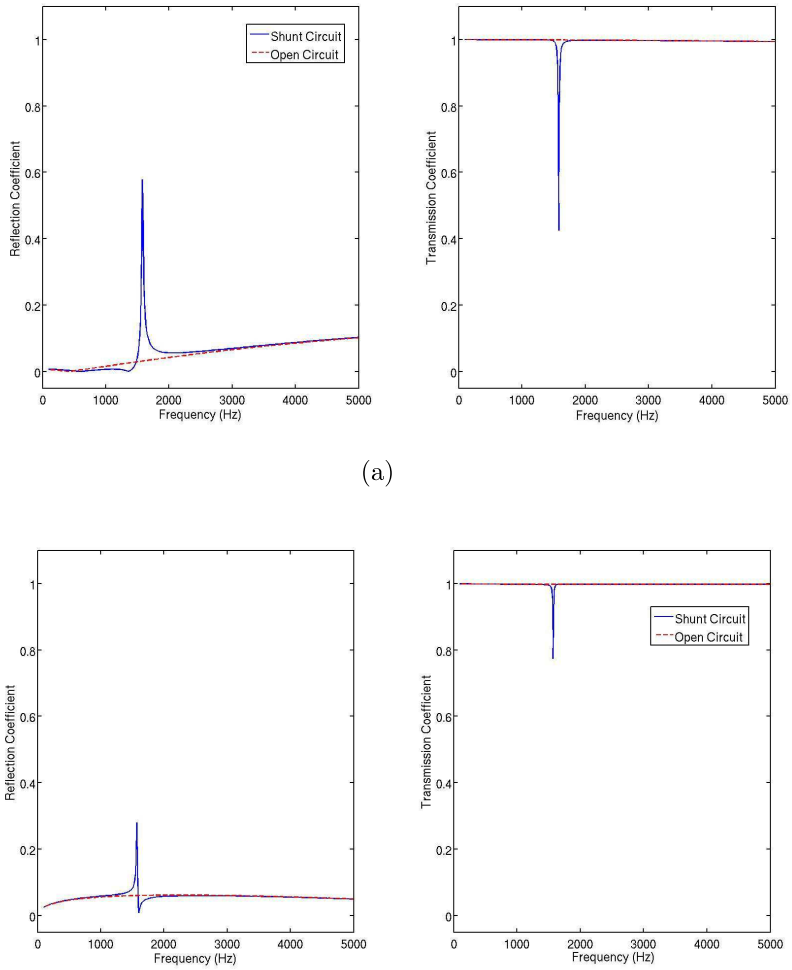

(a)

(b)

Figure 3.10: Reflection and transmission coefficients of the Z-axis flexural wave mode propagating in the beam (a)Case B (b)Case C. (Solid line)With R-L shunt circuit. (Dashed line)Open circuit.

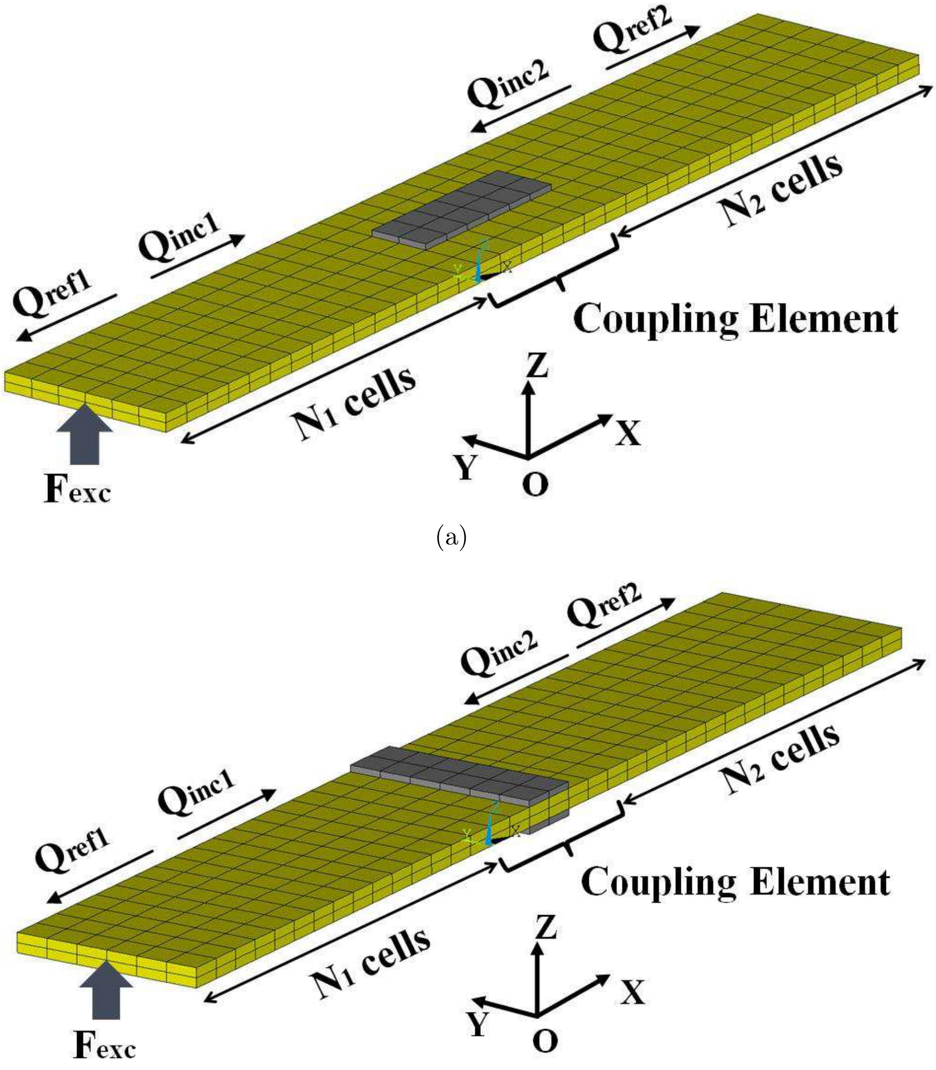

(a)

(b)

Figure 3.11: WFE model for the calculation of the forced response of the beam with shunted piezoelectric patches (a)in case B (b)in case C

of the coupling element.
By substituing these continuity conditions into the dynamics of the coupling element(see equation (2.107)), the boundary conditions at the right extremity of Waveguide 1 and those at the left extremity of Waveguide 2 can be obtained, as shown in Equation (3.10). $\mathbb{D}^*$ denotes the dynamic stiffness matrix of the coupling element condensed on the DOF located on the interfaces between the waveguides and the coupling element itself.

$$\mathbb{D}^* \begin{bmatrix} \mathbf{q}_{\mathtt{R1}}^{(\mathtt{N+1})} \\ \mathbf{q}_{\mathtt{L2}}^{(1)} \end{bmatrix} = - \begin{bmatrix} \mathbf{F}_{\mathtt{R1}}^{(\mathtt{N+1})} \\ \mathbf{F}_{\mathtt{L2}}^{(1)} \end{bmatrix} \tag{3.10}$$

Combined with the boundary conditions in Equation (3.8a) and Equation (3.8b) and the propagation relation(see equation (2.33)), an equation system which gives the wave amplitudes $\mathbf{Q}$ in both waveguides under the excitation force $\mathbf{F}_{\mathtt{exc}}$ can be developed as follows:

$$\mathbf{A} \begin{bmatrix} \mathbf{Q}_1^{\mathtt{inc(1)}} \\ \mathbf{Q}_1^{\mathtt{ref(1)}} \\ \mathbf{Q}_2^{\mathtt{inc(1)}} \\ \mathbf{Q}_2^{\mathtt{ref(1)}} \end{bmatrix} = \begin{bmatrix} \mathbf{F}_{\mathtt{exc}} \\ \mathbf{0} \\ \mathbf{0} \\ \mathbf{0} \end{bmatrix} \tag{3.11}$$

$$\mathbf{A} = \begin{bmatrix} \mathbf{\Phi}_{\mathtt{F1}}^{\mathtt{inc}} & \mathbf{\Phi}_{\mathtt{F1}}^{\mathtt{ref}} & \mathbf{0} & \mathbf{0} \\ (\mathbb{D}_{11}^* \mathbf{\Phi}_{\mathtt{q1}}^{\mathtt{inc}} + \mathbf{\Phi}_{\mathtt{F1}}^{\mathtt{inc}}) \mathbf{\Lambda}^{N} & (\mathbb{D}_{11}^* \mathbf{\Phi}_{\mathtt{q1}}^{\mathtt{ref}} + \mathbf{\Phi}_{\mathtt{F1}}^{\mathtt{ref}}) \mathbf{\Lambda}^{-N} & \mathbb{D}_{12}^* \mathbf{\Phi}_{\mathtt{q2}}^{\mathtt{inc}} & \mathbb{D}_{12}^* \mathbf{\Phi}_{\mathtt{q2}}^{\mathtt{ref}} \\ \mathbb{D}_{21}^* \mathbf{\Phi}_{\mathtt{q1}}^{\mathtt{inc}} \mathbf{\Lambda}^{N} & \mathbb{D}_{21}^* \mathbf{\Phi}_{\mathtt{q1}}^{\mathtt{ref}} \mathbf{\Lambda}^{-N} & \mathbb{D}_{22}^* \mathbf{\Phi}_{\mathtt{q2}}^{\mathtt{inc}} + \mathbf{\Phi}_{\mathtt{F2}}^{\mathtt{inc}} & \mathbb{D}_{22}^* \mathbf{\Phi}_{\mathtt{q2}}^{\mathtt{ref}} + \mathbf{\Phi}_{\mathtt{F2}}^{\mathtt{ref}} \\ \mathbf{0} & \mathbf{0} & \mathbf{\Phi}_{\mathtt{F2}}^{\mathtt{inc}} \mathbf{\Lambda}^{-N} & \mathbf{\Phi}_{\mathtt{F2}}^{\mathtt{ref}} \mathbf{\Lambda}^{N} \end{bmatrix}$$

The resolution of this equation system provides the wave amplitudes at the left boundary of the waveguides 1 and 2, and via equation (2.33), wave amplitudes at any node in the two waveguides can be obtained. The nodal displacement in Z-axis at the center of the free extremity of the beam is used for the calculation of the frequency response function(FRF) of the beam. As an example, the length of the beam is chosen to be 1 m, thus $N = 97$. The pair of piezoelectric patches share the same shunt circuit with $R = 100\ \Omega$ and $L = 2.8251\ H$, in order to tune a flexural mode around 1350 Hz. The FRF with shunt circuit and without shunt circuit (open circuit case) are calculated numerically. Additionally, a classical finite element harmonic analysis has been performed using ANSYS to extract the FRF of the same structure in the open circuit condition. SOLID45 elements [80] are used for the beam, and SOLID5 elements [80] with electric potential DOF are applied for the piezoelectric patches. The finite element mesh resolutions are the same as those mentioned in subsection 3.1.1. The comparison results are displayed in Figure 3.12. As shown in Figure 3.12(a), the FWFE results correspond very well to the finite element results in the frequency band from 0 to 5 kHz. The attenuation effect of the shunted piezoelectric patches around the tuning frequency (1350 Hz), which is close to the eigenfrequency of one of the flexural modes, is rather evident, as shown in Figure 3.12(b). In the same manner, another analysis is performed for the beam with a pair of shunted piezoelectric patches in case

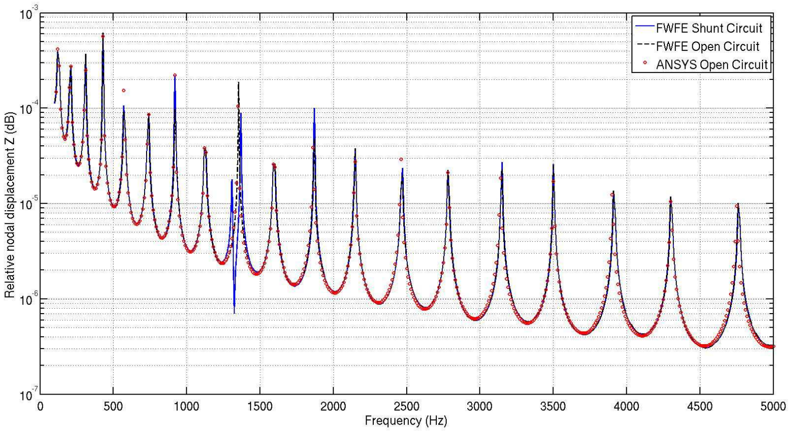

(a)

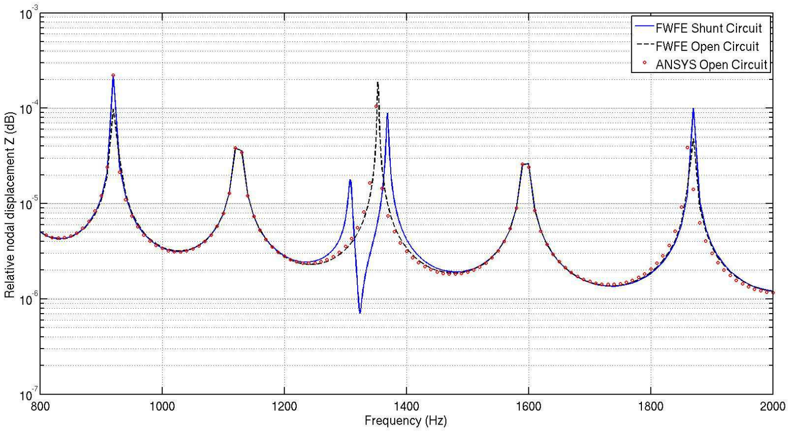

(b)

Figure 3.12: Comparison of the frequency responses in case B: (a)Frequency band from 0 to 5 kHz (b)Zoom around the tuning frequency (1350 Hz).(Solid line)FWFE with shunted circuit. (Dashed line)FWFE without shunt circuit. (○ markers)ANSYS results without shunt circuit.

C displayed in Figure 3.11(b). The comparison results of the FRF is shown in Figure 3.13. These results reveal again that FWFE can predict correctly the frequency response of the structure. It is an effective approach that can be employed to estimate the influence of the shunted piezoelectric patches on the flexural modes of the beam. It can be concluded from Figure 3.12(b) and Figure 3.13(b) that the longitudinally placed pair of piezoelectric patches lead to a larger attenuation frequency band than the transversally placed patches. It should also be noted that the FWFE formulation requires much less computational time compared to ANSYS. Furthermore, ANSYS is not capable of analyzing shunt circuits with negative capacitance, but the FWFE method is able to deal with all kinds of shunt impedance.

3.1.3 Time response calculation and reflection coefficient verification

In Subsection 3.1.2, the frequency responses are calculated with an excitation force of constant amplitude in the frequency domain. In order to evaluate the time response, the approach mentioned in Chapter 2 Subsection 2.1.4 is carried out. The reflection coefficients can be extracted from the time response and then be compared to those calculated with the DMM approach. This extraction technique can equally be applied in experiments to validate numerical results. Let's consider an aluminium beam with a pair of longitudinally placed $R-L$ shunted piezoelectric patches. According to the dispersion curves shown in Figure 3.8, it can be noted that in the frequency band from 0 to 20 kHz, the bending modes are dispersive as their dispersion curves are not linear, whereas the tension/compression mode is non-dispersive as its dispersion curve is linear. As non-dispersive waves can maintain their wave form during the propagation, and their group velocity is almost constant, it will be much easier to track them in the structure. The group velocity of the tension/compression mode is shown in Figure 3.14. It is almost constant in the frequency band from 0 to 20 kHz. As the wavenumber of the X-axis tension/compression mode is smaller than the Z-axis bending mode, the wavelength of the former mode is larger than the latter mode. So the same mesh resolution can be applied for the finite element models. Based on this group velocity, the length of the beam is chosen to be 3 meters which is large enough so that incident and reflected waves can be clearly distinguished. To minimize the effect of induced dispersion by the piezoelectric patches, narrow band signals are used, composed of 2.5 cycles modulated by a Hanning window with the central frequency f_0 equal to 9 kHz. The time wave form and the spectrum of this wave packet excitation force is displayed in Figure 3.15. The maximum amplitude is 100 N and the sampling frequency is 20 times greater than the

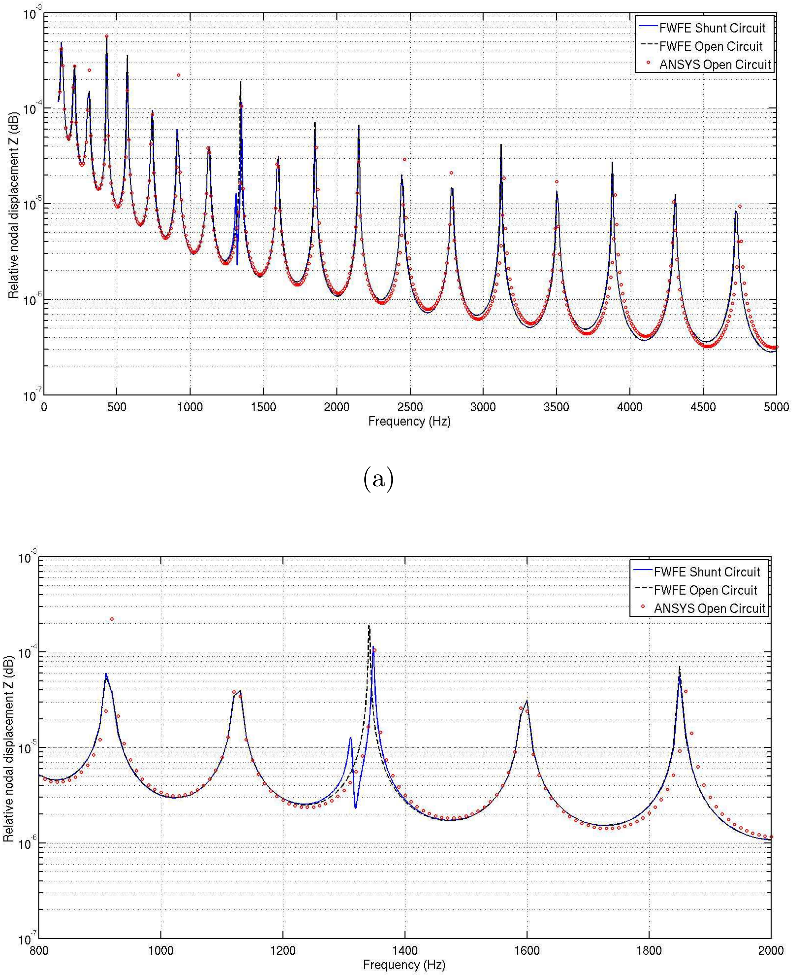

(a)

(b)

Figure 3.13: Comparison of the frequency responses in case C: (a)Frequency band from 0 to 5 kHz (b)Zoom around the tuning frequency (1350 Hz). (Solid line)Piezoelectric patches with shunted circuit. (Dashed line)Piezoelectric patches without shunt circuit. (○ markers)ANSYS results without shunt circuit.

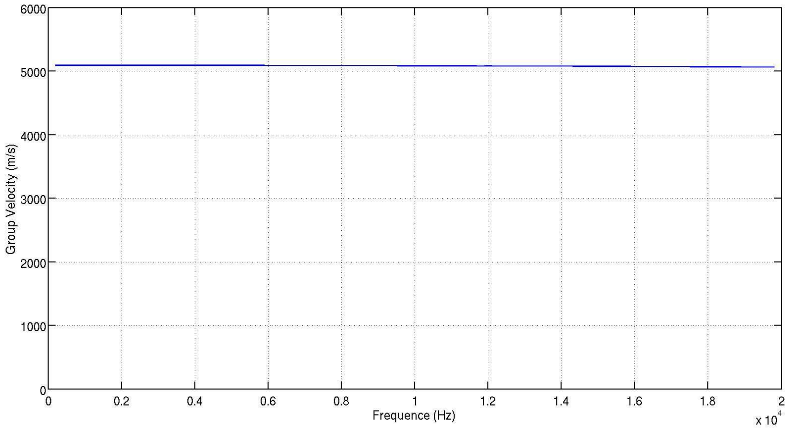

Figure 3.14: Group Velocity of the tension/compression wave in X-axis in case B.

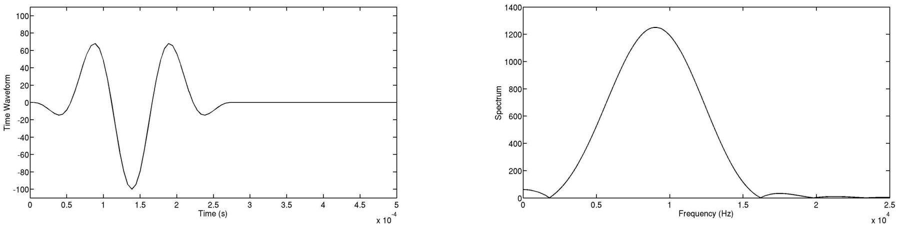

(a) (b)

Figure 3.15: The time wave form and the spectrum of the wave packet excitation. (a)Time wave form (b)Spectrum.

central frequency in order to guarantee the signal quality of the wave packet. This excitation force is applied to one extremity of the beam as the input, and the displacement of the measure point is taken as the output, as shown in Figure 3.16. The measure point lies at 25 cm from the extremity with excitation force. Subsequently, the forced response of the structure under white noise excitation is calculated, as shown in Figure 3.17. As an example, the mode at 9350 Hz is targeted, and then the shunt circuit is tuned to this frequency, with $R = 100\ \Omega$ and $L = 0.0575\ H$. From Figure 3.17(b), it can be seen that with the shunted piezoelectric patches, only a damping effect is obtained for the tension/compression mode, but for the flexural mode, a stronger attenuation effect is achieved, as shown in Figure 3.12(b), where the shunted piezoelectric patches play the role of a dynamic damper which creates an added DOF in the system. With the transfer function, the wave packet excitation is applied to the system in order to acquire the frequency response. Then the IDFT of

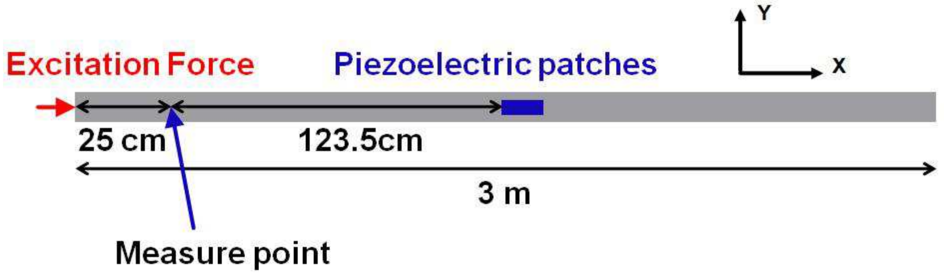

Figure 3.16: Configuration for the time response simulation of the tension/compression wave in X-axis.

this frequency response is carried out to calculate the time response of the structure, as displayed in Figure 3.18. As those wave packets are apparently unconnected in this case, no wave packet decomposition techniques are needed. It can be noted that when the beam is equipped with the piezoelectric patches, the reflection of the
tension/compression wave is no longer null due to the added mass and stiffness. When the shunt circuit is applied onto the piezoelectric patches, the reflection becomes stronger and the damping effect can be observed in the reflected packet.
In order to verify the reflection coefficients calculated via the DMM approach and provide an effective experimental evaluation technique for the reflection coefficient based on time response of the structure, the following extraction procedure is proposed:

1. The Hilbert Transform is applied to the time response of the structure, and its absolute value is representative of the envelope of the signal. The first peak represents the maximum amplitude of the incident wave, and the second peak for the reflected wave, as shown in Figure 3.19.

2. The imaginary part of the wavenumber k calculated with the WFE method is used to calculate the spatial damping. As the propagation of this mode can be characterized by an exponential law $A = A_0e^{ikx}$, the spatial damping ratio $\gamma_x = - \mid Im(k) \mid$.

3. With the group velocity V_g of this wave mode, the damping ratio in time domain can be calculated as $\gamma_t = - \mid Im(k)V_g \mid$.

4. On the plot of the Hilbert Transform result, a damping curve can be drawn to take into account the damping effect caused by the distance between the measure point and the piezoelectric patches so as to evaluate the reflection coefficient correctly. This curve passes the first peak of

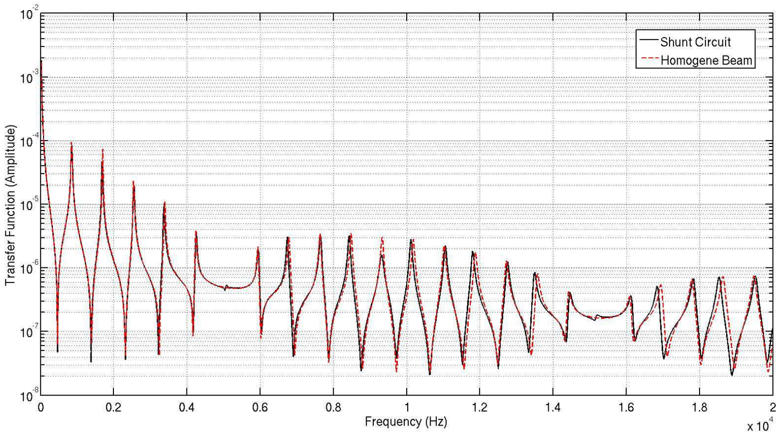

(a)

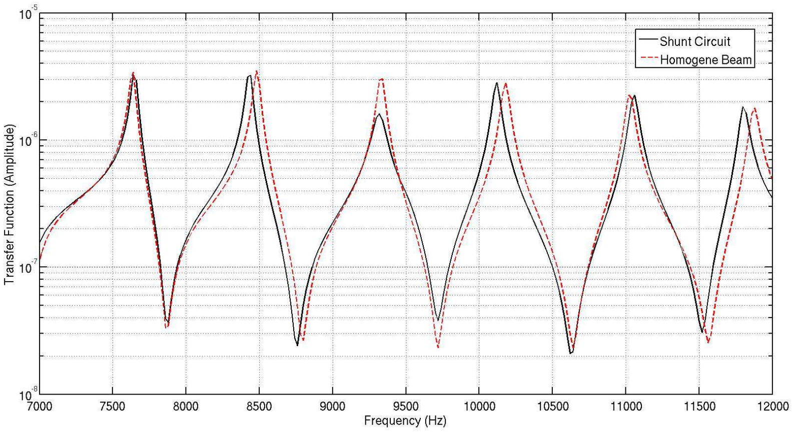

(b)

Figure 3.17: The forced response of the structure under white noise excitation (transfer function) tuned at 9350 Hz. (a)Frequency response (b)Zoom around the tuning frequency. (Solid line)Piezoelectric patches with shunted circuit. (Dashed line)Beam without piezoelectric patches.

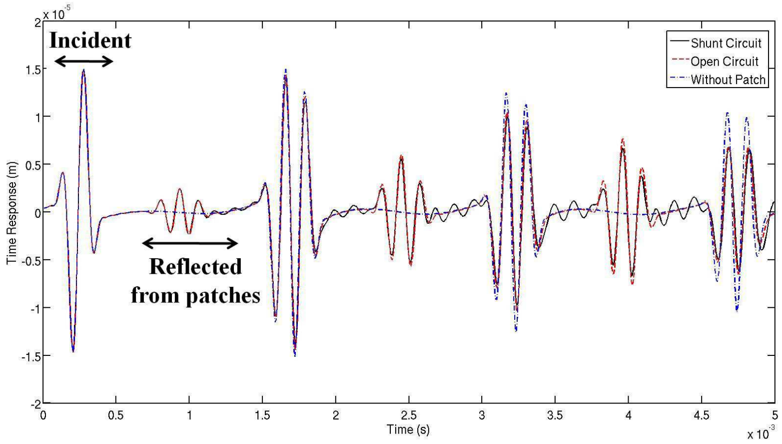

Figure 3.18: Time response of the structure under wave packet excitation. (Solid line)Piezoelectric patch with shunt circuit. (Dashed line)Piezoelectric patches without shunt circuit. (Dash-dotted line)Beam without piezoelectric patches.

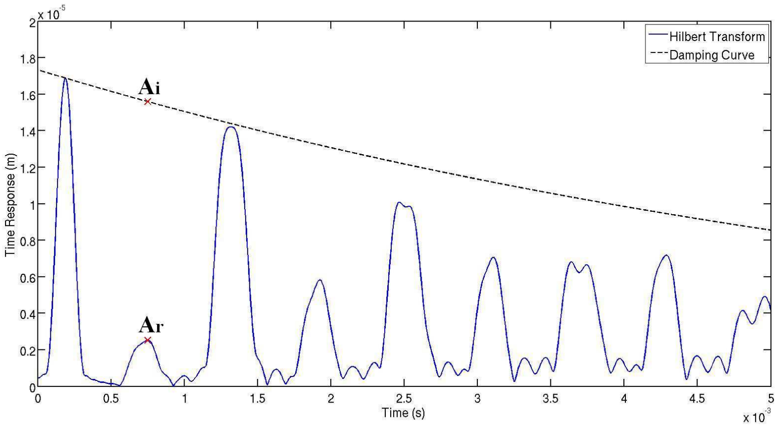

Figure 3.19: Hilbert Transform of the time response and the damping curve to extract the reflection coefficient of the tension/compression wave. (Solid line)Absolute value of the Hilbert Transform of the time response. (Dashed line)Damping curve based on spatial damping.

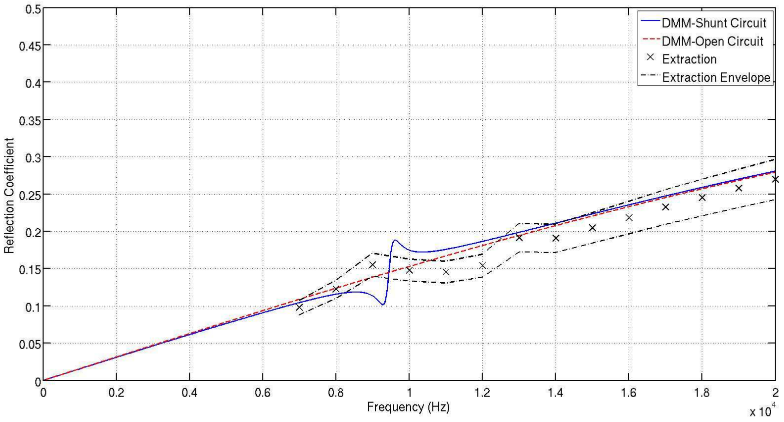

Figure 3.20: Comparison of reflection coefficients of the tension/compression wave in X-axis calculated through the DMM approach and the extraction procedure. (Solid line)Calculation with DMM, piezoelectric patch with shunt circuit. (Dashed line)Calculation with DMM, piezoelectric patch without shunt circuit. (× markers)Calculation with extraction procedure. (Dash-dotted line)Envelope of the extracted reflection coefficients.

the Hilbert Transform result and follows the exponential decreasing law defined by $A = A_0 e^{\gamma_t t}$. $\mathbf{A_r}$ denotes the amplitude of the reflected wave, and $\mathbf{A_i}$ represents the amplitude of the incident wave with the attenuation effect taken into account, as shown in Figure 3.19. The reflection coefficient can be calculated as $\mathbf{R} = \mathbf{A_r}/\mathbf{A_i}$.

5. By varying the central frequency f_0 of the wave packet excitation, reflection coefficients at different frequencies can be acquired frequency by frequency in order to verify the reflection coefficients calculated with the DMM approach.

The reflection coefficients of the tension/compression mode tuned at 9350 Hz are calculated via the DMM approach, and then compared to those obtained through the extraction procedure. It should be mentioned that this extraction procedure is a rather coarse evaluation tool for the reflection coefficients. If an error of ±10% is applied to each extracted reflection coefficient, then the envelope of the extracted reflection coefficients can be obtained. The results are shown in Figure 3.20. For the frequency band below 7 kHz, it is difficult to evaluate correctly the reflection coefficient with the extraction procedure as the span of the wave packet in time domain becomes so large that it's hard to distinguish incident and reflected waves, unless the length of the beam becomes larger. And for the frequency band around the tuning frequency, it is also difficult to evaluate precisely the reflection coefficient with the Hilbert Transform, as the added damping effect needs to be considered properly. But globally, the results issued from the DMM approach are verified by those through the extraction procedure, as the envelope covers most of the DMM results in the open circuit case. This procedure will be employed for the experimental validation of numerically calculated reflection coefficients.

3.2 Traveling wave control in thin-walled beam structures through $R-L$ shunted piezoelectric patches

Thin-walled structures are widely used nowadays, especially in aerospace engineering domain, where we should solve materials-consumption problems with preservation of necessary strength and sufficient lightness. The aeronautical structures are often large and complex, where the propagation phenomena play an important role in the dynamical behavior of these structures. The thin-walled components, especially straight ones of constant cross-section that can be regarded as one-dimensional waveguides, are often carriers of mechanical energy from the source. The energy transfer leads to sound radiation and unwanted vibration, and then problems like fatigue and structural borne sound will appear. Mastering the dynamical behavior of thin-walled structures can provide efficient and satisfactory means for the structure design.

For this purpose, prediction and evaluation tools should be developed for thin-walled structures. As waveguides, their dynamic properties can be described by dispersion curves, for which many approaches are available. The most well-known methods are based on theories like Euler-Bernoulli and Timoshenko beams. However, these beam theories are limited by the hypothesis of undeformed cross-section, which is only valid at low frequencies and for compact cross-sections. In the work of Gavric [81], it is mentioned that when thin-walled beams are concerned, even a relatively low-frequency excitation can produce transfer of mechanical energy by propagating waves associated with deformed cross-section modes. The application of finite element method(FEM) somehow solved this kind of problem, and can give precise prediction of propagational wavenumbers and modes of thin-walled beams. Gavric [81, 82] proposed a particular finite element scheme allowing the extraction of wavenumbers from the resolution of a four-order matrix equation. Gendy *et al.* [83] presented a three-dimensional, two-field variational formulation and the corresponding finite element discretization for free vibration analysis of coupled extensional/flexural/torsional modes of curved beams with arbitrary thin-walled sections. Mitra *et al.* [84] developed a composite thin wall beam element of arbitrary cross-section with open or closed contour. Later, Houillon *et al.* [61] provided a propagative approach in order to extract propagation parameters and the dispersion curves of thin-walled structures of any cross-section. The formulations applied in this work can be referred as wave finite element(WFE) method [46, 47, 48], which has been initiated by Mead [57] and Zhong and Williams [45] for wave mode description into elastic systems with complex cross-sections. This method is not constrained by

low-frequency analytical assumptions and can be applied in the mid-frequency range, where cross-section modes propagate [46, 68].
In this section, the DMM with shunted piezoelectric elements is firstly employed to calculate the reflection and transmission coefficients of the pumping wave mode and the X-axis extensional wave mode. A full finite element description that takes the mechanical-electrical coupling into account is given to the thin-walled beams. The influence of the shunted piezoelectric patches on the propagation of these wave modes is carefully investigated. Subsequently, the FWFE approach is applied for the evaluation of the dynamical behavior of the structure in frequency domain. Unlike the DMM approach which gives predictions for the beam structure with free boundary conditions, frequency response functions can be obtained for the thin-walled beam structure with forced boundary conditions. Waveguides are of finite length in this case. Thereafter, based on the frequency responses, the calculation of time responses of the structure under wave packet excitation is carried out. The same extraction procedure presented in Subsection 3.1.3 is used to calculate reflection coefficients of the X-axis extensional mode so as to verify the results issued from the DMM approach.

3.2.1 DMM approach applied for pumping wave and X-axis extensional wave

The structures to be studied here are thin-walled beams with 4 identical $R-L$ shunted piezoelectric patches. The finite element model of the coupled system is shown in Figure 3.21. The connection between the 4 piezoelectric patches and the $R-L$ shunt circuit is displayed in Figure 3.22. It should be mentioned that by choosing the polarities of the piezoelectric patches, different wave modes can be targeted and controlled. The finite element model of the coupling element is shown in Figure 3.23, with the definition of geometric parameters. Two different cases are studied: in Case A the piezoelectric patches are bonded in a longitudinal way (see Figure 3.23(a)), while in Case B, these patches are bonded in a transversal way (see Figure 3.23(b)). Definitions and numerical values of the geometric parameters are listed in Table 3.2. The parameter L_b represents the length of the thin-walled beam involved in the coupling element. The material of the beam is aluminium and considered as isotropic, with Young's modulus $E_b = 70\ GPa$ and Poisson's ratio $\nu_b = 0.34$, and density $\rho_b = 2700\ kg/m^3$. The piezoelectric patches are fabricated by Saint-Gobain Quartz (type SG P189) and the corresponding material characteristics are listed in Appendix A. This type of piezoelectric patch works mainly in the 3-1 mode.

At first, the thin-walled beam is regarded as a waveguide and the cor-

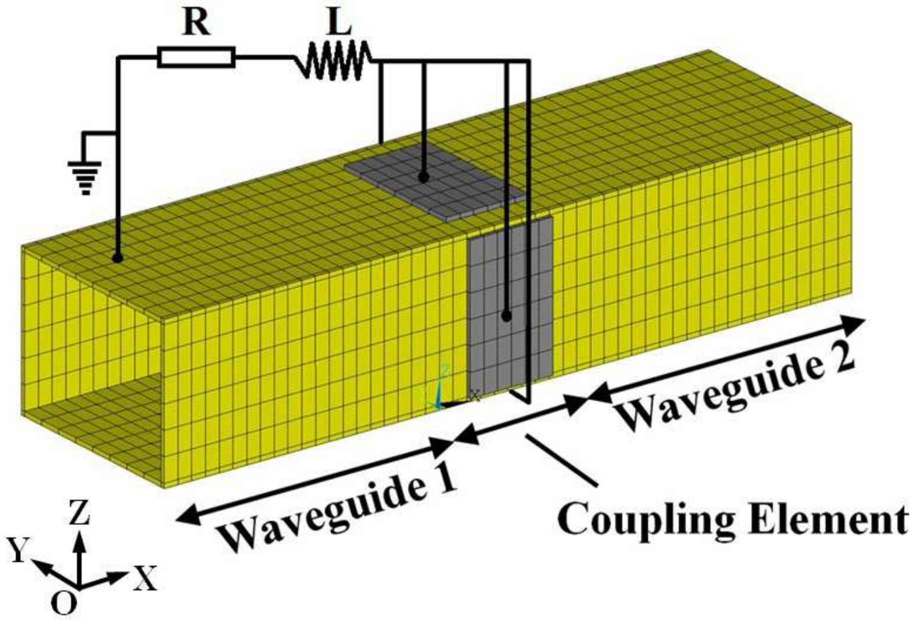

Figure 3.21: Finite element model of a thin-walled beam with symmetric shunted piezoelectric patches. The coupling element is the part of the beam with 4 identical piezoelectric patches.

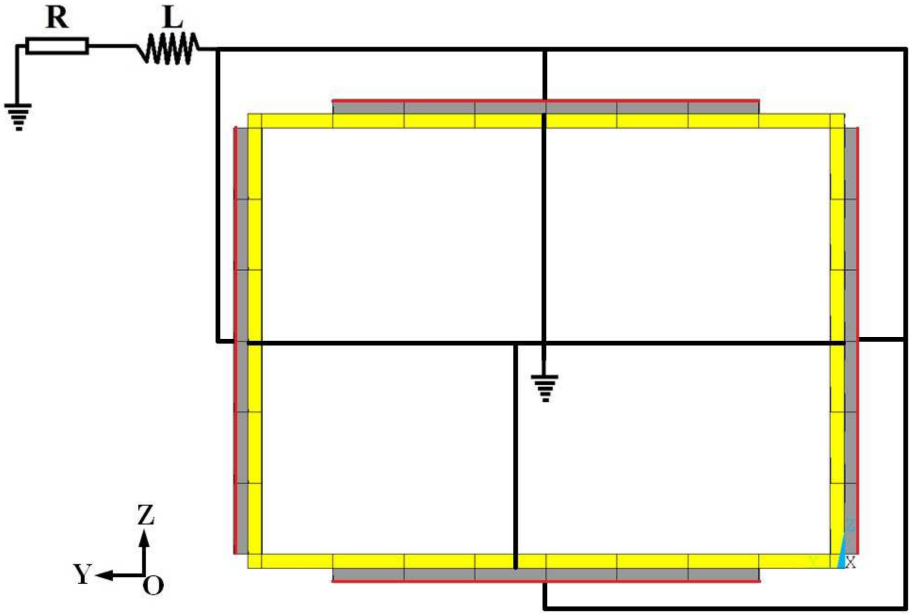

Figure 3.22: Configuration of the connection between the 4 piezoelectric patches and the $R-L$ shunt circuit.

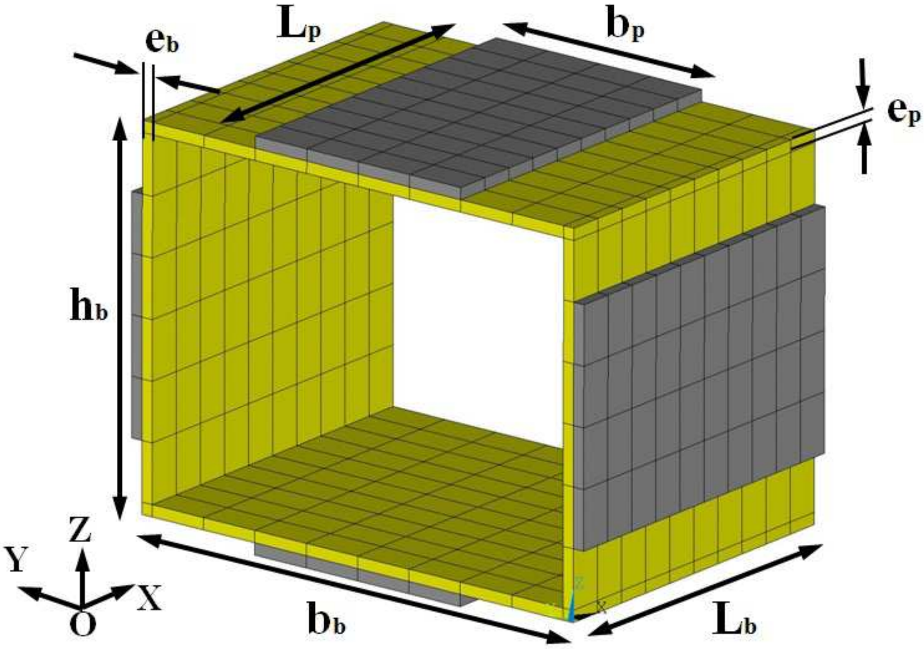

(a)

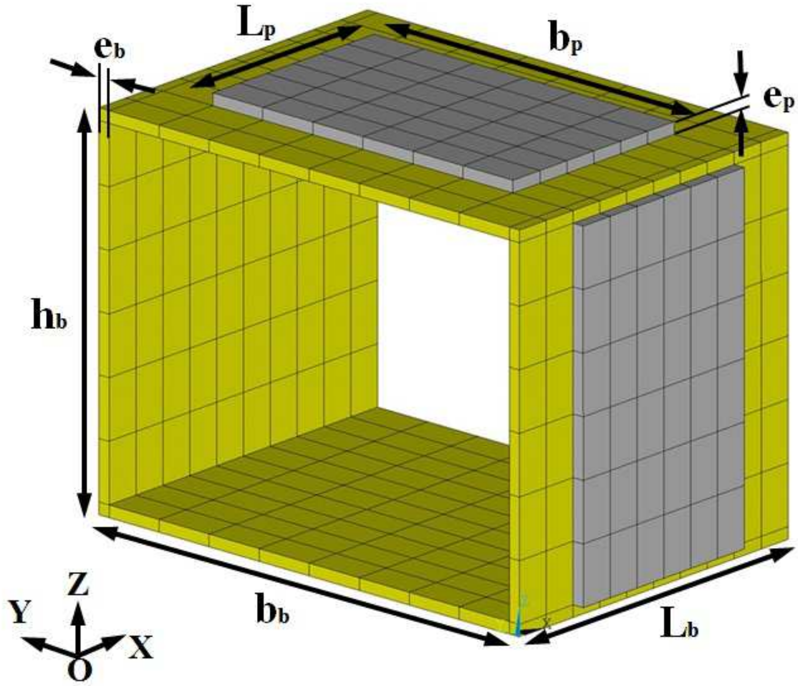

(b)

Figure 3.23: Finite element model of the coupling element and definition of geometric parameters in (a)Case A(longitudinally bonded patches) (b)Case B(transversally bonded patches).

Table 3.2: Numeric values of the geometric parameters in the coupling element shown in Figure 3.23. The units of all the parameters are in meter (m).

Case	L_b	L_p	b_b	b_p	h_b	e_b	e_p
A	0.03	0.03	0.042	0.02	0.032	0.001	0.001
B	0.03	0.02	0.042	0.03	0.032	0.001	0.001

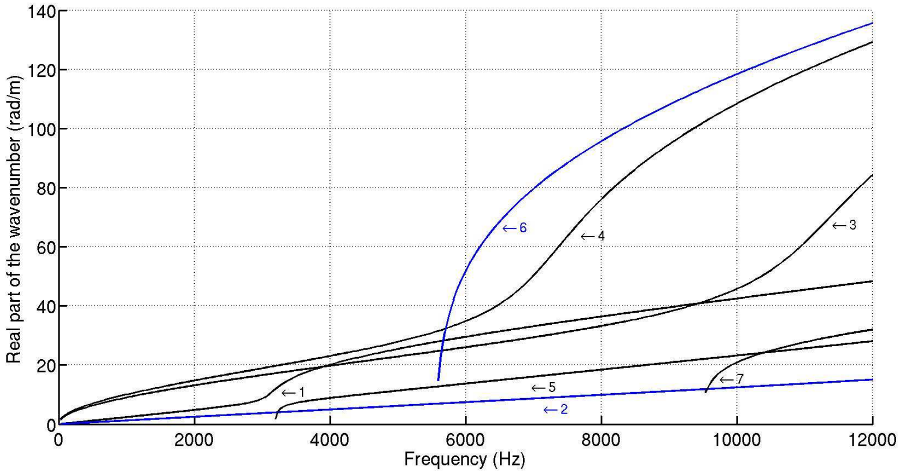

Figure 3.24: Dispersion curves of the wave modes propagating in the thin-walled beam in case A: (1)1st Torsional wave in X-axis (2)Extensional wave in X-axis (3)Flexural wave in Y-axis (4)Flexural wave in Z-axis. (5)2nd Torsional wave in X-axis. (6)Symmetric pumping mode. (7)Higher order cross-section mode. These wave modes are identified through their mode shapes (eigenvectors) issued from the WFE approach.

responding dispersion curves of the wave modes propagating in the structure are extracted via the WFE approach, as shown in Figure 3.24. These curves describe the evolution of the wavenumber k in the frequency domain. The wavelength(λ) of each mode can be calculated based on these results, as $\lambda = 2\pi/k$. The global mesh resolution is chosen to be $0.003\times0.005\times0.001\ m^3$, as the minimum wavelength of the concerned wave modes is about 0.04m in the concerned frequency band(from 0 to 12 kHz). In the finite element model of the waveguide there are 128 nodes/32 elements while in the coupling element there are 924 nodes/480 elements. The mode shapes of the wave modes propagating in the thin-walled beam are shown in Figure 3.25. For the control of the symmetric pumping mode (Mode 6), the 2 horizontal piezoelectric patches should work in compression mode, whereas the 2 vertical piezoelectric patches should work in tension mode; for the control of the extensional mode,

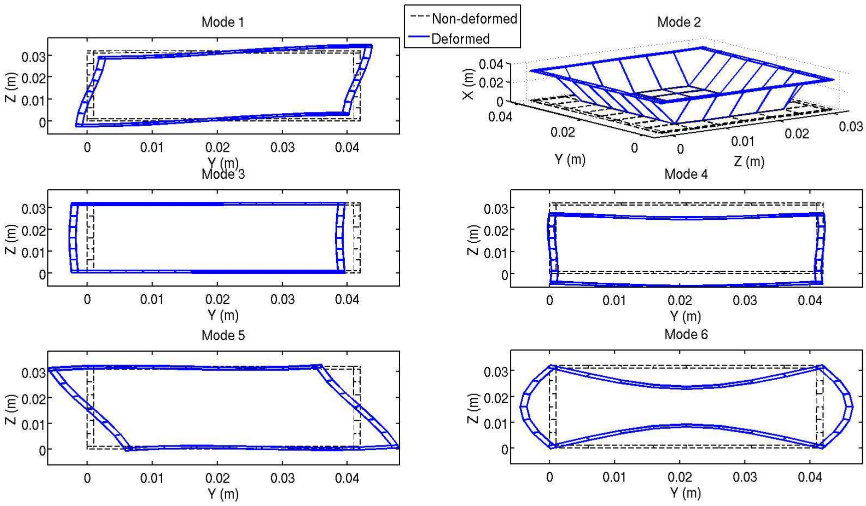

Figure 3.25: Mode shapes of the waves propagating in the thin-walled beam in case A: (1)1st Torsional wave in X-axis (2)Extensional wave in X-axis (3)Flexural wave in Y-axis (4)Flexural wave in Z-axis. (5)2nd Torsional wave in X-axis. (6)Symmetric pumping mode. (Solid line)Deformed mode shape. (Dashed line)Non-deformed section.

all the 4 patches should work in the same mode (tension or compression). The DMM method is subsequently applied to the thin-walled beam in Case A for analyzing the symmetric pumping wave mode, and gives the reflection and transmission coefficients, as displayed in Figure 3.26(a), with $R = 10\ \Omega$ and $L = 0.016\ H$. The results for the X-axis extensional wave mode are shown in Figure 3.26(b). The tuning frequency f_{tune} of the piezoelectric patches is about 9 kHz. Around this frequency, the impedance of the structure is greatly modified by the shunted piezoelectric patches so that the wave propagation characteristics change significantly. The tuning frequency can be calculated according to equation (3.12):

$$f_{tune} = \frac{1}{2\pi\sqrt{4LC_{p3}^{S}}} \tag{3.12}$$

where $C_{p3}^{S} = (1 - k_{31}^{2})C_{p3}^{T}$ is the capacitance of the piezoelectric patch measured at constant strain, and the 4 in front of L is due to the fact that the 4 piezoelectric patches are connected in parallel. If each piezoelectric patch has an independent shunt circuit, the 4 in front of L will disappear. The subscript 1 represents the X-axis direction while the subscript 3 denotes the Z-axis direction. k_{31} is the electromechanical coupling coefficient. C_{p3}^{T} is the capacitance of the piezoelectric patch measured at constant stress. It can be

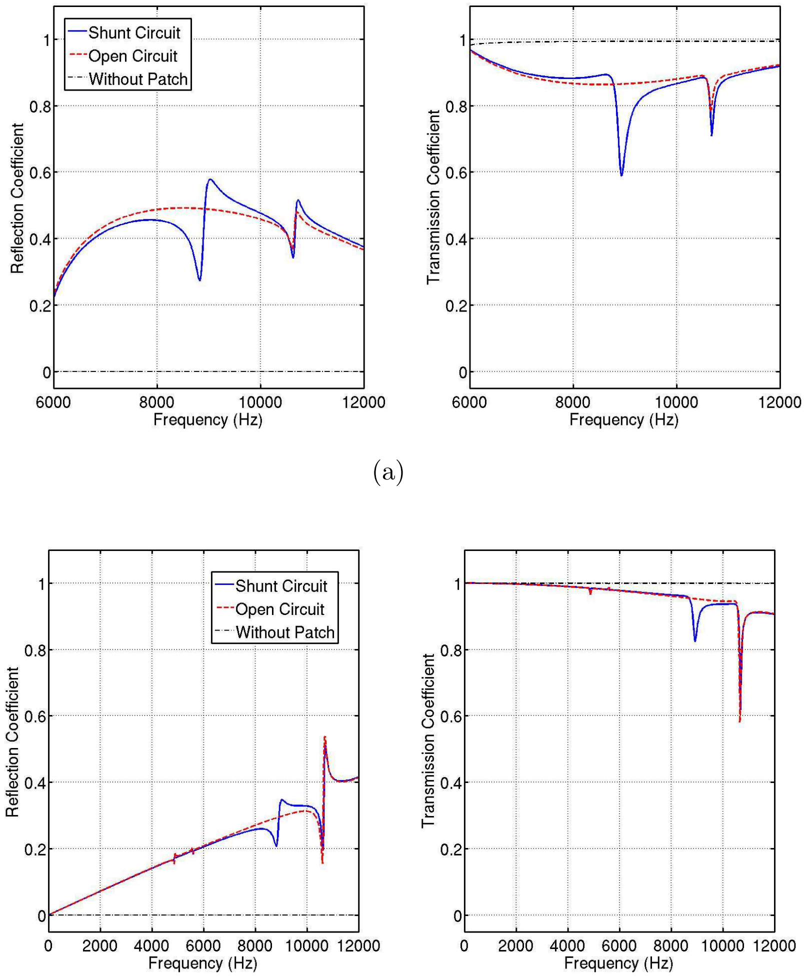

(a)

(b)

Figure 3.26: Reflection and transmission coefficients of wave modes in the thin-walled beam in Case A. (a)Symmetric pumping wave mode. (b)X-axis extensional wave mode. (Solid line)With R-L shunt circuit. (Dashed line)Shunt circuit open. (Point-dashed line)Beam without piezoelectric patches.

calculated in the following manner:

$$C_{p3}^{T} = \frac{\varepsilon^{T} A_3}{L_3} \tag{3.13}$$

where A_3 is the area of the surface of the piezoelectric patch perpendicular to Z-axis, $L_3 = e_p$ is the thickness of the piezoelectric patch in Z-axis direction. Equally for the thin-walled beam in Case B, the reflection and transmission coefficients of the symmetric pumping mode and the extensional mode are shown in Figure 3.27. It can be observed that the piezoelectric patches in Case A have a totally different effect on the symmetric pumping mode from the patches in Case B. This wave mode cuts on from about 5.6 kHz. In Case A, the piezoelectric patches are the most efficient around 8.5 kHz in the frequency band from 6 to 12 kHz, when the shunt circuit is open. In Case B, the shunted piezoelectric patches become less efficient from the cut-on frequency to about 7.5 kHz, and then the efficiency turns out to be better at higher frequencies. And in both cases, around the tuning frequency(about 9 kHz), the effect of the $R-L$ shunt circuit on the piezoelectric patches is rather evident. By simply varying the inductance L in the circuit, this tuning frequency can be displaced to desired frequency band. For the extensional wave in X-axis, in both cases, the shunted piezoelectric patches have similar influence on this wave mode. Around the tuning frequency, the patches in Case A results in a slightly stronger variation in the reflection and transmission coefficients, which indicates that the configuration in Case A is better for the control of the extensional wave in X-axis in this thin-walled beam.

3.2.2 Forced WFE applied for the control of symmetric pumping wave

For the calculation of the forced response of the thin-walled beam with shunted piezoelectric patches, the FWFE method mentioned in Chapter 2 Subsection 2.1.3 can be applied. The thin-walled beam to be studied is displayed in Figure 3.28. In the formulation of FWFE, the lengths of the waveguides are no longer infinite and should be specified, as well as the boundary conditions. As shown in Figure 3.28, one extremity of the beam is excited by imposed displacement $\mathbf{q_{exc}}$, and the other extremity is free. The amplitude of the excitation displacement remains constant in the frequency domain. The imposed displacement is chosen to be one of the modal displacements so that only the mode with this modal displacement is excited in the thin-walled beam. The first waveguide consists of N_1 identical unit cells while the second one consists of N_2 identical unit cells. The part of the beam covered with shunted piezoelectric patches is considered to be the coupling element. For

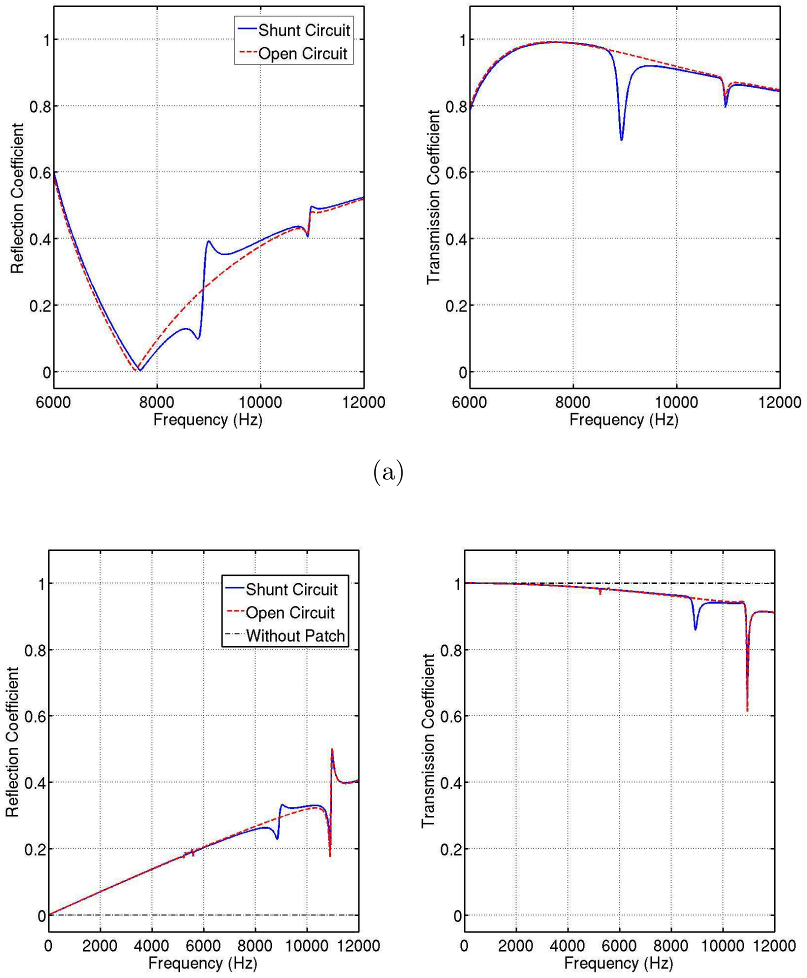

(a)

(b)

Figure 3.27: Reflection and transmission coefficients of wave modes in the thin-walled beam in Case B. (a)Symmetric pumping wave mode. (b)X-axis extensional wave mode. (Solid line)With R-L shunt circuit. (Dashed line)Shunt circuit open. (Point-dashed line)Beam without piezoelectric patches.

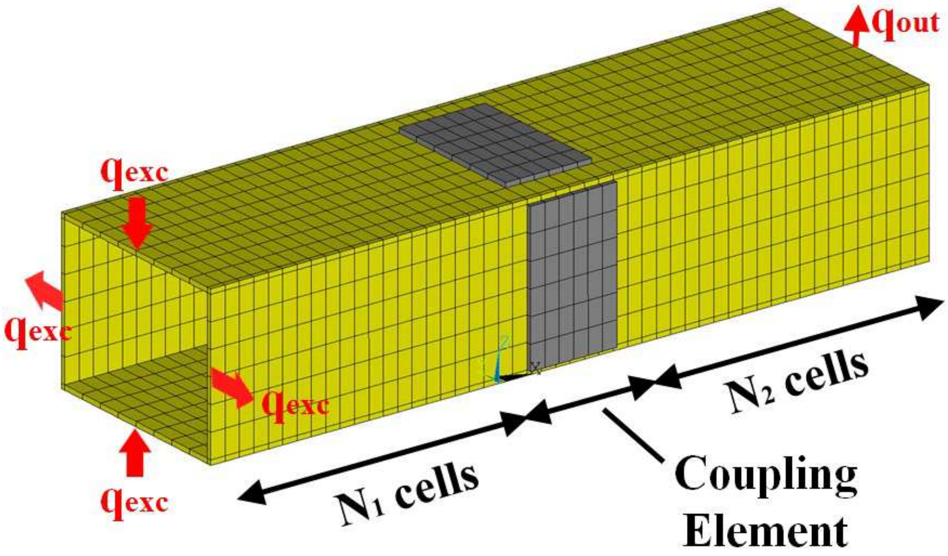

Figure 3.28: Finite element model for the calculation of the forced response of the thin-walled beam with 4 identical shunted piezoelectric patches.

the sake of simplicity, it is assumed that $N_1 = N_2 = N$. The two waveguides are identical as they belong to the same beam, thus $\mathbf{\Lambda}_1^{\mathtt{inc}} = \mathbf{\Lambda}_2^{\mathtt{ref}} = \mathbf{\Lambda}$, and $\mathbf{\Lambda}_1^{\mathtt{ref}} = \mathbf{\Lambda}_2^{\mathtt{inc}} = \mathbf{\Lambda}^{-1}$(see equation (2.34)). The boundary conditions of the system can be written in the following manner:

$$\mathbf{\Phi}_{\mathbf{q1}}^{\mathtt{inc}}\mathbf{Q}_1^{\mathtt{inc(1)}} + \mathbf{\Phi}_{\mathbf{q1}}^{\mathtt{ref}}\mathbf{Q}_1^{\mathtt{ref(1)}} = \mathbf{q}_{\mathtt{exc}} \tag{3.14a}$$

$$\mathbf{\Phi}_{\mathbf{F2}}^{\mathtt{inc}}\mathbf{Q}_2^{\mathtt{inc(N+1)}} + \mathbf{\Phi}_{\mathbf{F2}}^{\mathtt{ref}}\mathbf{Q}_2^{\mathtt{ref(N+1)}} = \mathbf{0} \tag{3.14b}$$

The boundary condition at the left extremity of Waveguide 1 is a Dirichlet boundary condition(equation (3.14a)), whereas the boundary condition at the right extremity of Waveguide 2 is a Neumann one(equation (3.14b)).
The continuity conditions of displacement and force between the waveguides and the coupling element form the coupling condition and can be expressed as:

$$\begin{bmatrix} \mathbf{q}_{\mathtt{LC}} \\ \mathbf{F}_{\mathtt{LC}} \end{bmatrix} = \begin{bmatrix} \mathbf{q}_{\mathtt{R1}}^{\mathtt{(N+1)}} \\ -\mathbf{F}_{\mathtt{R1}}^{\mathtt{(N+1)}} \end{bmatrix} \tag{3.15a}$$

$$\begin{bmatrix} \mathbf{q}_{\mathtt{RC}} \\ \mathbf{F}_{\mathtt{RC}} \end{bmatrix} = \begin{bmatrix} \mathbf{q}_{\mathtt{L2}}^{\mathtt{(1)}} \\ -\mathbf{F}_{\mathtt{L2}}^{\mathtt{(1)}} \end{bmatrix} \tag{3.15b}$$

where $\mathbf{q}_{\mathtt{LC}}$ and $\mathbf{F}_{\mathtt{LC}}$ stand for the nodal displacement and the nodal force at the left boundary of the coupling element, and $\mathbf{q}_{\mathtt{RC}}$ and $\mathbf{F}_{\mathtt{RC}}$ at the right boundary of the coupling element. By substituing these continuity conditions into the dynamics of the coupling element(see equation (2.107)), the boundary conditions at the right extremity of Waveguide 1 and those at the left extremity of Waveguide 2 can be obtained, as shown in equation (3.16). $\mathbb{D}^*$ denotes the dynamic stiffness matrix of the coupling element condensed on the DOF located on the interfaces between the waveguides and the coupling element itself.

$$\mathbb{D}^* \begin{bmatrix} \mathbf{q}_{\mathtt{R1}}^{(\mathtt{N+1})} \\ \mathbf{q}_{\mathtt{L2}}^{(1)} \end{bmatrix} = - \begin{bmatrix} \mathbf{F}_{\mathtt{R1}}^{(\mathtt{N+1})} \\ \mathbf{F}_{\mathtt{L2}}^{(1)} \end{bmatrix} \tag{3.16}$$

Combined with the boundary conditions in equation (3.14a) and equation (3.14b) and the propagation relation(see equation (2.33)), an equation system which gives the wave amplitudes $\mathbf{Q}$ in both waveguides under the excitation displacement $\mathbf{q}_{\mathtt{exc}}$ can be developed as follows:

$$\begin{bmatrix} \mathbf{\Phi}_{\mathtt{q1}}^{\mathtt{inc}} & \mathbf{\Phi}_{\mathtt{q1}}^{\mathtt{ref}} & \mathbf{0} & \mathbf{0} \\ (\mathbb{D}_{11}^* \mathbf{\Phi}_{\mathtt{q1}}^{\mathtt{inc}} + \mathbf{\Phi}_{\mathtt{F1}}^{\mathtt{inc}})\mathbf{\Lambda}^N & (\mathbb{D}_{11}^* \mathbf{\Phi}_{\mathtt{q1}}^{\mathtt{ref}} + \mathbf{\Phi}_{\mathtt{F1}}^{\mathtt{ref}})\mathbf{\Lambda}^{-N} & \mathbb{D}_{12}^* \mathbf{\Phi}_{\mathtt{q2}}^{\mathtt{inc}} & \mathbb{D}_{12}^* \mathbf{\Phi}_{\mathtt{q2}}^{\mathtt{ref}} \\ \mathbb{D}_{21}^* \mathbf{\Phi}_{\mathtt{q1}}^{\mathtt{inc}} \mathbf{\Lambda}^N & \mathbb{D}_{21}^* \mathbf{\Phi}_{\mathtt{q1}}^{\mathtt{ref}} \mathbf{\Lambda}^{-N} & \mathbb{D}_{22}^* \mathbf{\Phi}_{\mathtt{q2}}^{\mathtt{inc}} + \mathbf{\Phi}_{\mathtt{F2}}^{\mathtt{inc}} & \mathbb{D}_{22}^* \mathbf{\Phi}_{\mathtt{q2}}^{\mathtt{ref}} + \mathbf{\Phi}_{\mathtt{F2}}^{\mathtt{ref}} \\ \mathbf{0} & \mathbf{0} & \mathbf{\Phi}_{\mathtt{F2}}^{\mathtt{inc}} \mathbf{\Lambda}^{-N} & \mathbf{\Phi}_{\mathtt{F2}}^{\mathtt{ref}} \mathbf{\Lambda}^N \end{bmatrix} \begin{bmatrix} \mathbf{Q}_1^{\mathtt{inc(1)}} \\ \mathbf{Q}_1^{\mathtt{ref(1)}} \\ \mathbf{Q}_2^{\mathtt{inc(1)}} \\ \mathbf{Q}_2^{\mathtt{ref(1)}} \end{bmatrix} = \begin{bmatrix} \mathbf{q}_{\mathtt{exc}} \\ \mathbf{0} \\ \mathbf{0} \\ \mathbf{0} \end{bmatrix} \tag{3.17}$$

The resolution of this equation system provides the wave amplitudes at the left boundary of the waveguides 1 and 2, and via equation (2.33), wave amplitudes at any node in the two waveguides can be obtained. As shown in Figure 3.28, the Z-axis component of the nodal displacement $\mathbf{q}_{\mathtt{out}}$ at the free extremity of the beam is used for the calculation of the frequency response function(FRF) of the thin-walled beam. As an example, the length of the waveguides is chosen to be 0.6 m, and the length of the unit cell in X-axis is 3 mm, thus $N = 200$. The pair of piezoelectric patches share the same shunt circuit with $R = 10\ \Omega$ and $L = 0.016\ H$, in order to tune the wave modes around 9 kHz. The symmetric pumping mode is targeted, and its modal displacement at a fixed frequency(about 7 kHz) is taken as the imposed displacement excitation $\mathbf{q}_{\mathtt{exc}}$. The FRF with shunt circuit and open circuit case are calculated numerically. Results for the beam in Case A are displayed in Figure 3.29. As shown in Figure 3.29, the attenuation effect of the shunted piezoelectric patches around the tuning frequency (9 kHz), which is close to one of the eigenfrequencies of one of the symmetric pumping mode, is rather evident. In the same manner, another analysis is carried out for the thin-walled beam in case B(see Figure 3.23(b)). The comparison results of the FRF are shown in Figure 3.30. In both Figure3.29(a) and 3.30(a), it is clear that the pumping mode cuts on at about 5.6 kHz as the amplitude of the response becomes much larger from this frequency. These results reveal that FWFE can predict correctly the frequency response of the structure, and the

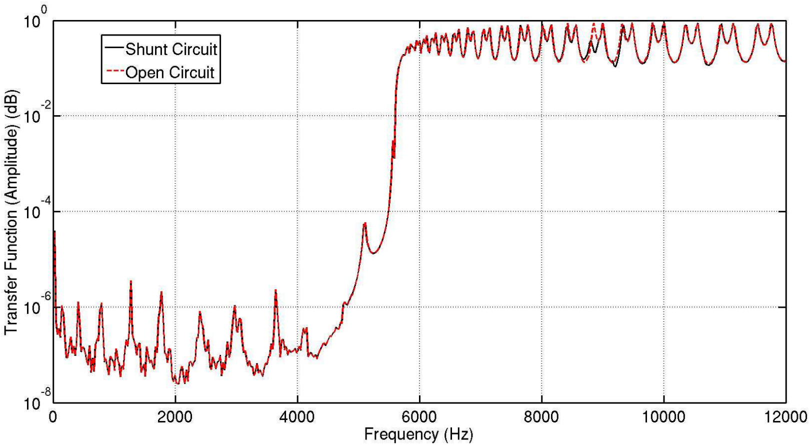

(a)

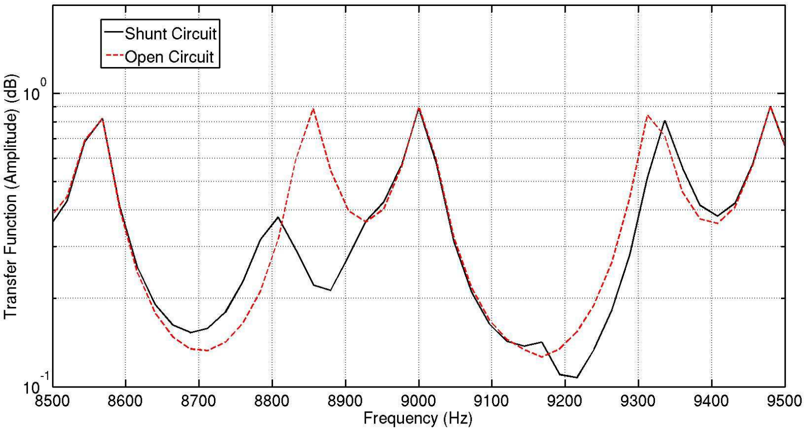

(b)

Figure 3.29: Comparison of the frequency responses in case A: (a)Frequency band from 6 to 12 kHz (b)Zoom around the tuning frequency (9 kHz). (Solid line)FWFE with shunted circuit. (Dashed line)FWFE without shunt circuit.

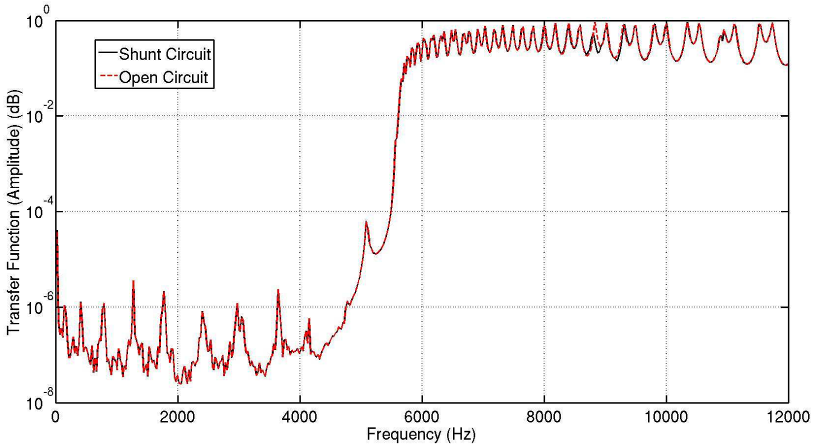

(a)

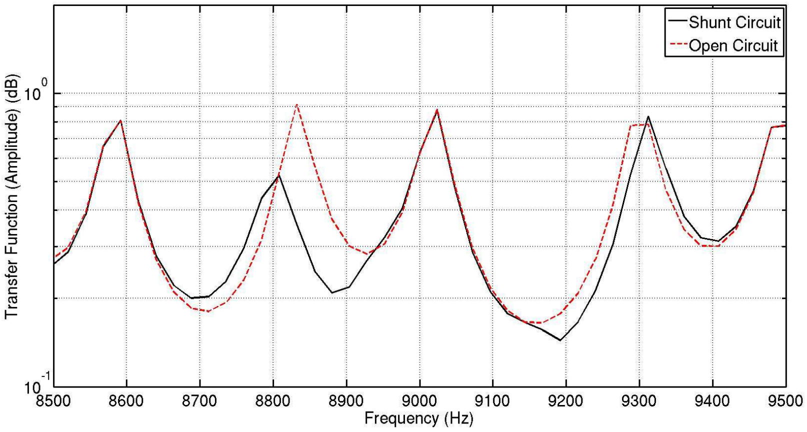

(b)

Figure 3.30: Comparison of the frequency responses in case B: (a)Frequency band from 6 to 12 kHz (b)Zoom around the tuning frequency (9 kHz). (Solid line)FWFE with shunted circuit. (Dashed line)FWFE without shunt circuit.

efficiency of the FWFE formulation has already been tested and compared to classical FE method [51] or transfer matrix method [69]. It is an effective approach that can be employed to estimate the influence of the shunted piezoelectric patches on the symmetric pumping mode of the beam. It can also be concluded from Figure 3.29(b) and Figure 3.30(b) that the longitudinally bonded piezoelectric patches in Case A lead to a stronger attenuation effect than the transversally bonded patches in Case B.

It should also be noted that the FWFE formulation requires much less computational time compared to ANSYS, especially at high frequencies, where very small element size is required to guarentee the computational precision with classical finite element method. Furthermore, ANSYS is not capable of analyzing shunt circuits with negative capacitance, but the FWFE method is able to deal with all kinds of shunt impedance.

3.2.3 Time response calculation and reflection coefficient verification

In Subsection 3.2.2, the frequency responses are calculated with an excitation displacement of constant amplitude in the frequency domain. In order to evaluate the time response, the approach mentioned in Chapter 2 Subsection 2.1.4 is adopted. The reflection coefficients can be extracted from the time response and then be compared to those calculated with the DMM approach. This extraction technique can equally be applied in experiments to validate numerical results. Let's consider an aluminium beam with 4 identical longitudinally placed $R-L$ shunted piezoelectric patches in Case A. According to the dispersion curves shown in Figure 3.24, it can be noted that in the frequency band from 0 to 12 kHz, except the extensional mode in X-axis, the other modes are dispersive as their dispersion curves are not linear. As non-dispersive waves can maintain their wave form during the propagation, and their group velocity is almost constant, it will be much easier to track them in the structure. The group velocity of the extensional wave mode is shown in Figure 3.31. It is almost constant in the frequency band from 0 to 10 kHz. Based on this group velocity, the length of the waveguides is chosen to be 2.4 meters which is large enough so that incident and reflected waves can be clearly distinguished. The same mesh resolution as that in the forced response calculation in Subsection 3.2.2 is utilized. The structure is excited by uniformly distributed force in X-axis at one extremity. To minimize the effect of induced dispersion by the piezoelectric patches, narrow band signals are used, composed of 2.5 cycles modulated by a Hanning window with the central frequency f_0 equal to 7 kHz. The time wave form and the spectrum of this excitation force is displayed in Figure 3.32. The maximum amplitude is

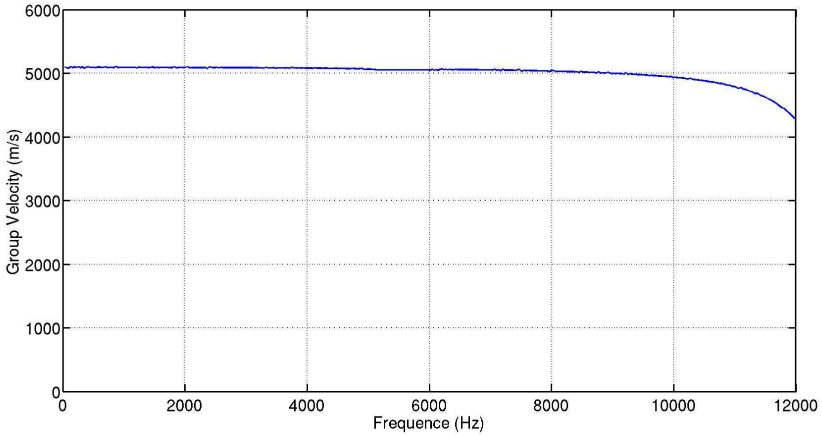

Figure 3.31: Group Velocity of the X-axis extensional wave.

0.1 N and the sampling frequency is 20 times greater than the central frequency in order to guarantee the signal quality of the wave packet. This excitation force is amplified (by multiplying a constant gain G to the amplitude) and then applied to one extremity of the thin-walled beam as the input, and the X-axis component of the nodal displacement at the measure point is taken as the output, as shown in Figure 3.33. The measure point lies at 30 cm from the extremity with the imposed force. Subsequently, the transfer function is calculated, as shown in Figure 3.34. The shunt circuit is tuned to about 9 kHz, with $R = 100\ \Omega$ and $L = 0.016\ H$, as one of the eigenfrequencies of this mode is close to 9 kHz. With the shunted piezoelectric patches, a damping effect is obtained for the X-axis extensional mode around the tuning frequency. With this transfer function, the wave packet excitation is applied to the system in order to acquire the frequency response. Then the IDFT of this frequency response is carried out to calculate the time response of the structure, as displayed in Figure 3.35. As those wave packets are apparently unconnected in this case, no wave packet decomposition techniques are needed. In order to verify the reflection coefficients calculated via the DMM approach and provide an effective experimental evaluation technique for the reflection coefficient based on time response of the structure, the following extraction procedure is proposed:

1. The Hilbert Transform is applied to the time response of the structure, and its absolute value is representative of the envelope of the signal. The first peak represents the maximum amplitude of the incident wave, and the second peak for the reflected wave, as shown in Figure 3.36.

2. The imaginary part of the wavenumber k calculated with the WFE

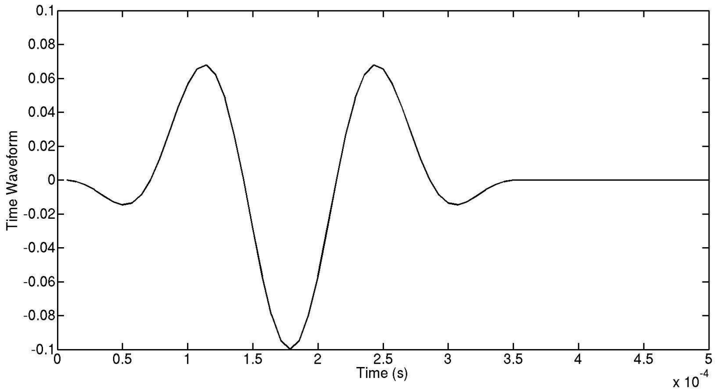

(a)

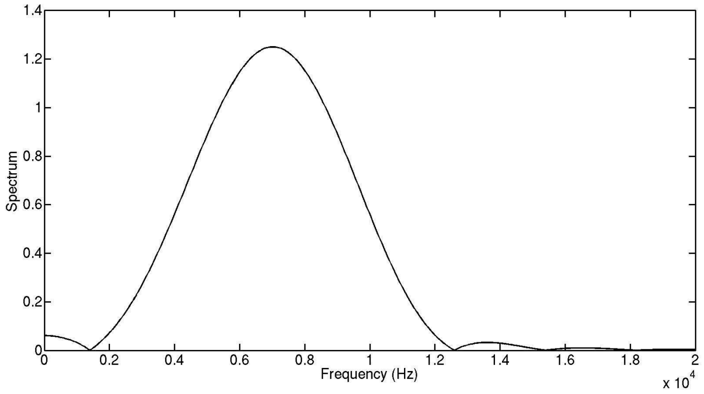

(b)

Figure 3.32: The time wave form and the spectrum of the wave packet excitation. Central frequency $f_0 = 7\ kHz$. (a)Time wave form. (b)Spectrum.

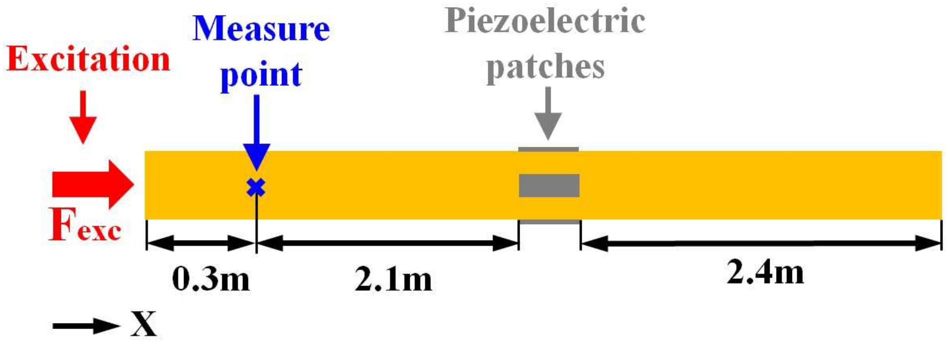

Figure 3.33: Configuration for the time response simulation of the X-axis extensional wave.

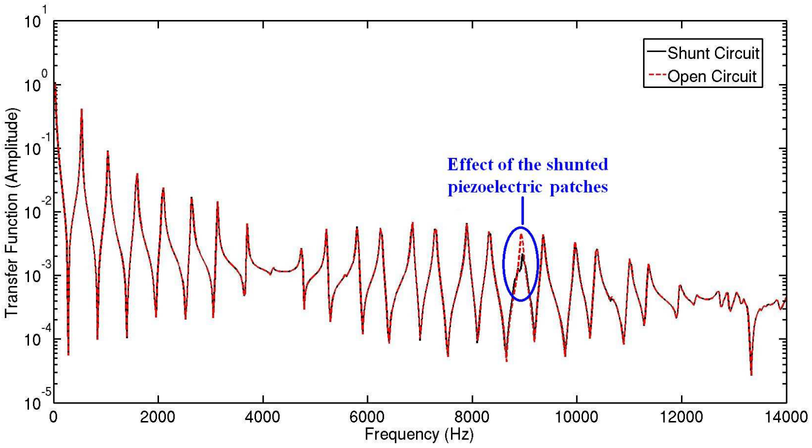

Figure 3.34: The forced response of the structure under white noise excitation (transfer function) tuned at 9 kHz. (Solid line)Piezoelectric patches with shunted circuit. (Dashed line)Shunt circuit open.

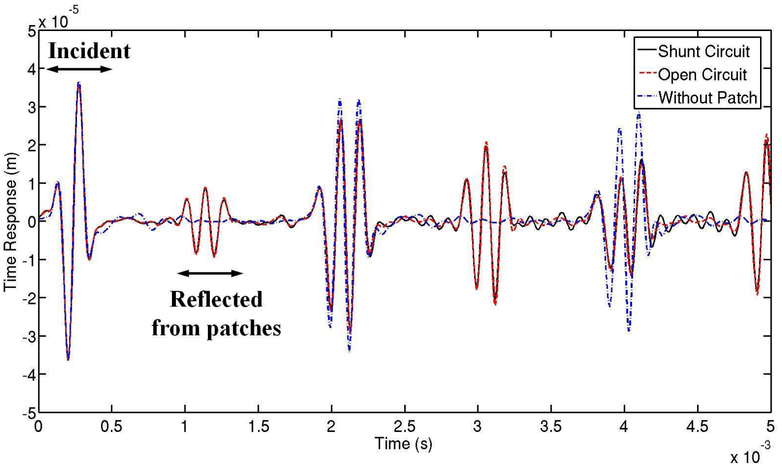

Figure 3.35: Time response of the structure under wave packet excitation. (Solid line)Piezoelectric patch with shunt circuit. (Dashed line)Piezoelectric patches with open shunt circuit. (Dash-dotted line)Beam without piezoelectric patches.

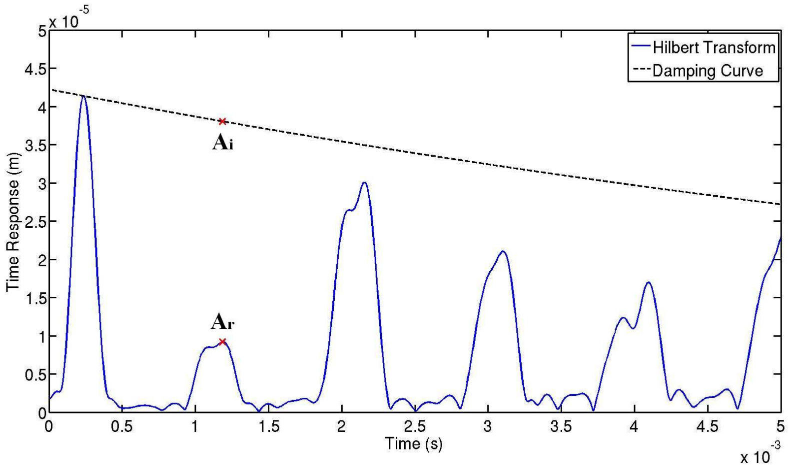

Figure 3.36: Hilbert Transform of the time response and the damping curve to extract the reflection coefficient of the X-axis extensional wave. (Solid line)Absolute value of the Hilbert Transform of the time response. (Dashed line)Damping curve based on spatial damping calculation.

method is used to calculate the spatial damping. As the propagation of the mode can be characterized by an exponential law $A = A_0 e^{ikx}$, the spatial damping ratio $\gamma_x = - \mid Im(k) \mid$.

3. With the group velocity V_g of the wave mode, the damping ratio in time domain can be calculated as $\gamma_t = - \mid Im(k)V_g \mid$.

4. On the plot of the Hilbert Transform result, a damping curve can be drawn to take into account the damping effect caused by the distance between the measure point and the piezoelectric patches so as to evaluate the reflection coefficient correctly. This curve passes the first peak of the Hilbert Transform result and follows the exponential decreasing law defined by $A = A_0 e^{\gamma_t t}$. $\mathbf{A_r}$ denotes the amplitude of the reflected wave, and $\mathbf{A_i}$ represents the amplitude of the incident wave with the attenuation effect taken into account, as shown in Figure 3.36. The reflection coefficient can be calculated as $\mathbf{R} = \mathbf{A_r}/\mathbf{A_i}$.

5. By varying the central frequency f_0 of the wave packet excitation, reflection coefficients at different frequencies can be acquired frequency by frequency in order to verify the reflection coefficients calculated with the DMM approach.

The reflection coefficients of the extensional wave mode tuned at 9 kHz are calculated via the DMM approach, and then compared to those obtained through the extraction procedure. It should be mentioned that this extraction

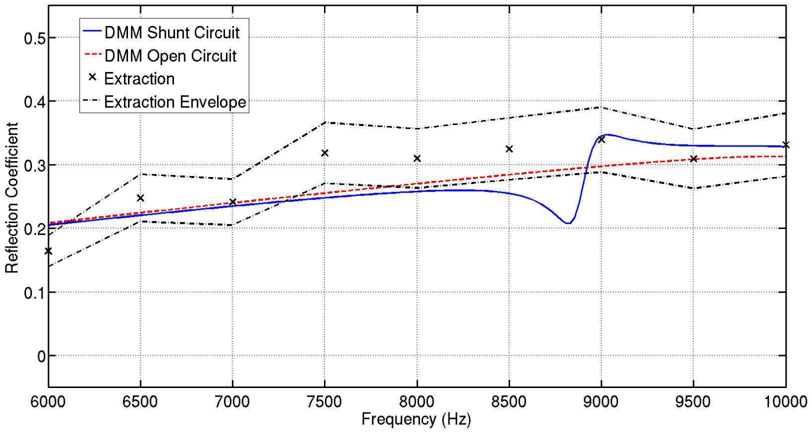

Figure 3.37: Comparison of reflection coefficients of the extensional wave in X-axis calculated through the DMM approach and the extraction procedure. (Solid line)Calculation with DMM, piezoelectric patch with shunt circuit. (Dashed line)Calculation with DMM, piezoelectric patch without shunt circuit. (× markers)Calculation with extraction procedure. (Dash-dotted lines)Envelope of the extracted reflection coefficients.

procedure is a rather coarse evaluation tool for the reflection coefficients. If an error of $\pm 15\%$ is applied to each extracted reflection coefficient, then the envelope of the extracted reflection coefficients can be obtained. The results are shown in Figure 3.37. For the frequency band below 6 kHz, it is difficult to evaluate correctly the reflection coefficient with the extraction procedure as the span of the wave packet in time domain becomes too large to distinguish incident and reflected waves, unless the length of the beam becomes larger. And for the frequency band around the tuning frequency, it is also difficult to evaluate precisely the reflection coefficient with the Hilbert Transform, as the added damping effect needs to be considered properly. On the whole, the results issued from the DMM approach are verified by those through the extraction procedure, as the envelope covers most of the DMM results in the open circuit case. This procedure will be employed for the experimental validation of numerically calculated reflection coefficients.

3.3 Concluding remarks

Effective prediction tools for wave propagation characteristics and dynamic behavior of smart structures equipped with $R - L$ shunted piezoelectric elements are provided in this work, and general formulations which can be applied for all kinds of slender homogeneous smart structures(solid, hollow) are developed. The main results can be summarized as follows:

- The finite element based WFE approach is developed and its corresponding DMM is extended to consider shunted piezoelectric elements in beam structures. The wave modes propagating in the structure are correctly captured and the influence of the shunted piezoelectric patches on the control of the Z-axis flexural wave mode is investigated through the reflection and transmission coefficients of this wave mode.

- An analytical model based on Euler-Bernoulli beam theory, the homogenization of sandwich beams and Hagood's shunted piezoelectric patch model is developed to verify numerically calculated reflection and transmission coefficients of the Z-axis flexural mode.

- The forced responses of the beam structure excited in the Z-axis flexural mode and the X-axis tension/compression mode are calculated via the FWFE formulation, and the results for the Z-axis flexural mode correspond very well with those issued from a classical FE harmonic analysis.

- Time response of the structure excited in the X-axis tension/compression mode with wave packet is evaluated via an IDFT approach applied to the frequency response. By following an extraction procedure, reflection coefficients of this wave mode can be evaluated according to the time response of the structure so as to verify the reflection coefficients calculated through the DMM approach.

The numerical techniques presented in this work enable the evaluation of the performance of shunted piezoelectric patches on the control of wave propagation, and facilitate design modifications and systematic investigations of geometric and electric parameters of beam structures with shunted piezoelectric patches.

Chapter 4

Multi-modal wave propagation and diffusion in smart composite structures with $R-L$ shunted piezoelectric patches

---

Contents

In this Chapter, wave propagation and diffusion in **heterogeneous** waveguides (multi-layered) will be investigated, through the Modified Wave Finite Element method in Subsection 2.2. Firstly the WFE method is applied for the analysis of wave propagation in the multi-layered composite beam. Then the MWFE formulation is applied to the same structure and results like dispersion curves issued from these two different approaches are compared. The DMM with shunted piezoelectric elements is subsequently employed to calculate the reflection and transmission coefficients of the Z-axis bending wave in the multi-layered beam. The influence of the shunted piezoelectric patches on the propagation of this wave mode is carefully investigated with DMM. The finite element model of the multi-layered beam with symmetric $R-L$ shunted piezoelectric patches is shown in Figure 4.1.

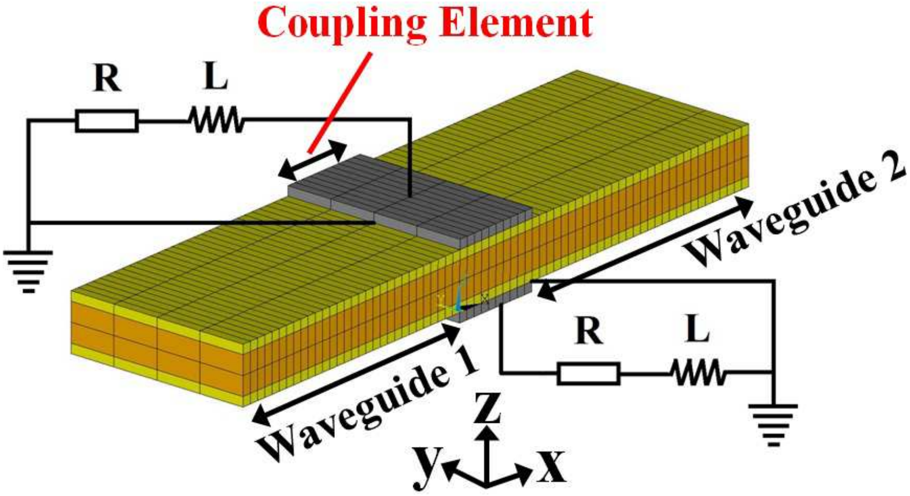

Figure 4.1: Finite element model of a multi-layered beam with symmetric $R-L$ shunted piezoelectric patches.

4.1 Dispersion analysis with WFE and MWFE

The structure to be studied here is a 3-layered beam with 2 identical $R-L$ shunted piezoelectric patches. The finite element model of the waveguide is shown in Figure 4.2, with the definition of geometric parameters. Numerical values of the parameters are listed in Table 4.1.

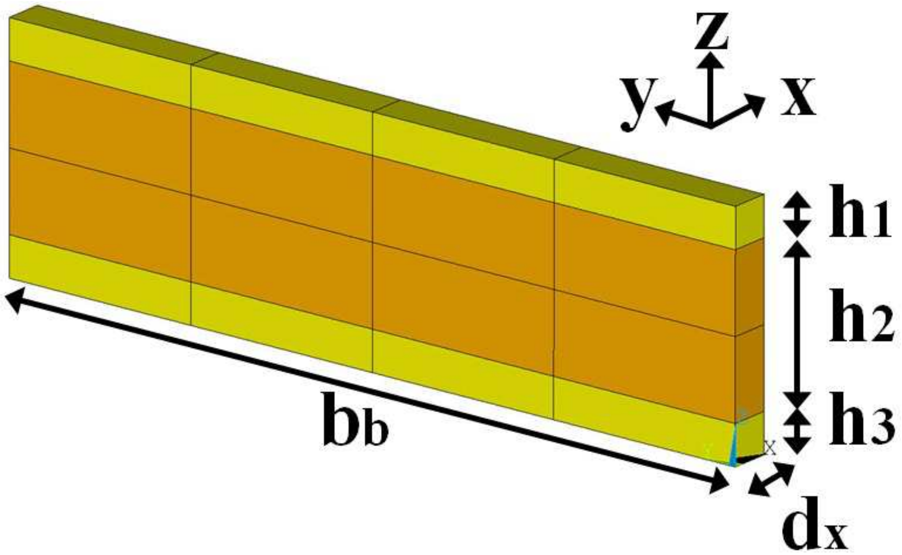

Figure 4.2: Finite element model of the unit cell representative of the multi-layered beam as a waveguide.

Table 4.1: Numeric values of the geometric parameters in the waveguide shown in Figures 4.2 and 4.8. The units of all the parameters are in meter (m).

d_x	b_b	h_1	h_2	h_3	L_b	h_p
0.001	0.02	0.001	0.004	0.001	0.01	0.001

The material of the outer layers of the multi-layered beam is steel and considered as isotropic, with Young's modulus $E_b = 210\ GPa$ and Poisson's ratio $\nu_b = 0.33$, and density $\rho_b = 7850\ kg/m^3$. The core of the multi-layered beam is much softer and lighter than the skin layers, with Young's modulus $E_b = 2\ MPa$ and Poisson's ratio $\nu_b = 0.3$, and density $\rho_b = 1000\ kg/m^3$. A loss factor $\eta = 0.001$ is added to the finite element model as the system is considered to be dissipative.

Both the WFE and MWFE approaches are applied to the same structure. The analysis is carried out on the frequency band from 0 to 3 kHz so that several cross-section modes can appear. First of all, the dispersion curves of the uncoupled layers are calculated via the WFE approach. The results are shown in Figure 4.3.

Later the second MWFE modeling is applied and full wave mode bases of all the 3 uncoupled layers are used. The dimension of the MWFE problem is $\sum_i m^i = 105$, which is considerably larger than the dimension of the WFE problem($n = 75$), due to the substructuring technique. By looking at the dispersion curves provided by the second MWFE modeling in Figure 4.4, it is clear that the two methods give nearly identical results. This validates the underlying substructuring technique of the MWFE formulation.

Unlike the WFE formulation, the MWFE formulation is able to capture the essential global wave modes of the multi-layered system. For each layer, the chosen local wave modes are expected to significantly contribute to the dynamics of the system. Specifically, for the outer layers in steel, these local wave modes represent rigid cross-section wave motions, while for the soft middle layer, these local wave modes represent not only rigid cross-section wave motions but also a set of contributing cross-section modes. The first MWFE modeling is used to construct the global wave modes, from the set of reduced wave mode bases attached to the uncoupled layers, with $m^1 = m^3 = 4$ and $m^2 = 30$. Now the dimension of the MWFE problem is $\sum_i m^i = 38$, which appears much smaller than the dimension of the WFE problem($n = 75$). The dispersion curves associated with the global wave modes are displayed in Figure 4.5.

It can be noticed from Figure 4.5 that for the 4 rigid cross-section modes (Modes 1 to 4) and the shearing mode (Mode 5), MWFE and WFE give sim-

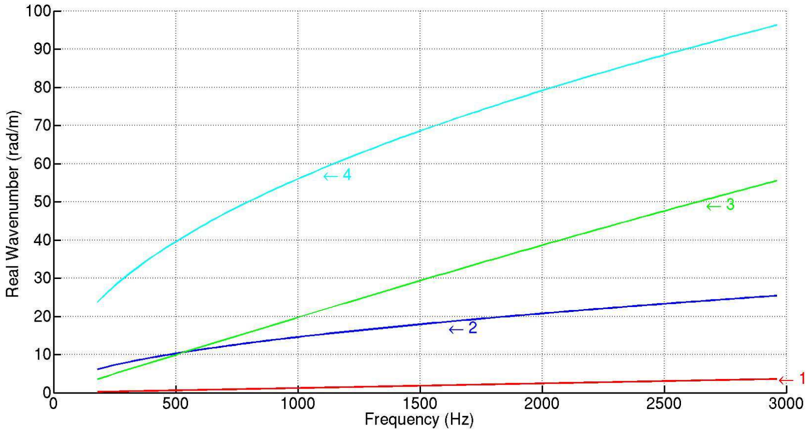

(a) Layers 1 and 3

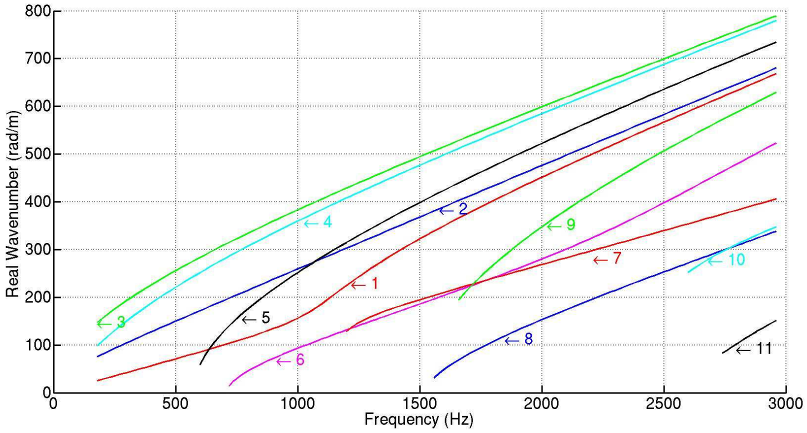

(b) Layer 2

Figure 4.3: Dispersion curves of wave modes propagating in(a)Layers 1 and 3 (b)Layer 2, in the frequency band from 0 to 3 kHz, using the WFE approach.

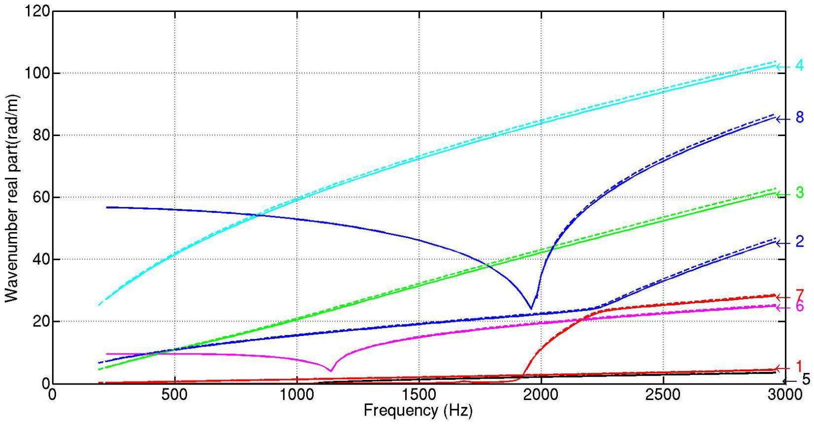

Figure 4.4: Dispersion curves for the global waveguide obtained using the second MWFE modeling, based on the full wave mode basis of each uncoupled layer. (solid lines)MWFE results (dashed lines)WFE results.

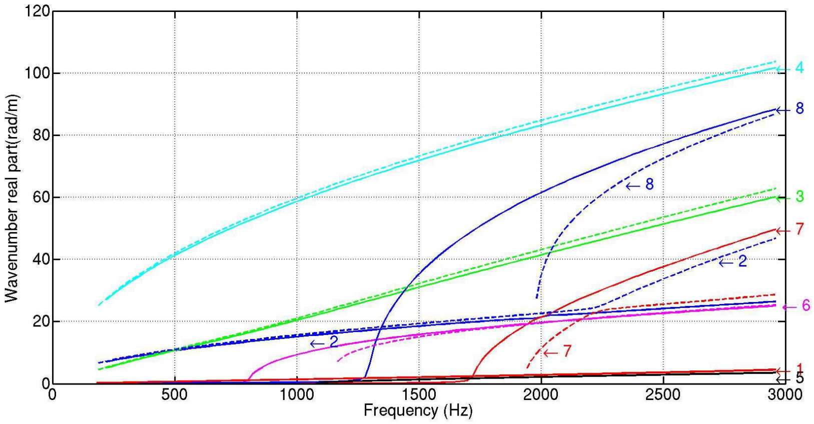

Figure 4.5: Dispersion curves for the global waveguide obtained using the first MWFE modeling, based on the reduced wave mode basis of each uncoupled layer. (solid lines)MWFE results (dashed lines)WFE results.

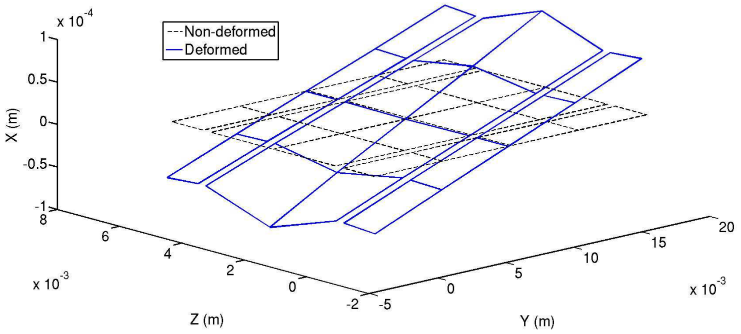

(a) Mode 2

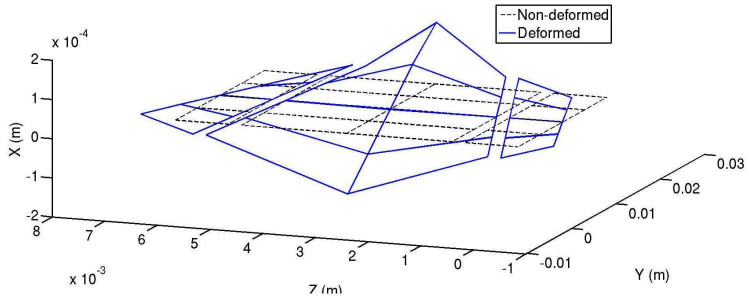

(b) Mode 7

Figure 4.6: Deformed modal shapes of (a)the Y-axis bending wave mode (Mode 2) and (b)the 2nd X-axis torsional wave (Mode 7), at the frequency $f_0 = 2000\ Hz$. (solid line)Deformed mode shape (dashed line)undeformed cross-section.

ilar results; however, for the other 3 cross-section modes (Modes 6 to 8), with the MWFE method, their cutting-on frequencies are generally smaller than those obtained with the WFE method.

It should also be noticed that for Mode 2 and Mode 7, their dependency at about 2.2 kHz with the WFE method can be removed through the local wave mode basis truncation of the first MWFE formulation. When the sizes of the mode bases overestimate the dynamics of each layer, the mode dependency will occur. In this case, the wave mode classification criterion is not capable of distinguishing theses two wave modes around this frequency, as their deformed shapes are similar to each other, as shown in Figures 4.6 and 4.7.

It should be mentioned that the deformed shapes are obtained using the second MWFE modeling. The continuity of displacement components at the coupling interfaces is well respected.

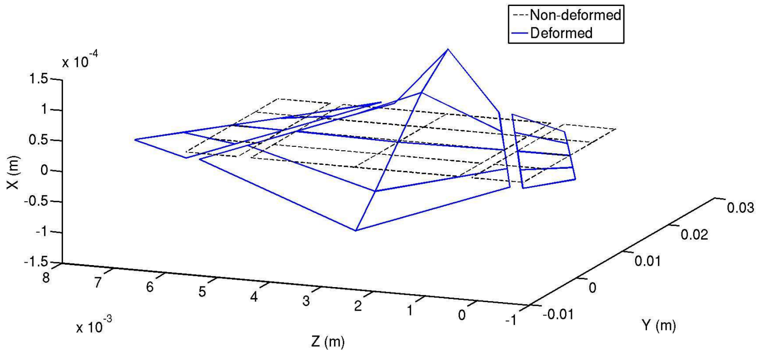

(a) Mode 2

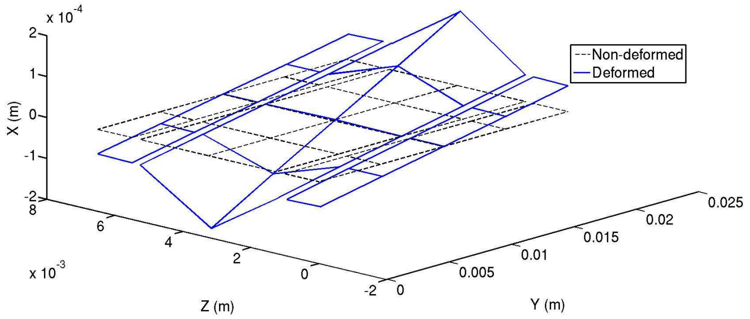

(b) Mode 7

Figure 4.7: Deformed modal shapes of (a)the Y-axis bending wave mode (Mode 2) and (b)the 2nd X-axis torsional wave (Mode 7), at the frequency $f_0 = 2780\ Hz$. (solid line)Deformed mode shape (dashed line)undeformed cross-section.

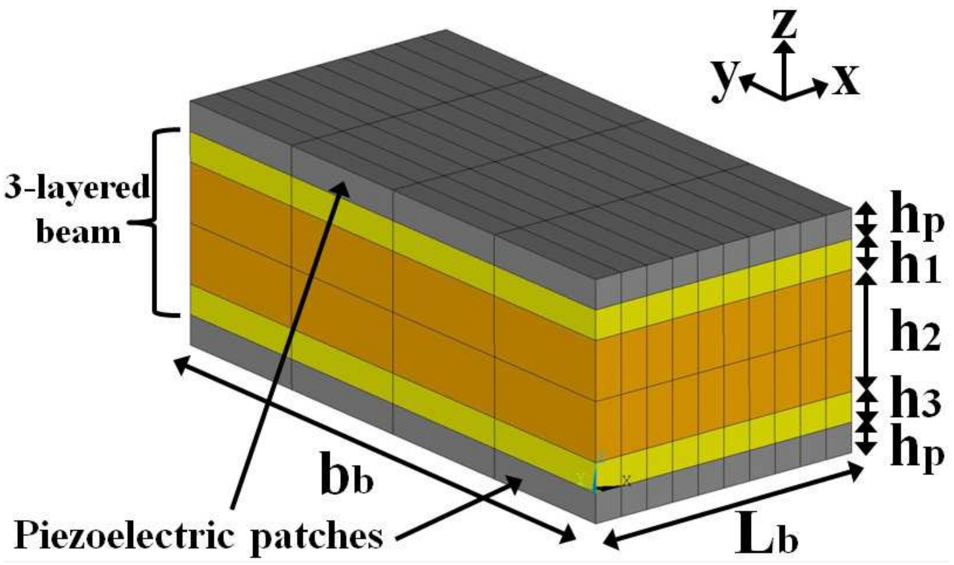

Figure 4.8: Finite element model of the coupling element in the three-layered system with 2 shunted piezoelectric patches.

The physical wave behavior of the three-layered system is correctly captured with the reduced mode basis, and the gain of computational time is rather evident, which represents another advantage of the MWFE modeling.

4.1.1 Energy diffusion analysis with DMM for the Z-axis bending mode

In this section, the energy diffusion problem is dealt with via the DMM proposed in Subsection 2.1.2 of Chapter 2.

The three-layered beam is equipped with two identical $R-L$ shunted piezoelectric patches. These piezoelectric patches are fabricated by Saint-Gobain Quartz (type SG P189) and the corresponding material characteristics are listed in Appendix A. This type of piezoelectric patch works mainly in the 3-1 mode. The finite element model of the coupling element and the definition of geometric parameters are displayed in Figure 4.8. Numerical values of the parameters are listed in Table 4.1.

As in this work, the mostly concerned mode is the Z-axis bending wave mode (Mode 4), and with the MWFE modeling, this mode can already be successfully captured, the dimension of the MWFE problem stays the same for the moment($m^1 = m^3 = 4$ and $m^2 = 30$). The deformed modal shapes of the Z-axis bending mode issued from the WFE and MWFE methods are displayed in Figure 4.9(a) and Figure 4.9(b) respectively.

The reflection and transmission coefficients of the Z-axis bending wave mode

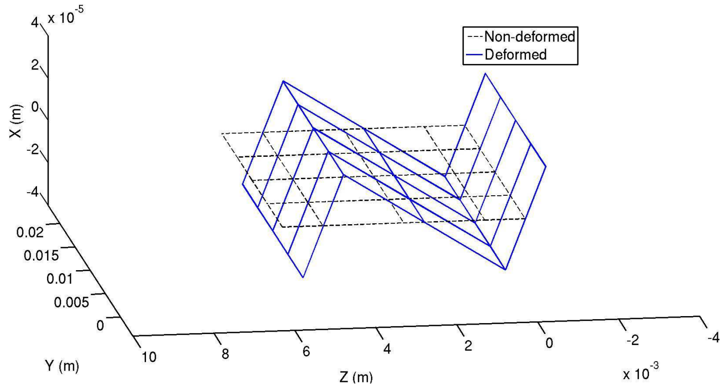

(a) WFE

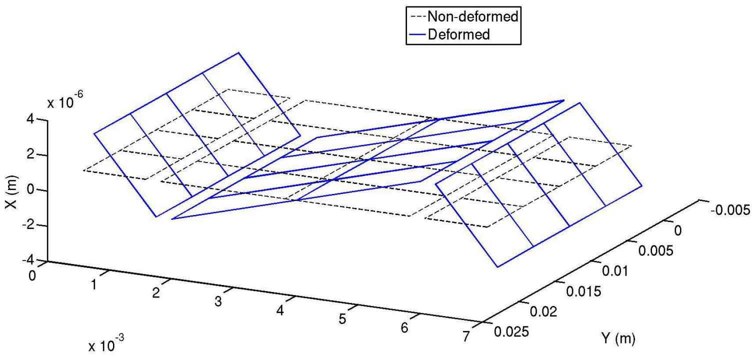

(b) MWFE

Figure 4.9: Deformed modal shapes of the Z-axis bending wave mode (Mode 4) issued from (a)WFE formulation (b)first MWFE formulation, at the frequency $f_0 = 380\ Hz$. (solid line)Deformed mode shape (dashed line)undeformed cross-section.

can be calculated with the DMM of the two different formulations(WFE and MWFE). In the shunt circuit, a resistance $R = 10\ \Omega$ and an inductance of $L = 3\ H$ are used, to obtain a tuning frequency at about $2.2\ kHz$. The tuning frequency can be calculated according to Equation (4.1):

$$f_{tune} = \frac{1}{2\pi\sqrt{LC_{p3}^S}} \tag{4.1}$$

where C_{p3}^S is the capacitance of the piezoelectric patch measured at constant strain. The subscript 1 represents the X-axis direction while the subscript 3 denotes the Z-axis direction. It can be calculated in the following manner:

$$C_{p3}^S = \frac{\varepsilon^S \times A_3}{L_3} \tag{4.2}$$

where $A_3 = b_b \times L_b$ is the area of the surface of the piezoelectric patch perpendicular to Z-axis, $L_3 = h_p$ is the thickness of the piezoelectric patch in Z-axis direction.

For the two different formulations WFE and MWFE, the corresponding DMM are obtained in slightly different ways: with the WFE formulation, the coupling element in the DMM is treated in a traditional manner, with all the structural and electric DOF condensed to the DOF at left and right boundaries; however, with the MWFE formulation, the coupling element is treated layer by layer: for the layer with bonded shunted piezoelectric patch, the structural and electric DOF in the piezoelectric patch are condensed, and only the structural DOF of the layer remain; for the layer not connected to the piezoelectric patches, it is modeled in a general manner. Then all the layers are assembled with the MWFE formulation, and the DOF in the set of layers are condensed to the DOF at the left and right boundaries. It should also be mentioned that the diffusion matrix $\mathbb{C}$ depends not only on the dynamics of the coupling element, but also on the wave modes extracted after the calculation of the eigenvalue problem in equation (2.63) in Chapter 2 associated to the waveguides. In fact, the dimension of $\mathbb{C}$ depends directly on the number of wave modes retained n_c after the calculation of the eigenvalue problem (2.63) in Chapter 2 ($n_c < 2\sum_i m^i$), which can be chosen according to the number of propagating wave modes in the waveguides in the frequency band of interest for example. In the WFE and MWFE approaches, the dimension of the diffusion matrix $\mathbb{C}$ is chosen to be the same($n_c \times n_c$).

Firstly, the first MWFE formulation is applied, with $m^1 = m^3 = 4$ and $m^2 = 30$, and results are compared to those issued from the WFE method, as shown in Figure 4.10.

It can be noted that generally, the reflection coefficients obtained via the

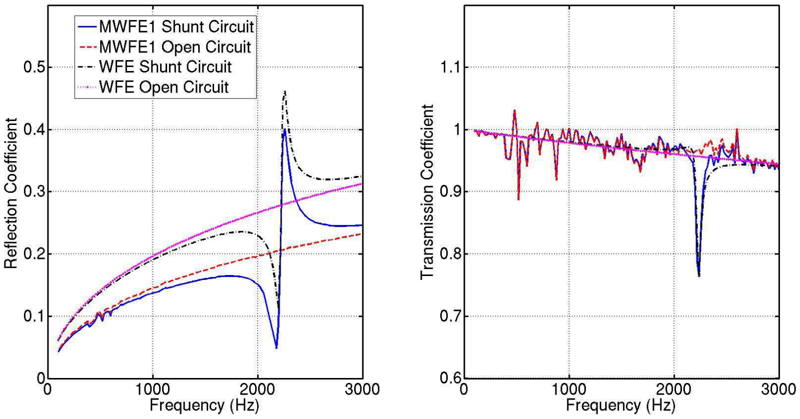

Figure 4.10: Reflection and transmission coefficients of the Z-axis bending wave mode using the first MWFE formulation and WFE method.

WFE approach are bigger than those issued from the MWFE approach. This fact might be due to the continuity conditions imposed by the two approaches: WFE method used classical finite element model of the coupling element, the layers are bonded together, while the MWFE method used Boolean operators to consider the continuity conditions between the layers, then the coupling element in the WFE approach seems to be more rigid than that in the MWFE approach.

Subsequently, the first MWFE formulation (with $m^1 = m^3 = 4$ and $m^2 = 30$) is used and reflection and transmission coefficients are compared to those issued from the second MWFE formulation (with $m^1 = m^3 = 30$ and $m^2 = 45$, full mode bases of the 3 layers), as displayed in Figure 4.11.

It can be seen from Figure 4.11 that with the DMM of the first MWFE formulation, greater reflection coefficients are obtained than that of the second MWFE formulation. This might be explained as follows: as in the first MWFE modeling, there are much less wave modes than in the second MWFE modeling, and the dependency of global wave modes is removed thanks to the truncation of local wave mode bases of each uncoupled layer, the energy of the incident Z-axis bending wave will not be distributed to high order parasite wave modes. Both in Figure 4.10 and 4.11 there are some fluctuations in the transmission coefficients obtained via the first MWFE modeling. This might result from numerical error during the computation. Globally, the first and second MWFE modelings give similar results, especially for the frequency band around the tuning frequency $f = 2.2\ kHz$.

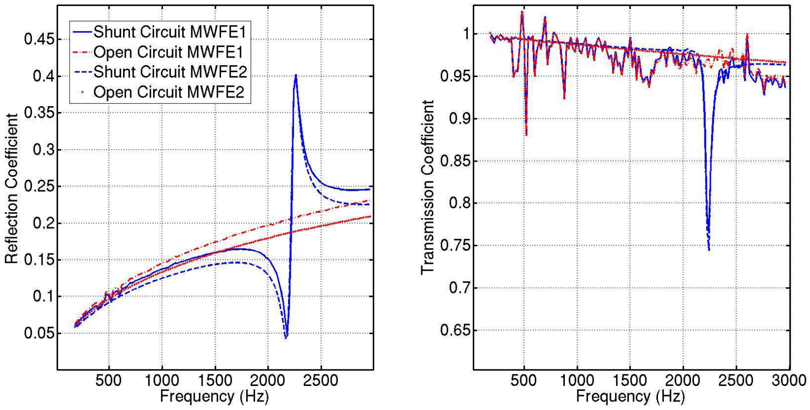

Figure 4.11: Reflection and transmission coefficients of the Z-axis bending wave mode using the first MWFE formulation and second MWFE method.

4.2 Parametric studies

In Subsection 4.1, it has been observed that with the second MWFE formulation, when full modal bases are applied for the layers, it gives nearly the same dispersion curves as the WFE formulation. However, when the first MWFE formulation is applied, as truncated modal bases of the layers are applied, this method gives different results from the WFE formulation. For the cross-section modes (Modes 6 to 8 in Figure 4.5), the cut-on frequencies predicted with MWFE formulation and WFE formulation are quite distinct. Additionally, as mentioned in Subsection 4.1.1, with the MWFE formulations, fluctuations in the transmission coefficients can be noted. In order to understand the influence of the parameters applied in the MWFE modeling on the prediction of dispersion curves and diffusion coefficients, and at the same time try to improve the quality of the numerical results, it's interesting to perform several parametric studies.

4.2.1 Parametric studies on dispersion curves

Here the influence of the sizes of the local wave mode bases on dispersion curves will be investigated. In Subsection 4.1, with the first MWFE modeling, the sizes of the modal basis of each layer are $m^1 = m^3 = 4$ and $m^2 = 30$, and the dimension of the MWFE problem is $\sum_i m^i = 38$. If larger modal basis is used for the outer layers 1 and 3, for example, $m^1 = m^3 = 6$ and $m^2 = 30$, the results are closer to WFE results, as displayed in Figure 4.12. The cut-on frequency of Mode 8 calculated with the new wave mode bases using the first

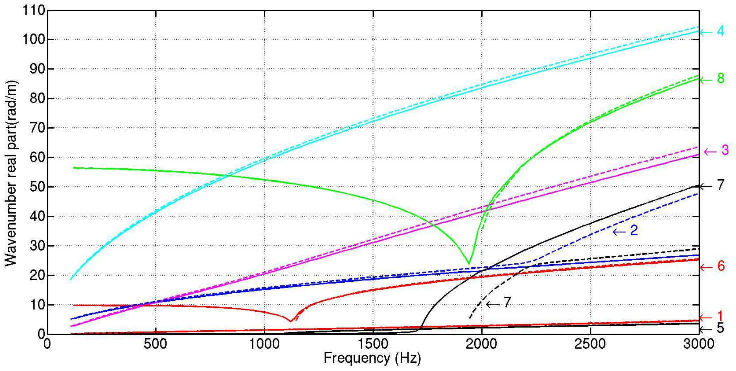

(a) original view

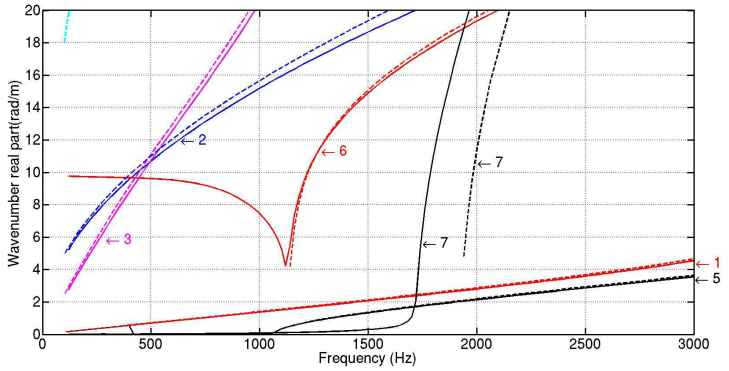

(b) zoom

Figure 4.12: Dispersion curves in the waveguide using the first MWFE formulation with different mode bases and WFE method. (solid lines)first MWFE results (dashed lines)WFE results.

MWFE method is almost the same as that calculated with WFE method. However, for the cut-on frequency of Mode 7, there is always a difference between the two methods. When the sizes of the modal bases are applied in the second MWFE modeling, similar results can be found, except for Mode 2 and Mode 7, as the mode dependency occurs between these two modes, as displayed in Figure 4.13. If even larger wave mode bases are used in the second MWFE formulation, for example, $m^1 = m^3 = 6$ and $m^2 = 45$, MWFE results converge to WFE results. In this case, full mode wave basis is applied for Layer 2 ($m^2 = 45$). The resulted dispersion curves are shown in Figure 4.14. It can be concluded from the previous results that the sizes of the mode basis of Layers 1 and 3 have a direct influence on the Mode 8, while the size of the mode basis of Layer 2 has an effect on the Mode 7. The deformed shape of Mode 8 is given in Figure 4.15. The other cross-section modes (Mode 5

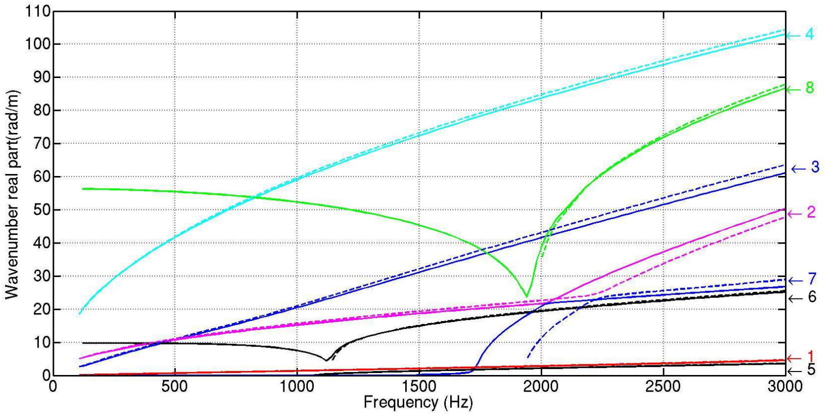

Figure 4.13: Dispersion curves in the waveguide using the second MWFE formulation with different mode bases and WFE method. (solid lines)second MWFE results (dashed lines)WFE results.

and Mode 6) can be correctly captured in all cases with proper mode basis sizes. With the MWFE modeling, dependent wave modes should be avoided in the mode bases of the 3 layers in order to guarantee the convergence of this method, thus the size of the mode basis of each layer should not be too large so as not to overestimate the dynamics of each layer.

4.2.2 Parametric studies on diffusion coefficients

Here, a set of mode bases of different sizes are given in Table 4.2. The effect of the mode basis size on the calculation of the reflection and transmission coefficients of the bending mode in Z-axis (Mode 4) is then investigated in detail.

Firstly, the influence of the dimension of the inner layer (Layer 2) is analyzed. Mode bases 1, 2 and 3 are used, as the dimension of the mode bases in layers 1 and 3 are the same ($m^1 = m^3 = 6$), and the dimension of the layer 2 m^2 varies from 30 to 45. It should be mentioned that m^1 larger than 6 is never used as in the frequency band of interest, the number of propagating modes is 4. Only the 4 propagating modes and 2 evanescent modes (X-axis torsion and Z-axis bending) are retained as the imaginary parts of their wavenumbers are not too far away from 0. The wavenumber of other wave modes are with a large imaginary part and will not be taken into the mode basis. All the wave modes in the mode bases are classified according to the imaginary part of their wavenumber: wavenumber with smaller imaginary part is on the top of the mode basis. The reflection coefficients calculated with the 3 different mode bases using MWFE formulation, as well as those obtained via the WFE

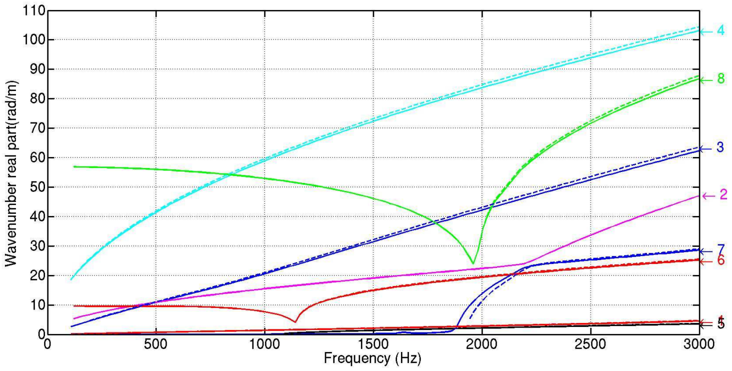

(a) original view

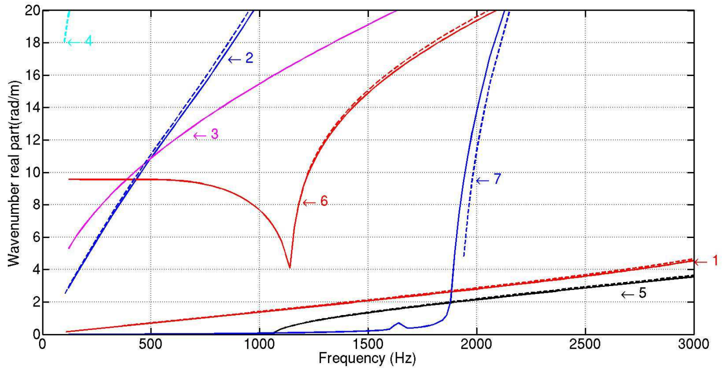

(b) zoom

Figure 4.14: Dispersion curves in the waveguide using the first MWFE formulation with different mode bases and WFE method. (solid lines)first MWFE results (dashed lines)WFE results.

approach, are compared in Figure 4.16.

It can be seen from Figure 4.16 that mode basis $1(m^2 = 40)$ and mode basis $2(m^2 = 30)$ give nearly the same reflection coefficients as those issued from the WFE method, while mode basis $3(m^2 = 45)$ results in much lower reflection coefficients. The fluctuations in the transmission coefficients becomes weaker when m^2 becomes larger. Here, according to this comparison, in order to capture correctly the diffusion characteristic of the Z-axis bending wave, $m^2 = 30$ is likely to be the best mode basis dimension for layer 2 when $m^1 = m^3 = 6$ for the outer layers 1 and 3.

Later the influence of the sizes of the outer layers 1 and 3 is studied. Mode bases 3, 4 and 5 are applied, as the dimension of the mode basis in layer 2 stays the same $m^2 = 45$, and m^1 varies from 4 to 6. The reflection coefficients calculated with the 3 different mode bases using MWFE formulation, as well

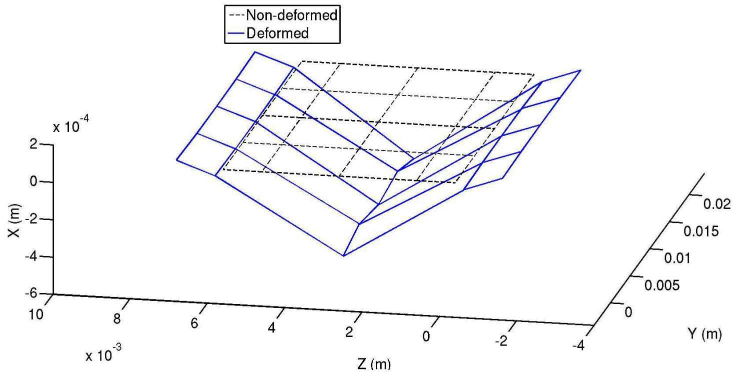

(a) WFE

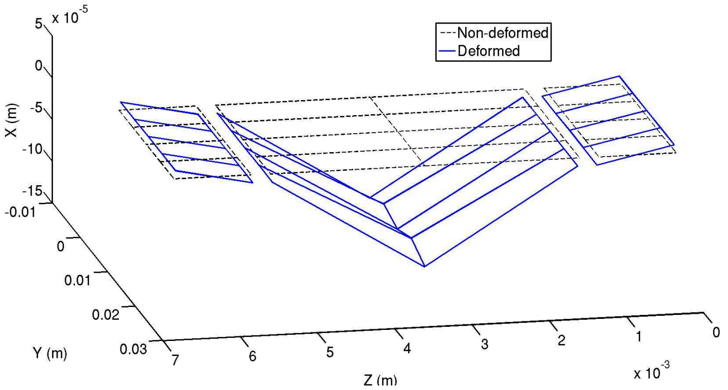

(b) MWFE

Figure 4.15: Deformed modal shapes of Mode 8 issued from (a)WFE formulation (b)second MWFE formulation, at the frequency $f_0 = 2780\ Hz$. (solid line)Deformed mode shape (dashed line)undeformed cross-section.

as those obtained via the WFE approach, are compared in Figure 4.17. It can be seen from Figure 4.17 that with $m^2 = 45$, reflection coefficients obtained via the MWFE approach are generally larger than WFE results, and for the results with mode bases 4 and 5($m^1 = m^3 = 5$ and 4 respectively), the transmission coefficients are not accurate. Here the best mode basis dimension for outer layers 1 and 3 is $m^1 = m^3 = 6$, when $m^2 = 45$. If the mode basis dimension of the inner layer 2 is changed to $m^2 = 30$, the results are displayed in Figure 4.18. With $m^2 = 30$, the reflection coefficients obtained with mode bases 2, 8 and 9 are much closer to WFE results than those acquired with $m^2 = 45$. And with mode basis 2($m^1 = m^3 = 6$), the reflection coefficients are nearly the same as WFE results, and the fluctuation in transmission coefficients is not too strong. It can be noted that in order to correctly capture the global dynamics of the

Table 4.2: Size of mode bases

Mode Basis	m^1	m^2	m^3
1	6	40	6
2	6	30	6
3	6	45	6
4	5	45	5
5	4	45	4
6	5	40	5
7	4	40	4
8	5	30	5
9	4	30	4
10	5	36	5

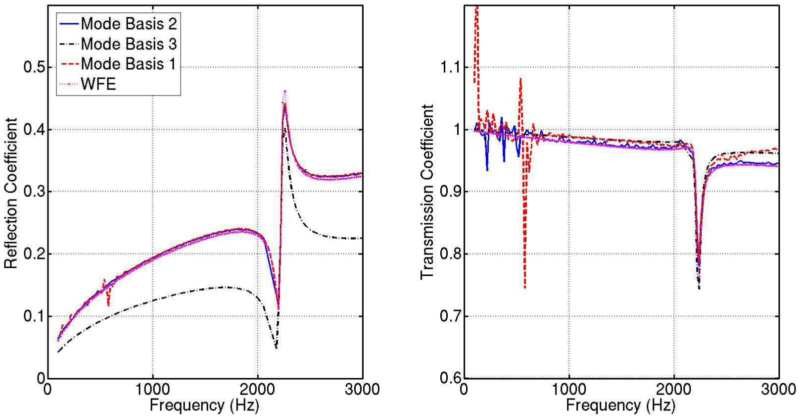

Figure 4.16: Reflection coefficients using the second MWFE formulation with different mode bases (1, 2 and 3) and WFE method. (solid line)Mode basis 2($m^2 = 30$) (dashed line)Mode basis 1($m^2 = 40$) (point-dashed line)Mode basis 3($m^2 = 45$) (point markers)WFE results. $m^1 = m^3 = 6$.

multi-layered system, a "rich" mode basis is not necessarily the best choice. Proper dimensions of local mode bases should be used.

By following the same procedure, if m^2 is fixed to 40, and by varying $m^1 = m^3$ from 4 to 6, it is interesting to see from Figure 4.19 that only with the mode basis 1($m^1 = m^3 = 6$), the transmission coefficients can be acquired correctly. The last parametric study case is carried out with $m^1 = m^3 = 5$ and by varying m^2 from 30 to 45, using mode bases 6, 8 and 10. The results are given in Figure 4.20. It can be noted that with mode basis 6($m^2 = 40$) and mode basis 10($m^2 = 36$), the transmission coefficients are more accurate. If

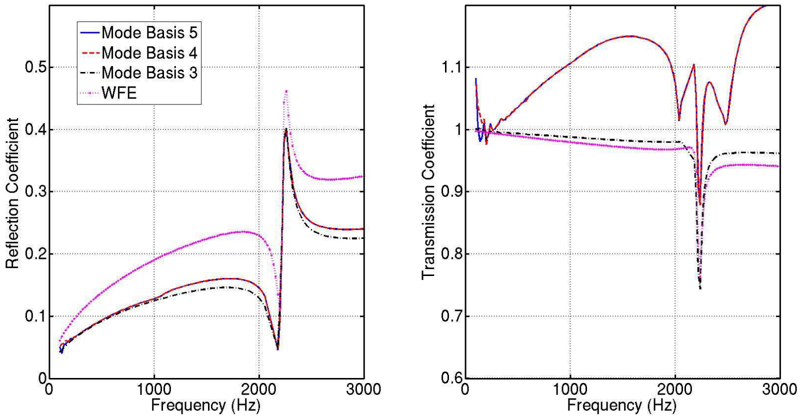

Figure 4.17: Reflection coefficients using the second MWFE formulation with different mode bases (3, 4 and 5) and WFE method. (solid line)Mode basis 5($m^1 = m^3 = 4$) (dashed line)Mode basis 4($m^1 = m^3 = 5$) (point-dashed line)Mode basis 3($m^1 = m^3 = 6$) (point markers)WFE results. $m^2 = 45$.

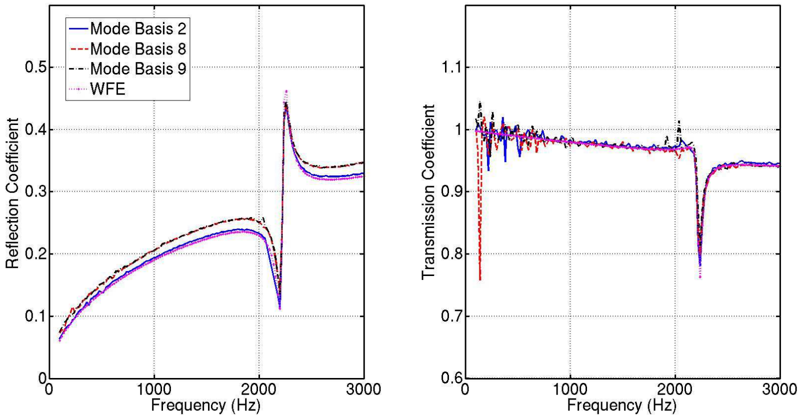

Figure 4.18: Reflection coefficients using the second MWFE formulation with different mode bases (2, 8 and 9) and WFE method. (solid line)Mode basis 2($m^1 = m^3 = 6$) (dashed line)Mode basis 8($m^1 = m^3 = 5$) (point-dashed line)Mode basis 9($m^1 = m^3 = 4$) (point markers)WFE results. $m^2 = 30$.

the evanescent X-axis torsion wave (5^{th} mode in the mode bases, the 6^{th} being the evanescent Z-axis bending wave) is taken into the mode basis of the outer layers 1 and 3, smaller dimension of the mode basis of layer 2 should be chosen. From all the parametric studies performed here, it can be concluded that the most important mode basis dimension is m^2. With a proper m^2 chosen ($m^2 < 40$ for example), reflection and transmission coefficients are less sensitive to

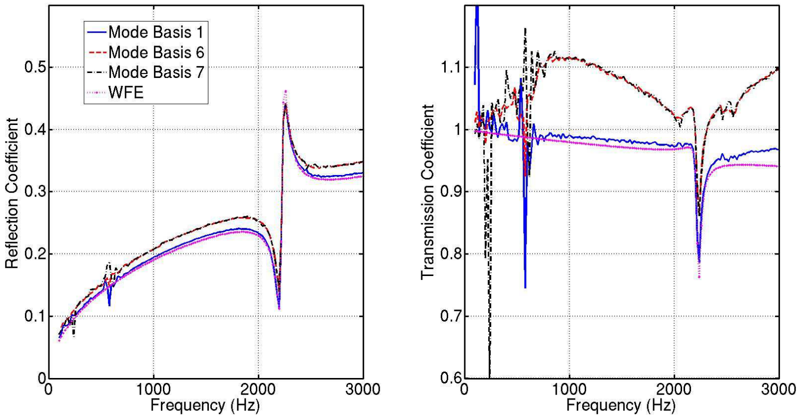

Figure 4.19: Reflection coefficients using the second MWFE formulation with different mode bases (1, 6 and 7) and WFE method. (solid line)Mode basis 1($m^1 = m^3 = 6$) (dashed line)Mode basis 6($m^1 = m^3 = 5$) (point-dashed line)Mode basis 7($m^1 = m^3 = 4$) (point markers)WFE results. $m^2 = 40$.

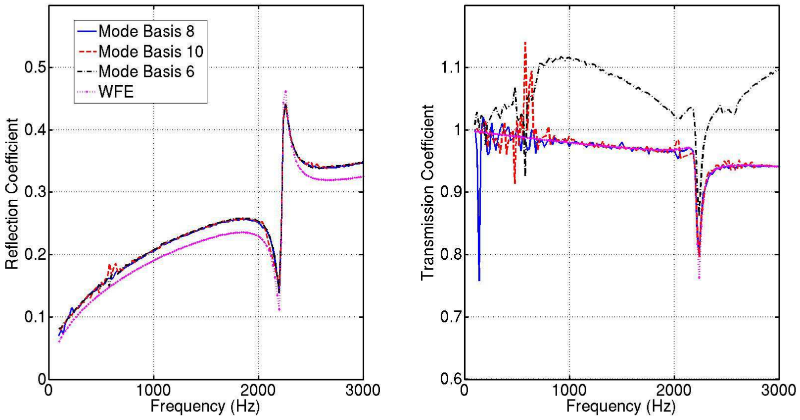

Figure 4.20: Reflection coefficients using the second MWFE formulation with different mode bases (6, 8 and 10) and WFE method. (solid line)Mode basis 8($m^2 = 30$) (dashed line)Mode basis 10($m^2 = 36$) (point-dashed line)Mode basis 6($m^2 = 40$) (point markers)WFE results. $m^1 = m^3 = 5$.

m^1 and m^3. However, if m^2 is larger and overestimates the dynamics of the inner layer 2, m^1 and m^3 should be properly chosen to obtain correct results($m^1 = m^3 = 6$ for example). Generally speaking, larger mode basis dimension for outer layers 1 and 3 tends to give transmission coefficients with less fluctuation.

4.3 Concluding remarks

In this chapter, multi-layered beams with $R - L$ shunted piezoelectric patches are calculated using the MWFE formulation adjusted to consider piezoelectric elements. The control of energy diffusion parameters of wave modes propagating in such composite beams has been studied with two different kinds of MWFE formulation and the associated DMM approach. A modal reduction technique has been applied in the MWFE formulation so as not to overestimate the dynamics of the multi-layered system. Pertinent local wave mode bases of the uncoupled layers with correct dimensions should be applied in the MWFE formulation.

Through parametric studies on the dimensions of local wave mode bases in the MWFE formulations, several conclusions can be drawn:

- For the analysis of wave dispersion, it can be concluded that the dimensions of the local mode bases of outer Layers 1 and 3 have an impact on Mode 6 and Mode 8, while the dimension of the local mode basis of the inner Layer 2 influences mainly the Mode 7. Mode conversion between Mode 2 and Mode 7 occurs when the dimension of the local mode basis of the inner Layer 2 is too large, or the MWFE formulation itself does not guarantee the continuity of the forces at the interfaces of the uncoupled layers (second MWFE).

- For the analysis of energy diffusion, it can be summarized that the dimension of the local mode basis of Layer 2 is the most important parameter. If the dimension of this mode basis doesn't overestimate the dynamics of this layer, reflection coefficients issued from the MWFE formulations are close to those issued from the classical WFE method. Additionally, when the dimension of the local mode basis of Layer 2 is smaller, the reflection and transmission calculated for the Z-axis bending wave are less sensitive to dimensions of the local wave mode bases of Layers 1 and 3. These dimensions influence mainly the fluctuation in transmission coefficients.

CHAPTER 5

Wave propagation control in smart structures using shunted piezoelectric patches with negative capacitance

---

Contents

5.1 Introduction

The issue of wave propagation control in smart structures with shunted piezoelectric patches using negative capacitance is addressed in this chapter. The vibration control of structures through piezoelectric shunts with negative capacitance has always been a research topic during recent years, as its capability of tailoring the dynamic behavior of the structure in a large frequency range makes this technique extremely interesting for numerous industrial applications. It is considered a promising technique according to previous work, and theoretical, numerical analysis and experimental validation are carried out to evaluate and test the efficiency of this control technique [18, 19, 6, 20, 21, 22, 23]. Tuning theories developed by Behrens *et al.* [24], Park and Palumbo [25] and Cunefare [19] all showed that a negative capacitance was needed to allow for maximum performance of the shunt. Structures with periodically distributed shunted piezoelectric patches will be designed to obtain intelligent vibroacoustic interfaces in order to realize optimal reflection or optimal damping of unwanted incident energy from excitation sources.

In this chapter, numerical tools developed in previous chapters are applied to analyze the effect of only one unit cell in the smart structure with periodic shunted piezoelectric patches. This unit cell contains only one shunted piezoelectric patch or a pair of shunted piezoelectric patches. A simple system of a beam structure with piezoelectric patches can be firstly studied with these numerical approaches. The analysis of the effect of the shunt circuit with negative capacitance on the wave modes propagating in the system is firstly carried out. Then intensive calculations such as parametric optimizations to be carried out to obtain optimal geometric and electric parameters in the smart structure through appropriate optimization procedures and criterions.

5.2 Energy diffusion analysis and forced response of beam structures with $R - C_{neg}$ shunted piezoelectric patches

The finite element model of the coupled system and the definitions of geometric parameters of the coupling element are given in Figure 5.1. The mesh resolution is $5mm \times 5mm \times 1.5mm$ for the beam and $5mm \times 5mm \times 1mm$ for the piezoelectric patches. Linear 8-node solid elements are applied for both the structural and piezoelectric domains. The beam is in aluminium and considered as isotropic, with Young's modulus $E_b = 70\ GPa$ and Poisson's ratio $\nu_b = 0.34$, and density $\rho_b = 2700\ kg/m^3$. The characteristics of the piezoelectric patch are listed in Appendix A. Numerical values of the geometric parameters are given in Table 5.1.

L_{beam}	b_{beam}	h_{beam}	b_{patch}	h_{patch}
0.03	0.03	0.004	0.01	0.001

Table 5.1: Numeric values of the geometric parameters in the waveguide and the coupling element shown in Figure 5.1. The units of all the parameters are in meter (m).

In contrast to the $R-L$ shunt circuit on the piezoelectric patch, the $R-C_{neg}$ circuit has the advantage of large frequency band effect. Detailed theoretical studies of C_{neg} can be found in the work of Collet *et al.* [85], and extracted in Appendix E. According to the conclusions in this work, there are two d-

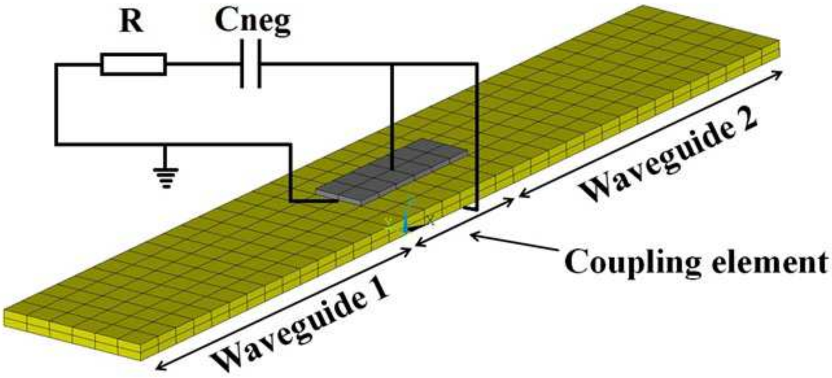

(a) Coupled system

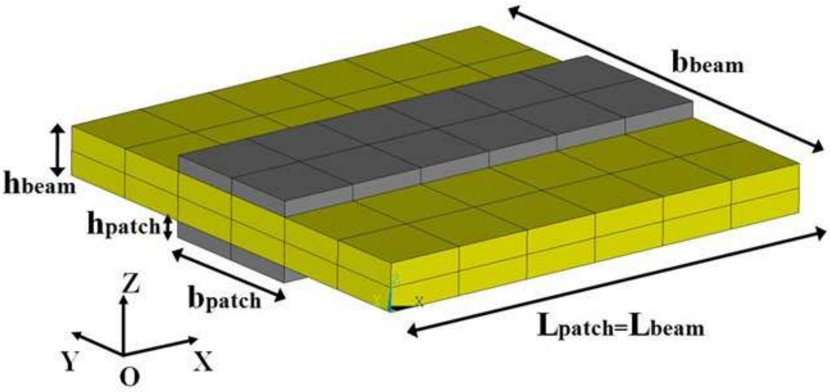

(b) Coupling element

Figure 5.1: Finite element model of the coupled system with a pair of $R-C_{neg}$ shunted piezoelectric patches.

ifferent effects of the negative capacitance on the mechanical characteristics of the piezoelectric patch: softener and stiffener. If $C_{neg} < -C_p^T$ (C_p^T is the capacitance of the piezoelectric patch under constant stress), the stiffness of the piezoelectric patch becomes smaller. The effects are studied here through the numerical tools developed previously, by carrying out two numerical simulations with two C_{neg} lying in the softener and stiffener domain respectively. The targeted wave mode to be controlled is the Z-axis bending wave. Reflection and transmission coefficients are calculated with the DMM of the system, and the comparison of results is displayed in Figure 5.2. Via a propagation point of view, the softening effect results in a smaller reflection shown in Figure 5.2(a), while the stiffening effect leads to a stronger reflection shown in Figure 5.2(b).

Later, beam structures of finite length can also be studied with the Forced

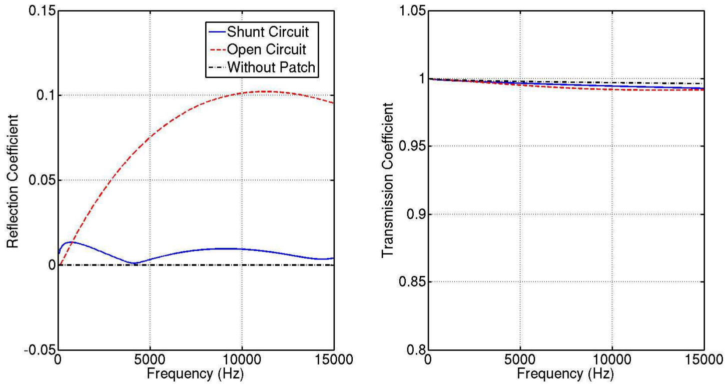

(a) $C_{neg} = -6.008\ nF$ Softener

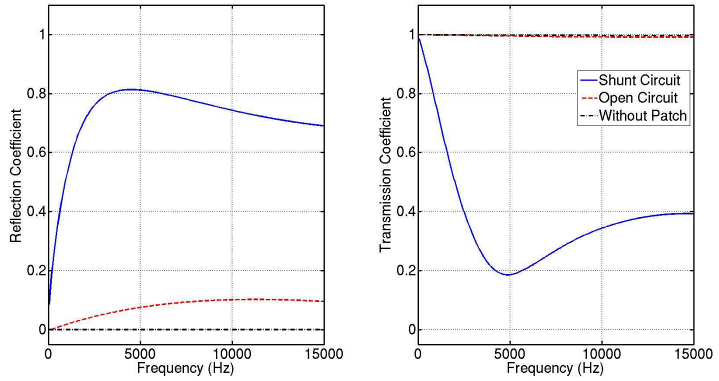

(b) $C_{neg} = -5.019\ nF$ Stiffener

Figure 5.2: Reflection and transmission coefficients of the Z-axis bending wave with C_{neg} as (a)Softener (b)Stiffener, in the frequency band from 0 to 15 kHz, using the WFE approach. $C_p^T = 5.7566\ nF$, $C_p^S = 3.5488\ nF$. The resistance in the shunt circuit $R = 10\ \Omega$.

WFE formulation [47]. The finite element model in the FWFE formulation is given in Figure 5.3, with boundary conditions displayed. If $C_{neg} = -6.008\ nF$ is taken as a softener, and $N_1 = N_2 = 25$, the forced response of the structure can be calculated with the FWFE formulation. The total length of the coupled beam is 25 cm. The forced response of the coupled system is shown in Figure 5.4. It can be seen that with the shunted negative capacitance, the structure becomes softer as the resonance frequencies are smaller than the uncontrolled case. The alternatively controlled resonant peaks are due to the position of the shunted piezoelectric patches, as they can only control "symmetric" bending modes, as shown in Figure 5.5.

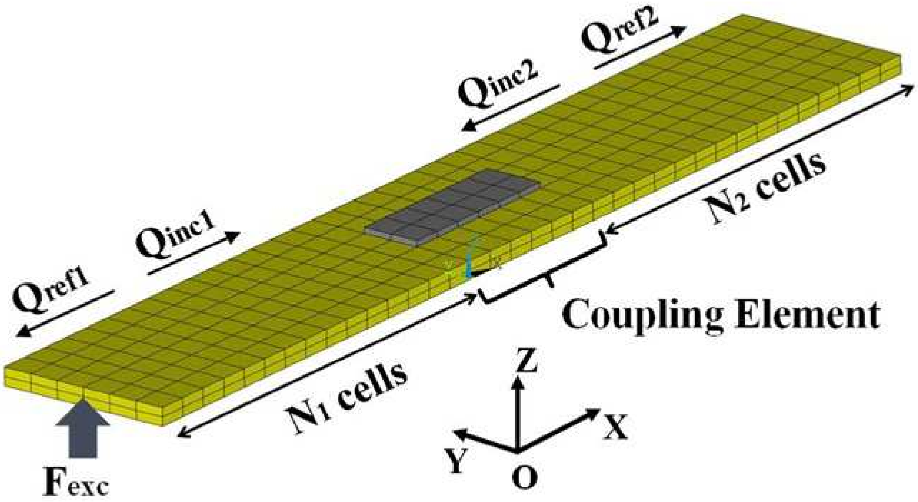

Figure 5.3: Finite element model of the coupled system with a pair of $R - C_{neg}$ shunted piezoelectric patches. The beam is of finite length, with forced boundary condition at one extremity and free boundary condition at the other extremity.

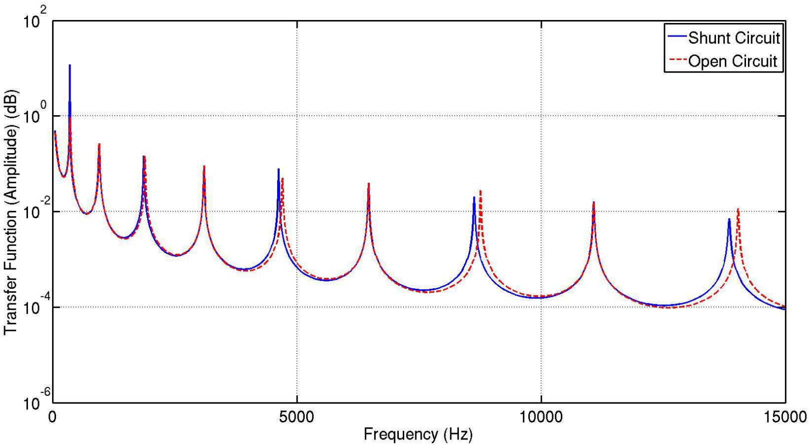

Figure 5.4: Forced response of the finite beam system with a pair of $R - C_{neg}$ shunted piezoelectric patches. The amplitude of the force applied to one extremity of the beam is considered to be constant in the whole frequency band from 0 to 15 kHz, and the nodal displacement of the other extremity with free boundary condition is regarded as the output of the system.

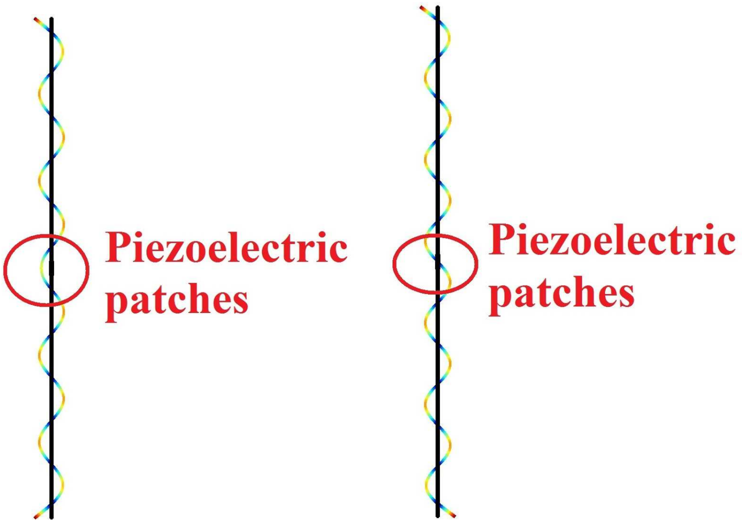

(a) (b)

Figure 5.5: Bending modes of the beam with a pair of shunted piezoelectric patches (a)Symmetric mode (b)Anti-symmetric mode.

5.3 Optimization of shunt impedance and patch thickness

The final objective of the development of all the formulations and numerical tools is to design smart structures with shunted piezoelectric patches. These numerical tools enable intensive calculations such as optimizations so as to obtain optimal geometric or electric parameters of the smart structures such as the thickness of the shunted piezoelectric patches, or the shunt impedance in the circuit.

In order to achieve these goals, firstly, pertinent optimization criterions should be defined. Here, two different types of optimization criterion are applied: the transmission criterion and the absorbed active electrical power criterion. All these criterions are based on power flow in the coupled system, but consider the effect of the shunted piezoelectric patches on the control of the Z-axis bending wave in different ways.

The definitions of the state vectors and the power flows in the coupled system is demonstrated in Figure 5.6. The power flows in the system can be calculated in the following manner:

$$\begin{aligned} \mathbf{P}_{Ri}^{(1)} &= \frac{1}{2} Re\{i\omega \mathbf{q}_{Ri}^{(1)*} \mathbf{F}_{Ri}^{(1)}\} \\ \mathbf{P}_{Li}^{(2)} &= \frac{1}{2} Re\{i\omega \mathbf{q}_{Li}^{(2)*} \mathbf{F}_{Li}^{(2)}\} \end{aligned} \qquad (5.1)$$

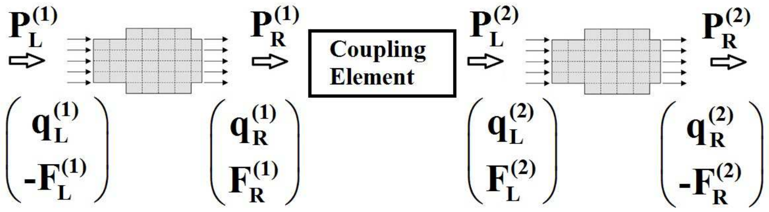

Figure 5.6: Definitions of the state vectors and the power flows in the coupled system.

Three kinds of power flow can be distinguished as follows:

$$\begin{aligned}
\mathbf{P}_{\mathtt{inc}i} &= \frac{1}{2}Re\left[i\omega(\mathbf{\Phi}_{\mathrm{q}i}^{\mathtt{inc(1)}}\mathbf{Q}_i^{\mathtt{inc(1)}})^*(\mathbf{\Phi}_{\mathrm{F}i}^{\mathtt{inc(1)}}\mathbf{Q}_i^{\mathtt{inc(1)}})\right]\\
\mathbf{P}_{\mathtt{ref}i} &= \frac{1}{2}Re\left[i\omega(\mathbf{\Phi}_{\mathrm{q}i}^{\mathtt{ref(1)}}\mathbf{Q}_i^{\mathtt{ref(1)}})^*(\mathbf{\Phi}_{\mathrm{F}i}^{\mathtt{ref(1)}}\mathbf{Q}_i^{\mathtt{ref(1)}})\right]\\
\mathbf{P}_{\mathtt{trans}i} &= \frac{1}{2}Re\left[i\omega(\mathbf{\Phi}_{\mathrm{q}i}^{\mathtt{ref(2)}}\mathbf{Q}_i^{\mathtt{ref(2)}})^*(\mathbf{\Phi}_{\mathrm{F}i}^{\mathtt{ref(2)}}\mathbf{Q}_i^{\mathtt{ref(2)}})\right]
\end{aligned} \tag{5.2}$$

The power flow entering into the coupling element from waveguide 1 be calculated in the following way:

$$\begin{aligned}
\mathbf{P}_{entr} &= \frac{1}{2}Re\{i\omega\mathbf{q}_R^{(1)*}\mathbf{F}_R^{(1)}\} \qquad (5.3)\\
&= \frac{1}{2}Re\{i\omega(\mathbf{\Phi}_{\mathrm{q}}^{\mathtt{inc(1)}}\mathbf{Q}^{\mathtt{inc(1)}} + \mathbf{\Phi}_{\mathrm{q}}^{\mathtt{ref(1)}}\mathbf{Q}^{\mathtt{ref(1)}})^*(\mathbf{\Phi}_{\mathrm{F}}^{\mathtt{inc(1)}}\mathbf{Q}^{\mathtt{inc(1)}} + \mathbf{\Phi}_{\mathrm{F}}^{\mathtt{ref(1)}}\mathbf{Q}^{\mathtt{ref(1)}})\}
\end{aligned}$$

In the same manner, the power flow getting out of the coupling element into waveguide 2 can be obtained as follows:

$$\begin{aligned}
\mathbf{P}_{exit} &= \frac{1}{2}Re\{i\omega\mathbf{q}_L^{(2)*}\mathbf{F}_L^{(2)}\} \qquad (5.4)\\
&= \frac{1}{2}Re\{i\omega(\mathbf{\Phi}_{\mathrm{q}}^{\mathtt{inc(2)}}\mathbf{Q}^{\mathtt{inc(2)}} + \mathbf{\Phi}_{\mathrm{q}}^{\mathtt{ref(2)}}\mathbf{Q}^{\mathtt{ref(2)}})^*(\mathbf{\Phi}_{\mathrm{F}}^{\mathtt{inc(2)}}\mathbf{Q}^{\mathtt{inc(2)}} + \mathbf{\Phi}_{\mathrm{F}}^{\mathtt{ref(2)}}\mathbf{Q}^{\mathtt{ref(2)}})\}
\end{aligned}$$

The power flow dissipated and absorbed by the coupling element $\mathbf{P}_{absorb} = \mathbf{P}_{entr} - \mathbf{P}_{exit}$, and finally, the power flow absorbed by the shunt circuit can be calculated in this way:

$$\mathbf{P}_{absorb-elec} = \mathbf{P}_{absorb}^{shunt} - \mathbf{P}_{absorb}^{open} \tag{5.5}$$

$\mathbf{P}_{absorb}^{shunt}$ is the power flow calculated when the shunt circuit is connected to the piezoelectric patches, while $\mathbf{P}_{absorb}^{open}$ is the power flow obtained when the circuit is open. The two optimization criterions can be defined as follows:

- The relative transmission criterion $\mathbf{Tr}_{rel}$ can be defined in this way:

$$\mathbf{Tr}_{rel}(\omega) = \frac{\mathbf{P}_{exit}^{shunt}(\omega) - \mathbf{P}_{exit}^{open}(\omega)}{\mathbf{P}_{inc}^{shunt}(\omega)} = f_1(R, C_{neg}) \tag{5.6}$$

- The absorbed electric power flow criterion:

$$\mathbf{P}_{absorb-elec}(\omega) = f_2(R, C_{neg}) \tag{5.7}$$

The structure to be optimized is also a beam, but with only one shunted piezoelectric patch. The finite element model of the coupling element is shown in Figure 5.7. The piezoelectric patch covers the whole surface of the beam. Geometric parameters are also defined in Figure 5.7 and numerical values are given in Table 5.2. The thickness of the piezoelectric patch h_p is a variable. During the optimization process, the thickness will be fixed and corresponding optimal impedance will be calculated thickness by thickness.

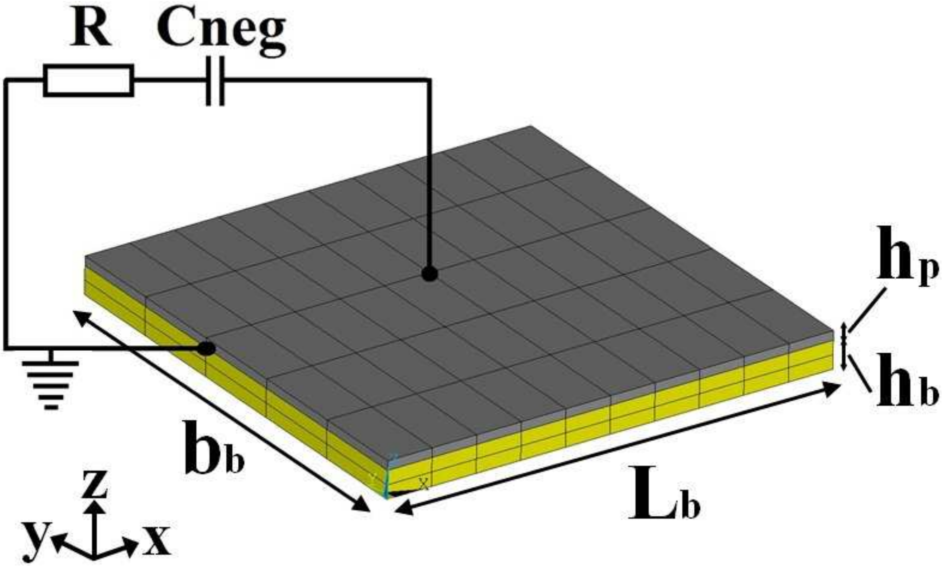

Figure 5.7: Finite element model of the coupling element in the coupled system with one $R - C_{neg}$ shunted piezoelectric patches.

L_b	b_b	h_b	h_p
0.05	0.05	0.003	*variable*

Table 5.2: Numeric values of the geometric parameters in the coupling element shown in Figure 5.7. The units of all the parameters are in meter (m).

The mesh resolution is chosen to be $0.005 \times 0.005 \times 0.0015\ m^3$ for the beam and $0.005 \times 0.005 \times h_p\ m^3$ for the patch. A loss factor $\eta = 0.002$ is added to the finite element model. The relative negative capacitance is defined in the following way:

$$\overline{C}_{neg} = \frac{C_{neg}}{C_p^T} \tag{5.8}$$

Firstly, the relative transmission criterion is applied, and the optimization is carried out using the classical minimization algorithm based on the Nelder-Mead simplex method. The thickness of the piezoelectric patch h_p varies from 0.1 mm to 1.0 mm. Here the resistance R and the negative capacitance C_{neg} are both variables during the optimization process in the frequency band from 0 to 5 kHz.
The evolution of the optimal relative negative impedance $\overline{C}_{neg}^{opt}$ in the frequency domain for all the tested thicknesses is shown in Figure 5.8(a), and the evolution of the optimal resistance R^{opt} is shown in Figure 5.8(b). It can be concluded that $\overline{C}_{neg}^{opt}$ is almost constant in the frequency band from 0 to 5 kHz, and lies in the "stiffener" range $-C_p^T < C_{neg}$. When the patch thickness is bigger, the optimal C_{neg} tends to $-C_p^T$. And for the optimal resistance in the shunt circuit, it is generally negative in order to compensate for the

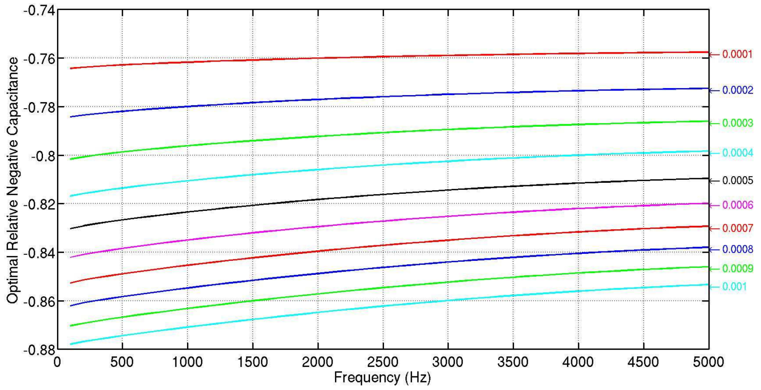

(a) $\overline{C}_{neg}^{opt}$

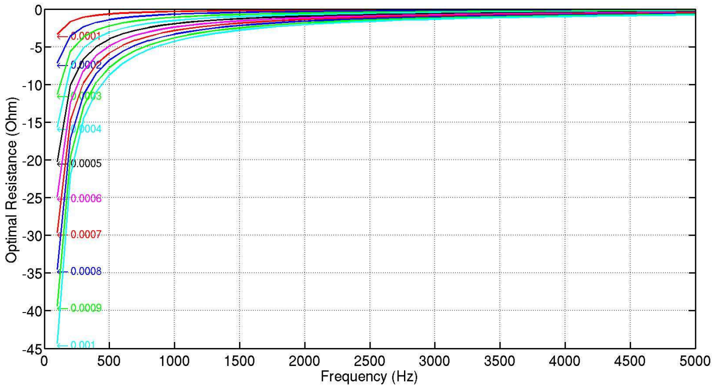

(b) R^{opt}

Figure 5.8: Evolution of optimal (a)relative negative capacitance (b)resistance in the shunt circuit in the frequency domain for each patch thickness.

structural damping [6]. If the structure is less damped, the absolute value of R^{opt} becomes smaller. And for a smaller thickness, the absolute value of R^{opt} is smaller.

The evolution of the optimization criterion in the frequency domain is given in Figure 5.9. It can be noted that at lower frequencies, the transmission is much larger than higher frequency results. However, it is difficult to evaluate the effect of the thickness on the transmission through these results. The relative transmission $\mathbf{Tr}_{rel}$ is then averaged over the frequency band from 0 to 5 kHz for each thickness, and the evolution of the averaged relative transmission with the patch thickness is given in Figure 5.10. It can be concluded that within the frequency band from 0 to 5 kHz and loss factor $\eta = 0.002$, an optimal thickness can be found at 0.6 mm for the shunted piezoelectric patch. Subsequently the absorbed electric power flow criterion is applied to carry out

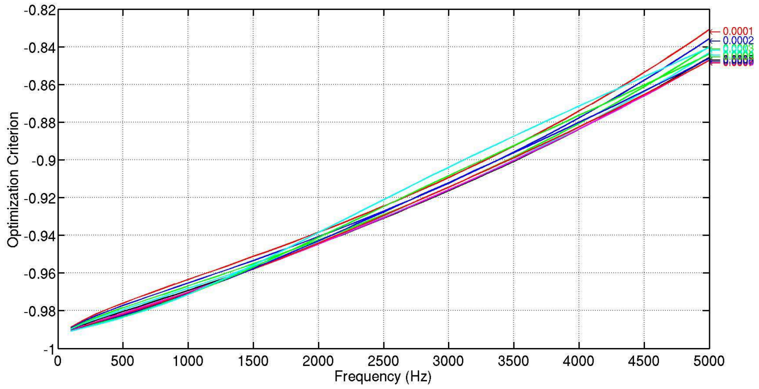

(a) Original view

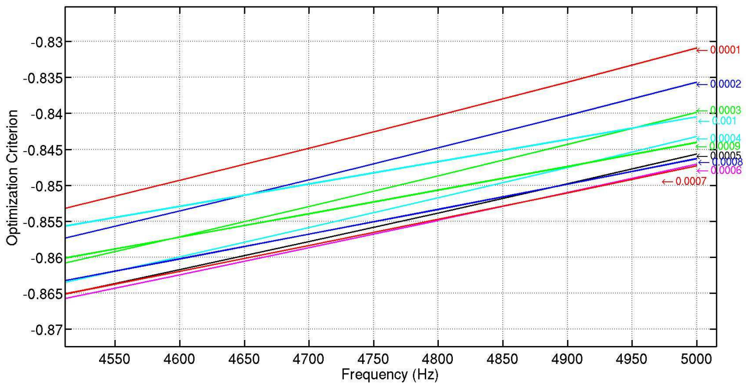

(b) Zoom

Figure 5.9: Evolution of the relative transmission optimization criterion in the frequency domain for each patch thickness.

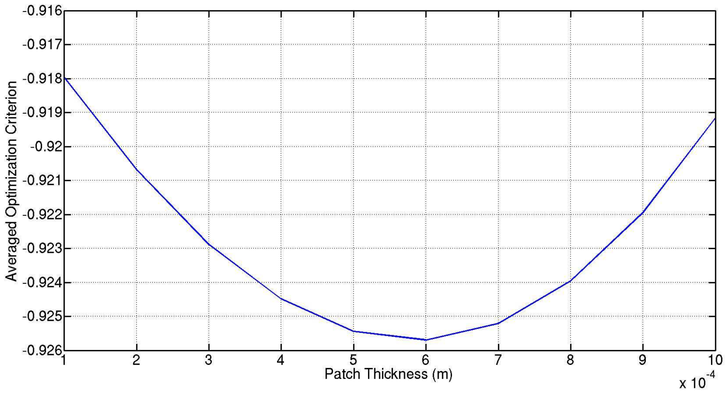

Figure 5.10: Evolution of the averaged relative transmission optimization criterion with patch thickness.

similar optimizations. This time, the patch thickness h_p varies in a larger band from 0.1 mm to 1.6 mm. The resistance R and the negative capacitance C_{neg} are both variables during the optimization process in the frequency band from 0 to 5 kHz. The evolution of the optimal relative negative impedance $\overline{C}_{neg}^{opt}$ in the frequency domain for all the tested thicknesses is shown in Figure 5.11(a), and the evolution of the optimal resistance R^{opt} is shown in Figure 5.11(b). It can also be noted that, just as in the previous case using the relative transmission criterion, $\overline{C}_{neg}^{opt}$ is almost constant in the frequency band from 0 to 5 kHz, and lies in the "stiffener" range $-C_p^T < C_{neg}$. And when the patch thickness is bigger, the optimal C_{neg} tends to $-C_p^T$. Nevertheless, for the optimal resistance in the shunt circuit, it is generally positive, and at lower frequencies, the optimal R is larger for all the tested thicknesses. For larger thicknesses, the optimal R is also larger.

The evolution of the optimization criterion in the frequency domain is given in Figure 5.12. It can be noted that at higher frequencies, the absorption is much larger than lower frequency results. And for a bigger patch thickness, the absorption is larger. However, there is no "optimal thickness" that generates optimal absorption within the frequency range of interest, at least for all the tested patch thicknesses in this case.

During the optimization process, the resistance in the shunt circuit can be fixed, and if the absorption criterion is applied, optimization results for the relative negative capacitance are similar to those obtained by varying the resistance and capacitance at the same time through the Nelder-Mead simplex method. These results are displayed in Figure 5.13. The evolution of $\overline{C}_{neg}^{opt}$ is almost constant in the frequency band from 0 to 5 kHz, and lies always in the "stiffener" range $-C_p^T < C_{neg}$. The evolution of the absorption optimization

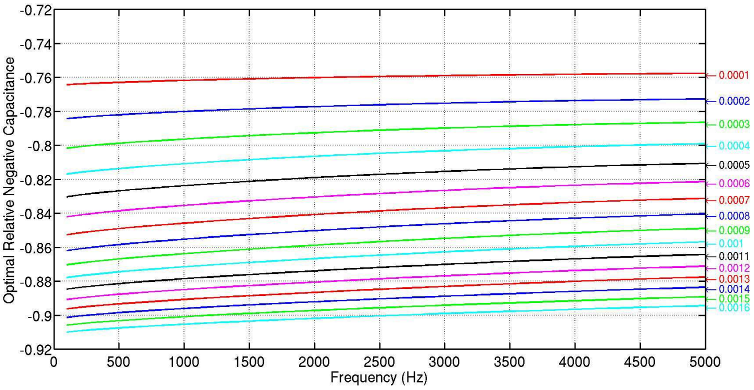

(a) $\overline{C}_{neg}^{opt}$

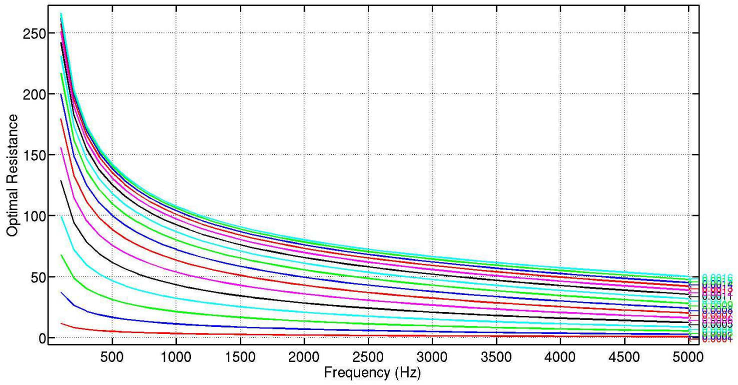

(b) R^{opt}

Figure 5.11: Evolution of optimal (a)relative negative capacitance (b)resistance in the shunt circuit in the frequency domain for each patch thickness.

criterion is given in Figure 5.14. As there is only one variable parameter(C_{neg}), if the average of the absorbed electric power flow in the shunt circuit in the frequency domain is taken as the optimization criterion, the evolution of this averaged power flow with the relative negative capacitance can be obtained, as shown in Figure 5.15. The same optimal relative negative capacitance $\overline{C}_{neg}^{opt}$ can be found for each patch thickness. And this time, an optimal thickness can be targeted at 0.6 mm, as it gives the largest absorbed electric power flow among all the tested patch thicknesses. However, it should be mentioned that this "optimal thickness" changes with the fixed R. In a realistic synthetic circuit that can generate the C_{neg} effect, there is always a residual resistance that varies with the frequency, and the negative capacitance is not constant in the frequency band of interest. All these influences should be taken into

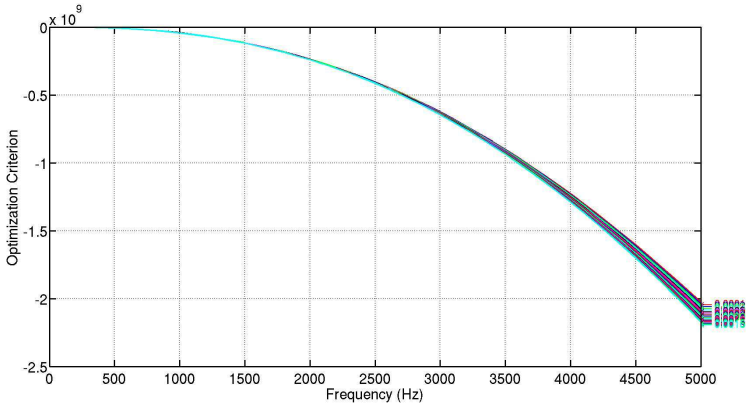

(a) Original view

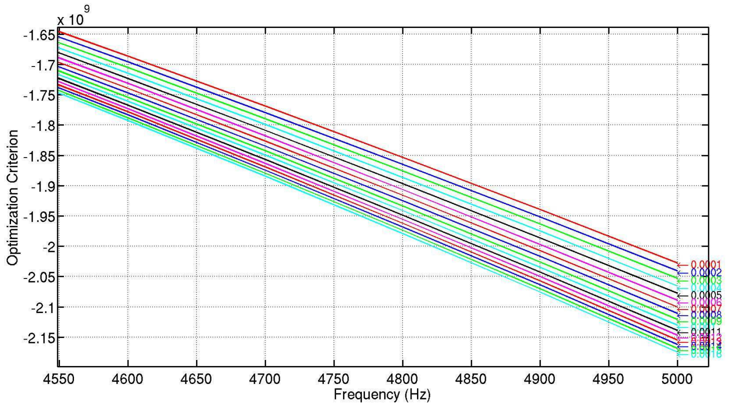

(b) Zoom

Figure 5.12: Evolution of the relative transmission criterion in the frequency domain for each patch thickness (a)Original view (b)Zoom

account correctly in order to get the real optimal parameters.
Anyway, with the numerical tools proposed in this work, optimal geometric and electric parameters can be obtained through rigorous optimization process with appropriate optimization criterions. This is the final objective of this work.

5.4 Conclusions

The performance of shunted piezoelectric patches with negative capacitance is numerically investigated. Both the softening and stiffening effects are observed via reflection and transmission coefficients as well as frequency response function. Due to the capability of control on large frequency band by using

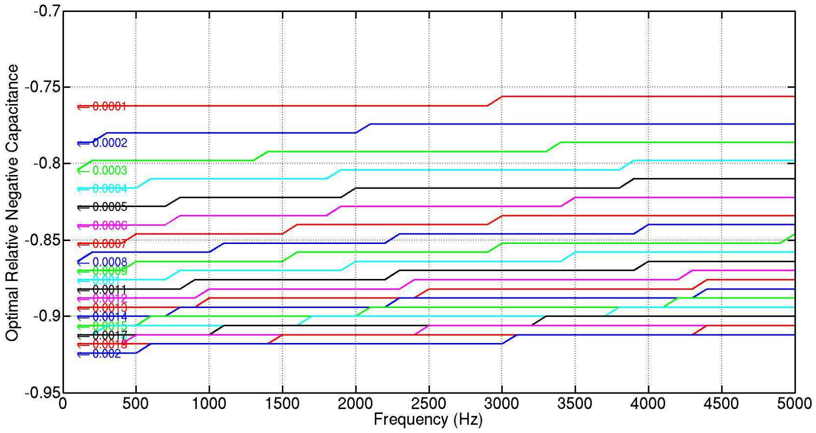

Figure 5.13: Evolution of the optimal relative negative capacitance in the frequency domain for each patch thickness, $R = 20\ \Omega$.

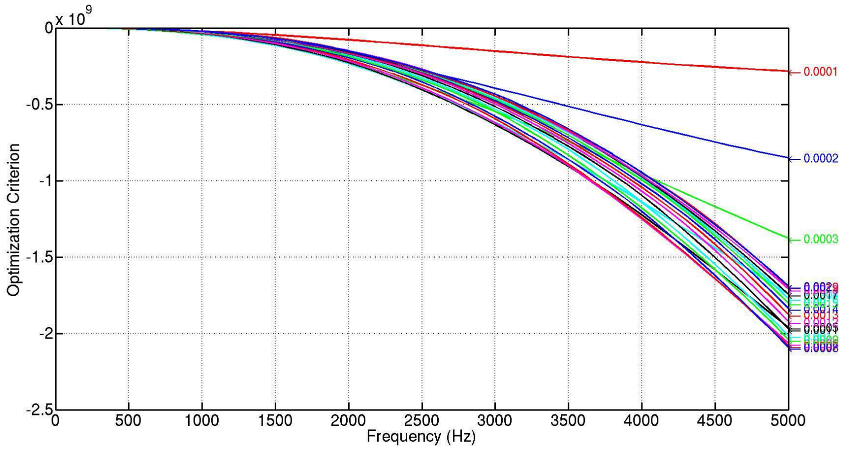

Figure 5.14: Evolution of the absorption optimization criterion in the frequency domain for each patch thickness. $R = 20\ \Omega$.

negative capacitance in the shunt circuit on piezoelectric patches, optimizations have been carried out to obtain optimal electric and geometric parameters in the smart beam structure to achieve optimal control effect. Different optimization criterions based on power flow analysis are defined to realize maximum transmission or absorption of incident power flow when the structure is excited on Z-axis bending mode. Optimization results are consistent with previous studies by Collet*et al.* [6]. The potential of these numerical tools for the design of smart structures is well revealed, and the optimization approaches based on other types of criterions can be integrated in the design procedure for smart structures with shunted piezoelectric patches so as to

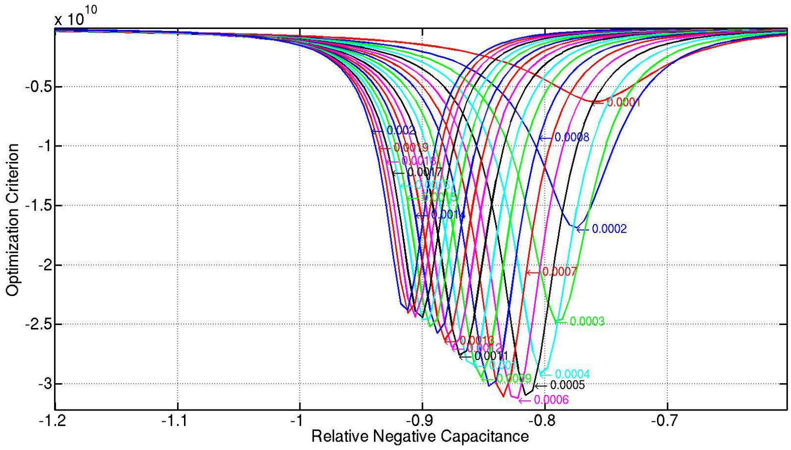

Figure 5.15: Evolution of the averaged absorption optimization criterion in the frequency domain for each patch thickness. $R = 20\ \Omega$.

obtain desired control effects on different kinds of wave modes.

Chapter 6

Multi-mode wave propagation in damaged stiffened panels

Contents

6.1 Introduction

The safety of structures is of great concern in aerospace and civil engineering. Structures which are both light and resistant is one of the most important objectives to achieve in structure designing. Stiffened structures are extensively used as they can ensure a good compromise between the structural rigidity and the weight. In addition to the issue of designing stiffened structures, the maintenance of stiffened structures is another tricky problem. And therefore the detection of defects in such structures draws more and more attention.

In order to perform the defect detection with precision and without causing any damage to structures, the technology of non-destructive testing (NDT) [86] is one of the most important methods in use. For example, among all the classical NDT methods, the ultrasound testing method [87, 88], is widely used and has been proved to be efficient and precise. However, it is considered to be a local method, since if a very dispersive area of the wave mode is used, it will be difficult to achieve global damage detection as vibration amplitudes decay very fast in the structure.

In thin plate-like structures, the plate's thickness behaves like a wave guide [89, 90] for waves called Lamb waves [91]. These propagating waves have shown a great potential[92, 90] in the NDT domain. The attractive features of guided waves include sensitivity to a variety of damage types, as well as the ability to travel over relatively long distances [93] within the structure under investigation. The guided waves' interaction with the structure's damage [94] can be studied to determine the existence, type, localization and size of damage. Besides these local methods which are signal-based, there are also global methods which are model-based [95].

Although global methods and local methods are based on different approaches, these methods face the same physical difficulties and are sensitive to common phenomena. Local defects can lead to a change of stiffness in the structure [95], and this change has an influence on the global mechanical behavior, resulting in a variation of dynamical characteristics like eigenfrequencies of the structure. Unlike ultrasound waves, waves at low and medium frequencies (under 5kHz with a material thickness of several millimeters) are less used for damage detection as they appear to be less sensitive to defects. It is due to the fact that their wavelength is bigger than the size of defects, and for the targeted applications, the background noise at these frequencies is relatively high. But for structures which have 2-scale dynamic behaviors [96, 97] such as stiffened panels, waves at medium frequencies can possibly be applied to detect defects in the structure. As revealed in Ichchou *et al.* [31], at low and medium frequencies, two wave modes can exist at the same time: the waves related to the structural orthotropy (global mode, first scale dynamics) and waves guided by the ribs, which belong to the second scale dynamics. This latter exhibits guided waves propagating in the rib's direction and stationary waves propagating in the direction perpendicular to the ribs. The guided waves' wavelength is much smaller than that of the structural orthotropy wave modes. At very low frequencies, the propagation behavior is mainly carried by the global mode. At medium frequencies, the second propagation behavior (guided waves) appears. This behavior can possibly be used to investigate the structural health of stiffened panels. A local change in the ribs might influence the stationary waves and subsequently leads to a change in the second scale dynamical behavior. Waves at medium frequencies can also be used for damage detection in some other places if the influence of local singularities on global vibration signature can be properly captured.

Techniques for the analysis of full wave field data in the wavenumber/frequency domain are effective tools for damage detection, visualization and characterization [98]. In the work of Sharma *et al.* [99] and Ichchou *et* *al.* [31], a scanning laser Doppler vibrometer (SLDV) was used to measure the velocity of the inspected surface in points belonging to a predefined grid. Scanning the grid and post-processing the data allow the detection and the visualization of the full wavefield as it propagates in the structure [98]. The resulting images describe the main features of the propagating wave and show its interactions with discontinuities that may be encountered along the wave path. The damage can be immediately detected and located by means of limited processing. The wavefield time-domain data can be fed to signal processing algorithms to obtain detailed images of the defect. The application of multi-dimensional Fourier transforms (FTs) in space and time can then provide the representation of the component response in the frequency/wavenumber domain. In this domain, all wave components propagating in directions opposite to the direction of propagation of the main injected pulse are clearly highlighted. As a consequence, the presence of reflections and mode conversions caused by the presence of damage are immediately noticeable [100]. The application of two-dimensional FT (2D FT) has previously been proposed in the work of Alleyne and Cawley [101] for the analysis of multi-mode wave signals for the identification of dispersion relations and the characterization of various modes. The 2D FT was also applied to treat the displacement of a stiffened panel and to obtain the panel's wavenumber characteristics in the wavenumber/frequency domain [31]. A filtering in the wavenumber/frequency domain can be carried out to eliminate waves that contain no damage information [98, 31].

This chapter aims at explaining in detail a novel application of the guided waves for the damage detection in stiffened panels at medium frequencies. This relatively new technique, named Inhomogeneous Wave Correlation (I-WC) technique [31, 36, 102], is able to provide a global vision of the vibration signature of the structure through a wave propagation approach (instead of modal analysis) by extracting propagation information like wavenumber from measurements or simulations. With integrated signal processing and filtering methods, waves containing no information about defects can be eliminated as the influence of local singularities on the vibration signature of the structure can be highlighted.

6.2 Outline of some K-space tools

The k-space discussed here is a 2D plane containing wavenumber vectors $\overrightarrow{k}(k_x, k_y)$, and the corresponding k-space tools can be defined as techniques which provide wavenumber information in the (k_x, k_y) plane. Among several conventional k-space tools, this section presents also a new technique that can provide wave propagation constants like wavenumbers for 1D and 2D structures. As explained in Ichchou *et al.* [31], the 2D structures are defined below in the (x, y) plane. The method assumes a harmonic field $\hat{w}(x, y)$(where hat symbol $\hat{.}$ states for the ω-dependence of $w(x, y)$), either from a harmonic field or from a temporal Fourier transform, given by:

$$w(x,y,t) = \int_0^{+\infty} \widehat{w}(x,y)\mathrm{e}^{\mathrm{i}\omega t}\mathrm{d}\omega \tag{6.1}$$

The new technique, named Inhomogeneous Wave Correlation (IWC) technique, extends available k-space tools through a rigorous optimization process. Among such available k-space tools, the Discrete Fourier Transform (DFT) and the Continuous Fourier Transform (CFT) are the most frequently employed methods for extracting wavenumber content in structures. For the sake of clarity, DFT and CFT are briefly described in order to underline the novelty of the proposed IWC approach [36].

6.2.1 Discrete and Continuous Fourier Transform

Discrete Fourier Transform (DFT) is an extensively used transform in many engineering areas. Its applications cover signal processing and all related technical areas. In practice, the DFT assumes that:

1. **(H1)** The displacement field $\widehat{w}(x, y)$ is given over a uniform spatial grid $\Big(x_i = i\Delta x, y_j = j\Delta y\Big)_{\substack{0\leq j\leq N_2-1\\ 0\leq i\leq N_1-1}}$. Δx and Δy are the space increments along x and y axis respectively, N_1 and N_2 are the number of measured data along x and y axis respectively.

2. **(H2)** Outside this grid the field is assumed to be $2D-$periodic ($\backslash$ symbol defines the euclidian ratio residue), namely :

$$\forall i,j \in \mathbb{N}^2\ , \quad \hat{w}(i\Delta x, j\Delta y) = \hat{w}\Big((i\backslash N_1)\Delta x, (j\backslash N_2)\Delta y\Big) \tag{6.2}$$

It can be readily shown that the family of exponential functions with discrete wavenumbers:

$$\Big(k_{xp} = p\Delta k_x, k_{yq} = q\Delta k_y\Big)_{\substack{0\leq q\leq N_2-1\\ 0\leq p\leq N_1-1}}$$

with $\Delta k_x = \frac{2\pi}{N_1 \Delta x}$ and $\Delta k_y = \frac{2\pi}{N_2 \Delta y}$ form a basis for complex functions space, so that the field $\hat{w}$ can be written in a single format :

$$\hat{w}(x_i, y_j) = \sum_{p=0}^{N_1-1} \sum_{q=0}^{N_2-1} \widehat{\hat{w}}(k_{xp}, k_{yq})\, \mathrm{e}^{\mathrm{i}(k_{xp}x_i + k_{yq}y_j)} \tag{6.3}$$

The Discrete Fourier Transform $\hat{w} \longrightarrow \widehat{\hat{w}}$ is thus the following :

$$\widehat{\hat{w}}(k_{xp}, k_{yq}) = \frac{1}{N_1 N_2} \sum_{i=0}^{N_1-1} \sum_{j=0}^{N_2-1} \hat{w}(x_i, y_j) \mathrm{e}^{-\mathrm{i}(k_{xp}x_i + k_{yq}y_j)} \tag{6.4}$$

The DFT presents two major advantages. Firstly, it is bijective, an inverse transform is possible (Inverse DFT, IDFT). This inverse transform allows easy filtration in the k-space. And secondly, it is very rapid. Through Fast Fourier Transform (FFT) like algorithm, very fast data processing can be achieved.
However, this method has some drawbacks. The first one is aliasing : due to the field discretization, its DFT is $\frac{2\pi}{\Delta x}$-periodic :

$$\widehat{\hat{w}}(k_x, k_y) = \widehat{\hat{w}}(k_x + \tfrac{2\pi}{\Delta x}, k_y) = \widehat{\hat{w}}(k_x, k_y + \tfrac{2\pi}{\Delta y})$$

This property implies erroneous DFT treatments for fields comprising wavenumbers k_x outside the domain $\left[-\frac{\pi}{\Delta x}\ \frac{\pi}{\Delta x}\right]$ or k_y outside $\left[-\frac{\pi}{\Delta y}\ \frac{\pi}{\Delta y}\right]$. The second drawback is leakage: since the field $\hat{w}$ is given in a finite space, a singular wave (k_x, k_y) which should appear in the k-space as a Dirac distribution, will appear with a cardinal-sine shape. Finally, as the wave content of the given field $\hat{w}$ is only known over a k-space grid, the k-space discrimination is then very weak and wave-vectors are therefore poorly estimated.
The Continuous Fourier Transform (CFT) aims mainly to improve the k-space discrimination described above. The CFT tries, thus, to estimate the wave content of a given spatial field function for all possible values of (k_x, k_y). For this reason, the assumption **(H2)** is not considered. The field is considered nil outside measurements locations. The CFT definition is thus the following :

$$\widehat{\hat{w}}(k_x, k_y) = \sum_{i=0}^{N_1-1} \sum_{j=0}^{N_2-1} \hat{w}(x_i, y_j) \mathrm{e}^{-\mathrm{i}(k_x x_i + k_y y_j)} \tag{6.5}$$

Such a transform is not yet bijective as new information is artificially invented in the CFT process, but the CFT can be evaluated for any wavenumber value, making it very accurate. Moreover, the treated field does not need to be given in a uniform grid. However, for each measured location $(x_i, y_i)_{i \in \mathbb{N}_N}$ the corresponding elementary surface $\mathrm{d}S_i$ should be estimated.

6.2.2 Inhomogeneous Wave Correlation method (IWC)

We now introduce an inhomogeneous wave, noted $\widehat{o}_{k,\gamma,\theta}$ (a wave with heading θ, γ wave attenuation and apparent wavelength equal to $\frac{2\pi}{k}$). In fact, the wave attenuation is a way of introducing damping. Lyon and Dejong [103] formulates the link between this wave attenuation and the classical damping loss factor as : $\gamma = \frac{\eta c_\varphi}{2c_g}$, with c_φ and c_g being the phase and group velocities respectively.
The inhomogeneous wave is defined as follows:

$$\widehat{o}_{k,\gamma,\theta}(x,y) = \mathrm{e}^{-\mathrm{i}k(\theta)\left(1+\mathrm{i}\gamma(\theta)\right)\left(x.\cos(\theta)+y.\sin(\theta)\right)} \tag{6.6}$$

Thereafter, the correlation between this inhomogeneous wave and the complete wave field is calculated, like a Modal Assurance Criterion[104], using the following formula:

$$IWC(k,\gamma,\theta) = \frac{\left|\iint_S \widehat{w}.\widehat{o}^*_{k,\gamma,\theta}\,\mathrm{d}x\mathrm{d}y\right|}{\sqrt{\iint_S |\widehat{w}|^2\mathrm{d}x\mathrm{d}y.\iint_S |\widehat{o}_{k,\gamma,\theta}|^2\mathrm{d}x\mathrm{d}y}} \tag{6.7}$$

where * denotes the complex conjugate. The identification of a complex wave number for a given direction θ leads to maximization (with a fixed θ) of the function $(k,\gamma) \longrightarrow IWC(k,\gamma,\theta)$. To apply the IWC method in practice, it is first assumed that the wave field $\widehat{w}$ is known on arbitrary data points $(x_i,y_i)_{i\in\mathbb{N}_n}$. The integrations over the whole surface S in equation 6.7 are replaced by a finite weighted sum:

$$\iint_S \bullet \ \mathrm{d}x\mathrm{d}y \quad \longrightarrow \quad \textstyle\sum_n \bullet \ \rho_i S_i \tag{6.8}$$

where ρ_i is the coherence of measurement data at point M_i ($\rho_i = 1$ if the coherence is not available), and S_i is an estimation of the surface around point M_i. The algorithm first puts angle θ into a discrete set of values (θ_j). For each of these angles, the maximum of IWC is located at a value (k_j,γ_j). Thus the method creates two functions $\theta \rightarrow k(\theta)$ and $\theta \rightarrow \gamma(\theta)$ defined on a set of discrete values (θ_j). Finally, the trio $(\theta_{j0},k_{j0},\gamma_{j0})$ is removed from the list if γ_{j0} is greater than 1. The identified wavenumber corresponds to a wave heading in the structure. The optimization process can be used to remove fictitious waves. In fact, if $\gamma(\theta)$ is set to zero, the IWC method is totally equivalent to the DFT and CFT methods. Extending the DFT and CFT, the IWC method employs similarly arbitrary distributed data points, with the possibility of using measured coherence signals (if available). In practice, the spacing resolution needed depend on the quality of expected wavenumber estimation. Indeed, the estimation error follows an inverse spacing tendency. Previous work [105] windowed the field to avoid the effect of near-field due to sources and boundary conditions. But the near-field mainly corresponds to imaginary wavenumbers. The introduction of a loss factor makes it possible to distinguish near-field from far-field: the near-field corresponds to a high apparent loss factor (imaginary part of the wavenumber greater than its real part). The algorithm using the IWC method can eliminate the identified wavenumbers with high apparent loss factors. This allows the use of the vibrational field of the whole surface S of the structure. It should be noted that the input field can be either experimental or numerical. In the following section, this technique will be applied to numerically tested stiffened panels.

6.3 Stiffened panel case study: numerical experiments

In this section, the previously introduced methods are applied to three cases of stiffened panels in order to study the interaction between defects and guided waves in stiffened panels.

6.3.1 Damage detection in stiffened panels using guided waves at low and medium frequencies

Three study cases were performed. Finite element models of the stiffened panels were built for each case and the models in case A are shown in Figure 6.1(a) (for the panel without defect) and 6.1(b) (for the panel with defects). The geometry definition and geometric parameters of the stiffened panels in the three cases A, B and C are shown in Figure 6.1(c) and Table 6.1. The ribs are made of steel while the panel is made of aluminium. This choice of materials has been made because of two reasons:

Case	Area (m^2)	H (m)	A (m)	B (m)	P (m)
A	4	0.005	0.001	0.015	0.25
B	4	0.005	0.001	0.015	0.5
C	4	0.005	0.001	0.015	0.125

Table 6.1: Geometric parameters of the ribbed panels in the three cases studied.

- Experiment on a structure of this material choice will be done as numerical simulations have already been done in our previous work [31] and this present work;
- The "two-scale" dynamics of the stiffened panel needs to be shown: under excitations of a certain frequency band and with certain geometric sizes, the panel itself is in high (or medium) frequency band while the ribs remain in the low frequency band.

The finite element models and numerical experiments were realized in ANSYS using SOLID45 elements with a global element size of $0.02 \times 0.02 \times 0.005$ m^3 for the panel and $0.02 \times 0.015 \times 0.001$ m^3 for the ribs. The computations aimed to obtain the displacement field of the stiffened panels under harmonic excitation (a punctual force was applied at the center of the panel). Along

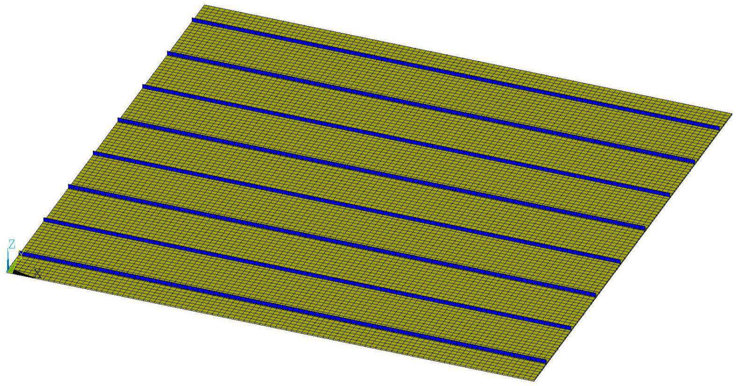

(a) Panel without defect

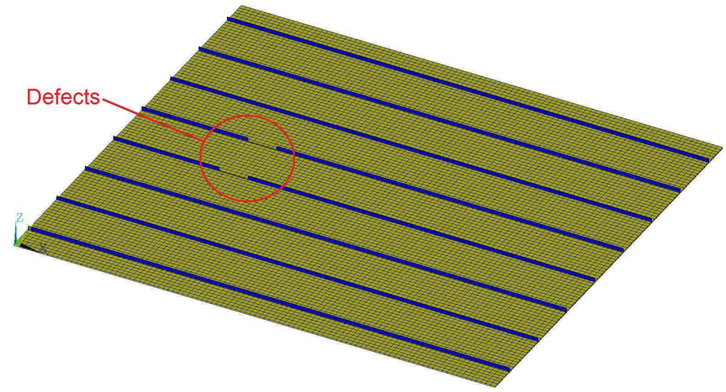

(b) Panel with defects

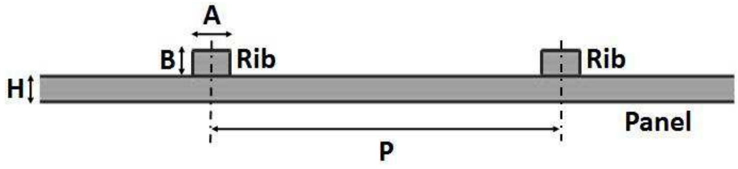

(c) Ribbed panel geometry

Figure 6.1: The finite element model and geometry of the ribbed panel without and with defects in case A.

the edges of the stiffened panel, free boundary conditions were used. In order to avoid resonance at eigenfrequencies, a constant modal damping of 0.004 was used in the numerical computation. After that, the nodal displacement in z-axis was extracted numerically over a frequency range from 0 to 4 kHz. At first, a numerical simulation was performed on the stiffened panel without defect in case A. The displacement field was obtained by a harmonic analysis with ANSYS and processed using the IWC method presented in Subsection 6.2.2. The k-space plot was subsequently extracted, which contains the information about the wave propagation constants in the stiffened panel. In the k-space plot, the numerically obtained results were compared to the structural orthotropy model [106], which comes from the homogenized model proposed long ago by Timoshenko [107, 108]. The model used here was deduced from a quasi-static homogenization process, where the equivalent mass density and stiffness were calculated as a function of the parameters of the ribs and the plate. Figure 6.3(a) shows the k-space obtained at 2kHz, which is the IWC result of the displacement field displayed in Figure 6.2(a). The black dotted lines in Figure 6.2 represent the ribs. The white dashed line in Figure 6.3(a) represents the homogenized model, and the white straight lines in this figure correspond to the ribs (more precisely, to the $k_x = \frac{2\pi}{P}$ and $k_x = \frac{-2\pi}{P}$ branches, with P defined in Table 6.1), the remaining results are those of the IWC method. Then, a filtering process of the k-space was realized: only the two "vertical bars" around the ellipse were retained. This filtering process can

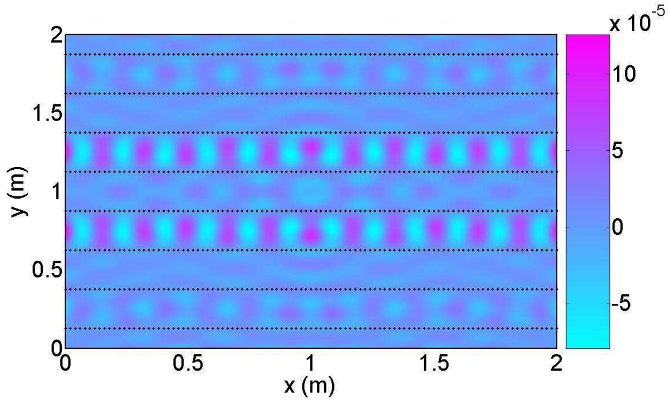

(a) Panel without defect

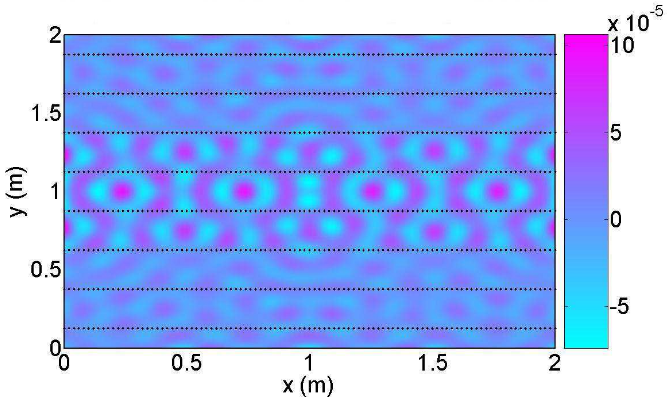

(b) Panel with defects

Figure 6.2: Case A: Displacement field of the ribbed panel without and with defects at 2kHz. The unit in z-axis is in meter.

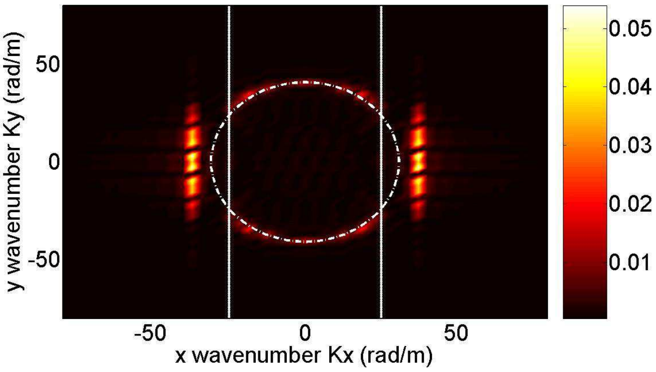

(a) Panel without defect

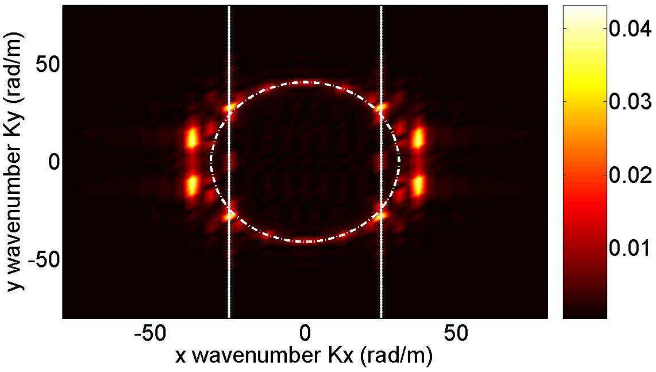

(b) Panel with defects

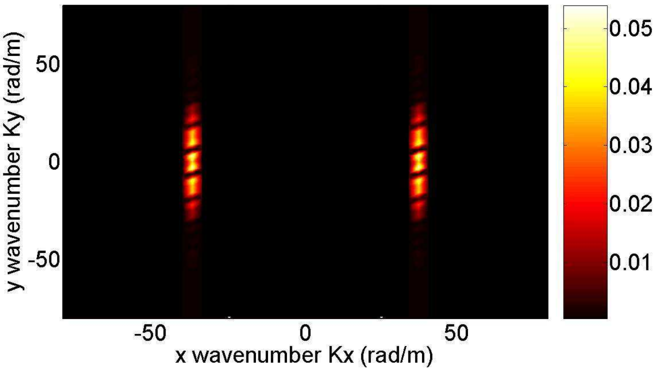

(c) Filtered k-space of the panel without defect

Figure 6.3: Case A: k-space of the ribbed panel without and with defects at 2kHz. The unit in z-axis is in meter.

be done by setting such threshold values that wave numbers $k_x > threshold^+$ or $k_x < threshold^-$ are set to zero, as shown in Figure 6.3(c). The Inverse

Discrete Fourier Transform (IDFT) process was subsequently applied to the filtered k-space data, and guided waves can be seen clearly in the rib direction x on the newly obtained displacement field in Figure 6.4(a). The black dotted lines in this figure represent the ribs. In order to assess the ability of defect detection by guided waves, two symmetric defects are applied on the two ribs in the middle of the panel for each case, and the finite element model used in case A is shown in Figure 6.1(b). The geometry and the corresponding geometric parameters of the defects are listed in Figure 6.5 and Table 6.2. The defect size is 0.12 m, which seems to be exaggerative, was chosen after an estimation of the wavelength of guided waves from the k-space plot displayed in Figure 6.3(a). Another way to calculate λ will be given later in subsection 6.3.2. Following the same steps as for the stiffened panel without defect, the k-space (see Figure 6.3(b)) was extracted from the calculated dis-

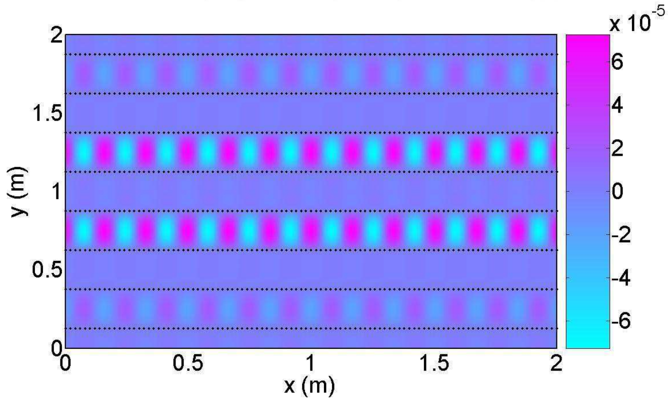

(a) Panel without defect

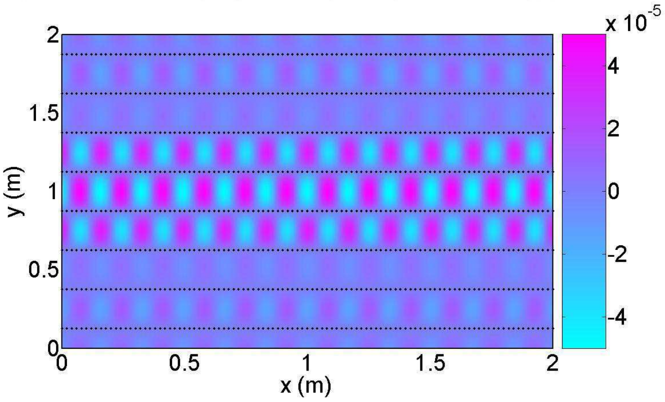

(b) Panel with defects

Figure 6.4: Case A: IDFT of the filtered k-space: guided waves in the ribbed panel without and with defects at 2kHz. The unit in z-axis is in meter. The black dotted lines represent the ribs.

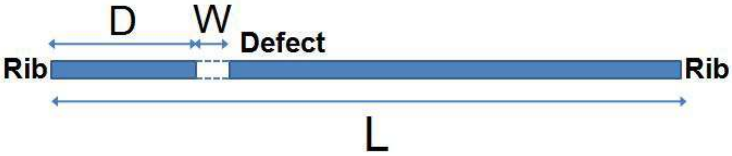

Figure 6.5: Geometry of defects in ribs.

L (m) total length of the rib	D (m) distance off the rib edge	W (m) width of the defect
2	0.44	0.12

Table 6.2: Geometrical parameters of the defects in the ribs.

placement field (see Figure 6.2(b)) of the stiffened panel with defects, at the same frequency 2kHz.

Thereafter, a comparison has been done between the results of the stiffened panel without defect and those of the stiffened panel with defects, and it can be seen from Figure 6.3 that the structural orthotropy stays almost unchanged, on the contrary, the two bars (representing guided waves) around the ellipse (representing the structural orthotropy) are different. The influence of the defects on the displacement field can be seen after the IDFT process, as displayed in Figure 6.4. For the panel with defects, three bright stripes can be seen in the displacement field, but for the stiffened panel without defect, there are only two bright stripes. The difference between the displacement fields of the two stiffened panels indicates that, defects have an important influence on the dynamical behavior of the panels, and the excited guided waves are sensitive to structure defects at this frequency. At higher frequencies, for example, at 3.6kHz, on the k-space plot, two new vertical bars appeared (see Figure 6.6). The filtering process and IDFT were applied to each pair of bars and the results were shown in Figure 6.7(a) (for the pair close to the ellipse) and in Figure 6.8(a) (for the pair farther from the ellipse). The two figures 6.7(a) and 6.8(a) both show the guided waves in the stiffened panel. Actually, the two guided waves are of different levels. Here two kinds of levels can be defined: the level of bars and the level of guided waves. The level of bars can be determined according to the appearance sequence of the bars in the k-space: for example, in Figure 6.6(a), the pair nearer to the ellipse is of a higher level (level-2) as it appears at a higher frequency, while the pair farther to the ellipse represents a lower level pair (level-1). The level of guided waves can be determined according to the number of node lines of the

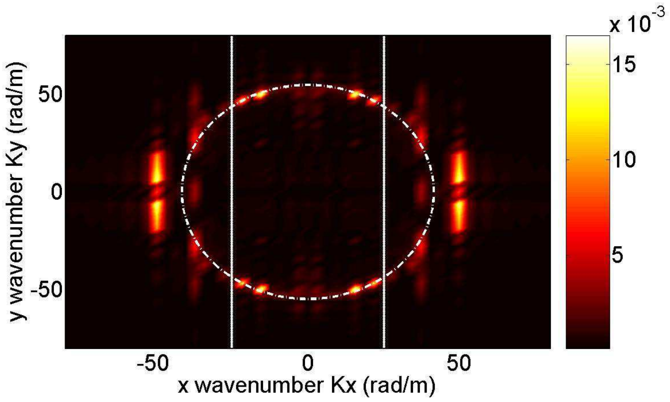

(a) Panel without defect

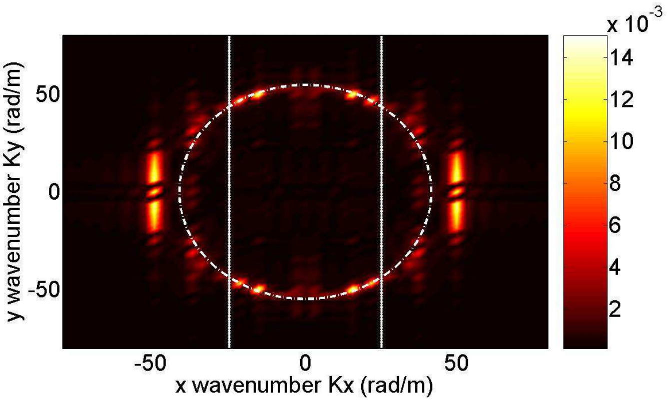

(b) Panel with defects

Figure 6.6: Case A: k-space of the ribbed panel without and with defects at 3.6kHz. The unit in z-axis is in meter.

stationary wave perpendicular to the rib direction: for example, the guided wave in Figure 6.7(a) is of level-3 as two node lines can be seen between the two ribs, and in Figure 6.8(a) the guided wave is of level-1 as no node line can be observed between the two ribs. Another computation was done for the same stiffened panel with defects in Figure 6.1(b) at 3.6kHz and similar results have been found, as shown in Figure 6.7(b) and Figure 6.8(b). In Figure 6.7, the difference between the displacement field is very clear; on the contrary, in Figure 6.8, this difference is less evident, which means that in this case, the guided waves of level-3 are more sensitive to the defects than the guided waves of level-1.

Other stiffened panels with different rib distances have also been studied, as in cases B and C. The k-spaces of the panels without defect in these two cases are shown in Figure 6.9. As the distance between the ribs increases from case C (0.125m) to case A (0.25m), then case B (0.5m), the stiffness of the stiffened

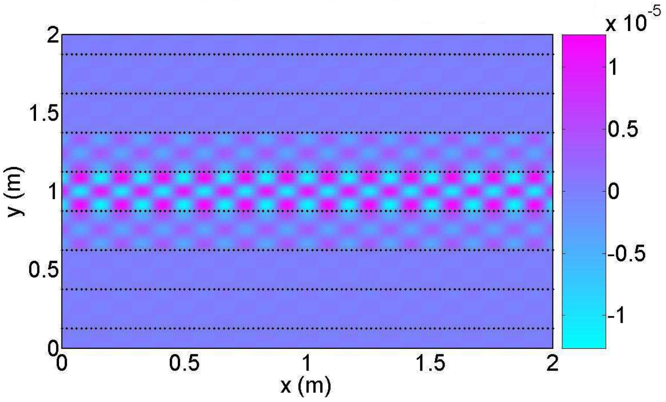

(a) Panel without defect: level-2 pair

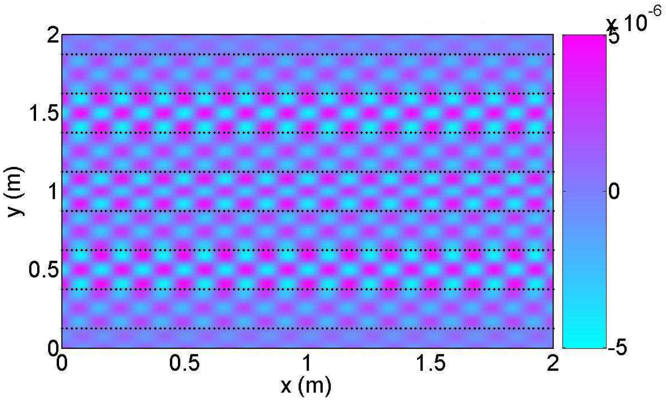

(b) Panel with defects: level-2 pair

Figure 6.7: Case A: IDFT of the level-2 pair of bars in the k-space at 3.6kHz. The unit in z-axis is in meter. The black dotted lines represent the ribs.

panel changes, so does the stationary wave in the direction orthogonal to the ribs (y direction), and different guided waves are excited (see Figure 6.10 for case B, and Figure 6.11 for case C). In case B, the IDFT of the level-1 bars is nearly the same for the two panels. However, if this displacement field is filtered by setting the displacement between the two ribs in the middle to zero, as the amplitude is the strongest, then the displacement field between other ribs can be observed clearly, and another propagation style can be found, as shown in Figure 6.10(b) and Figure 6.10(c). In Figure 6.10(b), the guided waves in the panel can be regarded as a pure phenomenon of propagation, but in Figure 6.10(c), the propagation feature is combined with a phase difference, and it looks like the wave scattering effect: guided waves are scattered by the defects. The filtering process in the new displacement field is often needed to observe the "scattered waves", as their amplitude is often much smaller than that of the excited guided waves. It should also be noticed that this filter-

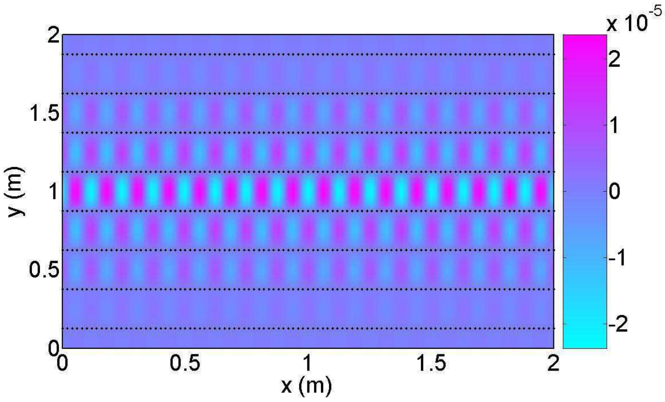

(a) Panel without defect: level-1 pair

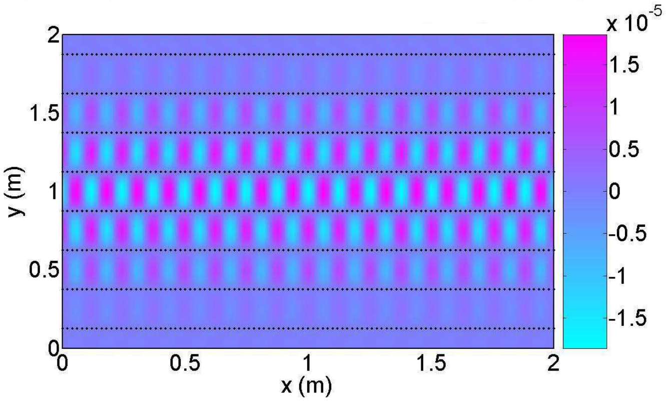

(b) Panel with defects: level-1 pair

Figure 6.8: Case A: IDFT of the level-1 pair of bars in the k-space at 3.6kHz. The unit in z-axis is in meter. The black dotted lines represent the ribs.

ing process is totally different from the k-space filtering, and it can be called "displacement field filtering". In case C, as shown in Figure 6.11(a) and Figure 6.11(b), guided waves are much less sensitive to defects than those in case B, as the difference between the filtered displacement fields are not so obvious, nor is the wave scattering effect. As a conclusion, first and foremost, the use of guided waves for the defect detection is feasible and the four steps for implementing the treatment process of the IWC method can be summarized as follows:

- Extraction: k-space is extracted from the measured or calculated displacement field of the stiffened panel in following an optimization process;
- Filtering: the structural orthotropy is "filtered" from the k-space, only the guided wave feature in the k-space is retained;

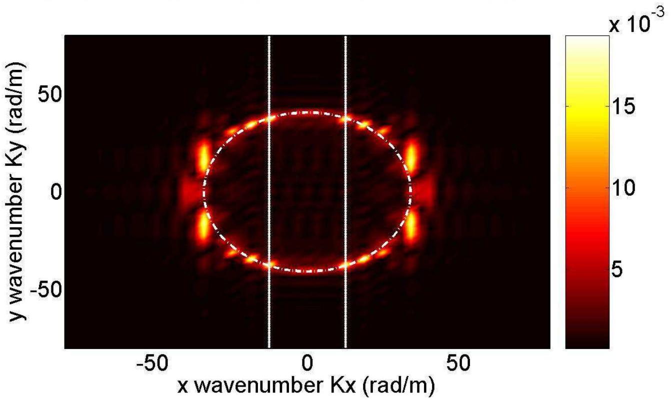

(a) Case B: panel without defect

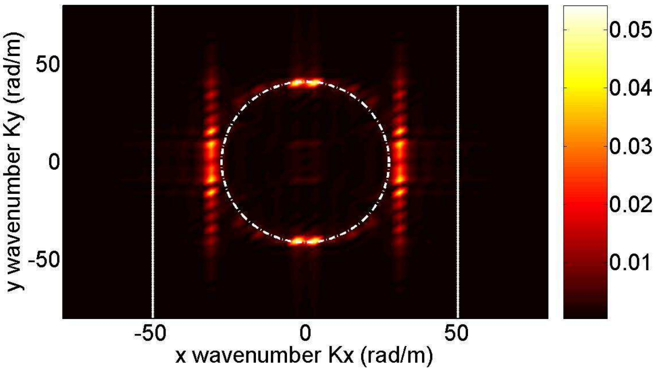

(b) Case C: panel without defect

Figure 6.9: k-space of the ribbed panels in case B and case C at 2kHz. The unit in z-axis is in meter.

- IDFT: the filtered k-space is dealt with using IDFT, and a new displacement field can be obtained, which represents the propagation of guided waves in the stiffened panel;
- Comparison: the difference between the newly obtained displacement field of a stiffened panel without defect and that of the damaged stiffened panel are analyzed and the sensitivity of the guided waves to defects can be determined. If the difference is obvious enough, the corresponding guided wave is sensitive to defects.

Secondly, the distance of ribs has an influence on the level of the excited guided waves: higher level guided waves are observed with a bigger rib distance, as the cut-off frequency of the waveguide (the ribs and the panel) is lower. Moreover, defects tend to have a bigger influence on a less rigid panel, as in case B, there are only 4 ribs in the panels, while in case C, there are 16 ribs in the panels,

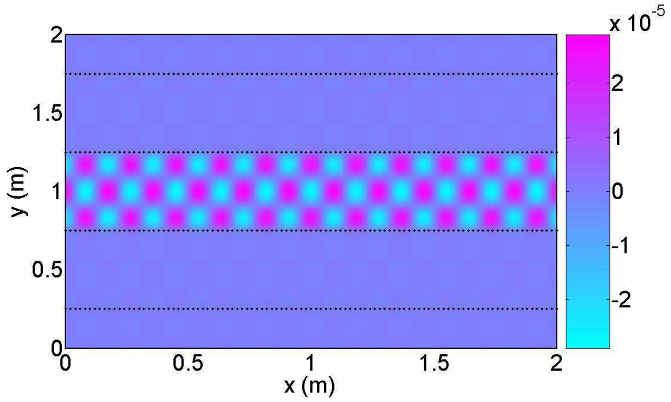

(a) Case B: with defects

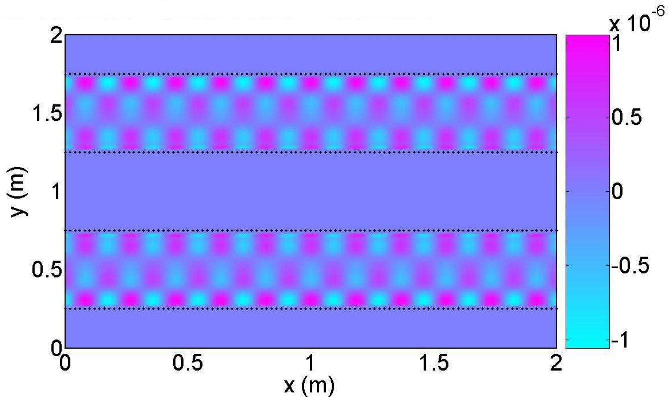

(b) Case B: without defect (filtered)

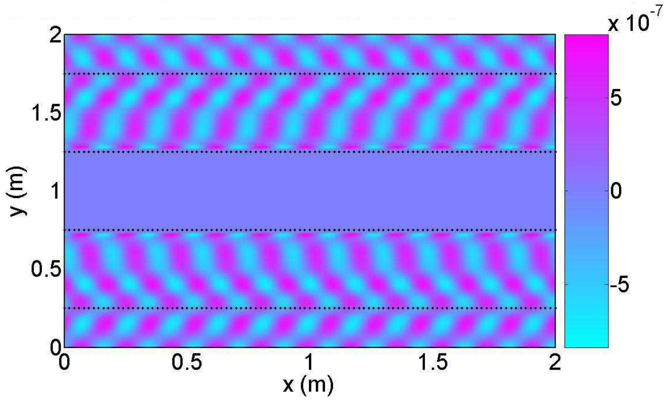

(c) Case B: with defects (filtered)

Figure 6.10: Cases B: IDFT of the level-1 pair of bars in the k-space at 2kHz. The unit in z-axis is in meter. The black dotted lines represent the ribs.

and guided waves are the least sensitive in case C. Almost all discontinuities such as joints, manholes, if they are in the simulated or measured zone of the

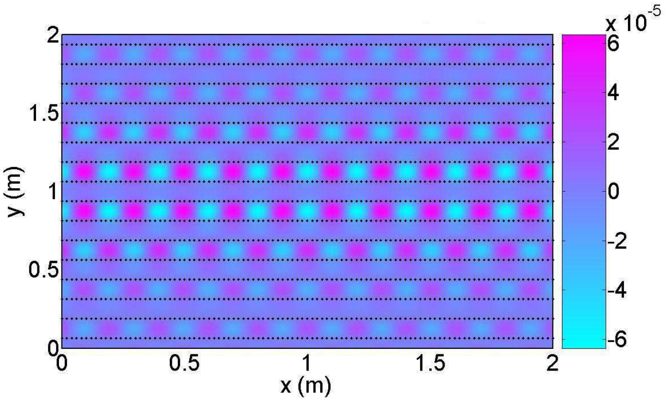

(a) Case C: without defect

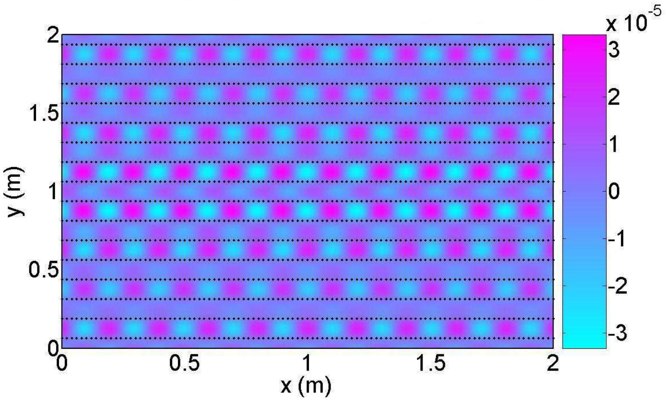

(b) Case C: with defects

Figure 6.11: Cases C: IDFT of the level-1 pair of bars in the k-space at 2kHz. The unit in z-axis is in meter. The black dotted lines represent the ribs.

panel, can be dealt with by the IWC technique. However, for plate edges, as mentioned in Section 6.2, there is a periodic hypothesis which indicates that the displacement field is supposed to be 2D periodic outside the simulated or measured displacement field. Thus plate edges are not taken into consideration if the IWC technique is applied.

6.3.2 Analysis of energy diffusion in damaged stiffened panels

In order to interpret the phenomenon observed in the previous subsection and to better understand the interaction between guided waves and the defects in the stiffened panel, the finite element diffusion model proposed in Mencik and Ichchou [46] was used. The reflection coefficient of a specific incident wave or several specific incident waves propagating in the damaged stiffened panel can be calculated so as to reveal the influence of the damage on wave propagation (see Ichchou *et al.* [49]).

Here, the propagation of guided waves in damaged stiffened panels is analyzed with an energy diffusion model representative of the stiffened panel. For the sake of simplicity, a plate made of aluminium with only two ribs made of steel was chosen for the numerical simulation. The definition of the geometric parameters of the stiffened panel and their values are the same as those indicated in Figure 6.1(c) and in case A in Table 6.1. The finite element model of this simplified stiffened panel (see Figure 6.12) was realized in ANSYS using SOLID45 elements with a global mesh resolution of $0.01 \times 0.02 \times 0.005$ m^3 in the panel and $0.01 \times 0.001 \times 0.005$ m^3 in the ribs. The diffusion model of the damaged stiffened panel (see Figure 6.13) was also created in ANSYS with the same element type and mesh resolution. The defect in the stiffened panel lies in the rib and its size is 0.12 m in the rib direction, just as the two symmetric defects in the stiffened panel displayed in Figure 6.1(b). The mass and stiffness matrices of the diffusion model were extracted and imported into MATLAB for post-treatments of the energy diffusion problem. As displayed in Figure 6.3 and Figure 6.6, the wavenumber of guided waves can be read directly from the k-Space. In fact, there is another way to analyze propagating wave modes and calculate their wavenumber: the resolution of the eigenvalue problem shown in (2.6) provides not only the incident and reflected wave modes (eigenvectors), but also the associated wavenumbers (eigenvalues). After that, dispersion curves describing the evolution of wavenumbers of the wave modes propagating in the waveguides can be drawn, as shown in Fig-

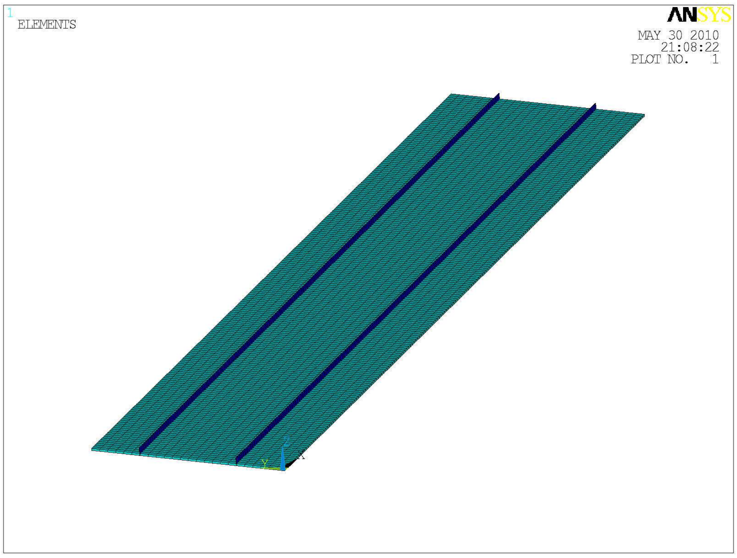

Figure 6.12: Finite Element model of the simplified ribbed panel.

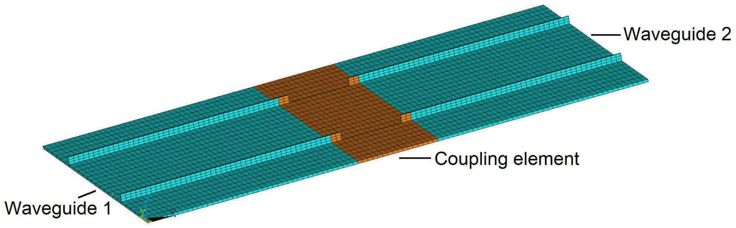

Figure 6.13: Diffusion model of the damaged ribbed panel.

ure 6.14. In the considered frequency band (0-4kH Hz), several types of waves

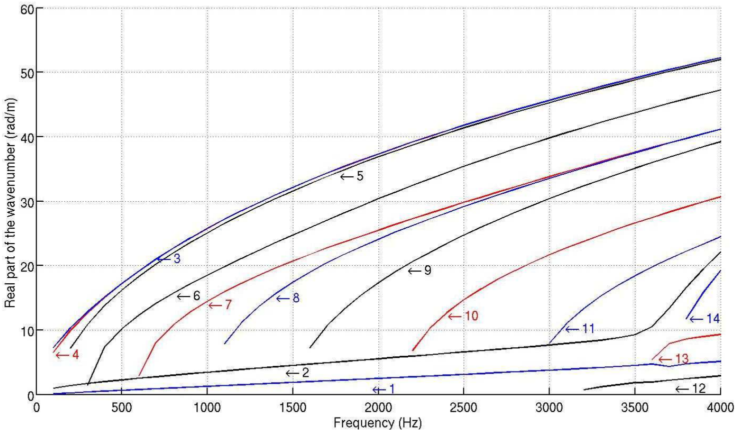

Figure 6.14: Dispersion curves of the wave modes in the waveguide: (1)1st Traction/Compression (2)1st Bending wave in y-axis (3)1st Bending wave in z-axis (4)1st Torsional wave in x-axis (5)2nd Bending wave in z-axis (6)1st antisymmetric Torsional wave in y-axis (7)1st symmetric Torsional wave in y-axis (8)2nd antisymmetric Torsional wave in y-axis (9)2nd symmetric Torsional wave in y-axis (10)3rd antisymmetric Torsional wave in y-axis (11)3rd symmetric Torsional wave in y-axis (12)3rd Bending wave in y-axis (13)4th Bending wave in y-axis (14)4th symmetric Torsional wave in y-axis

can propagate at the same time in x direction. By comparing the displacement fields in Figures 6.4 and 6.7 with the wave modes calculated from the eigenvalue problem (see equation (2.10)), four types of incident wave modes propagating in the rib direction and representative of the displacement fields of the stiffened panels were chosen, and the reflection coefficients of these wave modes were calculated with the diffusion model of the damaged stiffened panel. The deformed shape of the four wave modes are displayed in Figure 6.15 (1st and 2nd bending mode in z-axis) and Figure 6.16 (1st and 2nd symmetric torsional mode in y-axis). The solid lines represent the deformed shape while the dashed lines represent the non-deformed shape. These four wave modes can be identified by comparing the displacement fields in Figures 6.4 and 6.7 with the deformed shape of the wave modes. For instance, from the displacement displayed in Figure 6.4(b), the 1st bending mode (mode 3) can be identified and its wavenumber is around 40 rad/m. Moreover, as shown in Figure 6.14, at 2kHz, the wavenumber of the 1st bending mode (mode 3) is slightly smaller than 40 rad/m, which corresponds to a wavelength around 0.15 m. This fact explains why a defect size of 0.12 m, which seems exaggerative but close to the wavelength of the guided waves, was applied in the ribs of the panel. Then a comparison of the reflection coefficient between the case without defect and the case with defect was carried out in order to reveal the influence of the defect on the wave reflection for specific incident wave modes. As the reflection coefficient should be calculated frequency by frequency, at a specific frequency, symmetric wave modes which are propagating were chosen

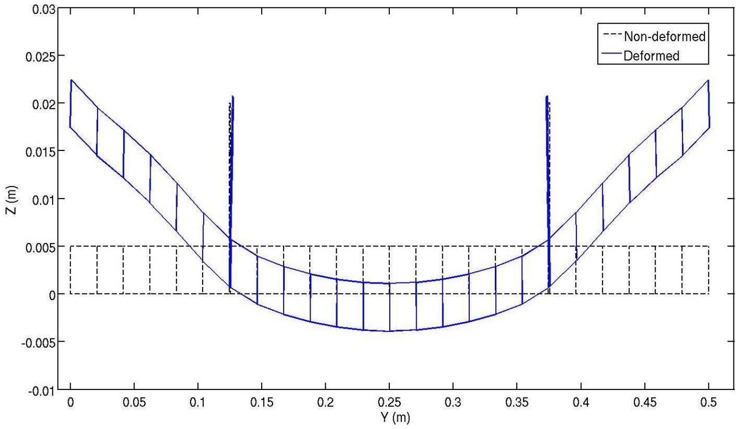

(a) 1st Bending wave

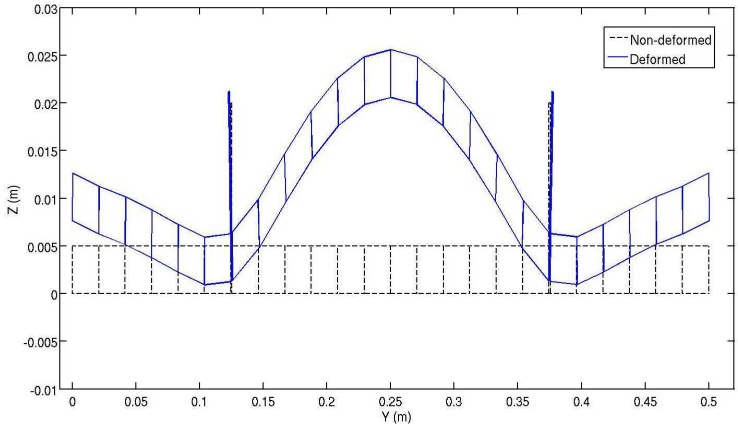

(b) 2nd Bending wave

Figure 6.15: Deformed shape of the two Bending wave modes in z-axis at 2kHz.

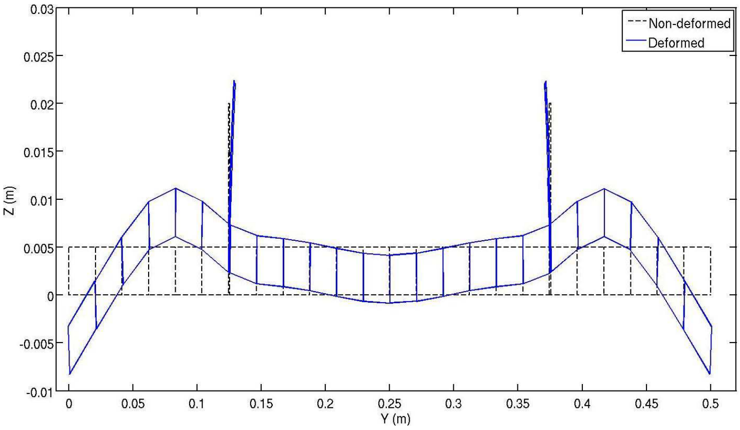

(a) 1st symmetric Torsional wave

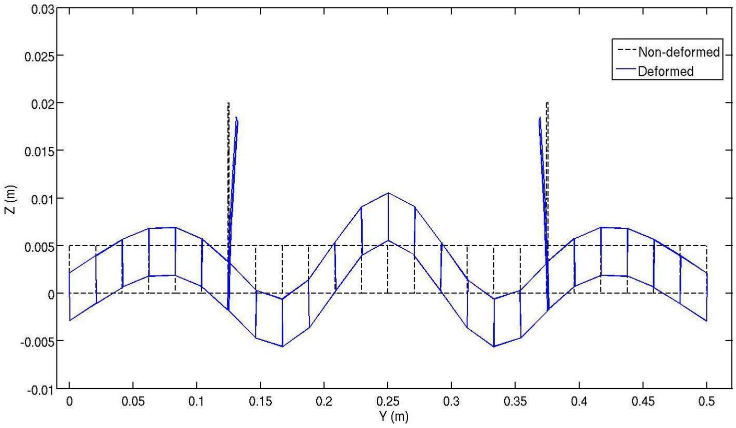

(b) 2nd symmetric Torsional wave

Figure 6.16: Deformed shape of the two symmetric Torsional wave modes in y-axis at 3.6kHz.

as incident wave modes in waveguide 1 with an wave amplitude $\mathbf{Q}^{\texttt{inc}(1)} = 1$. This choice of incident modes is due to the fact that as mentioned in Subsection 6.3.1, the stiffened panel was excited by a punctual force applied at the center of the panel, thus antisymmetric modes with no displacement at the central point would not be excited. It was also assumed that there were no incident waves in waveguide 2 (see Figure 6.13 for the waveguides), therefore $\mathbf{Q}^{\texttt{inc}(2)} = 0$. After that, the reflection coefficients of the four representative modes were calculated through equation (2.14) and presented in Figures 6.17 and 6.18. Here solid lines indicate the case with defect while dashed lines indicate the case without defect. According to the comparison, the defect in the stiffened panel does influence the reflection of the incident wave modes, as the difference between the case without defect and the case with defect is rather clear. For the case without damage, there is no wave reflection; when

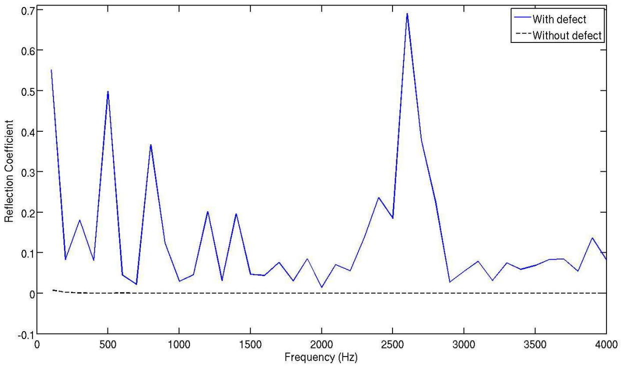

(a) 1st Bending wave

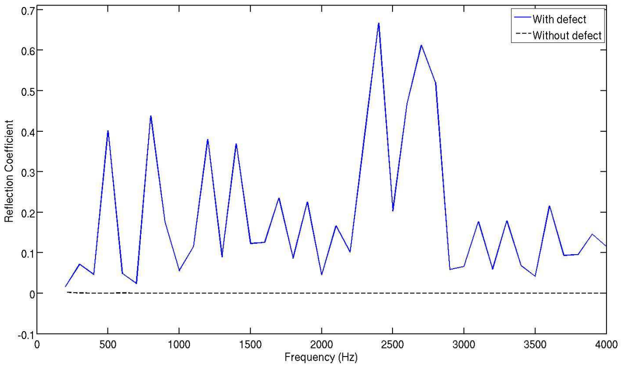

(b) 2nd Bending wave

Figure 6.17: Diffusion of the two Bending wave modes in z-axis.

damage exists in the stiffened panel, it influences the wave propagation. The value of the reflection coefficient gives an idea of the influence level: if the value is relatively big, the influence of the defect on this wave mode is strong; if the value is rather small, the influence of the defect on this wave mode is low. This influence depends on the damage size, on frequency, and on wave modes. If the influence can be properly observed, for example, by means of the reflection coefficient, the presence of defect can be detected. The incidents wave modes propagating in the rib direction are actually guided waves, and according to their interaction with the defect, their sensitivity to defects can be determined.

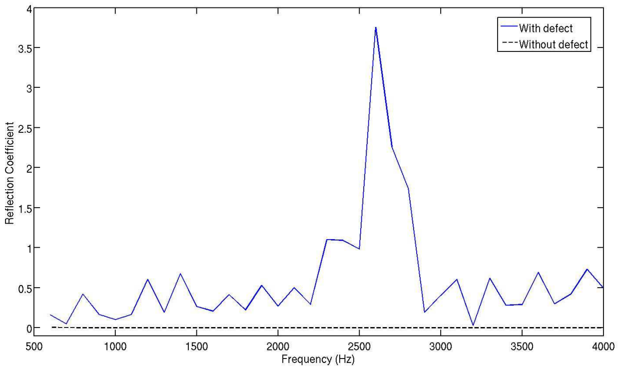

(a) 1st symmetric Torsional wave

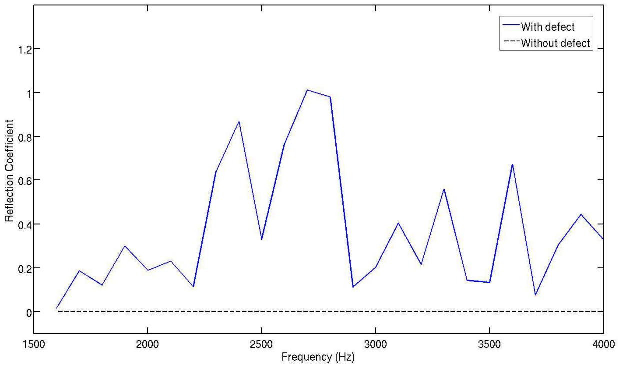

(b) 2nd symmetric Torsional wave

Figure 6.18: Diffusion of the two symmetric Torsional wave modes in y-axis.

6.4 Conclusions

New insights into the use of guided waves at medium frequencies for the damage detection in stiffened panels were provided in this work. The sensitivity of guided waves to defects in ribs of the stiffened panel at medium frequency range has been carefully analyzed. The main results can be summarized as follows:

- The IWC technique can be used to extract the k-space of two-dimensional structures, like panels, from their displacement field under harmonic excitation. With the help of a filtering process in the k-space and the IDFT, two dynamical behaviors can be found in the k-space of stiffened panels: one with an elliptic form being related to the structural orthotropy, and another one with a shape of symmetrical bars being related to guided waves in the stiffened panel. A new (reconstructed) displacement field can be obtained, which shows guided waves with a pure propagative feature along the rib direction x and a stationary feature in the direction y which is orthogonal to the ribs. The number of guided wave modes increases with the frequency, which leads to a **multi-mode wave propagation** phenomenon in the rib-stiffened plate. Those guided waves can subsequently be used for damage detection in stiffened panels at medium frequencies through a signal processing technique linking the displacement field and the wavenumber domain (the k-space). The presence of defects in structure is determined by comparing the new displacement field to the reference one.

- The IWC technique is able to provide a global vision of the structural vibration signature which can be influenced by the dynamical behavior of local singularities. By applying a propagative approach (instead of the modal approach), information like wavenumber can be extracted from experimental measurements or numerically simulated data (displacement field). For these extracted parameters, the previously quoted filtering process can highlight local singularities and hence defect locations. The sensitivity of guided waves to defects depends on many parameters, especially those who have an important influence on the stiffened panel's dynamics.

- The interaction between defects and guided waves in stiffened panels are also studied by using an energy diffusion analysis. The impact of defects on the propagation of guided waves along the rib can be observed by studying the energy diffusion of waves propagating in the stiffened panel through a finite element diffusion model. For a specific incident wave mode, or several specific incident wave modes, the reflection coefficient can be calculated and after that, a comparison between the case of a stiffened panel without defect and the case with defect can be performed to determine the influence of defects on the propagation of guided waves.

Finally, it must be mentioned that a frequency band from 0 to 4 kHz has been used throughout this work because in this frequency band, there is a limited number of modes that coexist. Thus, energy is shared only between these modes. This fact simplifies largely the capture of wave modes and their energy diffusion features. Further investigations should be done to complete the present work, as in this paperwork, the study of the sensitivity of guided waves to defects in stiffened panels is limited to numerical analysis. Physical models should also be established to explain the observed phenomena. Experiments will also be carried out not only to validate analytical and numerical results, but also to determine the effective area of local singularities' influence on the global structure's dynamics. Sensors could then be installed to right places in order to properly capture the global displacement field and tell if defects exist in the structure. The localization of defects as well as their severity should also be considered in the future.

Chapter 7

Conclusions and perspectives

Contents

7.1 General conclusions

This Ph.D. dissertation gives detailed formulations for the effective prediction tools of wave propagation(WFE) and diffusion(DMM) characteristics, as well as those for the dynamic behavior(FWFE) of smart structures equipped with shunted piezoelectric elements. These general formulations can be applied for all kinds of slender smart structures(solid, hollow, multi-layered, etc.), and take into account all kind of shunt circuits.

In Chapter 2, the finite element based WFE approach is developed and its corresponding DMM is extended to consider shunted piezoelectric elements in beam structures. Detailed description of the WFE approach is given for the analysis of solid and hollow beam structures. The MWFE formulation is also depicted carefully for the analysis of multi-layered composite structures. Finally, the finite element formulation for the piezoelectric field is described, with the shunt circuit taken into account.

Subsequently, in Chapters 3 and 4, all these aforementioned formulations are applied in three different situations (solid beam, hollow beam, and 3-layered composite beam). It can be noted that the wave modes propagating in the structure are correctly captured and the influence of the shunted piezoelectric patches on the control of specific wave modes can be investigated through the reflection and transmission coefficients. During the analyses of solid and hollow beams, the forced responses of the smart structures are calculated via the FWFE formulation. Then the time responses of the structure are evaluated via the IDFT approach applied to the frequency response. Reflection coefficients can be evaluated in another way according to the time response of the structure via a specific extraction technique proposed in this work. For the analysis of multi-layered composite structures, emphasis is put on the

parametric study of the dimensions of wave mode bases. The influence on the prediction of wave propagation and diffusion characteristics is investigated with care by varying the dimensions of the wave mode basis of each layer.
In Chapter 5, the performance of shunted piezoelectric patches with negative capacitance on the control of propagation and diffusion parameters is numerically analyzed and both the softening and stiffening effects are observed via the reflection and transmission coefficients as well as the frequency response function. In order to achieve desired functionalities of the smart structure, proper optimization criterions are defined through power flow analysis in the coupled system. The obtained optimization results in this chapter reveal the potential of the numerical tools proposed in the present work for the design of smart structures. Optimal electric and geometric parameters can be obtained via rigorous optimization procedures. Finally, in the design of smart structures with shunted piezoelectric patches, optimal parameters will be applied to control wave propagation and energy diffusion characteristics in a large frequency range.
In Chapter 6, the damage detection in stiffened panels using guided waves at medium frequencies is analyzed carefully with the IWC technique to extract the k-space from the displacement field under harmonic excitation. With a filtering process in the k-space and the IDFT, a reconstructed displacement field can be obtained to determine the presence of defects in structure. WFE and DMM are also applied to study the wave propagation and diffusion along the ribs of the stiffened panel in order to explain the observed phenomena. This technique can potentially be applied for the structural health monitoring of smart composite structures.
All the numerical techniques presented in this work enable the evaluation of the performance of shunted piezoelectric patches on the control of wave propagation, and facilitate design modifications and systematic investigations of geometric and electric parameters of smart structures with shunted piezoelectric patches. The performance of the intelligent vibroacoustic interface on wave propagation control and on structural health monitoring can firstly be evaluated numerically with all these techniques, and then be tested experimentally in the future work.

7.2 Future work

Experimental validation of the numerical results will be the first concern in the future work. Two different types of test will be carried out:

- Excitation with white noise to obtain the Frequency Response Function(FRF). The excitation point can be placed at any point along the central axis of the beam, with a shaker(low frequencies) or piezoelectric patch(medium and high frequencies).

- Excitation with wave packet to obtain the reflection coefficient. The excitation point can be placed at one extremity of the beam, with a piezoelectric patch or a pair of piezoelectric patches.

The experiment layout is defined in Figure 7.1. The shunted piezoelectric patches are placed in the middle of the beam. This experiment configuration is realized by suspending the beam vertically, as shown in Figure 7.2. The $R-L$ shunt circuit is realized via a synthetic circuit(Antoniou's circuit) displayed in Figure 7.3. The measurement of the FRF is much easier to realize

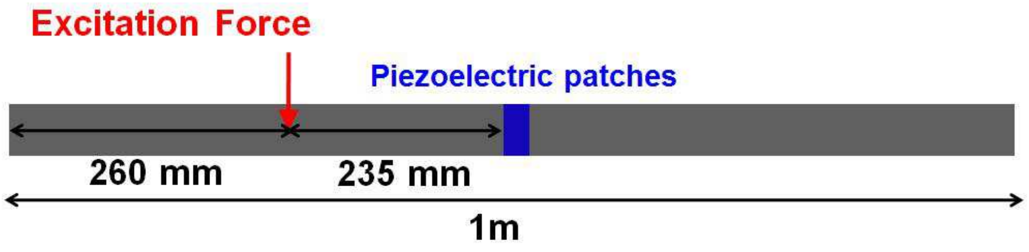

Figure 7.1: Defined experiment layout.

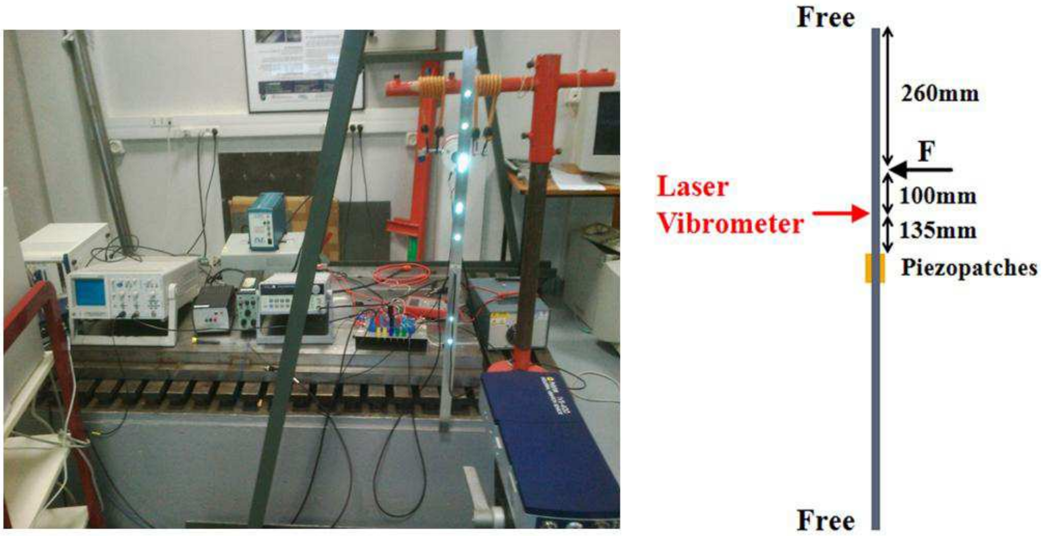

Figure 7.2: Realized experiment layout. Excitation with a shaker or piezoelectric patch. Measurement of vibration velocity with a laser vibrometer.

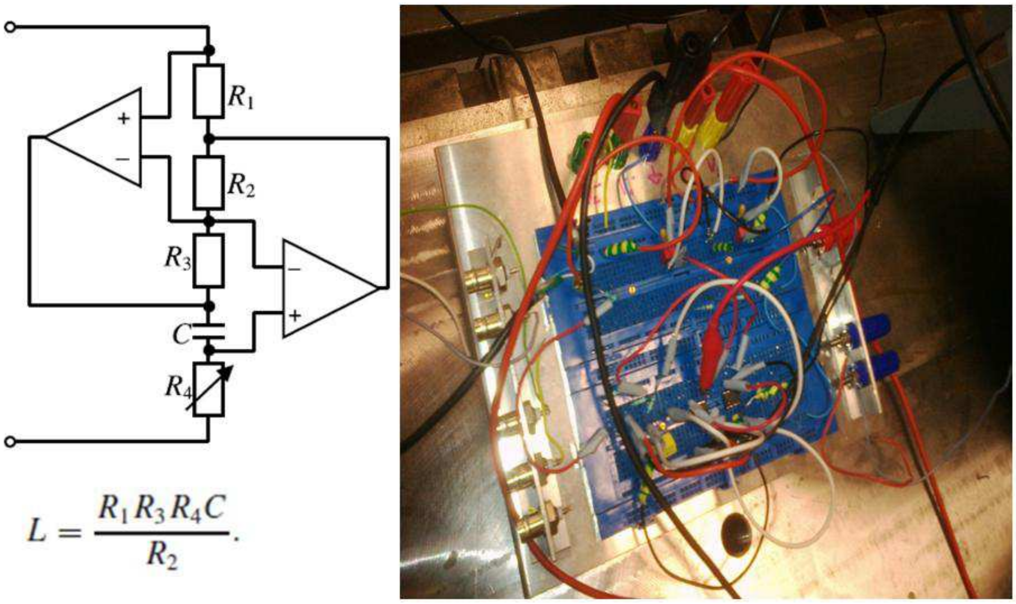

Figure 7.3: Antoniou's circuit.

than the measurement of the reflection coefficient with wave packet excitation. As the extensional wave in the beam is non-dispersive, it's much easier to capture the incident and reflected wave packets with the vibrometer, if the beam is long enough; however, for the dispersive bending wave modes, it's difficult to correctly capture the incident and reflected wave packets. Geometric parameters should be defined carefully to obtain desired results.

Wave propagation and energy diffusion in 2D smart structures will be the second concern in our future work. The wave propagation in 2D smart structures with periodically shunted piezoelectric patches has already been studied by Spadoni *et al.* [9] and Casadei *et al.* [12], etc. However, numerical tools for the evaluation of energy diffusion in such structures should be properly developed.

At last, the experiment on the energy diffusion in 1D smart structures with periodically shunted piezoelectric patches should be carried out. Thorp *et al.* [8] has already studied the wave propagation in such structures. The effect of periodic structure on energy diffusion should be investigated experimentally as well.

Appendix A

Material properties of the piezoelectric patch (type SG P189)

Mass density ρ: $\rho = 7650\ kg/m^3$.
Material stiffness matrix $\mathbf{c}^E$:

$$\mathbf{c}^E = 10^{10} \times \begin{bmatrix} 15.37 & 8.23 & 8.06 & 0 & 0 & 0 \\ 8.23 & 15.37 & 8.06 & 0 & 0 & 0 \\ 8.06 & 8.06 & 13.74 & 0 & 0 & 0 \\ 0 & 0 & 0 & 4.59 & 0 & 0 \\ 0 & 0 & 0 & 0 & 4.59 & 0 \\ 0 & 0 & 0 & 0 & 0 & 3.57 \end{bmatrix} Pa$$

The piezoelectric stress coupling matrix $\mathbf{e}$:

$$\mathbf{e} = \begin{bmatrix} 0 & 0 & 0 & 0 & 12.88 & 0 \\ 0 & 0 & 0 & 12.88 & 0 & 0 \\ -6.187 & -6.187 & 12.80 & 0 & 0 & 0 \end{bmatrix} N/(V \cdot m)$$

The piezoelectric strain coupling matrix $\mathbf{d}$:

$$\mathbf{d} = 10^{-10} \times \begin{bmatrix} 0 & 0 & 0 & 0 & 2.806 & 0 \\ 0 & 0 & 0 & 2.806 & 0 & 0 \\ -0.920 & -0.920 & 1.984 & 0 & 0 & 0 \end{bmatrix} m/V$$

The permittivity matrix under constant strain $\boldsymbol{\varepsilon}^S$:

$$\boldsymbol{\varepsilon}^S = 10^{-8} \times \begin{bmatrix} 1.011 & 0 & 0 \\ 0 & 1.011 & 0 \\ 0 & 0 & 0.591 \end{bmatrix} C/(V \cdot m)$$

The permittivity matrix under constant stress $\boldsymbol{\varepsilon}^T$:

$$\boldsymbol{\varepsilon}^T = 10^{-8} \times \begin{bmatrix} 1.372 & 0 & 0 \\ 0 & 1.372 & 0 \\ 0 & 0 & 0.959 \end{bmatrix} C/(V \cdot m)$$

Appendix B

Full development of the dynamic equilibrium of the unit cell in the WFE method

---

The dynamical equilibrium (before condensation) of any substructure k displayed in Figure 2.1 in Subsection 2.1.1 can be formulated in this manner:

$$\mathbf{D}\begin{pmatrix}\mathbf{q}_{\mathtt{L}}^{(k)}\\ \mathbf{q}_{\mathtt{I}}^{(k)}\\ \mathbf{q}_{\mathtt{R}}^{(k)}\end{pmatrix}=\begin{pmatrix}\mathbf{F}_{\mathtt{L}}^{(k)}\\ \mathbf{0}\\ \mathbf{F}_{\mathtt{R}}^{(k)}\end{pmatrix}, \tag{B.1}$$

where $\mathbf{q}_{\mathtt{I}}$ represents the displacements of the internal DOFs of the substructure and $\mathbf{D}$ is a symmetric matrix $\mathbf{D}^{\mathtt{T}}=\mathbf{D}$, representing the complex dynamical stiffness of the substructure:

$$\mathbf{D}=-\omega^2\mathbf{M}+\mathbf{K}(1+\mathtt{i}\eta). \tag{B.2}$$

Precisely, equation (B.1) is formulated in this way:

$$\begin{bmatrix}\mathbf{D}_{\mathtt{LL}} & \mathbf{D}_{\mathtt{LI}} & \mathbf{D}_{\mathtt{LR}}\\ \mathbf{D}_{\mathtt{IL}} & \mathbf{D}_{\mathtt{II}} & \mathbf{D}_{\mathtt{IR}}\\ \mathbf{D}_{\mathtt{RL}} & \mathbf{D}_{\mathtt{RI}} & \mathbf{D}_{\mathtt{RR}}\end{bmatrix}\begin{pmatrix}\mathbf{q}_{\mathtt{L}}^{(k)}\\ \mathbf{q}_{\mathtt{I}}^{(k)}\\ \mathbf{q}_{\mathtt{R}}^{(k)}\end{pmatrix}=\begin{pmatrix}\mathbf{F}_{\mathtt{L}}^{(k)}\\ \mathbf{0}\\ \mathbf{F}_{\mathtt{R}}^{(k)}\end{pmatrix}, \tag{B.3}$$

Equation (B.3) can be simplified by expressing displacements $\mathbf{q}_{\mathtt{I}}$ from the other kinematic quantities. Indeed, it can be shown that

$$\left[\begin{array}{c|c}\mathbf{D}_{\mathtt{LL}}-\mathbf{D}_{\mathtt{LI}}\mathbf{D}_{\mathtt{II}}^{-1}\mathbf{D}_{\mathtt{IL}} & \mathbf{D}_{\mathtt{LR}}-\mathbf{D}_{\mathtt{LI}}\mathbf{D}_{\mathtt{II}}^{-1}\mathbf{D}_{\mathtt{IR}}\\ \hline \mathbf{D}_{\mathtt{RL}}-\mathbf{D}_{\mathtt{RI}}\mathbf{D}_{\mathtt{II}}^{-1}\mathbf{D}_{\mathtt{IL}} & \mathbf{D}_{\mathtt{RR}}-\mathbf{D}_{\mathtt{RI}}\mathbf{D}_{\mathtt{II}}^{-1}\mathbf{D}_{\mathtt{IR}}\end{array}\right]\begin{pmatrix}\mathbf{q}_{\mathtt{L}}^{(k)}\\ \mathbf{q}_{\mathtt{R}}^{(k)}\end{pmatrix}=\begin{pmatrix}\mathbf{F}_{\mathtt{L}}^{(k)}\\ \mathbf{F}_{\mathtt{R}}^{(k)}\end{pmatrix}, \tag{B.4}$$

and finally we will be able to obtain equation (2.1) and equation (2.2) describing the condensed dynamical relation of substructure k on the DOFs of the left and right boundaries. According to the symmetry of matrix $\mathbf{D}$ and considering equation (B.4), it appears that matrix $\mathbf{D}^*$ in equation (2.1) is symmetric.

It can be shown that matrix $\mathbf{S}$ in equation (2.3) and equation (2.4) is symplectic. Indeed,

$$\mathbf{J}_n\mathbf{S} = \left[\begin{array}{c|c} \mathbf{D}^*_{\mathtt{RL}} - \mathbf{D}^*_{\mathtt{RR}}(\mathbf{D}^*_{\mathtt{LR}})^{-1}\mathbf{D}^*_{\mathtt{LL}} & -\mathbf{D}^*_{\mathtt{RR}}(\mathbf{D}^*_{\mathtt{LR}})^{-1} \\ \hline (\mathbf{D}^*_{\mathtt{LR}})^{-1}\mathbf{D}^*_{\mathtt{LL}} & (\mathbf{D}^*_{\mathtt{LR}})^{-1} \end{array}\right], \tag{B.5}$$

and

$$\mathbf{S}^{\mathtt{T}}\mathbf{J}_n\mathbf{S} = \left[\begin{array}{c|c} \begin{array}{c} -(\mathbf{D}^*_{\mathtt{LL}})^{\mathtt{T}}(\mathbf{D}^*_{\mathtt{LR}})^{-\mathtt{T}}\mathbf{D}^*_{\mathtt{RL}} \\ +(\mathbf{D}^*_{\mathtt{LL}})^{\mathtt{T}}(\mathbf{D}^*_{\mathtt{LR}})^{-\mathtt{T}}\mathbf{D}^*_{\mathtt{RR}}(\mathbf{D}^*_{\mathtt{LR}})^{-1}\mathbf{D}^*_{\mathtt{LL}} \\ +(\mathbf{D}^*_{\mathtt{RL}})^{\mathtt{T}}(\mathbf{D}^*_{\mathtt{LR}})^{-1}\mathbf{D}^*_{\mathtt{LL}} \\ -(\mathbf{D}^*_{\mathtt{LL}})^{\mathtt{T}}(\mathbf{D}^*_{\mathtt{LR}})^{-\mathtt{T}}(\mathbf{D}^*_{\mathtt{RR}})^{\mathtt{T}}(\mathbf{D}^*_{\mathtt{LR}})^{-1}\mathbf{D}^*_{\mathtt{LL}} \end{array} & \begin{array}{c} (\mathbf{D}^*_{\mathtt{LL}})^{\mathtt{T}}(\mathbf{D}^*_{\mathtt{LR}})^{-\mathtt{T}}\mathbf{D}^*_{\mathtt{RR}}(\mathbf{D}^*_{\mathtt{LR}})^{-1} \\ +(\mathbf{D}^*_{\mathtt{RL}})^{\mathtt{T}}(\mathbf{D}^*_{\mathtt{LR}})^{-1} \\ -(\mathbf{D}^*_{\mathtt{LL}})^{\mathtt{T}}(\mathbf{D}^*_{\mathtt{LR}})^{-\mathtt{T}}(\mathbf{D}^*_{\mathtt{RR}})^{\mathtt{T}}(\mathbf{D}^*_{\mathtt{LR}})^{-1} \\ \end{array} \\ \hline \begin{array}{c} -(\mathbf{D}^*_{\mathtt{LR}})^{-\mathtt{T}}\mathbf{D}^*_{\mathtt{RL}} \\ +(\mathbf{D}^*_{\mathtt{LR}})^{-\mathtt{T}}\mathbf{D}^*_{\mathtt{RR}}(\mathbf{D}^*_{\mathtt{LR}})^{-1}\mathbf{D}^*_{\mathtt{LL}} \\ -(\mathbf{D}^*_{\mathtt{LR}})^{-\mathtt{T}}(\mathbf{D}^*_{\mathtt{RR}})^{\mathtt{T}}(\mathbf{D}^*_{\mathtt{LR}})^{-1}\mathbf{D}^*_{\mathtt{LL}} \end{array} & \begin{array}{c} (\mathbf{D}^*_{\mathtt{LR}})^{-\mathtt{T}}\mathbf{D}^*_{\mathtt{RR}}(\mathbf{D}^*_{\mathtt{LR}})^{-1} \\ -(\mathbf{D}^*_{\mathtt{LR}})^{-\mathtt{T}}(\mathbf{D}^*_{\mathtt{RR}})^{\mathtt{T}}(\mathbf{D}^*_{\mathtt{LR}})^{-1} \\ \end{array} \end{array}\right]. \tag{B.6}$$

Observing that matrix $\mathbf{D}^*$ is symmetric,

$$(\mathbf{D}^*_{\mathtt{LL}})^{\mathtt{T}} = \mathbf{D}^*_{\mathtt{LL}} \quad , \quad (\mathbf{D}^*_{\mathtt{LR}})^{\mathtt{T}} = \mathbf{D}^*_{\mathtt{RL}} \quad , \quad (\mathbf{D}^*_{\mathtt{RL}})^{\mathtt{T}} = \mathbf{D}^*_{\mathtt{LR}} \quad , \quad (\mathbf{D}^*_{\mathtt{RR}})^{\mathtt{T}} = \mathbf{D}^*_{\mathtt{RR}} \quad , \tag{B.7}$$

it can be easily seen that

$$\mathbf{S}^{\mathtt{T}}\mathbf{J}_n\mathbf{S} = \begin{bmatrix} \mathbf{0} & \mathbf{I}_n \\ -\mathbf{I}_n & \mathbf{0} \end{bmatrix}. \tag{B.8}$$

From the coupling conditions — $\mathbf{q}_{\mathtt{L}}^{(k)} = \mathbf{q}_{\mathtt{R}}^{(k-1)}$ and $-\mathbf{F}_{\mathtt{L}}^{(k)} = \mathbf{F}_{\mathtt{R}}^{(k-1)}$ (cf. Figure 2.1) — two consecutive substructures k and $k-1$ are related through the following expression,

$$\mathbf{u}_{\mathtt{L}}^{(k)} = \mathbf{u}_{\mathtt{R}}^{(k-1)} \quad \forall k \in \{2, \ldots, N\}, \tag{B.9}$$

which leads to (cf. equation (2.3))

$$\mathbf{u}_{\mathtt{L}}^{(k)} = \mathbf{S}\mathbf{u}_{\mathtt{L}}^{(k-1)}. \tag{B.10}$$

The analysis of the dynamical behavior of the waveguide is based on Bloch's theorem [74], which states that solutions $\mathbf{u}_{\mathtt{L}}$ are of the form

$$\mathbf{u}_{\mathtt{L}}^{(k)} = \mu\mathbf{u}_{\mathtt{L}}^{(k-1)} \quad \forall k \in \{2, \ldots, N\}. \tag{B.11}$$

From equation (B.10), the boundary value problem in equation (2.6) can be established.

If the kinematic quantities are represented through state vectors $\mathbf{u}_{\mathtt{L}}^{(k)} = ((\mathbf{q}_{\mathtt{L}}^{(k)})^{\mathtt{T}}(\mathbf{F}_{\mathtt{L}}^{(k)})^{\mathtt{T}})^{\mathtt{T}}$ and $\mathbf{u}_{\mathtt{R}}^{(k)} = ((\mathbf{q}_{\mathtt{R}}^{(k)})^{\mathtt{T}}(-\mathbf{F}_{\mathtt{R}}^{(k)})^{\mathtt{T}})^{\mathtt{T}}$, with the definition in equation (2.7), it can be shown that matrix $\mathbf{S}'$ is symplectic. And in order to prove that the eigenvalues of matrix $\mathbf{S}'$ are the same of those of matrix $\mathbf{S}$, let us consider the wave modes $\{(\mu_i, \mathbf{\Phi}_i)\}_i$, solutions of matrix $\mathbf{S}$. A specific mode i is associated to the following equation :

$$\mathbf{S} \begin{pmatrix} (\mathbf{\Phi}_{\mathtt{q}})_i \\ (\mathbf{\Phi}_{\mathtt{F}})_i \end{pmatrix} = \mu_i \begin{pmatrix} (\mathbf{\Phi}_{\mathtt{q}})_i \\ (\mathbf{\Phi}_{\mathtt{F}})_i \end{pmatrix}. \tag{B.12}$$

Observing that

$$\begin{pmatrix} (\mathbf{\Phi}_{\mathtt{q}})_i \\ (\mathbf{\Phi}_{\mathtt{F}})_i \end{pmatrix} = \begin{bmatrix} \mathbf{I}_n & \mathbf{0} \\ \mathbf{0} & -\mathbf{I}_n \end{bmatrix} \begin{pmatrix} (\mathbf{\Phi}_{\mathtt{q}})_i \\ -(\mathbf{\Phi}_{\mathtt{F}})_i \end{pmatrix}, \tag{B.13}$$

it can be easily shown that

$$\mathbf{S}' \begin{pmatrix} (\mathbf{\Phi}_{\mathtt{q}})_i \\ -(\mathbf{\Phi}_{\mathtt{F}})_i \end{pmatrix} = \mu_i \begin{pmatrix} (\mathbf{\Phi}_{\mathtt{q}})_i \\ -(\mathbf{\Phi}_{\mathtt{F}})_i \end{pmatrix}. \tag{B.14}$$

Thus, it has been demonstrated that the wave modes which are solutions of matrix $\mathbf{S}'$ are defined by $\{(\mu_i, \mathbf{\Phi}'_i)\}_i$ where

$$\mathbf{\Phi}'_i = \begin{pmatrix} (\mathbf{\Phi}_{\mathtt{q}})_i \\ -(\mathbf{\Phi}_{\mathtt{F}})_i \end{pmatrix} \quad \forall i. \tag{B.15}$$

Finally, it can be shown that amplitudes $\mathbf{Q}$ associated with eigenvectors $\mathbf{\Phi}$ of matrix $\mathbf{S}$ are the same as those associated with eigenvectors $\mathbf{\Phi}'$ of matrix $\mathbf{S}'$. Indeed, the state vector of a substructure k can be described by:

$$\begin{pmatrix} \mathbf{q}_{\mathrm{L}}^{(k)} \\ -\mathbf{F}_{\mathrm{L}}^{(k)} \end{pmatrix} = \begin{bmatrix} \mathbf{\Phi}_{\mathtt{q}} \\ \mathbf{\Phi}_{\mathtt{F}} \end{bmatrix} \mathbf{Q}^{(k)}. \tag{B.16}$$

Observing that

$$\begin{pmatrix} \mathbf{q}_{\mathrm{L}}^{(k)} \\ -\mathbf{F}_{\mathrm{L}}^{(k)} \end{pmatrix} = \begin{bmatrix} \mathbf{I}_n & \mathbf{0} \\ \mathbf{0} & -\mathbf{I}_n \end{bmatrix} \begin{pmatrix} \mathbf{q}_{\mathrm{L}}^{(k)} \\ \mathbf{F}_{\mathrm{L}}^{(k)} \end{pmatrix} \quad \text{and} \quad \begin{bmatrix} \mathbf{\Phi}_{\mathtt{q}} \\ \mathbf{\Phi}_{\mathtt{F}} \end{bmatrix} = \begin{bmatrix} \mathbf{I}_n & \mathbf{0} \\ \mathbf{0} & -\mathbf{I}_n \end{bmatrix} \begin{bmatrix} \mathbf{\Phi}'_{\mathtt{q}} \\ \mathbf{\Phi}'_{\mathtt{F}} \end{bmatrix}, \tag{B.17}$$

it appears that

$$\begin{pmatrix} \mathbf{q}_{\mathrm{L}}^{(k)} \\ \mathbf{F}_{\mathrm{L}}^{(k)} \end{pmatrix} = \begin{bmatrix} \mathbf{\Phi}'_{\mathtt{q}} \\ \mathbf{\Phi}'_{\mathtt{F}} \end{bmatrix} \mathbf{Q}^{(k)}, \tag{B.18}$$

which leads to

$$\mathbf{Q}'^{(k)} = \mathbf{Q}^{(k)} \tag{B.19}$$

Let us consider a specific eigenvalue, say μ_i, of problem (equation (2.6)), that is,

$$\mathbf{S}\boldsymbol{\Phi}_i = \mu_i \boldsymbol{\Phi}_i. \tag{B.20}$$

Multiplying equation (B.20) by $\mathbf{S}^{\mathsf{T}}\mathbf{J}_n$ leads to

$$\mathbf{S}^{\mathsf{T}}\mathbf{J}_n\mathbf{S}\boldsymbol{\Phi}_i = \mu_i \mathbf{S}^{\mathsf{T}}\mathbf{J}_n\boldsymbol{\Phi}_i. \tag{B.21}$$

Considering the fact that matrix $\mathbf{S}$ is symplectic (cf. equation (B.8)), equation (B.21) is written

$$\mathbf{J}_n\boldsymbol{\Phi}_i = \mu_i \mathbf{S}^{\mathsf{T}}\mathbf{J}_n\boldsymbol{\Phi}_i. \tag{B.22}$$

Considering the transpose of equation (B.22) and the properties of matrix $\mathbf{J}_n$ (equation (2.5)), the following relationship can be established:

$$(\boldsymbol{\Phi}_i^{\mathsf{T}}\mathbf{J}_n)\mathbf{S} = \frac{1}{\mu_i}(\boldsymbol{\Phi}_i^{\mathsf{T}}\mathbf{J}_n) \tag{B.23}$$

Hence, $(\boldsymbol{\Phi}_i)^{\mathsf{T}}\mathbf{J}_n$ is a left eigenvector of matrix $\mathbf{S}$, meaning that $1/(\mu_i)$ is then an eigenvalue of $\mathbf{S}$. In this way, the eigenvalues can finally be defined in equation (2.9) in Subsection 2.1.1.

Appendix C

Diffusion Matrix in case of non compatible meshes at interfaces Γ_i

---

In a general manner, it can be supposed that, on a specific coupling surface Γ_i, the number of DOFs of the coupling element, say n^i_{c}, is different from that of the coupled substructure (say n_i). Nevertheless, the continuity of the displacement field on coupling surfaces Γ_1 and Γ_2 can be ensured by the introduction of two Lagrange multiplier fields $\boldsymbol{\lambda}_1$ and $\boldsymbol{\lambda}_2$ [109]. The variational formulation of the two substructures coupled with the coupling element can then be established in the following form [109, 110]:

$$
\begin{aligned}
&\sum_{i=1,2}\left(-\omega^2\int_{\Omega_i}\rho(\delta\mathbf{w}^{(i)})^{\mathsf{T}}\mathbf{w}^{(i)}\,d\mathbf{x}+\int_{\Omega_i}(\boldsymbol{\varepsilon}(\delta\mathbf{w}^{(i)}))^{\mathsf{T}}\boldsymbol{\sigma}(\mathbf{w}^{(i)})\,d\mathbf{x}\right)\\
&+\left(-\omega^2\int_{\Omega_{\mathsf{c}}}\rho(\delta\mathbf{w}^{\mathsf{c}})^{\mathsf{T}}\mathbf{w}^{\mathsf{c}}\,d\mathbf{x}+\int_{\Omega_{\mathsf{c}}}(\boldsymbol{\varepsilon}(\delta\mathbf{w}^{\mathsf{c}}))^{\mathsf{T}}\boldsymbol{\sigma}(\mathbf{w}^{\mathsf{c}})\,d\mathbf{x}\right)\\
&+\int_{\Gamma_1}(\delta\boldsymbol{\lambda}_1)^{\mathsf{T}}(\mathbf{w}^{\mathsf{c}}-\mathbf{w}^{(1)})\,ds(\mathbf{x})+\int_{\Gamma_2}(\delta\boldsymbol{\lambda}_2)^{\mathsf{T}}(\mathbf{w}^{\mathsf{c}}-\mathbf{w}^{(2)})\,ds(\mathbf{x})\\
&+\int_{\Gamma_1}(\delta\mathbf{w}^{\mathsf{c}}-\delta\mathbf{w}^{(1)})\boldsymbol{\lambda}_1\,ds(\mathbf{x})+\int_{\Gamma_2}(\delta\mathbf{w}^{\mathsf{c}}-\delta\mathbf{w}^{(2)})\boldsymbol{\lambda}_2\,ds(\mathbf{x})\\
&=\int_{S_1}(\delta\mathbf{w}^{(1)})^{\mathsf{T}}\mathbf{f}^{(1)}\,ds(\mathbf{x})+\int_{S_2}(\delta\mathbf{w}^{(2)})^{\mathsf{T}}\mathbf{f}^{(2)}\,ds(\mathbf{x}),
\end{aligned}
\tag{C.1}
$$

where $\mathbf{w}^{(i)}$ and $\mathbf{w}^{\mathsf{c}}$ stand for the displacement field of substructure i ($i=1,2$) and the displacement field of the coupling element, defined in Ω_i and Ω_{c} respectively; $\mathbf{f}^{(i)}$ ($i=1,2$) stands for the force applied to substructure i on S_i. In the context of the Finite Element Method, substructures 1, 2 and the coupling element are discretized into several elements $\{\Omega^{(1)}_e\}_{e=1,\ldots,m_1}$, $\{\Omega^{(2)}_e\}_{e=1,\ldots,m_2}$ and $\{\Omega^{\mathsf{c}}_e\}_{e=1,\ldots,m_{\mathsf{c}}}$:

$$
\mathbf{w}^{(i)}=\mathbf{N}^{(i)}_e\mathbf{q}^{(i)}_e\quad\text{in }\Omega^{(i)}_e\quad(i=1,2)\quad,\quad\mathbf{w}^{\mathsf{c}}=\mathbf{N}^{\mathsf{c}}_e\mathbf{q}^{\mathsf{c}}_e\quad\text{in }\Omega^{\mathsf{c}}_e\,,
\tag{C.2}
$$

where $\mathbf{N}^{(i)}_e$ and $\mathbf{N}^{\mathsf{c}}_e$ stand for the matrices of the interpolation functions of element $\Omega^{(i)}_e$ ($i=1,2$) and Ω^{c}_e, respectively, defined such that

$$\mathbf{N}_e^{(i)}(\mathbf{x}) = \mathbf{0} \quad \text{for } \mathbf{x} \notin \Omega_e^{(i)} \quad (i = 1,2) \quad , \quad \mathbf{N}_e^{\mathrm{c}}(\mathbf{x}) = \mathbf{0} \quad \text{for } \mathbf{x} \notin \Omega_e^{\mathrm{c}} \,. \tag{C.3}$$

Moreover, it is assumed that the Lagrange multiplier fields $\boldsymbol{\lambda}_1$ and $\boldsymbol{\lambda}_2$ can be discretized in the following way:

$$\boldsymbol{\lambda}_1 = \boldsymbol{\xi}_1 \mathbf{p}_1 \quad \text{on } \Gamma_1 \quad , \quad \boldsymbol{\lambda}_2 = \boldsymbol{\xi}_2 \mathbf{p}_2 \quad \text{on } \Gamma_2 \,, \tag{C.4}$$

where $\mathbf{p}_1$ and $\mathbf{p}_2$ are $s_1 \times 1$ and $s_2 \times 1$ vectors, respectively. Thus, according to equations (C.2) to (C.4), equation (C.1) can be written in the discrete form:

$$\begin{aligned}
&\sum_{i=1,2} \left[(\delta \mathbf{q}^{(i)})^{\mathrm{T}} \mathbf{D}^{(i)} \mathbf{q}^{(i)} \right] + (\delta \mathbf{q}^{\mathrm{c}})^{\mathrm{T}} \mathbb{K} \mathbf{q}^{\mathrm{c}} \\
&+ (\delta \mathbf{p}_1)^{\mathrm{T}} \left[\sum_{e=1}^{m_{\mathrm{c}}} \int_{\Gamma_1} (\boldsymbol{\xi}_1)^{\mathrm{T}} \mathbf{N}_e^{\mathrm{c}} \, ds(\mathbf{x}) \; \mathbf{q}_e^{\mathrm{c}} - \sum_{e=1}^{m_1} \int_{\Gamma_1} (\boldsymbol{\xi}_1)^{\mathrm{T}} \mathbf{N}_e^{(1)} \, ds(\mathbf{x}) \; \mathbf{q}_e^{(1)} \right] \\
&+ (\delta \mathbf{p}_2)^{\mathrm{T}} \left[\sum_{e=1}^{m_{\mathrm{c}}} \int_{\Gamma_2} (\boldsymbol{\xi}_2)^{\mathrm{T}} \mathbf{N}_e^{\mathrm{c}} \, ds(\mathbf{x}) \; \mathbf{q}_e^{\mathrm{c}} - \sum_{e=1}^{m_2} \int_{\Gamma_2} (\boldsymbol{\xi}_2)^{\mathrm{T}} \mathbf{N}_e^{(2)} \, ds(\mathbf{x}) \; \mathbf{q}_e^{(2)} \right] \\
&+ \left[\sum_{e=1}^{m_{\mathrm{c}}} (\delta \mathbf{q}_e^{\mathrm{c}})^{\mathrm{T}} \int_{\Gamma_1} (\mathbf{N}_e^{\mathrm{c}})^{\mathrm{T}} (\boldsymbol{\xi}_1) \, ds(\mathbf{x}) - \sum_{e=1}^{m_1} (\delta \mathbf{q}_e^{(1)})^{\mathrm{T}} \int_{\Gamma_1} (\mathbf{N}_e^{(1)})^{\mathrm{T}} (\boldsymbol{\xi}_1) \, ds(\mathbf{x}) \right] \mathbf{p}_1 \\
&+ \left[\sum_{e=1}^{m_{\mathrm{c}}} (\delta \mathbf{q}_e^{\mathrm{c}})^{\mathrm{T}} \int_{\Gamma_2} (\mathbf{N}_e^{\mathrm{c}})^{\mathrm{T}} (\boldsymbol{\xi}_2) \, ds(\mathbf{x}) - \sum_{e=1}^{m_2} (\delta \mathbf{q}_e^{(2)})^{\mathrm{T}} \int_{\Gamma_2} (\mathbf{N}_e^{(2)})^{\mathrm{T}} (\boldsymbol{\xi}_2) \, ds(\mathbf{x}) \right] \mathbf{p}_2 \\
&= \sum_{e=1}^{m_1} (\delta \mathbf{q}_e^{(1)})^{\mathrm{T}} \int_{\Gamma_1} (\mathbf{N}_e^{(1)})^{\mathrm{T}} \mathbf{f}_1 \, ds(\mathbf{x}) + \sum_{e=1}^{m_2} (\delta \mathbf{q}_e^{(2)})^{\mathrm{T}} \int_{\Gamma_2} (\mathbf{N}_e^{(2)})^{\mathrm{T}} \mathbf{f}_2 \, ds(\mathbf{x}).
\end{aligned} \tag{C.5}$$

Expressing displacements $\mathbf{q}_e^{(i)}$ of an element $\Omega_e^{(i)}$ $(i = 1,2)$ and displacements $\mathbf{q}_e^{\mathrm{c}}$ of an element Ω_e^{c} from displacements $\mathbf{q}^{(i)}$ of substructure i and displacements $\mathbf{q}^{\mathrm{c}}$ of the coupling element [111],

$$\mathbf{q}_e^{(i)} = \mathbf{L}_e^{(i)} \mathbf{q}^{(i)} \quad \text{and} \quad \mathbf{q}_e^{\mathrm{c}} = \mathbf{L}_e^{\mathrm{c}} \mathbf{q}^{\mathrm{c}}, \tag{C.6}$$

allows one to reformulate equation (C.5) in this way:

$$\begin{aligned}
&\sum_{i=1,2} \left[(\delta \mathbf{q}^{(i)})^{\mathrm{T}} \mathbf{D}^{(i)} \mathbf{q}^{(i)} \right] + (\delta \mathbf{q}^{\mathrm{c}})^{\mathrm{T}} \mathbb{K} \mathbf{q}^{\mathrm{c}} \\
&+ (\delta \mathbf{p}_1)^{\mathrm{T}} \left[\mathbf{B}_1^{\mathrm{c}} \mathbf{q}^{\mathrm{c}} - \mathbf{B}_1^{(1)} \mathbf{q}^{(1)} \right] + (\delta \mathbf{p}_2)^{\mathrm{T}} \left(\mathbf{B}_2^{\mathrm{c}} \mathbf{q}^{\mathrm{c}} - \mathbf{B}_2^{(2)} \mathbf{q}^{(2)} \right) \\
&+ \left[(\delta \mathbf{q}^{\mathrm{c}})^{\mathrm{T}} (\mathbf{B}_1^{\mathrm{c}})^{\mathrm{T}} - (\delta \mathbf{q}^{(1)})^{\mathrm{T}} (\mathbf{B}_1^{(1)})^{\mathrm{T}} \right] \mathbf{p}_1 + \left[(\delta \mathbf{q}^{\mathrm{c}})^{\mathrm{T}} (\mathbf{B}_2^{\mathrm{c}})^{\mathrm{T}} - (\delta \mathbf{q}^{(2)})^{\mathrm{T}} (\mathbf{B}_2^{(2)})^{\mathrm{T}} \right] \mathbf{p}_2 \\
&= (\delta \mathbf{q}^{(1)})^{\mathrm{T}} \mathbf{F}^{(1)} + (\delta \mathbf{q}^{(2)})^{\mathrm{T}} \mathbf{F}^{(2)}
\end{aligned} \tag{C.7}$$

where

$$\mathbf{B}_1^{\mathtt{c}} = \sum_{e=1}^{m_{\mathtt{c}}} \int_{\Gamma_1} (\boldsymbol{\xi}_1)^{\mathtt{T}} \mathbf{N}_e^{\mathtt{c}} \, ds(\mathbf{x}) \; \mathbf{L}_e^{\mathtt{c}} \quad , \quad \mathbf{B}_2^{\mathtt{c}} = \sum_{e=1}^{m_{\mathtt{c}}} \int_{\Gamma_2} (\boldsymbol{\xi}_2)^{\mathtt{T}} \mathbf{N}_e^{\mathtt{c}} \, ds(\mathbf{x}) \; \mathbf{L}_e^{\mathtt{c}} \quad , \tag{C.8}$$
$$\mathbf{B}_1^{(1)} = \sum_{e=1}^{m_1} \int_{\Gamma_1} (\boldsymbol{\xi}_1)^{\mathtt{T}} \mathbf{N}_e^{(1)} \, ds(\mathbf{x}) \; \mathbf{L}_e^{(1)} \quad , \quad \mathbf{B}_2^{(2)} = \sum_{e=1}^{m_2} \int_{\Gamma_2} (\boldsymbol{\xi}_2)^{\mathtt{T}} \mathbf{N}_e^{(2)} \, ds(\mathbf{x}) \; \mathbf{L}_e^{(2)}.$$

According to the convention $\mathbf{q}^{(i)} = \left[(\mathbf{q}_{\mathtt{L}}^{(i)})^{\mathtt{T}}(\mathbf{q}_{\mathtt{I}}^{(i)})^{\mathtt{T}}(\mathbf{q}_{\mathtt{R}}^{(i)})^{\mathtt{T}}\right]^{\mathtt{T}} (i = 1, 2)$ and $\mathbf{q}^{\mathtt{c}} = [(\mathbf{q}_1^{\mathtt{c}})^{\mathtt{T}}(\mathbf{q}_{\mathtt{I}}^{\mathtt{c}})^{\mathtt{T}}(\mathbf{q}_2^{\mathtt{c}})^{\mathtt{T}}]^{\mathtt{T}}$ and according to the definitions of the interpolation functions (cf. equation (C.3)), it appears that matrices $\mathbf{B}_1^{\mathtt{c}}$, $\mathbf{B}_2^{\mathtt{c}}$, $\mathbf{B}_1^{(1)}$ and $\mathbf{B}_2^{(2)}$ are expressed in this way:

$$\mathbf{B}_1^{\mathtt{c}} = \left[\begin{array}{cc} \mathbf{B}_1^{*\mathtt{c}} & \mathbf{0} \end{array}\right] , \; \mathbf{B}_2^{\mathtt{c}} = \left[\begin{array}{cc} \mathbf{0} & \mathbf{B}_2^{*\mathtt{c}} \end{array}\right] , \; \mathbf{B}_1^{(1)} = \left[\begin{array}{cc} \mathbf{0} & \mathbf{B}_1^{*(1)} \end{array}\right] , \; \mathbf{B}_2^{(2)} = \left[\begin{array}{cc} \mathbf{B}_2^{*(2)} & \mathbf{0} \end{array}\right], \tag{C.9}$$

where $\mathbf{B}_1^{*\mathtt{c}}$, $\mathbf{B}_2^{*\mathtt{c}}$, $\mathbf{B}_1^{*(1)}$ and $\mathbf{B}_2^{*(2)}$ are $s_1 \times n_{\mathtt{c}}^1$, $s_2 \times n_{\mathtt{c}}^2$, $s_1 \times n_1$ and $s_2 \times n_2$ matrices, respectively.

The equation of motion of each substructure, diplayed in equation (2.15) in Subsection 2.1.2, is deduced from the variational formulation, equation (C.7). Identifying the corresponding terms, the coupling forces are expressed in terms of the Lagrange multipliers:

$$\mathbf{F}_{\mathtt{R}}^{(1)} = (\mathbf{B}_1^{*(1)})^{\mathtt{T}} \mathbf{p}_1 \; , \; \mathbf{F}_{\mathtt{L}}^{(2)} = (\mathbf{B}_2^{*(2)})^{\mathtt{T}} \mathbf{p}_2 \; , \; \mathbf{F}_{\mathtt{R}}^{\mathtt{c}} = -(\mathbf{B}_2^{*\mathtt{c}})^{\mathtt{T}} \mathbf{p}_2 \; , \; \mathbf{F}_{\mathtt{L}}^{\mathtt{c}} = -(\mathbf{B}_1^{*\mathtt{c}})^{\mathtt{T}} \mathbf{p}_1 \tag{C.10}$$

Assuming that matrices $\mathbf{B}_1^{*\mathtt{c}}$ and $\mathbf{B}_2^{*\mathtt{c}}$ are square — that is, $s_1 = n_{\mathtt{c}}^1$ and $s_2 = n_{\mathtt{c}}^2$ — and invertible, then forces $\mathbf{F}_{\mathtt{R}}^{(1)}$ and $\mathbf{F}_{\mathtt{L}}^{(2)}$ applied at the right and left boundaries of substructures 1 and 2 can be expressed from forces $\mathbf{F}_1^{\mathtt{c}}$ and $\mathbf{F}_2^{\mathtt{c}}$ applied to the coupling element. Hence,

$$\mathbf{F}_{\mathtt{R}}^{(1)} = -(\mathbf{B}_1^{*(1)})^{\mathtt{T}} (\mathbf{B}_1^{*\mathtt{c}})^{-\mathtt{T}} \mathbf{F}_1^{\mathtt{c}} \quad \text{and} \quad \mathbf{F}_{\mathtt{L}}^{(2)} = -(\mathbf{B}_2^{*(2)})^{\mathtt{T}} (\mathbf{B}_2^{*\mathtt{c}})^{-\mathtt{T}} \mathbf{F}_2^{\mathtt{c}}. \tag{C.11}$$

Alternatively, on coupling surfaces Γ_1 and Γ_2, the displacements of substructures 1 and 2 can be related to the displacements of the coupling element. Indeed, the variational formulation, equation (C.7), furnishes the following additional expressions:

$$\mathbf{B}_1^{\mathtt{c}} \mathbf{q}^{\mathtt{c}} - \mathbf{B}_1^{(1)} \mathbf{q}^{(1)} = 0 \quad \text{and} \quad \mathbf{B}_2^{\mathtt{c}} \mathbf{q}^{\mathtt{c}} - \mathbf{B}_2^{(2)} \mathbf{q}^{(1)} = 0. \tag{C.12}$$

According to equation (C.9), this leads to:

$$\mathbf{B}_1^{*\mathtt{c}}\mathbf{q}_1^{\mathtt{c}} - \mathbf{B}_1^{*(1)}\mathbf{q}_{\mathtt{R}}^{(1)} = 0 \quad \text{and} \quad \mathbf{B}_2^{*\mathtt{c}}\mathbf{q}_2^{\mathtt{c}} - \mathbf{B}_2^{*(2)}\mathbf{q}_{\mathtt{L}}^{(1)} = 0, \tag{C.13}$$

and then,

$$\mathbf{q}_1^{\mathtt{c}} = (\mathbf{B}_1^{*\mathtt{c}})^{-1}\mathbf{B}_1^{*(1)}\mathbf{q}_{\mathtt{R}}^{(1)} \quad \text{and} \quad \mathbf{q}_2^{\mathtt{c}} = (\mathbf{B}_2^{*\mathtt{c}})^{-1}\mathbf{B}_2^{*(2)}\mathbf{q}_{\mathtt{L}}^{(2)}. \tag{C.14}$$

To summarize, the constraints introduced at the coupling surfaces Γ_1 and Γ_2 using the Lagrange multipliers can be formulated in this way:

$$\begin{pmatrix} \mathbf{F}_{\mathtt{R}}^{(1)} \\ \mathbf{F}_{\mathtt{L}}^{(2)} \end{pmatrix} = -\mathbf{T}^{\mathrm{T}} \begin{pmatrix} \mathbf{F}_1^{\mathtt{c}} \\ \mathbf{F}_2^{\mathtt{c}} \end{pmatrix} \quad , \quad \begin{pmatrix} \mathbf{q}_1^{\mathtt{c}} \\ \mathbf{q}_2^{\mathtt{c}} \end{pmatrix} = \mathbf{T} \begin{pmatrix} \mathbf{q}_{\mathtt{R}}^{(1)} \\ \mathbf{q}_{\mathtt{L}}^{(2)} \end{pmatrix}, \tag{C.15}$$

where matrix $\mathbf{T}$ is written

$$\mathbf{T} = \begin{bmatrix} (\mathbf{B}_1^{*\mathtt{c}})^{-1}\mathbf{B}_1^{*(1)} & \mathbf{0} \\ \mathbf{0} & (\mathbf{B}_2^{*\mathtt{c}})^{-1}\mathbf{B}_2^{*(2)} \end{bmatrix}. \tag{C.16}$$

The dynamical equilibrium of the coupling element can be expressed in a condensed form (see equation (2.17) in Subsection 2.1.2), with all the DOFs condensed on the DOFs located on surfaces Γ_1 and Γ_2.
The relation between forces $(\mathbf{F}_{\mathtt{R}}^{(1)}, \mathbf{F}_{\mathtt{L}}^{(2)})$ applied at the right and left boundaries of substructures 1 and 2 and displacements $(\mathbf{q}_{\mathtt{R}}^{(1)}, \mathbf{q}_{\mathtt{L}}^{(2)})$ is easily found by considering equations (2.17) and (C.15):

$$-\mathbf{T}^{\mathrm{T}}\mathbb{D}^{c*}\mathbf{T} \begin{pmatrix} \mathbf{q}_{\mathtt{R}}^{(1)} \\ \mathbf{q}_{\mathtt{L}}^{(2)} \end{pmatrix} = \begin{pmatrix} \mathbf{F}_{\mathtt{R}}^{(1)} \\ \mathbf{F}_{\mathtt{L}}^{(2)} \end{pmatrix}. \tag{C.17}$$

In short, it is proposed, by the use of Lagrange multipliers, a relation between the forces applied by the common coupling element to waveguides 1 and 2, on surfaces Γ_1 and Γ_2, and the corresponding displacements. From equations (2.21) and (2.22) in Subsection 2.1.2, equation (C.17) can be written in this manner:

$$-\mathbf{T}^{\mathrm{T}}\mathbb{D}^{c*}\mathbf{T} \left[\, \mathbf{\Psi}_{\mathbf{q}}^{\mathtt{inc}} \; \middle| \; \mathbf{\Psi}_{\mathbf{q}}^{\mathtt{ref}} \, \right] \begin{pmatrix} \mathbf{Q}^{\mathtt{inc}(1)} \\ \mathbf{Q}^{\mathtt{inc}(2)} \\ \mathbf{Q}^{\mathtt{ref}(1)} \\ \mathbf{Q}^{\mathtt{ref}(2)} \end{pmatrix} = \left[\, \mathbf{\Psi}_{\mathbf{F}}^{\mathtt{inc}} \; \middle| \; \mathbf{\Psi}_{\mathbf{F}}^{\mathtt{ref}} \, \right] \begin{pmatrix} \mathbf{Q}^{\mathtt{inc}(1)} \\ \mathbf{Q}^{\mathtt{inc}(2)} \\ \mathbf{Q}^{\mathtt{ref}(1)} \\ \mathbf{Q}^{\mathtt{ref}(2)} \end{pmatrix}, \tag{C.18}$$

Finally, using the expressions in equation (2.24), equation (C.18) can be expressed in the following way,

$$\left[\, \mathbf{T}^{\mathrm{T}}\mathbb{D}^{c*}\mathbf{T}\,\mathbf{\Psi}_{\mathbf{q}}^{\mathtt{inc}} + \mathbf{\Psi}_{\mathbf{F}}^{\mathtt{inc}} \; \middle| \; \mathbf{T}^{\mathrm{T}}\mathbb{D}^{c*}\mathbf{T}\,\mathbf{\Psi}_{\mathbf{q}}^{\mathtt{ref}} + \mathbf{\Psi}_{\mathbf{F}}^{\mathtt{ref}} \, \right] \begin{pmatrix} \mathbf{Q}^{\mathtt{inc}(1)} \\ \mathbf{Q}^{\mathtt{inc}(2)} \\ \mathbf{Q}^{\mathtt{ref}(1)} \\ \mathbf{Q}^{\mathtt{ref}(2)} \end{pmatrix} = \mathbf{0} \tag{C.19}$$

Assuming that matrix $\left[\mathbf{T}^{\mathrm{T}}\mathbb{D}^{c*}\mathbf{T}\,\boldsymbol{\Psi}_{\mathbf{F}}^{\mathtt{ref}}+\boldsymbol{\Psi}_{\mathbf{q}}^{\mathtt{ref}}\right]$ is invertible, amplitudes $(\mathbf{Q}^{\mathtt{ref}(1)},\mathbf{Q}^{\mathtt{ref}(2)})$ of the modes reflected by the coupling element can be expressed from amplitudes $(\mathbf{Q}^{\mathtt{inc}(1)},\mathbf{Q}^{\mathtt{inc}(2)})$ of the modes incident to the coupling element through a diffusion matrix, namely $\mathbb{C}$, which expresses the reflection and transmission coefficients of the wave modes:

$$\begin{pmatrix} \mathbf{Q}^{\mathtt{ref}(1)} \\ \mathbf{Q}^{\mathtt{ref}(2)} \end{pmatrix} = \mathbb{C} \begin{pmatrix} \mathbf{Q}^{\mathtt{inc}(1)} \\ \mathbf{Q}^{\mathtt{inc}(2)} \end{pmatrix}, \tag{C.20}$$

where

$$\mathbb{C} = -\left[\mathbf{T}^{\mathrm{T}}\mathbb{D}^{c*}\mathbf{T}\,\boldsymbol{\Psi}_{\mathbf{q}}^{\mathtt{ref}}+\boldsymbol{\Psi}_{\mathbf{F}}^{\mathtt{ref}}\right]^{-1}\left[\mathbf{T}^{\mathrm{T}}\mathbb{D}^{c*}\mathbf{T}\,\boldsymbol{\Psi}_{\mathbf{q}}^{\mathtt{inc}}+\boldsymbol{\Psi}_{\mathbf{F}}^{\mathtt{inc}}\right] \tag{C.21}$$

APPENDIX D

Detailed formulations of the substructuring scheme in the MWFE method

---

Detailed MWFE formulations and discussions are given in the work of Mencik and Ichchou [68].

The typical multi-layered subsystem, say sub system k, belonging to a composite structure is displayed in Figure 2.3 in Subsection 2.2.1. The subsystem represents a set of M connected straight homogeneous layers, whose left and right boundaries are denoted respectively as $\{S^i_{\mathrm{L}}\}$ and $\{S^i_{\mathrm{R}}\}$: for each layer $i(i = 1, \ldots, M)$, the surfaces $\{S_{\mathrm{L}}\}$ and are assumed to contain the same number of DOFs, say n^i. Let us denote as Γ^i the coupling interface between each layer i and its surroundings, that is, the set of coupled layers $\{j\}_{j \neq i}$.

The MWFE formulation consists of constructing the *global* wave mode basis $\{\mathbf{\Phi_j}\}_\mathbf{j}$, attached to the heterogeneous multi-layered subsystems k, from a set of reduced *local* wave mode basis $\{\{\mathbf{\tilde{\Phi}^i_j}\}_{\mathbf{j=1,\ldots,2m^i}}\}$, having specific dimensions $\{2m^i\}(m^i \leq n^i \ \forall i)$ and attached to the set of homogeneous layers $\{i\}_i$ with free interfaces $\{\Gamma^i\}$. For each uncoupled layer i, the reduced basis $\{\mathbf{\tilde{\Phi}^i_j}\}_{\mathbf{j=1,\ldots,2m^i}}$ is assumed to support the cross-section (either $\{S^i_{\mathrm{L}}\}$ and $\{S^i_{\mathrm{R}}\}$) dynamics within the given frequency band and is extracted from the full local basis $\{\mathbf{\tilde{\Phi}^i_j}\}_{\mathbf{j=1,\ldots,2n^i}}$ which is obtained using the WFE formulation(see equation (D.1)):

$$\mathbf{S}^i \mathbf{\Phi}^i_j = \mu^i_j \mathbf{\Phi}^i_j, \quad |\mathbf{S}^i - \mu^i_j \mathbf{I}| = 0 \quad i = 1, \ldots, M. \tag{D.1}$$

For each uncoupled layer i, the eigenvalues $\{\mu^i_j\}_j$ relate the speeds of waves traveling along the x-axis, and the reduced local wave model matrix, say $\{\tilde{\mathbf{\Phi}}^i\}$, can be typically expressed from the $(n^i \times 2m^i)$ matrices $\{\tilde{\mathbf{\Phi}}^i_{\mathbf{q}}\}$ and $\{\tilde{\mathbf{\Phi}}^i_{\mathrm{F}}\}$, reflecting the displacement and force components.

The dynamic equilibrium of the subsystem k consists of formulating a set of local dynamic equilibrium equations, attached to the set of uncoupled homogeneous layers.

$$\mathbf{D}^i \mathbf{q}^i = \mathbf{F}^i \quad i = 1, \ldots, M. \tag{D.2}$$

and subjected to the set of constraints:

$$\mathbf{q}^{i}_{\Gamma^i} = \mathbf{q}^{\Theta^i}_{\Gamma^i} \quad i = 1, \dots, M. \tag{D.3}$$

For each layer i belonging to the subsystem k:$\mathbf{q}^i$ and $\mathbf{F}^i$ are the displacements and the forces applied to the uncoupled layer on $\{S^i_{\mathtt{L}}\} \cup \{S^i_{\mathtt{R}}\}$; Θ^i represents the surroundings of the layer i, that is, the set of coupled layers $\{j\}_{j \neq i}$; Γ^i denotes the coupling interface between the layer i and the surroundings Θ^i; $\mathbf{q}^{\Theta^i}$ stands for the displacements of the surroundings Θ^i; finally,$\mathbf{q}^i_{\Gamma^i}$ $\mathbf{q}^{\Theta^i}_{\Gamma^i}$ are the restrictions of the displacements $\mathbf{q}^i$ and $\mathbf{q}^{\Theta^i}$ to the coupling interface Γ^i. Here three Boolean operators are defined:

- $\mathbf{L}^i_{\Gamma^i}$: $\mathbf{q}^i_{\Gamma^i} = \mathbf{L}^i_{\Gamma^i}\mathbf{q}^i$
- $\mathbf{L}^{\Theta^i}_{\Gamma^i}$: $\mathbf{q}^{\Theta^i}_{\Gamma^i} = \mathbf{L}^{\Theta^i}_{\Gamma^i}\mathbf{q}^{\Theta^i}$
- $\overline{\mathbf{L}}^{\Theta^i}_{\Gamma^i}$: $\overline{\mathbf{q}}^{\Theta^i}_{\Gamma^i} = \overline{\mathbf{L}}^{\Theta^i}_{\Gamma^i}\mathbf{q}^{\Theta^i}$

By introducing them into equation (D.3), leads to

$$\mathbf{L}^i_{\Gamma^i}\mathbf{q}^i = \mathbf{L}^{\Theta^i}_{\Gamma^i}\mathbf{q}^{\Theta^i} \quad i = 1, \dots, M. \tag{D.4}$$

Relaxing the linear constraints (D.4) to determine the displacement solutions $\mathbf{q}^i$ and $\mathbf{q}^{\Theta^i}$ leads to the following variational problem formulated $\forall\delta\mathbf{q}^i$, $\forall\delta\mathbf{q}^{\Theta^i}$ and $\forall\delta\mathbf{p}^i$(see for instance reference [109]):

$$\begin{aligned} -(\delta\mathbf{q}^i)^{\mathtt{T}}\mathbf{D}^i q^i - (\delta\mathbf{q}^{\Theta^i})^{\mathtt{T}}\mathbf{D}^{\Theta^i} q^{\Theta^i} + (\delta\mathbf{q}^i)^{\mathtt{T}}\mathbf{F}^i + (\delta\mathbf{q}^{\Theta^i})^{\mathtt{T}}\mathbf{F}^{\Theta^i} \\ +\delta((\mathbf{p}^i)^{\mathtt{T}}(\mathbf{L}^i_{\Gamma^i}\mathbf{q}^i - \mathbf{L}^{\Theta^i}_{\Gamma^i}\mathbf{q}^{\Theta^i})) = 0 \quad i = 1, \dots, M. \end{aligned} \tag{D.5}$$

Here, $\mathbf{p}^i$ is a Lagrange multiplier field defined on the coupling interface Γ^i. Since the variational formulation (D.5) is defined for arbitrary $\delta\mathbf{q}^i$, $\delta\mathbf{q}^{\Theta^i}$ and $\delta\mathbf{p}^i$, one obtains

$$\left\{ \begin{array}{l} \mathbf{D}^i q^i = \mathbf{F}^i + (\mathbf{L}^i_{\Gamma^i})^{\mathtt{T}}\mathbf{p}^i \\ \mathbf{D}^{\Theta^i} q^{\Theta^i} = \mathbf{F}^{\Theta^i} - (\mathbf{L}^{\Theta^i}_{\Gamma^i})^{\mathtt{T}}\mathbf{p}^i \quad i = 1, \dots, M \\ \mathbf{L}^i_{\Gamma^i}\mathbf{q}^i - \mathbf{L}^{\Theta^i}_{\Gamma^i}\mathbf{q}^{\Theta^i} = 0 \end{array} \right. \tag{D.6}$$

Multiplying the second equation of the system (D.6) by the Boolean operator $\mathbf{L}^{\Theta^i}_{\Gamma^i}$ leads to:

$$\mathbf{p}^i = -\mathbf{L}^{\Theta^i}_{\Gamma^i}\mathbf{D}^{\Theta^i}\mathbf{q}^{\Theta^i} + \mathbf{L}^{\Theta^i}_{\Gamma^i}\mathbf{F}^{\Theta^i} \quad i = 1, \dots, M. \tag{D.7}$$

By introducing the following notation:

$$\mathbf{D}^{\Theta^i}\mathbf{q}^{\Theta^i} = \begin{bmatrix} \mathbf{D}^{\Theta^i}_{\Gamma^i} & \mathbf{C}^{\Theta^i}_{\Gamma^i} \\ (\mathbf{C}^{\Theta^i}_{\Gamma^i})^{\mathtt{T}} & \overline{\mathbf{D}}^{\Theta^i}_{\Gamma^i} \end{bmatrix} \begin{pmatrix} \mathbf{q}^{\Theta^i}_{\Gamma^i} \\ \overline{\mathbf{q}}^{\Theta^i}_{\Gamma^i} \end{pmatrix} \quad i = 1, \dots, M \tag{D.8}$$

and observing that:

$$\mathbf{L}^{\Theta^i}_{\Gamma^i}\mathbf{D}^{\Theta^i}\mathbf{q}^{\Theta^i} = \mathbf{D}^{\Theta^i}_{\Gamma^i}\mathbf{q}^{\Theta^i}_{\Gamma^i} + \mathbf{C}^{\Theta^i}_{\Gamma^i}\overline{\mathbf{q}}^{\Theta^i}_{\Gamma^i} \quad i = 1, \ldots, M. \tag{D.9}$$

where $\overline{\mathbf{q}}^{\Theta^i}_{\Gamma^i}$ stands for the displacements of the nodes of Θ^i which don't belong to Γ^i, results in:

$$\mathbf{p}^i = -\mathbf{D}^{\Theta^i}_{\Gamma^i}\mathbf{q}^{\Theta^i}_{\Gamma^i} - \mathbf{C}^{\Theta^i}_{\Gamma^i}\overline{\mathbf{q}}^{\Theta^i}_{\Gamma^i} + \mathbf{L}^{\Theta^i}_{\Gamma^i}\mathbf{F}^{\Theta^i} \quad i = 1, \ldots, M. \tag{D.10}$$

that is:

$$\mathbf{p}^i = -\mathbf{D}^{\Theta^i}_{\Gamma^i}\mathbf{L}^{\Theta^i}_{\Gamma^i}\mathbf{q}^{\Theta^i} - \mathbf{C}^{\Theta^i}_{\Gamma^i}\overline{\mathbf{q}}^{\Theta^i}_{\Gamma^i} + \mathbf{L}^{\Theta^i}_{\Gamma^i}\mathbf{F}^{\Theta^i} \quad i = 1, \ldots, M. \tag{D.11}$$

and by introducing the Boolean operator $\overline{\mathbf{L}}^{\Theta^i}_{\Gamma^i}$ defined in Subsection 2.2.1 into equation (D.11) leads to:

$$\mathbf{p}^i = -\mathbf{D}^{\Theta^i}_{\Gamma^i}\mathbf{L}^{\Theta^i}_{\Gamma^i}\mathbf{q}^{\Theta^i} - \mathbf{C}^{\Theta^i}_{\Gamma^i}\overline{\mathbf{L}}^{\Theta^i}_{\Gamma^i}\mathbf{q}^{\Theta^i} + \mathbf{L}^{\Theta^i}_{\Gamma^i}\mathbf{F}^{\Theta^i} \quad i = 1, \ldots, M. \tag{D.12}$$

Finally, by introducing equation (D.12) into the first equation of the equation system (D.6), the dynamic equilibrium equation of each layer i connected to the surrounding Θ^i can be obtained:

$$\left[\mathbf{D}^i + (\mathbf{L}^i_{\Gamma^i})^{\mathtt{T}}\mathbf{D}^{\Theta i}_{\Gamma^i}\mathbf{L}^i_{\Gamma^i}\right]\mathbf{q}^i + (\mathbf{L}^i_{\Gamma^i})^{\mathtt{T}}\mathbf{C}^{\Theta i}_{\Gamma^i}\overline{\mathbf{L}}^{\Theta i}_{\Gamma^i}\mathbf{q}^{\Theta i} = \boldsymbol{\mathcal{F}}^i \quad i = 1, \ldots, M \tag{D.13}$$

where

$$\boldsymbol{\mathcal{F}}^i = \mathbf{F}^i + \mathbf{L}^i_{\Gamma^i}\mathbf{L}^{\Theta i}_{\Gamma^i}\mathbf{F}^{\Theta^i} \quad i = 1, \ldots, M \tag{D.14}$$

stands for the restriction of the global forces $\mathbf{F}$ (cf.equation (B.1)), applied to the multi-layered subsystem k, to layer i. Equation (D.14) enforces the continuity of the global forces $\{\boldsymbol{\mathcal{F}}^i\}_i$ at the coupling interfaces $\{\Gamma^i\}_i$. In matrix form, the dynamic equilibrium of the set of coupled layers can be written in two parts, a local part and a coupling part:

$$\left[\mathbf{D}^{\mathtt{local}} + \mathbf{D}^{\mathtt{coupling}}\right]\begin{pmatrix}\mathbf{q}^1\\ \vdots \\ \mathbf{q}^M\end{pmatrix} = \begin{pmatrix}\boldsymbol{\mathcal{F}}^1\\ \vdots \\ \boldsymbol{\mathcal{F}}^M\end{pmatrix} = \left[\mathbf{I} + \mathbf{E}^{\mathtt{coupling}}\right]\begin{pmatrix}\mathbf{F}^1\\ \vdots \\ \mathbf{F}^M\end{pmatrix} \tag{D.15}$$

The matrix $\mathbf{D}^{\mathtt{local}}$ in equation (D.15) is expressed from the set of dynamic stiffness operators $\mathbf{D}_{i=1,\ldots,M}$ associated with the uncoupled layers,

$$\mathbf{D}^{\mathtt{local}} = \begin{bmatrix}\mathbf{D}^1 & \mathbf{0} & \ldots & \mathbf{0}\\ \mathbf{0} & \mathbf{D}^2 & \ldots & \mathbf{0}\\ \vdots & \vdots & \ddots & \vdots\\ \mathbf{0} & \mathbf{0} & \ldots & \mathbf{D}^M\end{bmatrix}. \tag{D.16}$$

while the matrix $\mathbf{D}^{\texttt{coupling}}$ describes the inertial, elastic and damping coupling forces between layers, at the interfaces $\{\Gamma^i\}_{i=1,\dots,M}$:

$$\mathbf{D}^{\texttt{coupling}} = \begin{bmatrix} \mathbf{D}^{\texttt{coupling}}_{\texttt{Layer1}-\texttt{Layer1}} & \mathbf{D}^{\texttt{coupling}}_{\texttt{Layer1}-\texttt{Layer2}} & \mathbf{0} & \dots & \mathbf{0} \\ \mathbf{D}^{\texttt{coupling}}_{\texttt{Layer2}-\texttt{Layer1}} & \mathbf{D}^{\texttt{coupling}}_{\texttt{Layer2}-\texttt{Layer2}} & \mathbf{D}^{\texttt{coupling}}_{\texttt{Layer2}-\texttt{Layer3}} & \dots & \mathbf{0} \\ \mathbf{0} & \mathbf{D}^{\texttt{coupling}}_{\texttt{Layer3}-\texttt{Layer2}} & \mathbf{D}^{\texttt{coupling}}_{\texttt{Layer3}-\texttt{Layer3}} & \dots & \mathbf{0} \\ \vdots & \vdots & \vdots & \ddots & \vdots \\ \mathbf{0} & \mathbf{0} & \mathbf{0} & \dots & \mathbf{D}^{\texttt{coupling}}_{\texttt{Layer}M-\texttt{Layer}M} \end{bmatrix}, \tag{D.17}$$

where

$$\begin{aligned} \mathbf{D}^{\texttt{coupling}}_{\texttt{Layer1}-\texttt{Layer1}} &= (\mathbf{L}^1_{\Gamma^1})^{\mathtt{T}}\mathbf{D}^2_{\Gamma^1}\mathbf{L}^1_{\Gamma^1} \\ \mathbf{D}^{\texttt{coupling}}_{\texttt{Layer}i-\texttt{Layer}i} &= (\mathbf{L}^i_{\Gamma^i})^{\mathtt{T}}\mathbf{D}^{i-1}_{\Gamma^i}\mathbf{L}^i_{\Gamma^i} + (\mathbf{L}^i_{\Gamma^i})^{\mathtt{T}}\mathbf{D}^{i+1}_{\Gamma^i}\mathbf{L}^i_{\Gamma^i} \quad i = 2,\dots,M-1 \\ \mathbf{D}^{\texttt{coupling}}_{\texttt{Layer}M-\texttt{Layer}M} &= (\mathbf{L}^M_{\Gamma^M})^{\mathtt{T}}\mathbf{D}^{M-1}_{\Gamma^M}\mathbf{L}^M_{\Gamma^M} \\ \mathbf{D}^{\texttt{coupling}}_{\texttt{Layer}i-\texttt{Layer}i-1} &= (\mathbf{L}^i_{\Gamma^1})^{\mathtt{T}}\mathbf{C}^{i-1}_{\Gamma^i}L^{i-1}_{\Gamma^i} \quad i = 2,\dots,M \\ \mathbf{D}^{\texttt{coupling}}_{\texttt{Layer}i-1-\texttt{Layer}i} &= (\mathbf{L}^{i-1}_{\Gamma^{i-1}})^{\mathtt{T}}\mathbf{C}^{i}_{\Gamma^{i-1}}L^{i}_{\Gamma^{i-1}} \quad i = 2,\dots,M \end{aligned} \tag{D.18}$$

The matrix $\mathbf{E}^{\texttt{coupling}}$ in equation (D.15) can be expressed as follows:

$$\mathbf{E}^{\texttt{coupling}} = \begin{bmatrix} \mathbf{0} & (\mathbf{L}^1_{\Gamma^1})^{\mathtt{T}}\mathbf{L}^2_{\Gamma^1} & \mathbf{0} & \dots & \mathbf{0} & \mathbf{0} \\ (\mathbf{L}^2_{\Gamma^2})^{\mathtt{T}}\mathbf{L}^1_{\Gamma^2} & \mathbf{0} & (\mathbf{L}^2_{\Gamma^2})^{\mathtt{T}}\mathbf{L}^3_{\Gamma^2} & \dots & \mathbf{0} & \mathbf{0} \\ \mathbf{0} & (\mathbf{L}^3_{\Gamma^3})^{\mathtt{T}}\mathbf{L}^2_{\Gamma^3} & \mathbf{0} & \dots & \mathbf{0} & \mathbf{0} \\ \vdots & \vdots & \vdots & \ddots & \vdots & \vdots \\ \mathbf{0} & \mathbf{0} & \mathbf{0} & \dots & \mathbf{0} & (\mathbf{L}^{M-1}_{\Gamma^{M-1}})^{\mathtt{T}}\mathbf{L}^{M}_{\Gamma^{M-1}} \\ \mathbf{0} & \mathbf{0} & \mathbf{0} & \dots & (\mathbf{L}^{M}_{\Gamma^{M}})^{\mathtt{T}}\mathbf{L}^{M-1}_{\Gamma^{M}} & \mathbf{0} \end{bmatrix}. \tag{D.19}$$

Appendix E

Finite Element modeling of shunted piezoelectric patches with negative capacitance

---

In this appendix the theoretical modeling of shunted piezoelectric patches with negative capacitance using the FE method is considered by extracting a part of the work done by Collet *et al.* [85].
By applying the finite element method on a piezoelectric domain, a discretized system can be written in the following form [85]:

$$\mathbf{M}\ddot{\mathbf{w}}(t) + \mathbf{C}\dot{\mathbf{w}}(t) + \mathbf{K}\mathbf{w}(t) + \mathbf{e}_{wv}\mathbf{V}(t) = \mathbf{F}(t) \tag{E.1a}$$

$$-\mathbf{e}_{wv}^{\mathsf{T}}\mathbf{w}(t) + \mathbf{C}_p^S\mathbf{V}(t) = \mathbf{Q}(t) \tag{E.1b}$$

where $\mathbf{M}$, $\mathbf{C}$, $\mathbf{K}$ stand respectively for mass, damping and open circuit stiffness matrices, $\mathbf{e}_{wv}$ is the piezoelectric coupling matrix depending on piezoelectric material coefficients $\mathbf{e}$ but also on geometric and support characteristics, $\mathbf{C}_p^S$ is the diagonal matrix of each equivalent piezoelectric capacitances for wero strain. $\mathbf{w}$ represents the vector of mechanical degrees of freedom and $\mathbf{V}$, the vector of the applied upper electrode voltage, whereas $\mathbf{Q}$ is the dual measured current. The main difference between the full (or well condensed) 3D and the simplified beam or plate approaches is located in evaluation of $\mathbf{C}_p^S$ and $\mathbf{e}_{wv}$ matrices.
If we now consider a serial $\mathbf{R} - \mathbf{C}_{neg}$ shunt circuit, the electronic introduced feedback can be formulated as follows:

$$\mathbf{V}(t) = -((\mathbf{C}_{neg})^{-1}\mathbf{Q}(t) + \mathbf{R}\frac{d\mathbf{Q}(t)}{dt}) \tag{E.2}$$

Then, based on the system equilibrium equations (E.1a) and (E.1b), the controlled equations are:

$$\mathbf{M}\ddot{\mathbf{w}}(t) + \mathbf{C}\dot{\mathbf{w}}(t) + (\mathbf{K} + \mathbf{e}_{wv}^{\mathsf{T}}(\mathbf{C}_p^S + \mathbf{C}_{neg})^{-1}\mathbf{e}_{wv})\mathbf{w}(t) = -\mathbf{e}_{wv}\mathbf{C}_{neg}(\mathbf{C}_{neg} + \mathbf{C}_p^S)^{-1}\mathbf{V}(t) + \mathbf{F}(t) \tag{E.3a}$$

$$-\mathbf{e}_{wv}^{\mathsf{T}}\mathbf{C}_{neg}(\mathbf{C}_{neg} + \mathbf{C}_p^S)^{-1}\mathbf{w}(t) + \mathbf{C}_p^S\mathbf{C}_{neg}(\mathbf{C}_{neg} + \mathbf{C}_p^S)^{-1}\mathbf{V}(t) = \mathbf{Q}(t) \tag{E.3b}$$

$$\mathbf{V}(t) = -\mathbf{R}\dot{\mathbf{Q}}(t) \tag{E.3c}$$

By comparing with equation (E.1a), we can show that this last system corresponds to a piezomechanical system in which we would have modified the initial short circuit stiffness $\mathbf{K}$ to $\mathbf{K} + \mathbf{e}_{wv}^{\mathtt{T}}(\mathbf{C}_p^S + \mathbf{C}_{neg})^{-1}\mathbf{e}_{wv}$. Thus if $\mathbf{e}_{wv}^{\mathtt{T}}(\mathbf{C}_p^S + \mathbf{C}_{neg})^{-1}\mathbf{e}_{wv}$ is a negative matrix, we can easily demonstrate that we could decrease the corresponding short circuit eigenfrequencies. By applying the model in the work of Hagood and Von Flotow [7], the effective stiffness introduced for the shunted piezoelectric laminated composite can be plotted in Figure E.1. For C_{neg} between C_p^T and C_p^S, the system is unstable as the effective stiffness becomes negative.

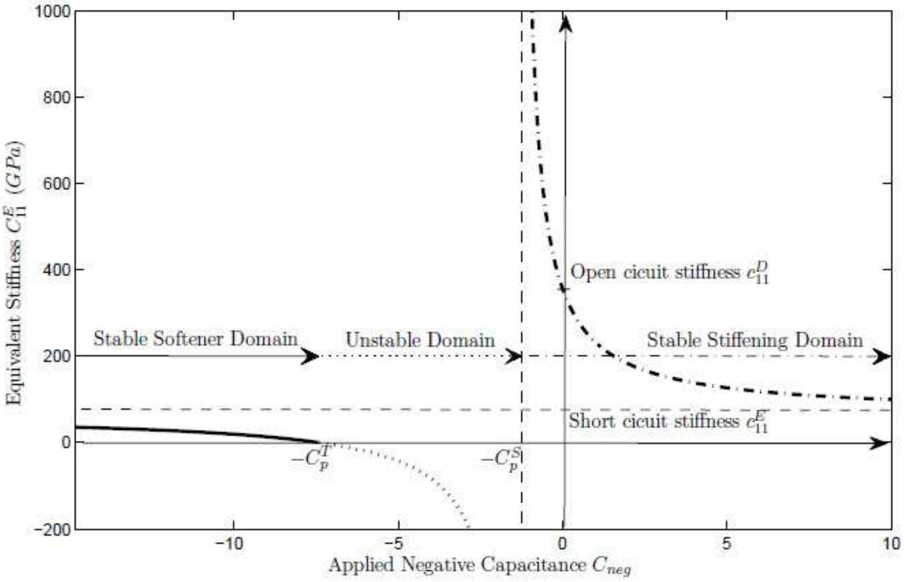

Figure E.1: The effective shunted piezoelectric composite stiffness as a function of the connected negative capacitance term [85].

Appendix F

Publications pendant la thèse

Revues internationales avec comité de lecture:

Papiers publiés:

- T.L. Huang, M.N. Ichchou and O. Bareille, Multi-mode wave propagation in damaged stiffened panels, *Structural Control and Health Monitoring*, 19(5)(2012) 609-629.(Reference [64])
- T.L. Huang, M.N. Ichchou, O. Bareille, M. Collet and M. Ouisse, Traveling wave control in thin-walled structures through shunted piezoelectric patches, *Mechanical Systems and Signal Processing*, 2012, doi:10.1016/j.ymssp.2012.06.014.

Papiers soumis:

- T.L. Huang, M.N. Ichchou, O. Bareille, M. Collet and M. Ouisse, Multimodal wave propagation in smart structures with shunted piezoelectric patches, *Journal of Computational Mechanics*. Under review.
- T.L. Huang, M.N. Ichchou, O. Bareille, M. Collet and M. Ouisse, Multimodal wave propagation in smart composite structures with shunted piezoelectric patches, *Journal of Intelligent Material Systems and Structures*. Under review.
- T.L. Huang, M.N. Ichchou, M. Collet, O. Bareille and M. Ouisse, Wave propagation control in smart structures with shunted piezoelectric patches, *Smart Materials and Structures*.

Congrès:

- T. Huang, M. Ichchou, O. Bareille and M. Collet, Wave propagation in smart structures through numerical approach, Proceedings of the V International Conference on Adaptive Modeling and Simulation, Paris, France, June 6-8, 2011.

- M. Collet, M. Ouisse, M. Ichchou, F. Tateo and T. Huang. Adaptive piezoelectric metacomposite: a new integrated technology to control vibroacoustic power flow. ACOUSTICS 2012, Nantes, France, Apr 23-27, 2012.

- T.L. Huang, M.N. Ichchou, O. Bareille. Defect detection in stiffened panels through guided structural waves. The International Conference on Structural Nonlinear Dynamics and Diagnosis, Marrakech, Morocco, Apr 30-May 02, 2012.

- T.L. Huang, M.N. Ichchou, O. Bareille, M. Collet and M. Ouisse. Multimodal wave propagation in smart composite structures with shunted piezoelectric patches. 1st International Conference on Dynamics of Composite Structures, Arcachon, France, May 22-24, 2012.

- T.L. Huang, F. Tateo, M.N. Ichchou and M. Collet. Energy analysis for the optimization of smart structures with shunted piezoelectric patches. VCB 18th conference of Vibrations Shocks and Noise. Paris, France, Jul 3-5, 2012.

- T.L. Huang, M.N. Ichchou, M. Collet, O. Bareille and M. Ouisse. Wave propagation control in smart structures with shunted piezoelectric patches. ISMA conference on Noise and Vibration Engineering. Leuven, Belgium, Sept 17-19, 2012.

- F. Tateo and T.L. Huang. Full electromechanical optimization of shunted piezoelectric patch for controlling elastodynamic waves' power flow. ASME Conference on Smart Materials, Adaptive Structures and Intelligent Systems. Stone Mountain, Georgia, USA, Sept 19-21, 2012.

- T.L. Huang, M.N. Ichchou, O. Bareille, M. Collet and M. Ouisse, Traveling wave control in thin-walled structures through shunted piezoelectric patches. The 23rd International Conference on Adaptive Structures and Technologies (ICAST 2012), Nanjing, China, Oct 11-13, 2012.

Bibliography

[1] M. Sahin, F. M. Karadal, Y. Yaman, O. F. Kircali, V. Nalbantoglu, F. D. Ulker, T. Caliskan, Smart structures and their applications on active vibration control: Studies in the department of aerospace engineering, metu, Journal of Electroceramics 20 (3-4) (2008) 167–174. (Cited on page 1.)

[2] B. Bandyopadhyay, T. Manjunath, M. Umapathy, Introduction to smart structures, in: Modeling, Control and Implementation of Smart Structures, Vol. 350 of Lecture Notes in Control and Information Sciences, Springer Berlin / Heidelberg, 2007, pp. 1–22. (Cited on page 1.)

[3] V. Giurgiutiu, Actuators and smart structures, in: S. Braun (Ed.), Encyclopedia of Vibrations, Academic Press, 2001, pp. 58–81. (Cited on page 1.)

[4] M. Collet, V. Walter, P. Delobelle, Active damping of a micro-cantilever piezocomposite beam, Journal of Sound and Vibration 260 (3) (2003) 453–476. (Cited on page 2.)

[5] Y. Meyer, T. Verdot, M. Collet, J. Baborowski, P. Muralt, Active isolation of electronic micro-components with piezoelectrically transduced silicon MEMS devices, Journal of Smart Materials and Structures 16 (1) (2007) 128–134. (Cited on pages 2 and 6.)

[6] M. Collet, K. A. Cunefare, M. N. Ichchou, Wave motion optimization in periodically distributed shunted piezocomposite beam structures, Journal of Intelligent Material Systems and Structures 20 (7) (2009) 787–808. (Cited on pages 2, 3, 4, 9, 12, 20, 111, 120 and 124.)

[7] N. W. Hagood, A. Flotow, Damping of structural vibrations with piezoelectric materials and passive electrical networks, Journal of Sound and Vibration 146 (1991) 243–268. (Cited on pages 3, 12, 52 and 176.)

[8] O. Thorp, M. Ruzzene, A. Baz, Attenuation and localization of wave propagation in rods with periodic shunted piezoelectric patches, Journal of Smart Materials and Structures 10 (5) (2001) 979–989. (Cited on pages 3 and 158.)

[9] A. Spadoni, M. Ruzzene, K. A. Cunefare, Vibration and wave propagation control of plate with periodic arrays of shunted piezoelectric

patches, Journal of Intelligent Material Systems and Structures 20 (8) (2009) 979–990. (Cited on pages 3, 12 and 158.)

[10] C. H. Nguyen, S. J. Pietrzko, FE analysis of a PZT-actuated adaptive beam with vibration damping using a parallel R-L shunt circuit, Finite elements in analysis and design 42 (14-15) (2006) 1231–1239. (Cited on pages 3 and 12.)

[11] J. Becker, O. Fein, M. Maess, L. Gaul, Finite element-based analysis of shunted piezoelectric structures for vibration damping, Computers and Structures 84 (31-32) (2006) 2340–2350. (Cited on pages 3, 12 and 43.)

[12] F. Casadei, M. Ruzzene, L. Dozio, K. A. Cunefare, Broadband vibration control through periodic arrays of resonant shunts: experimental investigation on plates, Journal of Smart Materials and Structures 19 (1) (2010) 015002. (Cited on pages 3, 12 and 158.)

[13] M. Tsai, K. Wang, On the structural damping characteristics of active piezoelectric actuators with passive shunt, Journal of Sound and Vibration 221 (1) (1999) 1–22. (Cited on page 3.)

[14] S. Behrens, S. Moheimani, A. Fleming, Multiple mode current flowing passive piezoelectricshunt controller, Journal of Sound and Vibration 226 (5) (2003) 929–942. (Cited on page 3.)

[15] S. Wu, broadband piezoelectric shunts for passive structural vibration control, in: Proceedings of SPIE - Smart Structures and Materials: Damping and Isolation, Vol. 4331, Newport Beach, CA, USA, 2001, pp. 251–261. (Cited on page 3.)

[16] A. Fleming, S. Moheimani, Adaptive piezoelectric shunt damping, S-mart Materials and Structures 12 (1) (2003) 36–48. (Cited on page 3.)

[17] D. Niederberger, A. Fleming, S. Moheimani, M. Morari, Adaptive multimode resonant piezoelectric shunt damping, Smart Materials and Structures 13 (5) (2004) 1025–1035. (Cited on page 3.)

[18] C. Park, A. Baz, Vibration control of beams with negative capacitive shunting of interdigital electrode piezoceramics, Journal of Vibration and Control 11 (3) (2005) 331–346. (Cited on pages 4 and 111.)

[19] K. Cunefare, Negative capacitance shunts for vibration suppression: wave based tuning and reactive input power, in: Proceedings of Active 2006, Adelaide, Australia, 2006. (Cited on pages 4 and 111.)

[20] B. Beck, K. Cunefare, M. Ruzzene, Broadband vibration suppression assessment of negative impedance shunts, in: ASME (Ed.), ASME S-MASIS08 Conference, Ellicott City, Maryland USA, 2008. (Cited on pages 4 and 111.)

[21] B. Beck, K. Cunefare, M. Ruzzene, Experimental implementation of negative impedance shunts on periodic structures, in: ASME (Ed.), ASME SMASIS09 Conference, Oxnard, CA USA, 2009. (Cited on pages 4 and 111.)

[22] B. Beck, K. Cunefare, M. Collet, M. Ruzzene, Periodic piezoelectric sensor-actuator array for vibration suppression on a beam, in: SPIE (Ed.), Proceedings of SPIE - Smart Structures and Materials, San Diego, CA USA, 2010. (Cited on pages 4 and 111.)

[23] B. Beck, K. Cunefare, M. Ruzzene, M. Collet, Experimental analysis of a cantilever beam with a shunted piezoelectric periodic array, Journal of Intelligent Material Systems and Structures DOI: 10.1177/1045389X11411119. (Cited on pages 4 and 111.)

[24] S. Behrens, A. Flemming, S. Moheimani, New method for multiple-mode shunt damping of structural vibration using a single piezoelectric transducer, in: Proceedings of SPIE - Smart Structures and Materials: Damping and Isolation, Vol. 4331, Newport Beach, CA, USA, 2001, pp. 239–250. (Cited on pages 4 and 111.)

[25] J. Park, D. Palumbo, A new approach to identify optimal properties of shunting elements for maximum damping of structural vibration using piezoelectric patches, in: Proceedings of Active 2004, Williamsburg, VA USA, 2004. (Cited on pages 4 and 111.)

[26] S. Behrens, A. Fleming, S. Moheimani, A broadband controller for shunt piezoelectric damping of structural vibration, Smart Materials and Structures 12 (1) (2003) 18–28. (Cited on page 4.)

[27] W. Clark, Vibration control with state-switched piezoelectric materials, Journal of Intelligent Material Systems and Structures 11 (2000) 263–271. (Cited on page 4.)

[28] A. Kurdila, W. Clark, W. Wang, D. McDaniel, Stability of a class of real time switched piezoelectric shunts, Journal of Intelligent Material Systems and Structures 13 (4) (2003) 107–116. (Cited on page 4.)

[29] Q. Lin, P. Ermanni, Semi-active damping of a clamped plate using pzt, International Journal of Solids and Structures 41 (7) (2004) 1741–1752. (Cited on page 4.)

[30] P. Monnier, M. Collet, Definition of the mechanical design parameters to optimize efficiency of integral force feedback active damping strategy, Journal of Structural Control 12 (2005) 65–89. (Cited on page 6.)

[31] M. N. Ichchou, J. Berthaut, M. Collet, Multi-mode wave propagation in ribbed plates: Part I, wavenumber-space characteristics, International Journal of Solids and Structures 45 (5) (2008) 1179–1195. (Cited on pages 9, 18, 128, 129, 130 and 134.)

[32] M. N. Ichchou, J. Berthaut, M. Collet, Multi-mode wave propagation in ribbed plates: Part II, predictions and comparisons, International Journal of Solids and Structures 45 (5) (2008) 1196–1216. (Cited on pages 9 and 18.)

[33] C. Soize, Modélisation probabiliste du flou structural en dynamique linéaire des système mécaniques complexes. i-éléments théoriques, La Recherche Aérospatiale 5 (1996) 23–48. (Cited on page 11.)

[34] C. Farhat, I. Harari, L. Franca, The discontinuous enrichment method, Computer Methods in Applied Mechanics and Engineering 190 (2001) 6455–6479. (Cited on page 11.)

[35] C. Soize, A model and numerical method in the medium frequency range for vibroacoustic predictions using the theory of structural fuzzy, Journal of the Acoustical Society of America 94 (2) (2003) 849–865. (Cited on page 11.)

[36] J. Berthaut, M. N. Ichchou, L. Jézéquel, K-space identification of apparent structural behavior, Journal of Sound and Vibration 280 (2005) 1125–1131. (Cited on pages 11, 129 and 130.)

[37] F. Sui, M. Ichchou, Prediction of vibracoustic energy using a new energy approach, Journal of Vibration and Acoustic, ASME transactions 126 (2) (2004) 184–190. (Cited on page 11.)

[38] A. Bocquillet, M. Ichchou, L. Jézéquel, Energetics of axisymmetric fluid-filled pipes up to high frequencies, Journal of Fluid Structures 17 (2003) 491–510. (Cited on pages 11, 18, 21 and 36.)

[39] E. Crawley, J. de Luis, Use of piezoceramic actuators as elements of intelligent structures, AIAA Journal 25 (1987) 1373–1385. (Cited on page 11.)

[40] C. K. Lee, Theory of laminated piezoelectric plates for the design of distributed sensors/actuators. i: Governing equations and reciprocal relationships, The Journal of the Acoustical Society of America 87 (3) (1990) 1144–1158. (Cited on page 11.)

[41] X. D. Zhang, C. T. Sun, Formulation of an adaptive sandwich beam, Smart Materials and Structures 5 (6) (1996) 814–823. (Cited on page 11.)

[42] Y. H. Hu, W. Y. Yao, Wave propagation modeling of the pzt sensing region for structural health monitoring, Smart Materials and Structures 16 (3) (2007) 706–716. (Cited on page 12.)

[43] C. Park, Dynamics modelling of beams with shunted piezoelectric elements, Journal of Sound and Vibration 268 (1) (2003) 115–129. (Cited on page 12.)

[44] A. Benjeddou, Advances in piezoelectric finite element modeling of adaptive structural elements: a survey, Computers and Structures 76 (2000) 347–363. (Cited on pages 12 and 38.)

[45] W. X. Zhong, F. Williams, On the direct solution of wave propagation for repetitive structures, Journal of Sound and Vibration 181 (3) (1995) 485–501. (Cited on pages 12, 20, 21, 30 and 70.)

[46] J.-M. Mencik, M. N. Ichchou, Multi-mode propagation and diffusion in structures through finite elements, European Journal of Mechanics - A/Solids 24 (5) (2005) 877–898. (Cited on pages 12, 18, 19, 22, 36, 53, 70, 71, 145 and 191.)

[47] J.-M. Mencik, M. N. Ichchou, Wave finite elements in guided elastodynamics with internal fluid, International Journal of Solids and Structures 44 (2007) 2148–2167. (Cited on pages 12, 18, 25, 26, 70 and 114.)

[48] M. N. Ichchou, S. Akrout, J.-M. Mencik, Guided waves group and energy velocities via finite elements, Journal of Sound and Vibration 305 (2007) 931–944. (Cited on pages 12, 18 and 70.)

[49] M. N. Ichchou, J.-M. Mencik, W. Zhou, Wave finite elements for low and mid-frequency description of coupled structures with damage, Computer methods in applied mechanics and engineering 198 (15-16) (2009) 1311–1326. (Cited on pages 12, 18 and 146.)

[50] W. Zhou, M. N. Ichchou, Wave propagation in mechanical waveguide with curved members using wave finite element solution, Computer Methods in Applied Mechanics and Engineering 199 (33-36) (2010) 2099–2109. (Cited on page 12.)

[51] W. Zhou, M. N. Ichchou, Wave scattering by local defect in structural waveguide through wave finite element method, Structural Health Monitoring 10 (4) (2011) 335–349. (Cited on pages 12 and 83.)

[52] W. Zhou, M. N. Ichchou, Finite element techniques for calculations of wave modes in one-dimensional structural waveguides, Structural Control and Health Monitoring 18 (7) (2011) 737–751. (Cited on page 12.)

[53] B. R. Mace, D. Duhamel, M. J. Brennan, L. Hinke, Finite element prediction of wave motion in structural waveguides, Journal of Acoustical Society of America 117 (5) (2005) 2835–2843. (Cited on pages 12 and 18.)

[54] D. Duhamel, B. R. Mace, M. J. Brennan, Finite element analysis of the vibrations of waveguides and periodic structures, Journal of Sound and Vibration 294 (1-2) (2006) 205–220. (Cited on pages 12, 18 and 28.)

[55] B. R. Mace, E. Manconi, Modelling wave propagation in two-dimensional structures using finite element analysis, Journal of Sound and Vibration 318 (4-5) (2008) 884–902. (Cited on page 12.)

[56] M. Collet, M. Ouisse, M. Ruzzene, M. N. Ichchou, Floquet-bloch decomposition for the computation of dispersion of two-dimensional periodic, damped mechanical systems, International Journal of Solids and Structures 48 (20) (2011) 2837–2848. (Cited on pages 12 and 21.)

[57] D. J. Mead, A general theory of harmonic wave propagation in linear periodic systems with multiple coupling, Journal of Sound and Vibration 27 (2) (1973) 235–260. (Cited on pages 17 and 70.)

[58] L. Houillon, Modélisation vibratoire des carrosseries automobiles en moyennes et hautes fréquences, Ph.D. thesis, Ecole Centrale de Lyon, Ecully, France. (Cited on page 18.)

[59] A. Bocquillet, Méthode energétique de caractérisations vibroacoustiques des réseaux complexes, Ph.D. thesis, Ecole Centrale de Lyon, Ecully, France. (Cited on page 18.)

[60] W. Zhou, Structural multi-mode wave propagation and health monitoring, Ph.D. thesis, Ecole Centrale de Lyon, Ecully, France. (Cited on page 18.)

[61] L. Houillon, M. Ichchou, L. Jezequel, Wave motion in thin-walled structures, Journal of Sound and Vibration 281 (2005) 483–507. (Cited on pages 18 and 70.)

[62] M. Maess, Methods for efficient acoustic-structure simulation of piping systems, Ph.D. thesis, University of Stuttgart, Stuttgart, Germany (2006). (Cited on page 18.)

[63] F. Chen, P. Wilcox, The effect of load on guided wave propagation, Ultrasonics 47 (2007) 111–122. (Cited on page 18.)

[64] T. L. Huang, M. N. Ichchou, O. A. Bareille, Multi-mode wave propagation in damaged stiffened panels, Structural Control and Health Monitoring 19 (5) (2012) 609–629. (Cited on pages 18 and 177.)

[65] N. W. M. Maess, L. Gaul, Dispersion curves of fluid filled elastic pipes by standard fe models and eigenpath analysis, Journal of Sound and Vibration 296 (2006) 264–276. (Cited on page 18.)

[66] A. Chen, F. Li, Y. Wang, Localization of flexural waves in a disordered periodic piezoelectric beam, Journal of Sound and Vibration 304 (3-5) (2011) 863–874. (Cited on page 18.)

[67] M. Leamy, Exact wave-based bloch analysis procedure for investigating wave propagation in two-dimensional periodic lattices, Journal of Sound and Vibration 331 (7) (2012) 1580–1596. (Cited on page 18.)

[68] J.-M. Mencik, M. N. Ichchou, A substructuring technique for finite element wave propagation in multi-layered systems, Computer Methods in Applied Mechanics and Engineering 197 (6-8) (2008) 505–523. (Cited on pages 18, 28, 29, 30, 36, 71, 171 and 191.)

[69] Y. Waki, B. R. Mace, M. Brennan, Numerical issues concerning the wave and finite element method for free and forced vibrations of waveguides, Journal of Sound and Vibration 327 (2009) 92–108. (Cited on pages 25 and 83.)

[70] J. Renno, B. Mace, On the forced response of waveguides using the wave and finite element method, Journal of Sound and Vibration 329 (2010) 5474–5488. (Cited on page 25.)

[71] Y. Yong, Y. K. Lin, Propagation of decaying waves in periodic and piecewise periodic structures of finite length, Journal of Sound and Vibration 129 (2) (1989) 99–118. (Cited on page 26.)

[72] J.-M. Mencik, M. N. Ichchou, L. Jézéquel, Propagation multimodale dans les systèmes périodiques couplés, Revue Européenne de Mécanique Numérique 15 (1-3) (2006) 293–306. (Cited on pages 26 and 28.)

[73] R. Ohayon, C. Soize, Structural Acoustics and Vibration, Academic Press, San Diego, 1998. (Cited on page 29.)

[74] L. Brillouin, Wave Propagation in Periodic Structures, McGraw-Hill, New York, 1946. (Cited on pages 33 and 162.)

[75] V. Piefort, Finite element modelling of piezoelectric active structures, Ph.D. thesis, Université Libre de Bruxelles, Brussels (2001). (Cited on page 41.)

[76] B. R. Mace, Wave reflection and transmission in beams, Journal of Sound and Vibration 97 (1984) 237–246. (Cited on page 51.)

[77] J. Murin, M. Aminbaghai, V. Kutis, Exact solution of the bending vibration problem of FGM beams with variation of material properties, Engineering structures 32 (6) (2010) 1631–1640. (Cited on page 52.)

[78] N. G. Stephen, On the vibration of one-dimensional periodic structures, Journal of Sound and Vibration 227 (1999) 1133–1142. (Cited on page 53.)

[79] G. Dai, W. Zhang, Cell size effects for vibration analysis and design of sandwich beams, Acta Mechanica Sinica 25 (6) (2009) 353–365. (Cited on page 53.)

[80] ANSYS, Theory reference, release 9.0, ANSYS Inc. (2004). (Cited on page 60.)

[81] L. Gavric, Finite element computation of dispersion properties of thin-walled waveguides, Journal of Sound and Vibration 173 (1) (1994) 113–124. (Cited on page 70.)

[82] L. Gavric, Computation of propagative waves in free rail using a finite element technique, Journal of Sound and Vibration 185 (3) (1995) 531–543. (Cited on page 70.)

[83] A. S. Gendy, A. F. Saleeb, Vibration analysis of coupled extensional/flexural/torsional modes of curved beams with arbitrary thin-walled sections, Journal of Sound and Vibration 174 (2) (1994) 261–274. (Cited on page 70.)

[84] M. Mitra, S. Gopalakrishnan, M. S. Bhat, A new super convergent thin walled composite beam element for analysis of box beam structures, International Journal of Solids and Structures 41 (5-6) (2004) 1491–1518. (Cited on page 70.)

[85] M. Collet, M. Ouisse, K. A. Cunefare, M. Ruzzene, B. Beck, L. Airoldi, F. Casadei, Vibration and Structural Acoustics Analysis, 1st Edition, Springer, Berlin, 2011, Ch. 10, pp. 265–302. (Cited on pages 112, 175, 176 and 199.)

[86] C. Hellier, Handbook of Nondestructive Evaluation, McGraw-Hill, New York, 2001. (Cited on page 127.)

[87] D. Fitting, L. Adler, Ultrasonic Spectral Analysis for Non-destructive Evaluation, Plenum Press, New York, 1981. (Cited on page 127.)

[88] J. Krautkramer, H. Krautkramer, Ultrasonic Testing of Materials, Springer Verlag, New York, 1990. (Cited on page 127.)

[89] J. L. Rose, Ultrasonic Waves in Solid Media, Cambridge University Press, 1999. (Cited on page 128.)

[90] J. L. Rose, A baseline and vision of ultrasonic guided wave inspection potential, Journal of Pressure Vessel Technology 124 (3). (Cited on page 128.)

[91] I. A. Viktorov, Rayleigh and Lamb Waves – Physical Theory and Applications, Plenum Press, New York, 1967. (Cited on page 128.)

[92] W. Staszewski, C. Bollerand, G. Tomlinson, Health monitoring of aerospace structures Smart Sensors and Signal Processing, Wiley, New York, 2004. (Cited on page 128.)

[93] A. Haig, P. Mudge, T.-H. Gan, W. Balachandran, Advanced transducer development for long range untrasonic inspection systems, Taylor & Francis/Balkema, Leidon, The Netherlands, 2008, pp. 79–82. (Cited on page 128.)

[94] D. N. Alleyne, P. Cawley, The interaction of Lamb waves with defects, IEEE Ultrasonics, Ferroelectrics, and Frequency Control Society 39 (1992) 381–396. (Cited on page 128.)

[95] D. Balageas, C.-P. Fritzen, A. Güemes, Structural Health Monitoring, ISTE, 2005. (Cited on page 128.)

[96] R. Grice, R. Pinnington, A method for the vibration analysis of built-up structures. part I: introduction and analytical analysis of the plate-stiffened beam., Journal of Sound and Vibration 230 (4) (2000) 825–849. (Cited on page 128.)

[97] R. Grice, R. Pinnington, A method for the vibration analysis of built-up structures. part II: analysis of the plate-stiffened beam using a combination offinite element analysis and analytical impedances, Journal of Sound and Vibration 230 (4) (2000) 851–875. (Cited on page 128.)

[98] M. Ruzzene, Frequency - wavenumber domain filtering for improved damage visualization, Journal of Smart Materials and Structures 16 (6) (2007) 2116–2129. (Cited on pages 128 and 129.)

[99] V. Sharma, S. Hanagud, M. Ruzzene, Damage index estimation in beams and plates using laser vibrometry, AIAA Journal 44 (4) (2006) 919–923. (Cited on page 128.)

[100] R. Basri, W. Chiu, Numerical analysis on the interaction of guided Lamb waves with a local elastic stiffness reduction in quasi-isotropic composite plate structures, Journal of Composite structures 66 (1-4) (2004) 87–99. (Cited on page 129.)

[101] D. Alleyne, P. Cawley, A two-dimensional Fourier transform method for the measurement of propagating multimode signals, Journal of the Acoustical Society of America 89 (3) (1991) 1159–1168. (Cited on page 129.)

[102] M. Ichchou, O. Bareille, J. Berthaut, Identification of effective sandwich structural properties via an inverse wave approach, Engineering Structures 30 (2008) 2591–2604. (Cited on page 129.)

[103] R. Lyon, R. Dejong, Theory and Application of Statistical Energy Analysis, Butterworth-Heinemann, 1995. (Cited on page 132.)

[104] D. Ewins, Modal testing, Research Studies Press, New York, 1984. (Cited on page 132.)

[105] N. S. Ferguson, C. R. Halkyard, B. G. Mace, K. H. Heron, The estimation of wavenumbers in two dimensional structures, in: Proceedings of ISMA 2002 - II, 2002, pp. 799–806. (Cited on page 133.)

[106] U. Orrenius, S. Finnveden, Calculation of wave propagation in rib-stiffened plate structures, Journal of Sound and Vibration 198 (2) (1996) 203–224. (Cited on page 136.)

[107] S. Timoshenko, On the correction of transverse shear deformation of the differential equations for transverse vibrations of prismatic bars., Philosophical Magazine 41 (1921) 744–746. (Cited on page 136.)

[108] S. Timoshenko, S. Woinowski-Krieger, Theory of Plates an Shells, 2nd Edition, McGraw-Hill, New York, 1989. (Cited on page 136.)

[109] R. Ohayon, R. Sampaio, C. Soize, Energetics of axisymmetric fluid-filled pipes up to high frequencies, in: Trans.ASME, Vol. 64, 1997, pp. 292–298. (Cited on pages 165 and 172.)

[110] Y. Fung, Foundations of Solid Mechanics, Prentice-Hall, Englewood Cliffs, NJ, 1965. (Cited on page 165.)

[111] M. Geradin, D. Rixen, Mechanical Vibrations: Theory and Application to Structural Dynamics, Wiley, Paris, 1994. (Cited on page 166.)

List of Figures

List of Tables

AUTORISATION DE SOUTENANCE

Vu les dispositions de l'arrêté du 7 août 2006,

Vu la demande du Directeur de Thèse

Monsieur M. ICHCHOU

et les rapports de

Monsieur A. BENJEDDOU
Professeur - SUPMECA - 3, rue Fernand Hainaut - 93407 SAINT-OUEN cedex

et de

Monsieur H. LISSEK
Directeur de Recherche - EPFL STI IEL LEMA - ELB 040 (Bâtiment ELB) Station 11 - CH-1015 Lausanne
Suisse

Monsieur HUANG Tianli

est autorisé à soutenir une thèse pour l'obtention du grade de **DOCTEUR**

Ecole doctorale MECANIQUE, ENERGETIQUE, GENIE CIVIL ET ACOUSTIQUE

Fait à Ecully, le 9 novembre 2012

P/Le directeur de l'E.C.L.
La directrice des Etudes

SCOLARITE
3ème Cycle

M-A. GALLAND